

## **Dissertation**

# **The Vortex Model in Lattice Quantum Chromo Dynamics**

ausgeführt zum Zwecke der Erlangung des akademischen Grades eines Doktors  
der technischen Wissenschaften unter der Leitung von

Ao.Univ.Prof. Dipl.-Ing. Dr.techn. Manfred Faber  
Institutsnummer E141  
Atominstitut der Österreichischen Universitäten

eingereicht an der Technischen Universität Wien  
Fakultät für Physik

von

Dipl.-Ing. Roman Bertle  
Matrikelnummer e9225543  
Dettergasse 1/2/2/7  
A-1160 Wien

Wien, am 14. September 2005

Mein Dank gilt Prof. Manfred Faber und den Kollegen am  
Atominstitut / Abteilung für Kernphysik für ihren Rat und Tat,  
für Ideen und Diskussionen. Besonders danke ich meinen Eltern für  
all ihre Unterstützung in den Jahren in denen diese Arbeit  
entstanden ist.

## Kurzfassung

Heutzutage wird die Quantenchromodynamik (QCD) als Teil des Standardmodelles der Teilchenphysik allgemein als die korrekte Theorie für die starke Wechselwirkung angesehen. Eine besondere Eigenschaft der QCD ist die Beobachtung, dass die fundamentalen Fermionen der Theorie nicht als freie Teilchen auftreten, sondern stets als Bausteine zusammengesetzter Teilchen, nämlich der Hadronen, z.B. Proton und Neutron. Wegen der Größe der starken Kopplungskonstanten  $g$  kann die Störungstheorie, welche die QCD bei hohen Energien erfolgreich behandeln kann, nicht auf Niederenergieprobleme wie den Quarkeinschluss angewandt werden. Eine Methode um die Niederenergie-QCD dennoch zu untersuchen ist eine Regularisierung der Theorie, welche die kontinuierliche Raumzeit durch ein diskretes euklidisches Gitter ersetzt. Das eröffnet den Weg sowohl zu analytischen Rechnungen wie auch zur numerischen Simulation der QCD durch das Monte-Carlo-Verfahren. Obwohl der Quarkeinschluss klar am Gitter gezeigt werden kann, existiert trotzdem noch immer kein unumstrittenes Modell für den Mechanismus des Quarkeinschlusses in der QCD. In den letzten Jahren allerdings rückte solch ein Modell, das Vortexmodell, wieder vermehrt in den Mittelpunkt des Interesses. Dieses Modell wurde bereits in den Siebzigern entwickelt, aber erst Ende der Neunziger konnte es durch die fortschreitende Rechentechnik numerisch am Gitter überprüft werden.

Im Vortexmodell ist das Zentrum der Eichgruppe entscheidend für den Quarkeinschluss; in dieser Arbeit untersuchen wir, wie für die Eichgruppe  $SU(2)$  die Zentrumsfreiheitsgrade aus Eichfeldkonfigurationen extrahiert werden können. Die Anregungen dieser Freiheitsgrade werden als P-Vortices bezeichnet und können als zweidimensionale Flächen auf dem vierdimensionalen Raumzeitgitter dargestellt werden; sie sollen die für den Quarkeinschluss verantwortlichen Objekte im QCD-Vakuum identifizieren. Diese Objekte sind Träger eines quantisierten magnetischen Flusses und werden als dicke Vortices bezeichnet.

Wir zeigen in ausführlichen numerischen Untersuchungen wie mit Hilfe von geeigneten Eichungen Vortices erfolgreich identifiziert werden können und beleuchten die Mängel der verschiedenen Detektionsmethoden sowie die Wege, diese Mängel zu überwinden. Hierauf untersuchen wir die Eigenschaften der extrahierten P-Vortices; wir finden, dass diese komplizierte, nichtorientierbare Zufallsflächen sind, die das ganze Gitter durchziehen. Diese und andere Vortexeigenschaften stehen in guter Übereinstimmung mit den Anforderungen für die Erklärung des Quarkeinschlusses. Der Zusammenhang zwischen Vortexeigenschaften und Quarkeinschluss wird weiter ausgedehnt auf Systeme bei endlicher Temperatur, solche in der Phase des Quark-Gluon-Plasmas und auch auf Systeme mit dynamischen Materiefeldern. Für all diese Systeme ist der Mechanismus des Quarkeinschlusses mehr oder weniger unterschiedlich, diese Änderungen spiegeln sich gut in den untersuchten Vortexeigenschaften wider.

Schlussendlich wird das Vortexmodell auch auf andere Infraroteigenschaften der QCD, die nicht unmittelbar mit dem Quarkeinschluss zusammenhängen, insbesondere auf die

topologischen Eigenschaften der Eichfelder, angewandt. Konkret zeigen wir, wie die topologische Suszeptibilität aus den extrahierten P-Vortices berechnet werden kann. Auf diese Weise liefert das Vortexmodell ein vereinheitlichtes Bild für den infraroten, niederenergetischen Sektor der QCD und kann sowohl den Quarkeinschluss als auch die chiralen und topologischen Eigenschaften der starken Wechselwirkung beschreiben.

## Abstract

Being part of the standard model of particle physics, quantum chromo dynamics (QCD) is generally believed to be the correct theory of the strong interactions. A particular feature of QCD is that its fundamental fermions, the quarks, cannot be observed as free particles, but are always confined in composite particles, the hadrons, such as the protons and neutrons. Due to the large value of the strong coupling constant  $g$ , perturbation theory, which can treat successfully QCD at high energies, cannot be applied to the low energy problem of confinement. One method to investigate low energy QCD is to regularise the theory reducing the continuous space-time to a discrete Euclidean lattice. This opens the way both for analytical calculations and for numerical simulations of QCD on computers via Monte Carlo methods. But although confinement could be persuasively shown on the lattice, there exists still no indisputable model explaining how confinement exactly emerges from QCD. In the last years there has arisen a new interest for the vortex model of confinement. This model has already been suggested in the seventies, but only since the late nineties the improving computer technology enabled numerical tests of the vortex model on the lattice.

The vortex model claims that the center of the gauge group is crucial for confinement; in this work we investigate how, for the gauge group  $SU(2)$ , the center degrees of freedom can be extracted from gauge field configurations. The excitations of the extracted d.o.f. are dubbed as P-vortices and can be represented by two-dimensional surfaces on the four-dimensional lattice; they are thought to indicate objects present in configurations before the extraction step. These objects are called thick vortices, carry quantised magnetic center charges and are responsible for confinement according to the vortex model.

In detailed numerical studies we show how using appropriate gauges one can successfully detect vortices, we highlight the shortcomings of various detection methods and investigate how to overcome these shortcomings. Next we look at the properties of the extracted P-vortex surfaces; we find that they are complicated, unorientable random surfaces percolating through the lattice. These and other P-vortex properties are in good agreement with the requirements to explain confinement. The connection between vortex properties and confinement is further extended to systems at finite temperature, in the phase of the quark-gluon plasma, and to systems with dynamical matter fields. For all these systems confinement is more or less changed, and this is properly reflected in the investigated vortex properties.

Finally, the vortex model could be applied to other infrared features of QCD not immediately related to confinement, namely the topological properties of gauge fields. In particular we show how the topological susceptibility present in QCD can be accurately calculated from the extracted P-vortex surfaces. This way the vortex model provides an unified picture for the infrared, low energy sector of QCD explaining both confinement and the chiral and topological features of the strong interaction.

# Contents

<b>1</b>	<b>Introduction</b>	<b>8</b>
<b>2</b>	<b>QCD on the Lattice</b>	<b>10</b>
2.1	Gauge Theory . . . . .	10
2.2	Lattice Formulation . . . . .	13
2.3	Quantisation . . . . .	15
2.3.1	Path integral formalism . . . . .	15
2.3.2	Gauge fields . . . . .	16
2.3.3	Hamiltonian Formalism . . . . .	16
2.3.4	Finite Temperature . . . . .	17
2.4	Continuum limit . . . . .	18
2.5	Monte Carlo Techniques . . . . .	19
<b>3</b>	<b>Confinement and the Vortex Model</b>	<b>22</b>
3.1	Colour confinement . . . . .	22
3.2	Wilson Loop . . . . .	23
3.3	Polyakov Loop . . . . .	25
3.4	Vortices . . . . .	26
<b>4</b>	<b>Detection of Vortices</b>	<b>29</b>
4.1	Introduction . . . . .	29
4.2	Maximal Center Gauges . . . . .	30
4.2.1	Numeric Tests – Overview . . . . .	33
4.2.2	Center Dominance and Vortex Density – Overview . . . . .	35
4.2.3	$N_{copy}$ and Lattice Size Dependence . . . . .	39
4.2.4	Gauge-Fixing Convergence Criterion . . . . .	42
4.2.5	Problems . . . . .	44
4.3	Laplacian Methods . . . . .	45
4.3.1	Gauging Using Eigenvectors . . . . .	45
4.3.2	From Eigenvectors to Gauge Matrices . . . . .	47
4.3.3	Gauge Singularities . . . . .	49
4.3.4	A Simple Configuration . . . . .	49
4.3.5	Numerical Investigations . . . . .	54
4.4	Conclusions . . . . .	65

<b>5</b>	<b>Structure of Vortices</b>	<b>66</b>
5.1	P-vortex Surface . . . . .	66
5.1.1	Visualisation of P-vortex Surfaces . . . . .	69
5.2	Vortex Density . . . . .	71
5.2.1	Scaling of the Density . . . . .	71
5.3	Correlations and Fluctuations . . . . .	73
5.4	Size of P-vortices . . . . .	78
5.5	Topological Properties . . . . .	81
5.6	Structure of P-vortices at Finite Temperature . . . . .	84
5.7	Structure of Thick Vortices . . . . .	95
5.8	Conclusions . . . . .	97
<b>6</b>	<b>Vortices with Matter Fields</b>	<b>99</b>
6.1	The SU(2)-Higgs Model . . . . .	99
6.2	Finite Temperature . . . . .	102
6.3	Zero Temperature . . . . .	106
6.3.1	The Kertész Line . . . . .	112
6.4	Discussion at Conclusions . . . . .	115
<b>7</b>	<b>Vortices and the Topological Properties of QCD</b>	<b>117</b>
7.1	Topological Properties of Yang-Mills Fields . . . . .	117
7.1.1	An Interlude about Instantons . . . . .	118
7.2	Topological Charge from Vortices . . . . .	119
7.3	Topological Charge of P-vortices on the Lattice . . . . .	120
7.3.1	Resolving Lattice Ambiguities . . . . .	121
7.3.2	Types of Singular Points . . . . .	121
7.3.3	Elimination of Short Range Fluctuations . . . . .	124
7.4	Numerical Measurements and Discussion . . . . .	124
7.5	Local Correlations . . . . .	133
<b>8</b>	<b>Conclusions and Outlook</b>	<b>137</b>
	<b>Bibliography</b>	<b>139</b>
	<b>Index</b>	<b>148</b>

# 1 Introduction

Within the standard model, the strong interaction is successfully described by quantum chromodynamics (QCD). QCD is a non-abelian, Yang-Mills quantum gauge theory with colour gauge group  $SU(2)$ . The fundamental fermions of QCD are the quarks which interact via gluons, the quanta of the gauge field. In QCD, hadronic particles such as the nucleons, proton and neutron, are thought to consist of quarks. Using perturbation theory, many high energy properties of the strong interaction could be satisfactorily described, such as asymptotic freedom. The latter means that the strength of the interaction between quarks decreases at short distances, which enables a perturbative treatment of QCD despite its large coupling constant  $g$ . Asymptotic freedom suggests that the inverse is also true, the effective coupling increases at low energies and thus at large distances. This increase gives a hint for the solution of a notable problem of QCD, the confinement problem. In nature, the fundamental particles of QCD, the quarks, are never observed as free particles, they are always contained in hadrons. Unfortunately confinement cannot be explained using perturbation theory because of the large coupling constant  $g$ .

Hence non-perturbative methods had to be pushed forward to treat confinement. It was Wilson [Wil44] who suggested to put quantum gauge theories on a discrete Euclidean lattice instead of on continuous space-time. Analytic calculations on the lattice such as the strong coupling expansion indeed could confirm the confinement hypothesis. Most convincing were numerical calculations following the pioneering work of Creutz [Cre80]; nowadays computer simulations are successfully used to study a wide range of properties of the strong interaction, such as particle spectra. The non-perturbative methods showed that the colour electric field between a colour charge-anticharge pair does not spread out as in electrodynamics, but squeezes into a flux tube, the string, connecting the charges. Because the energy density in such a flux tube is almost independent of its length, the potential between the charges increases linearly with their distance. Hence the charges cannot be separated using a finite amount of energy, they are confined. This picture is supported by the observations of Regge trajectories. If the spin of mesons is plotted against their squared mass, the mesons lie on straight lines. This can be understood in a simple model featuring a pair of massless quarks connected by a string, where the different mesons are excited rotational states.

Although confinement could be convincingly shown on the lattice, there exists still no indisputable model explaining how confinement emerges from QCD. But in the last years there has been renewed interest, within the lattice gauge theory community, in the center vortex theory of confinement which has already been pushed forward in the 70s [tH78, ACY78, NO79, Mac80a, AO80b, AO80a, Vin78, Yon78, Cor79, Fey81]. The revival of this old idea is due to a number of numerical studies, which all indicate that



center vortices are ubiquitous in the QCD vacuum and give rise to the linear confining potential [DFGO97, DFGO98, DFG<sup>+</sup>98, FGO99a, dFD99, ADdF00, LRT98, ELRT00, LTER99, GLSR00, Ber98, BFGO99, BVZ99, KT00, HLST00].

Vortices can be thought to be flux tubes carrying a quantised colour magnetic flux. This quantised flux takes values in the center of the gauge group, In QCD these are the  $SU(3)$  and  $Z_3$  groups, respectively, whereas in this work mainly the simpler gauge group  $SU(2)$  with its center  $Z_2$  is investigated. In the Euclidean path integral formulation, these vortices have the shape of two-dimensional closed surfaces in the four-dimensional space-time. The vortex surfaces have some finite thickness in which the center flux is spread out somewhat. The random fluctuations of these surfaces induce center disorder causing the linear rising potential between colour charges, and thus confinement.

To test the vortex picture numerically, various methods have been proposed to detect vortices in gauge field configurations. Most of these methods impose a gauge to isolate as much as possible of the center degrees of freedom, and then neglect the non-center part of the fields. Such a procedure replaces gauge fields containing the aforementioned thick vortices by a configuration of thin vortices, also called P-vortices. In P-vortices the center flux extending over a finite cross-section of thick vortices is compressed into an infinite thin surface. All preserved information about a configuration is described by the shape and position of the P-vortex surfaces in four-dimensional space-time.

In this work we investigate to what extend the non-perturbative properties of the strong interaction can be isolated in P-vortices. The structure of the work is as follows: In chapter 2 we give a short introduction to gauge theories on an Euclidean space-time lattice. We define the elements of the theory such as the action, observables and gauges. Finally Monte Carlo methods to simulate the theory on computers are introduced. In chapter 3 the phenomenon of quark confinement is discussed. Observables used to investigate confinement are introduced, and the vortex model is presented as an explanation for confinement. The basic features of the vortex model and some numeric results are introduced and discussed. The detailed investigations of the vortex model start in chapter 4, where various methods to detect and identify vortices in Monte Carlo simulations are defined, examined and discussed. We show the dependence of these methods on various parameters, their shortcomings and how to overcome the shortcomings. Chapter 5 deals with the properties and the structure of vortices found using the methods introduced in chapter 4. These properties agree well with the constraints imposed by the requirement that vortices explain the confining properties of the strong force. Up to chapter 6, all calculations have been done using the quenched approximation which decouples dynamic matter field (i.e. the quark fermion fields) from the investigated gauge fields with their vortex content. In chapter 6 the influence of matter fields is studied using the simpler  $SU(2)$ -Higgs model, and it is shown that the vortex picture of confinement holds also after including dynamic matter fields. Finally in chapter 7 it is shown that the vortex model is not only able to treat quark confinement, but can also explain other important features of the strong interaction at low energies, namely the topological properties, providing us with an unified picture of the infrared sector of QCD.

# 2 Quantum Chromo Dynamics on the Lattice

## Abstract

We give a short summary of gauge theory, introduce the formulation on the lattice and describe Monte Carlo techniques. This is mostly done in order to fix the notation; for details we refer to the textbooks on gauge theory [Ish89, IV97, KN63, Nak90, SU95], and on quantum fields on the lattice and the Monte Carlo method [Rot92, MM94].

## 2.1 Gauge Theory

Quantum chromo dynamics (QCD) is a non-abelian, Yang-Mills quantum gauge theory with colour gauge group  $SU(3)$ . In the language of fibre bundles we can describe gauge theories using vector and principal fibre bundles. In this section we briefly fix our notion. The gauge transformations are formulated as a principle bundle  $(P, M, \pi, G)$ , where  $P$  is the total space, the base space  $M$  is some manifold,  $\pi$  the projection from  $P$  on  $M$ , and the fibre is some Lie group  $G$ ; as abbreviation, we denote the whole principal bundle as  $P$ . In the continuum,  $M$  is Minkowski space-time, after performing Wick rotation it is the four-dimensional Euclidean space-time  $\mathbb{R}^4$ .

Gauge transformations act on fields transforming as some representation of the considered gauge group  $G$ . These fields are defined as vector bundles  $(E, M, \pi, V, G)$  associated to the principal bundle  $P$ , where  $E$  is the total space and the fibre is some vector space  $V$ . As shorthand notation we use  $E$  for the vector bundle. In the case of QCD, the fields are the fermionic spinor fields  $\psi_f$  with flavour index  $f$  which transform according to the fundamental representation of the gauge group  $SU(3)$ . In this work we will mainly use a simplified model for QCD taking instead of  $SU(3)$  the simpler, but still non Abelian group  $SU(2)$ . For our studies on the influence of the matter fields on the gauge fields in chapter 6, we will consider the numerical less involved scalar fields instead of quarks, where the fibre  $V$  is a two-dimensional complex vector space  $\mathbb{C}^2$  transforming with the fundamental representation of  $SU(2)$ . Finally, fields in the adjoint representation of the gauge group will be important for the investigations on Laplacian gauges presented in section 4.3. We write sections of a vector bundle (i.e. vector field configurations) as  $\varphi, \psi, \xi, \zeta, \dots$ , and sections of the tangent bundle  $T(M)$  (i.e. Lorentz vector fields) as  $v, w, u, \dots$ .

Gauge fields are related to connections on the principal bundle, and can be regarded

## 2.1 Gauge Theory

as  $\mathfrak{g}$ -valued one-forms on  $M$ , where  $\mathfrak{g}$  is the Lie algebra of the Lie group  $G$ . In the case of  $G = \text{SU}(2)$  we have the Lie algebra  $\mathfrak{su}(2)$ . We denote the operator of the covariant derivative  $\nabla$  as

$$\nabla_v: C^\infty(E) \rightarrow C^\infty(E). \quad (2.1)$$

The covariant derivative acts on smooth sections  $\varphi \in C^\infty(E)$  of the given vector bundle  $E$ .  $v$  is an (Euclidean) Lorentz vector field, i.e. a section of the tangent bundle  $T(M)$ .

Next we introduce (for a local region of  $M$ ) base vectors  $\partial_\mu$  ( $\mu = 1, 2, 3, 4$ ) in tangent space  $T(M)$ ,  $dx^\mu$  dual to  $\partial_\mu$  in cotangent space  $T^*(M)$  and  $e_i(x)$  ( $i = 1, \dots, \dim V$ ) in colour space  $V$ . In terms of gauge theory, the choice of  $e_i(x)$  is equivalent to choosing a gauge, and gauge transformations are written as

$$\bar{e}_i = S_i^j e_j \quad (2.2)$$

$\nabla$  acts on the colour space base vectors as

$$\nabla_v e_i = \omega_i^j(v) e_j, \quad (2.3)$$

where the matrix of one-forms  $\omega = [\omega_i^j]$  is the connection form and can be interpreted as a  $\mathfrak{g}$ -valued one-form. Under gauge transformations the connection form changes as

$$\bar{\omega} = S^{-1} \omega S - S^{-1} dS. \quad (2.4)$$

The exterior covariant derivative  $D_\nabla$  acts on some  $\mathfrak{g}$ -valued one-forms  $\varphi$  and is given by

$$D_\nabla \varphi = d\varphi + \omega \wedge \varphi, \quad (2.5)$$

where  $\wedge$  denotes a combination of the wedge product of forms and the action of the algebra on the vector.

Using also the base vectors in tangent space, and writing explicitly the dependence on  $x$ , we get the more familiar notion of a gauge field as

$$[\nabla_{\partial_\mu} e_i](x) = ig \mathcal{A}_{i\mu}^j(x) e_j(x) \quad (2.6)$$

where the matrices  $igA_\mu = [ig\mathcal{A}_i^j]_\mu = \omega(\partial_\mu)$  are elements of the Lie algebra  $\mathfrak{g}$ , and  $g$  is the gauge coupling constant. Algebra elements can be written using their generators  $\mathbf{T}_m = [\mathbf{T}_i^j]_m, m = 1, \dots, \dim \mathfrak{g}$ ; the Lie product (commutator) of the generators fulfil

$$[\mathbf{T}_m, \mathbf{T}_n] = C_{mn}^l \mathbf{T}_l, \quad (2.7)$$

where  $C_{mn}^l$  are the structure constants. Using the generators we can write the gauge field as  $A_\mu^m \mathbf{T}_m = A_\mu$ . Writing  $v = v^\mu \partial_\mu$  and  $\varphi = \varphi^i e_i$ , we arrive for the covariant derivative at

$$\nabla_{v^\mu \partial_\mu} (\varphi^i e_i) = ((\partial_\mu \varphi^i) v^\mu + ig \mathcal{A}_{j\mu}^i v^\mu \varphi^j) e_i = (\mathcal{D}_\mu \varphi^i) v^\mu e_i \quad (2.8)$$

with

$$\mathcal{D}_\mu \varphi^i := \partial_\mu \varphi^i + ig \mathcal{A}_{j\mu}^i \varphi^j \quad (2.9)$$

## 2.1 Gauge Theory

The gauge transformation for the  $A_\mu$  field reads

$$\bar{A}_\mu = S^{-1}A_\mu S + S^{-1}\partial_\mu S. \quad (2.10)$$

The parallel transport will be important on the lattice and is determined by the connection. It associates the fibres at two points  $x$  and  $y$  connected by some path  $\mathcal{C}_{xy}$  and is given by

$$\mathcal{U}[\mathcal{C}_{xy}] = \mathcal{P} \exp \left( - \int_{\mathcal{C}} \boldsymbol{\omega} \right), \quad (2.11)$$

where  $\mathcal{P}$  is the path ordering operator taking into account the non-abelian nature of  $G$ . Parallel transporters satisfy

- $\mathcal{U}[\emptyset] = \mathbf{1}$ ,
- $\mathcal{U}[\mathcal{C} \circ \mathcal{C}'] = \mathcal{U}[\mathcal{C}]\mathcal{U}[\mathcal{C}']$
- $\mathcal{U}[-\mathcal{C}] = \mathcal{U}^{-1}[\mathcal{C}]$ ,

where  $\emptyset$  is a trivial, zero length path,  $\mathcal{C} \circ \mathcal{C}'$  is the path composed from  $\mathcal{C}$  and  $\mathcal{C}'$ , and  $-\mathcal{C}$  is the path traversed in opposite direction as  $\mathcal{C}$ . The parallel transport transforms under gauge transformations as

$$\bar{\mathcal{U}}[\mathcal{C}_{xy}] = S^{-1}(x)\mathcal{U}[\mathcal{C}_{xy}]S(y) \quad (2.12)$$

If  $\mathcal{C}_{xy}$  is a closed loop with  $x = y$ , the parallel transport is called holonomy. It maps closed loops into the group  $G$ , its image is the holonomy group of the bundle  $P$  and a subgroup of  $G$ .

The algebra valued curvature 2-forms  $\boldsymbol{\Omega}$  are obtained by applying twice the exterior covariant derivative on a  $\mathfrak{g}$  valued form  $\varphi$ . Using

$$D_\nabla D_\nabla \varphi = (d\boldsymbol{\omega} + \boldsymbol{\omega} \wedge \boldsymbol{\omega}) \wedge \varphi \quad (2.13)$$

we get the curvature as (Cartan structure equation)

$$\boldsymbol{\Omega} = D_\nabla \boldsymbol{\omega} = d\boldsymbol{\omega} + \boldsymbol{\omega} \wedge \boldsymbol{\omega}. \quad (2.14)$$

The curvature transforms, as the holonomies, with the adjoint representation of the gauge group

$$\bar{\boldsymbol{\Omega}} = S^{-1}\boldsymbol{\Omega}S \quad (2.15)$$

and fulfils the Bianchi identity

$$D_\nabla \boldsymbol{\Omega} = 0. \quad (2.16)$$

To write (2.14) in components we use

$$d\boldsymbol{\omega} = \partial_\mu dx^\mu \wedge ig A_\nu^m \mathbf{T}_m dx^\nu \quad (2.17a)$$

$$\boldsymbol{\omega} \wedge \boldsymbol{\omega} = (ig)^2 A_\mu^m A_\nu^n \frac{1}{2} [\mathbf{T}_m, \mathbf{T}_n] dx^\mu dx^\nu \quad (2.17b)$$

## 2.2 Lattice Formulation

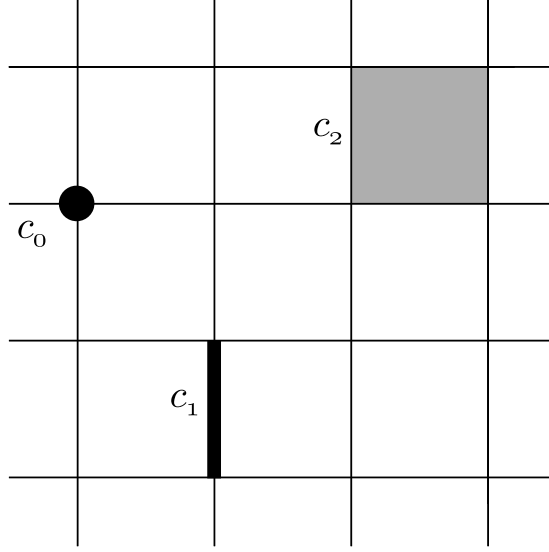


Figure 2.1: Symbolic picture of a two-dimensional lattice, highlighting a site ( $c_0$ ), a link ( $c_1$ ), and a plaquette ( $c_2$ ).

and get

$$F_{\mu\nu}^l = \partial_\mu A_\nu^m - \partial_\nu A_\mu^m + ig C_{mn}^l A_\mu^m A_\nu^n, \quad (2.18)$$

where the field strength is defined as  $\Omega = ig F_{\mu\nu}^l \mathbf{T}_l dx^\mu dx^\nu$ .

An important property of gauge fields is the *topological charge*. Dependent on the base space  $M$ , gauge fields can be topologically classified. The *Pontryagin index*, in physics also known as *topological winding number* or *topological charge*, depends on the curvature and is defined as

$$Q = -\frac{1}{8\pi^2} \int \text{Tr } \Omega \wedge \Omega. \quad (2.19)$$

The Pontryagin index is quantised and will be discussed in chapter 7.

## 2.2 Lattice Formulation

In lattice field theory, the continuous Euclidean space-time is replaced by a discrete lattice  $\Lambda = \{x | x_\mu/a \in \mathbb{Z}\}$ , where  $a$  is the lattice spacing, and the four Euclidean space-time directions are labelled with  $\mu = 1, \dots, 4$ . This leads to a regularisation of field theories because momenta are restricted to the first Brillouin zone of the inverse lattice. Usually finite hypercubic lattices are considered, in this work we use lattices of size  $aN_t \cdot (aN_s)^3$ , where the number of lattice sites is  $N_{vol} = N_t \cdot N_s^3$ . The asymmetry of the (Euclidean) lattice in time direction enables calculations for systems at finite temperature  $T$ , as we will show below. We exclusively use periodic boundary conditions.

In fig. 2.1 a part of a two-dimensional lattice is depicted symbolically. A lattice can also be regarded as a *cell complex* consisting of cells  $c_n$ , where  $c_0$  are the lattice sites,

## 2.2 Lattice Formulation

$c_1$  are the links connecting two sites, and being bordered by sites,  $c_2$  are the plaquettes bordered by  $c_1$ ,  $c_3$  are the cubes and  $c_4$  are the hypercubes. A site, a link and a plaquette are highlighted in fig. 2.1 on the previous page. On the lattice, (Lorentz) scalar fields have support on lattice sites, but vectors join neighbouring sites and are located on links  $c_i$ . The most important link field is the connection, which is a bilocal quantity on the lattice. It can be inferred from the continuum formulation using the parallel transport (2.11)

$$U_\mu = \mathcal{P} \exp \left( \int_x^{x+\hat{\mu}} ig A_\mu(x) dx \right), \quad (2.20)$$

where the integration paths  $\mathcal{C}$  are the links  $c_1$  with end points  $x$  and  $x + \hat{\mu}$ , and the vectors  $\hat{\mu} = ax^\mu$  of the affine space  $\mathbb{R}^4$  point from one lattice site to a neighbouring one. The matrices  $U_\mu = [\mathcal{U}_i^j]_\mu = \mathcal{U}(\partial_\mu)$ , the link variables, are elements of the Lie group  $G$ . As shorthand notation we also write sometimes  $U = [U_\mu]$ . They transform under gauge transformations as

$$\bar{U}_\mu(x) = S^{-1}(x) U_\mu(x) S(x + \hat{\mu}). \quad (2.21)$$

Reversely, from the link variables algebra valued lattice gauge fields can be defined using

$$U_\mu = \exp(igaA_\mu). \quad (2.22)$$

For small lattice spacings  $a \rightarrow 0$  the group elements  $U_\mu$  are supposed to be near the identity elements  $\mathbf{1}$  of the group. Expanding around  $\mathbf{1}$  gives the algebra element as

$$U_\mu = \mathbf{1} + igaA_\mu. \quad (2.23)$$

The action of the covariant derivative on colour space base vectors (2.8) reads on the lattice

$$[\nabla_\mu e_i](x) = \mathcal{U}_{i\mu}^j(x) e_j(x + \hat{\mu}) - e_i(x). \quad (2.24)$$

Applying the operator of covariant derivative on a section  $\varphi = \varphi^i e_i$  of the vector bundle  $E$  we get

$$\nabla_\mu(\varphi^i e_i) = (\mathcal{U}_{j\mu}^i(x) \varphi^j(x + \hat{\mu}) - \varphi^i(x)) e_i = (\hat{\nabla}_\mu \varphi^i) e_i \quad (2.25)$$

with

$$\hat{\nabla}_\mu \varphi^i := \mathcal{U}_{j\mu}^i(x) \varphi^j(x + \hat{\mu}) - \varphi^i(x). \quad (2.26)$$

The equivalent to the curvature on the lattice can be inferred from the holonomies and is called plaquette variable. The closed path  $\mathcal{C}$  in (2.11) is set to the border of the plaquettes  $c_2$ , which consists of four links  $c_1$ . Hence the plaquette variable can be written as the product of four link variables as depicted in fig. 2.2 on the following page, and is given by

$$U_{\mu\nu}(x) := U_\mu(x) U_\nu(x + \hat{\mu}) U_\mu^{-1}(x + \hat{\nu}) U_\nu^{-1}(x). \quad (2.27)$$

As shorthand notation we write sometimes  $U_P = [U_{\mu\nu}]$ . As for the link variables, also for the plaquette variables an algebra valued lattice field, the field strength, can be defined with

$$U_{\mu\nu} = \exp(iga^2 A_{\mu\nu}). \quad (2.28)$$

In the continuum limit  $a \rightarrow 0$ , expanding the link variables (2.22) in (2.27), the continuum relation (2.18) is revealed.

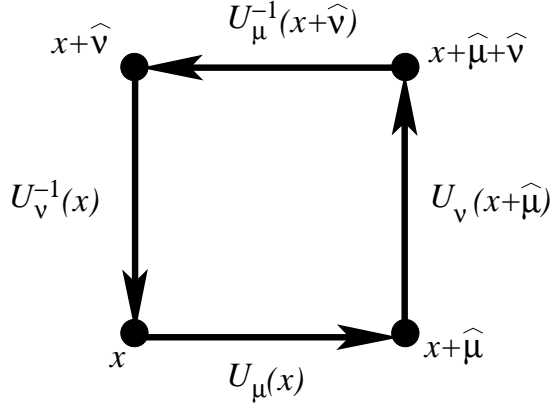


Figure 2.2: The product of the link variables around a plaquette gives the plaquette variable.

## 2.3 Quantisation

### 2.3.1 Path integral formalism

In the Euclidean path integral formalism, vacuum expectation values for operators  $O[\Sigma]$  depending on a configuration  $\Sigma$  of some fields are given by

$$\langle O \rangle = \frac{1}{Z} \int \mathcal{D}[\Sigma] O[\Sigma] \exp(-S[\Sigma]). \quad (2.29)$$

Here  $S[\Sigma]$  is the action,  $\mathcal{D}$  is an appropriate integration measure, and  $Z$  is the partition function defined as

$$Z = \int \mathcal{D}[\Sigma] \exp(-S[\Sigma]). \quad (2.30)$$

Hence the partition function resembles formally the partition function of a thermodynamic system, and many methods can be used both for thermodynamics and quantum field theory.

The expectation values (2.29) can be exactly calculated for rather simple models only. To treat more involved models like QCD or the  $SU(2)$  gauge theory, approximating methods have to be used. Namely for  $SU(N)$  gauge theories on the lattice there are at our disposal:

- Strong coupling expansion, which works for large values of the gauge coupling constant  $g$ .
- Weak coupling expansion for small value of  $g$ .
- Numerical calculations using Monte Carlo simulation on computers.

## 2.3 Quantisation

### 2.3.2 Gauge fields

In the continuum, the Yang-Mills action for gauge fields is given by

$$S^{YM}[\omega] = \frac{1}{4g^2} \int \text{Tr} (\Omega \wedge \star \Omega), \quad (2.31)$$

where  $\star$  is the Hodge dual operator. Writing the action in terms of the components  $A_\mu^m$  and  $F_{\mu\nu}^m$  we get for the Euclidean action

$$S^{YM}[A] = \frac{1}{4} \int d^4x F_{\mu\nu}^m(x) F^{m\mu\nu}(x). \quad (2.32)$$

On the lattice, we use the Wilson action [Wil44] which is given for  $SU(N)$  gauge theories by

$$S^W = \beta \sum_P \left( 1 - \frac{1}{2N} (\text{Tr } U_{\mu\nu}(x) + \text{Tr } U_{\mu\nu}^{-1}) \right) \quad (2.33a)$$

$$= \beta \sum_P \left( 1 - \frac{1}{N} \Re \text{Tr } U_{\mu\nu}(x) \right), \quad (2.33b)$$

where the sum  $\sum_P = \sum_{\mu < \nu, x}$  runs over all plaquettes  $c_2$ , and the inverse coupling  $\beta$  is defined as  $\beta = 2N/g^2$ . The latter definition of  $\beta$  gives the correct expression (2.31) in the continuum limit. We note that there are other lattice actions having the same continuum limit; but in this work we use the Wilson action for gauge fields only. The expression (2.33) does not explicitly depend on the lattice spacing  $a$ ; this holds for all lattice actions, because the action expressed in units of  $\hbar$  is a dimensionless quantity, and all fields in the lattice formulation can be scaled according to their canonical dimension with some power of  $a$  to make them dimensionless, too. The Wilson action (2.33) is supplemented by actions for other fields like fermion fields. In chapter 6 we will introduce the action for the  $SU(2)$  gauge-Higgs system. The integration measure is determined by the invariant Haar measure  $dU$  of the  $SU(N)$  group, it reads

$$\mathcal{D}[U] = \prod_{x,\mu} dU_\mu(x). \quad (2.34)$$

Introducing a discrete lattice, the functional path integral is modified to a finite number of well defined ordinary integrals over the gauge group.

### 2.3.3 Hamiltonian Formalism

In the Hamiltonian formalism, states are in the Hilbert space  $\mathcal{H}$  of square integrable functionals  $\Psi$  from the set of all configurations  $\Sigma$  on the three-dimensional spatial lattice in the field of complex numbers  $\mathbb{C}$

$$\Psi : \{\Sigma\} \rightarrow \mathbb{C}. \quad (2.35)$$



### 2.3 Quantisation

The scalar product reads

$$\langle \Psi | \Phi' \rangle = \int \mathcal{D}[\Sigma] \Psi^*[\Sigma] \Phi[\Sigma]. \quad (2.36)$$

Field operators  $\widehat{\Sigma}$  act multiplicatively on the state vectors

$$(\widehat{\Sigma}\Psi)[\Sigma] = \Sigma\Psi[\Sigma]. \quad (2.37)$$

The unitary operator of gauge transformations  $\widehat{S}$  is given by

$$(\widehat{S}\Psi)[\Sigma] = \Psi[\Sigma^S] = \Psi^S[\Sigma], \quad (2.38)$$

where  $\Sigma^S$  is the configuration transformed by the gauge transformation  $S$ . Gauge invariant states fulfil  $\Psi^S = \Psi$ , and an operator  $\widehat{O}$  is gauge invariant if it commutes with  $\widehat{S}$

$$[\widehat{S}, \widehat{O}] = 0. \quad (2.39)$$

Gauge dependent states indicate the presence of external charges. The simplest case is a single point-like charge at position  $\vec{x}$  in the fundamental representation; such a state transforms like

$$\Psi \rightarrow \widehat{S}^{(\nu)}(S(x))\Psi \quad (2.40)$$

where  $\widehat{S}^{(\nu)}(S(x))$  is in a faithful unitary irreducible representation  $\nu$  of the gauge group. Due to the gauge invariance of the Hamiltonian, external charges are static, and states with different external charge distributions decouple completely. This means the Hilbert space  $\mathcal{H}$  is divided in different charge sectors.

The vacuum expectation values of the product of time-ordered operators of the Hamilton formalism can be calculated using the path integral expression (2.29)

$$\langle T\widehat{O}_1\widehat{O}_2\cdots \rangle = \frac{1}{Z} \int \mathcal{D}[\Sigma] O_1 O_2 \cdots \exp(-S). \quad (2.41)$$

In section 3.2 we will illustrate this for the Wilson loop operator.

#### 2.3.4 Finite Temperature

The path integral formalism can also be used for the calculation of operator expectation values in systems at finite temperature  $T$ . On the lattice this is done by using a finite extent  $aN_t$  in time direction, and by imposing periodic boundary conditions in time direction. For the spatial directions, still the limit  $N_s \rightarrow \infty$  is regarded. The temperature is given by the temporal lattice extent as

$$T = \frac{1}{aN_t}. \quad (2.42)$$

## 2.4 Continuum limit

For the continuum limit, the lattice spacing  $a$  is sent to zero  $a \rightarrow 0$ , whereas the number of lattice sites diverges  $N_{vol} \rightarrow \infty$ . Renormalisation relates the dimensionless lattice observables to physical observables in dependence on  $a$ . For observables with the dimension of a mass this relation reads

$$m = \hat{m}/a, \quad (2.43)$$

where  $m$  is some physical mass and  $\hat{m}$  is calculated on the lattice. For lengths  $\xi$  the relation is

$$\xi = \hat{\xi}a. \quad (2.44)$$

Because  $a$  does not occur explicitly in the lattice expectation values, the system depends on dimensionless coupling parameters only, and/or some mass parameters. In the continuum limit, the lattice lengths  $\hat{\xi}$  have to diverge in order to keep the physical lengths  $\xi$  at a constant, physical value. We have noted above that the quantum dynamical partition function (2.30) corresponds to the partition function describing systems of statistical mechanics. In statistical mechanics lengths appear as correlation lengths  $\xi$ , and in the language of statistical mechanics the continuum limit is related to a critical region in the phase diagram of the corresponding statistical mechanical system where correlation lengths diverge, such as at second order phase transitions. If we note the parameters of the system as  $\alpha$ , correlation lengths behave like

$$\lim_{\alpha \rightarrow \alpha_{crit}} \hat{\xi}(\alpha) = \infty, \quad (2.45)$$

where  $\alpha_{crit}$  is a parameter set indicating a critical point.

In order to investigate the dependence of  $a$  on  $\alpha$ , we consider some observable  $O$  of dimension  $d$ . At some given values of  $a$  and  $\alpha$ , we can write

$$\langle O \rangle(a, \alpha(a)) = a^{-d} \langle \hat{O} \rangle(\alpha), \quad (2.46)$$

where  $\langle \hat{O} \rangle$  is the dimensionless expectation value calculated on the lattice. The physical value for the expectation value is gained in the continuum limit

$$\langle O_{phys} \rangle = \lim_{a \rightarrow 0} \langle O \rangle(a, \alpha(a)). \quad (2.47)$$

Therefore, if the dependence of  $\langle \hat{O} \rangle(\alpha)$  from  $\alpha$  can be calculated, we can infer the lattice spacing  $a$  for small values of  $a$  as a function of the parameters  $\alpha$  and of the physical value  $\langle O_{phys} \rangle$ . This relation between  $a$  and  $g$  depends on the observable  $O$  used, but universality known from statistical mechanics ensures that sufficiently close to the continuum the result is independent from  $O$ .

For the case of pure SU(2) lattice gauge theory mainly investigated in this work, the only parameter is the inverse coupling  $\beta = 4/g^2$ . The critical value for the continuum is

## 2.5 Monte Carlo Techniques

$g = 0$ . Using the weak coupling expansion mentioned in section 2.2 for the Wilson loop observable described in section 3.2, one finds in the two-loop approximation

$$a^2(\beta) = \frac{1}{\sigma_{phys}} \left( \frac{6\pi^2}{11} \beta \right)^{102/121} \exp \left( -\frac{6\pi^2}{11} \beta \right), \quad (2.48)$$

where  $\sigma_{phys}$  is the physical string tension (section 3.2). Having determined  $a(\beta)$ , which is valid in the limit  $a \rightarrow 0$ , we can test whether for expectation values of observables calculated on the lattice the right hand side of (2.46) is constant with respect to the parameter  $\beta$ . If this is the case, one speaks of *asymptotic scaling* of the observable. Usually a *scaling window* is found where the relation holds. For smaller values of  $\beta$  the lattice is too coarse and too far away from the continuum, whereas for larger values the physical volume  $a^4 N_t \cdot N_s^3$  is too small and finite size effects occur. The reason for the latter problem is that the number of lattice sites  $N_t \cdot N_s^3$  is limited due to restricted computer memory and speed.

## 2.5 Monte Carlo Techniques

The Monte Carlo method can be used to calculate numerically the expectations values of operators (2.29)

$$\langle O \rangle = \frac{1}{Z} \int \mathcal{D}[\Sigma] O[\Sigma] \exp(-S[\Sigma]). \quad (2.49)$$

This is done by generating an ensemble  $\{\Sigma\}$  of  $\mathcal{N}_e$  lattice field configurations  $\Sigma$ , where the probability that some field configuration is present in  $\{\Sigma\}$  is given by the Boltzmann distribution  $\exp(-S[\Sigma])$ . Then an estimate for  $\langle O \rangle$  is given by

$$\overline{O} = \frac{1}{\mathcal{N}_e} \sum_{\{\Sigma\}} O[\Sigma]. \quad (2.50)$$

In the limit of an infinite number of configurations  $\mathcal{N}_e \rightarrow \infty$ , the estimates  $\overline{O}$  approach the expectations values  $\langle O \rangle$ .

The configurations of the ensemble are generated by a discrete Markov process. Such a process consists of update steps which create from a given configuration  $\Sigma$  a new configuration  $\Sigma'$ , generating a sequence of configurations called the Markov chain. In order to produce a Boltzmann distributed ensemble, we require three properties for the probability  $P(\Sigma \rightarrow \Sigma')$  that  $\Sigma'$  is generated after  $\Sigma$  in the process:

**Strong ergodicity** Each configuration can be generated with finite probability from each configuration

$$P(\Sigma \rightarrow \Sigma') > 0. \quad (2.51)$$

This ensures that a Boltzmann distributed ensemble can be generated independently from the first starting configuration.

**Normalisation** The sum of probabilities equals 1:

$$\sum_{\Sigma'} P(\Sigma \rightarrow \Sigma') = 1. \quad (2.52)$$

**Detailed balance**

$$\frac{P(\Sigma \rightarrow \Sigma')}{P(\Sigma' \rightarrow \Sigma)} = \frac{\exp(-S[\Sigma'])}{\exp(-S[\Sigma])}. \quad (2.53)$$

This condition actually causes the Boltzmann distribution.

It can be shown that a Markov process fulfilling these requirements generates a Boltzmann distributed chain after a finite number of steps. One problem of this procedure is that configurations of the Markov chain can be correlated, which depending on the observable leads to increased statistical errors and requires larger ensembles. In order to reduce these errors, we measure observables not for all generated configurations, but separate the measurements by several Monte Carlo steps.

In our simulations we use two methods with the required properties:

**Heatbath algorithm** This algorithm is given by

$$P(\Sigma \rightarrow \Sigma') = \frac{1}{Z} \exp(-S[\Sigma']). \quad (2.54)$$

**Metropolis algorithm** This algorithm consists of two steps:

- First a new configuration  $\Sigma'$  is suggested, where this step fulfils

$$P_1(\Sigma \rightarrow \Sigma') = P_1(\Sigma' \rightarrow \Sigma). \quad (2.55)$$

- Second the new configuration is accepted with probability

$$P(\Sigma \rightarrow \Sigma') = \begin{cases} 1 & \text{if } S[\Sigma'] < S[\Sigma] \\ \exp(-S[\Sigma']) / \exp(-S[\Sigma]) & \text{if } S[\Sigma'] > S[\Sigma]. \end{cases} \quad (2.56)$$

If the new configuration is rejected, proceed with the first step and generate a new trial configuration.

For our lattice gauge theory simulations, the configurations are not updated at once. An update is composed of micro steps, where only one link variable of the lattice (or some other local variable such as a Higgs field at a site) is updated using the heatbath or Metropolis algorithm. Only the full update (sweep) fulfils the requested properties. We remark that there exist many more elaborated update methods, but they were not needed for our simulations.

Crucial for the detection of vortices is the choice of an appropriate gauge for the configuration, as will be described in chapter 4. Some gauges are imposed to maximise a functional  $R[\Sigma]$  of a field configuration  $\Sigma$ . This can be done by generating a sequence

## 2.5 Monte Carlo Techniques

of configurations, each created by a gauge transformation from the previous configuration, which approach a maximum of  $R$ . A gauge condition might not fix uniquely the gauge, and some reduced gauge freedom can remain. But apart from this there can be ambiguities in gauge fixing because the iterative methods might find not the global, but some local maximum of  $R[\Sigma]$ . The existence of such *Gribov copies* will emerge to be important for the detection of vortices. Two methods used for gauge fixing are:

**Over-relaxation** This method [Adl81] changes iteratively, locally the field to some combination of the original field, and of a field which maximises the functional locally. Over-relaxation finds quite effectively a (local) maximum of  $R[\Sigma]$ . We note that over-relaxation can also be used for Monte Carlo updates supplementing procedures like heatbath and the Metropolis method [BW87, Cre87].

**Simulated annealing** In simulated annealing [KGV83, Cer85], instead of the action the functional  $R$  is used in order to generate a Markov chain by the Metropolis algorithm with the “action”  $1/T R[\Sigma]$ , where  $T$  is some appropriately chosen temperature. This allows the system during the procedure also to depart from the maximum of  $R$ , and avoid in the way to be caught in a local maximum. During the Markov process, the temperature is slowly decreased to zero, and finally a maximum is reached.

## 3 Confinement and the Vortex Model

### Abstract

A description of colour confinement is given. We introduce the Wilson loop and the Polyakov loop observables to investigate the potential between colour charges and confinement. The vortex model of confinement explaining the observed results is introduced; see also the review article of Greensite [Gre03] for further information. Further we also present various already well known results on the vortex model.

### 3.1 Colour confinement

What is confinement? Quark confinement has been introduced as the phenomenon that quarks are never observed as isolated, free particles but are confined in composed particles, the hadrons. More general, no isolated particles with colour charge are seen in nature. There are several distinct ways how free colour charges can be prohibited; some of these ways as they are observed in different phases of various quantum gauge theories are:

- In the *Higgs phase*, the vacuum is filled with a condensate of dynamic colour charges. Any colour charged probe introduced into such a vacuum is screened by the condensate; thus at large distances the total charge inside a volume around the charge vanishes. See chapter 6 for more information on such phases in the framework of the vortex model.
- In a *confined phase*, the potential of a charge-anticharge pair at distance  $r$  raises linearly, for large  $r$ . The colour magnetic flux builds a flux tube called string between the charges. Thus charges cannot be separated because of the distance independent force attracting them. The main intend of the vortex model is to explain this behaviour of the potential.
- In QCD, the potential rises linearly at intermediate distances. But at some distance  $r_0$ , the string breaking distance, the energy of the string is high enough to create a new charge-anticharge pair. This breaks the string, the new state consists of two colourless compound objects at distance  $r_0$ , and the potential is constant for larger distances. We will discuss *string breaking* in chapter 6.

We note that the linear rising potential for large charge distances is present for system without dynamical matter fields only. This is the case for the *quenched approximation* of

### 3.2 Wilson Loop

QCD, where the gauge fields are the only dynamical degrees of freedom. The advantage of this approximation is that it gives reasonable results without the numerically costly simulation of fermion fields. We use this approximation in this work, but study the influence of dynamical matter fields in chapter 6.

In order to investigate numerically confinement, we next introduce some important observables.

### 3.2 Wilson Loop

The *Wilson loop* is used to measure the potential between a pair of infinitely massive colour charges. As introduced in section 2.3.3, states  $\Psi$  containing a static charge at position  $\vec{x}$  and an anticharge at position  $\vec{y}$ , where their distance is  $aI = \|\vec{x} - \vec{y}\|$ , transform under gauge transformation as

$$\Psi \rightarrow \hat{S}(S(\vec{x}))\hat{S}^{-1}(S(\vec{y}))\Psi. \quad (3.1)$$

These states lie in a charge sector of the Hilbert space noted  $\mathcal{H}_{xy}$ . The eigenstates of the Hamilton operator in  $\mathcal{H}_{xy}$  fulfil

$$\hat{H}\Psi^{(n)} = E^{(n)}\Psi. \quad (3.2)$$

The energy of the ground state depends only on the charge separation  $aI$  and is known as the *static potential*

$$V(I) = E_0(I) = \min_{\mathcal{H}_{xy}} \hat{H}. \quad (3.3)$$

For an arbitrary state  $\Psi \in \mathcal{H}_{xy}$ , the static potential can be inferred by

$$\langle \Psi | e^{-aJ\hat{H}} | \Psi \rangle = \sum_n |\langle \Psi^{(n)} | \Psi \rangle|^2 e^{-aJE^{(n)}}, \quad (3.4)$$

where

$$C_n := |\langle \Psi^{(n)} | \Psi \rangle|^2 \quad (3.5)$$

is the overlap between the trial state  $\Psi$  and the  $n^{\text{th}}$  eigenstate  $\Psi^{(n)}$ . In the limit of large Euclidean times  $J$  the lowest eigenstate dominates and we get

$$\lim_{J \rightarrow \infty} \langle \Psi | e^{-aJ\hat{H}} | \Psi \rangle = |\langle \Psi^{(0)} | \Psi \rangle|^2 e^{-aJV(I)}. \quad (3.6)$$

This works only if the overlap  $C_0$  between the ground state  $\Psi^{(0)}$  and the trial state  $\Psi$  is not zero.

A simple choice for  $\Psi$  is the trial state generated from the zero-charge vacuum state  $\Psi_{vac}$  by the operator given by the parallel transport (2.11):

$$\Psi_{xy} = \hat{\mathcal{U}}[\mathcal{C}_{xy}]\Psi_{vac}, \quad (3.7)$$

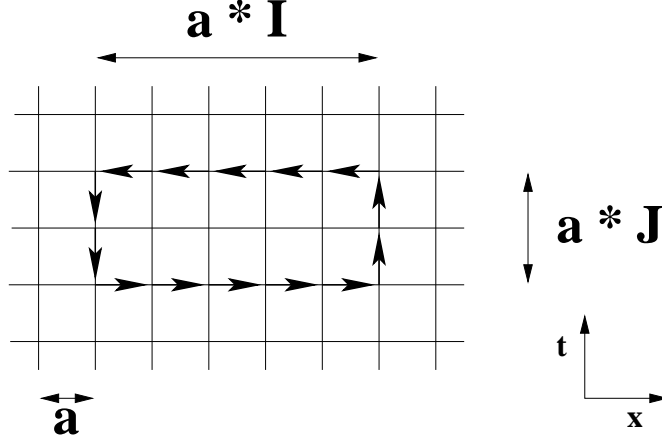


Figure 3.1: Diagram of the Wilson loop operator  $W(I, J)$  on the lattice. The loop is the expectation value of the trace of the product of link variables along a rectangular path. Here the loop extends  $a \cdot I$  in  $x$ -direction and  $a \cdot J$  in  $t$ -direction.

where  $\mathcal{C}$  is the straight line between  $\vec{x}$  and  $\vec{y}$ . As mentioned in section 2.3, expectation values of time-ordered operators in the Hamiltonian formalism correspond to vacuum expectation values (2.29) in the path integral formalism. In this formalism the expectation value (3.4) is given by the expression

$$W(\mathcal{C}) = \langle \text{Tr } \mathcal{P} \exp \left( - \int_{\mathcal{C}} \omega \right) \rangle. \quad (3.8)$$

The closed curve  $\mathcal{C}$  is of rectangular shape and is composed of the parallel transports  $\mathcal{C}_{xy}$  at time 0 and  $\mathcal{C}_{yx}$  at time  $aJ$ , and the straight parallel transport connecting the times 0 and  $aJ$ . For the lattice, the Wilson loop is depicted in fig. 3.1; it reads

$$W(I, J) = \langle \text{Tr } \prod_{l \in \mathcal{C}} U_l \rangle. \quad (3.9)$$

Here  $U_l$  are the link variables around the loop with extent  $aI$  in some spatial direction and  $aJ$  in time direction.<sup>1</sup> From the Wilson loop, the static potential follows up to a constant as

$$V(I) = - \lim_{J \rightarrow \infty} \frac{1}{J} \ln W(I, J), \quad (3.10)$$

where the lattice spacing  $a$  has been absorbed in the lattice definition of  $V$  to get a dimensionless quantity.

The Wilson loop is nothing but the vacuum expectation value of the trace of a holonomy. There are similar operators where the spatial straight lines are replaced by other combinations of the fields such that the loop remains gauge covariant; such operators

<sup>1</sup>It is also possible to study loops extending in two spatial directions; such loops will be discussed in section 5.6.



### 3.3 Polyakov Loop

correspond to other generated trial states in the Hamilton formalism which might have better ground state overlap. We will discuss this topic in section 6.3.

It can be shown that asymptotically for large distances the static potential does not increase faster than linearly [Sei78], and cannot decrease [SY82]. This suggests the following ansatz for the potential at large distances  $I$ :

$$V(I) = \alpha + \sigma I - c. \quad (3.11)$$

This potential can be supplemented, if appropriate, by a Coulomb like potential  $-e/I$  for small distances. The coefficient for the linear part is the *string tension*  $\sigma$ ; if  $\sigma > 0$ , the static potential is linearly rising asymptotically, and colour charges are confined due to the constant force between them. This is dubbed as the *Wilson criterion* for confinement. For the Wilson loop, the ansatz (3.11) yields

$$W(I, J) = \exp(-\sigma IJ - \alpha(I + J) + \gamma); \quad (3.12)$$

here the Wilson criterion means *area law*. The Wilson loop is dominated by a fall off which is exponential with  $A = IJ$  for large  $A$ , where  $A$  is the area bordered by the loop. On the other hand, for an asymptotically constant potential, the area term is zero and the Wilson loop decreases with an exponent proportional to the perimeter  $2(I + J)$  of the loop, which is called the *perimeter law*.

Only for large areas  $A$  the Wilson loop is governed, if confinement is present, by the area law. In order to extract the string tension  $\sigma$  already from smaller loops, the *Creutz ratio* [Cre80]

$$\chi(I, J) = -\ln \left( \frac{W(I+1, J+1)W(I, J)}{W(I, J-1)W(I-1, J)} \right) \quad (3.13)$$

can be used. In this expression perimeter law and constant factors cancel, and already for moderate areas the Creutz ratio approaches the string tension  $\chi(I, J) \xrightarrow{A \rightarrow \infty} \sigma$ .

### 3.3 Polyakov Loop

As introduced in section 2.3.4, expectation values of operators in systems of finite temperature  $T$  can be calculated by setting the temporal extent of the lattice to a finite value  $aN_t = 1/T$ , and by imposing periodic boundary conditions in time direction. Therefore the Wilson loop is not usable any more to infer the potential, because the  $N_t \rightarrow \infty$  limit of the loop cannot be performed. On the other hand, a parallel transport can be closed over the periodicity of the lattice, which leads to the *Polyakov loop* observable. The Polyakov loop is defined as the holonomy for a curve extending straightly in time direction. On the lattice it is composed of link variables in time direction and reads

$$L(\vec{x}) := \frac{1}{N} \text{Tr} \prod_{x_4=1}^{N_t} U_4(\vec{x}, x_4). \quad (3.14)$$

### 3.4 Vortices

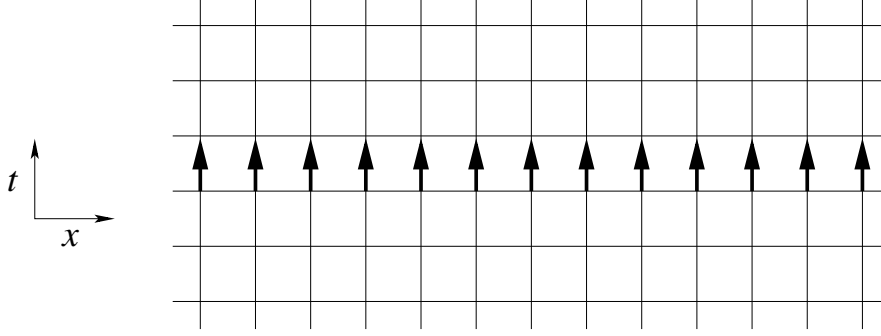


Figure 3.2: For an aperiodic gauge transformation, all time-like links in a given time-slice are multiplied with a center element.

The expectation value of the modulus of  $L(\vec{x})$ , averaged over the position  $\vec{x}$ , can be related to the free energy of a single static quark, measured relatively to the absence of the quark:

$$\langle |L| \rangle = \left\langle \left| \frac{1}{N_s^3} \sum_{\vec{x}} L(\vec{x}) \right| \right\rangle \stackrel{N_s \rightarrow \infty}{=} e^{-F/T}. \quad (3.15)$$

### 3.4 Vortices

The relevance of the center degrees of freedom for confinement can be seen from ***N*-ality**. The *N*-ality (representation class) classifies representations of a group according to the representation of their center. The center of a group is defined as the subgroup of elements commuting with all elements of the group. There is an infinity number of representations of the gauge groups  $SU(N)$ , but only  $N$  different representations for the center  $Z_N$  of  $SU(N)$ . The center in a representation of *N*-ality  $k = 0, \dots, N-1$  can be represented by numbers  $z_n = \exp(2\pi i k n / N)$ , where  $n = 0, \dots, N-1$  labels the center element  $z_n \in Z_N$ . Now the asymptotic string tension  $\sigma$  for static charges in a representation of some *N*-ality only depends on the presence or absence of dynamical fields of this *N*-ality. Fundamental charges have *N*-ality  $k = 1$  and can be screened by dynamical matter fields in the fundamental representation only, and not by adjoint fields. On the other hand, even in the absence of matter fields adjoint charges can be screened by gauge fields which transform under the adjoint representation with *N*-ality  $k = 0$ .

There exists a global center symmetry which allows to define an order parameter for confinement and deconfinement in systems at finite temperature [KPS81]. If all time-like link variables in a given time-slice of the lattice are multiplied with a center element, as depicted in fig. 3.2, the Yang-Mills action and most gauge independent observables are unchanged. This transformation is an example for a **singular (aperiodic) gauge transformation**  $S(\vec{x}, aN_t) = zS(\vec{x}, 1)$  generated by gauge transformations which are aperiodic in time direction. They are also called discontinuous or large gauge transformations. An observable affected by a aperiodic gauge transformation is the Polyakov

### 3.4 Vortices

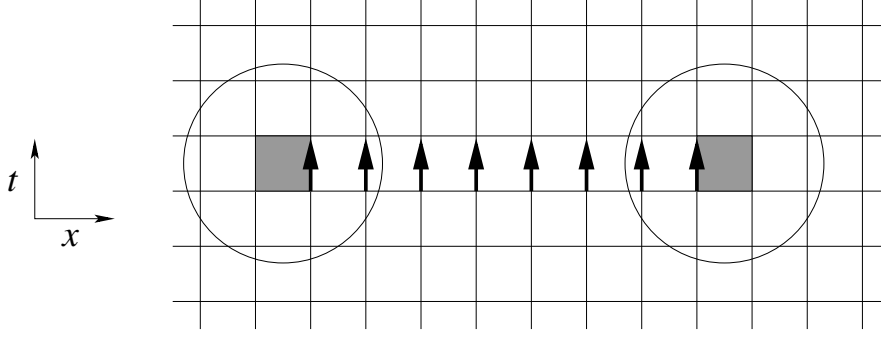


Figure 3.3: If in some three-volume the temporal links are multiplied with a nontrivial center element, thin center vortices (indicated by shaded plaquettes) are created at the border of the three-volume. The circles represent thick vortices, where the flux through the thin vortices is spread out over a finite area.

loop, which is sensible whether this global symmetry is broken and thus can serve as an order parameter for confinement. If fundamental matter fields such as fermions or Higgs field are present, the action and observables involving these fields are not invariant anymore. This impacts confinement, as we will see. On the other hand for observables in the adjoint representation the symmetry always holds, which is again related to  $N$ -ality.

In order to introduce vortices, we consider a change of the link variables as for the singular gauge transformations, but restrict the center multiplication to a region of the lattice which covers only some part of the whole three-dimensional time-slice. This is plotted in fig. 3.3. The 3D-volume where the links are flipped is the **Dirac volume**. The plaquettes in the Dirac volume remain unchanged. At the border of the Dirac volume, plaquettes are multiplied by the center element. The set of these plaquettes is called a **thin center vortex**, and the plaquettes are the **vortex plaquettes**. Using ordinary gauge transformations, the location of the Dirac volume can be changed; the thin vortex is a gauge invariant quantity, and the border of the Dirac volume is fixed. By generating a thin vortex plaquette, a quantised colour magnetic flux with the value of the center element is created; it flows through the vortex plaquette and can be represented by a plaquette of the dual lattice, the **P-vortex plaquette**. We will investigate P-plaquettes in detail in chapter 5.

It is important for the vortex model that the change of action caused by the generation of a thin vortex is only proportional to the surface, i.e. the vortex area, and not to the volume of the Dirac volume. This favours the occurrence of center vortices in field configurations [NO79, AO80b, AO80a, Ole82], enabling them to dominate the low-energy properties of QCD.

Singular gauge transformation can also be defined in the continuum; in fact it is in the continuum where aperiodic gauge transformation are singular, because the aperiodic gauge  $S(\vec{x}, t)$  is discontinuous at  $t = aN_t$ , and the gauge potential  $A$  is singular. Thin center vortices can be formulated in the continuum, too. Here the colour magnetic center flux is located on closed vortex surfaces which are boundaries of Dirac volumina.

### 3.4 Vortices

Because the flux is concentrated in infinite thin surfaces, the action density of thin continuum center vortices is singular; this imposes obstacles for the continuum limit of vortex detection methods [ER00a], as will be investigated in chapter 4. Because thin vortices are suppressed in the continuum limit due to their singular action density, the vortex model features so called **thick vortices**. Here the colour magnetic flux is spread out over a finite cross-section of the vortex; in fig. 3.3 on the preceding page such thick vortices are symbolically depicted as circles. The main tool to investigate vortices numerically are techniques which detect thick vortices assumed to be present in gauge field configurations by replacing them with a configuration of thin vortices; this will be discussed in detail in chapter 4.

Here we report shortly some results on the vortex model of confinement which lie somewhat outside the investigations done in this work; these include

- The *vortex free energy* defined using twisted boundary conditions can be used as an confinement criterion [MP79, Mac80a, MP80, Mac80b, MP82]; it has been measured successfully in Monte Carlo simulations [KT00, HLST00].
- A simple model [FGO98, FGO99b] taking into account the thickness of vortices is able to explain qualitatively *Casimir scaling* [AOP84, DDFGO96, FGO98]. Casimir scaling is the observation that at intermediate distances the string tension calculated from Wilson loops is proportional to the quadratic Casimir operator  $C_\nu$  of the representation  $\nu$  used for the loop. Here “string tension” refers not to the asymptotic string tension  $\sigma$  respecting  $N$ -ality, but to the slope of the static potential calculated e.g. from Creutz ratios.
- For gauge groups  $SU(N)$  with  $N > 4$ , it can be shown [GO02] that vortices are local minima of most, also effective, lattice actions, and percolate through the lattice. For  $N \leq 4$  there are good reasons [FGO00] that vortices are local minima of the effective action at large scales, thus dominating the long-range infrared sector of QCD, where confinement occurs.
- An effective model for QCD where thin vortex surfaces are the degrees of freedom can be constructed [ER00b]; many features found in vortices detected in gauge configurations are also present in the vortices of this effective model.

In the remnant of this work, we focus on the identification of vortices in gauge field configurations, on the properties of the detected vortices, and on the application of the vortex model on other low-energy properties of QCD apart from confinement, i.e. the topology of gauge fields.

# 4 Detection of Vortices

## Abstract

We discuss methods to detect vortices in Monte Carlo generated field configurations. This is done by choosing an appropriate gauge, and projecting link variables to the center of the gauge group. Numerically we show that indeed the position of vortices can be inferred this way. We discuss the short comings of this method and problems in the continuum limit, and how to overcome these problems eventually.

## 4.1 Introduction

In this section we want to describe methods to identify vortices in Monte Carlo generated gauge field configurations on the lattice<sup>1</sup>. As described in section 3.4, vortices carry magnetic colour fluxes quantised in terms of elements of the center  $Z_N$  of the gauge group  $SU(N)$ . In gauge field configuration, these vortices have some finite diameter and are therefore called thick vortices in order to distinguish them from the thin vortices generated by a discontinuous gauge transformation. Most vortex detection methods try to replace a field configuration consisting of a condensate of thick vortices and other fluctuations and excitations by a new configuration of thin vortices, which is done in two steps:

- First a suitable gauge is chosen.
- Then **center projection** [DFGO97] is performed.

(There exists also a way to identify vortices not by center projection but by looking at defects of the gauge fixing procedure. We will treat this method in section 4.3.) Center projection substitutes the group valued links by the center element of the group nearest to the link variable. The  $SU(N)$  links can be uniquely written as

$$U_\mu(x) = Z_\mu(x)V_\mu(x), \quad (4.1)$$

where  $Z_\mu(x)$  is the element of  $Z_N$  which is on the  $SU(N)$  manifold closest to  $U_\mu(x)$ . For  $SU(2)$ , the nearest center element can be found by choosing the sign of the trace:

$$Z_\mu(x) = \text{sign Tr}[U_\mu(x)]. \quad (4.2)$$

---

<sup>1</sup>Some of these methods work also in the continuum, as will be shown later.

## 4.2 Maximal Center Gauges

$V$  is closer to the trivial center element than to all other center elements. The hope is that  $V$  contains short range excitations of the gauge field only. In center projection,  $V_\mu(x)$  is neglected and the link variables replaced by  $Z_\mu(x)$ ; all what remains is a  $Z_N$  gauge field configuration. The excitations of this gauge theory are thin center vortices; we will call them **P-vortices** henceforth, indicating that they are obtained by a projection step. On the dual lattice they are composed of the **P-plaquettes**, which are dual to the thin vortex plaquettes. Hereafter the task is to ensure that P-vortices are really related to thick vortices of the unprojected lattice. With P-vortices it can be studied which features of the unprojected gauge configurations such as confinement could be preserved – and isolated – in vortices.

The choice of the gauge performed before the projection is crucial to capture the relevant degrees of freedom in  $Z$ ; several gauges are treated in this chapter. A necessary condition in order to localise vortices is the so called **vortex finding property** [FGOY99] of gauges: A procedure fulfilling this property fixes the gauge uniquely up to center degrees of freedom. The gauge has to be center blind. This means that starting from two gauge field configuration  $U$  and  $U'$ , where the link variables between the configurations differ only by multiplication with center elements, the gauging procedure yields configurations  $U_g$  and  $U'_g$  differing by exactly the same multiplication with a center element as  $U$  and  $U'$ , modulo a center gauge transformation. What is the impact of such a gauge on the detection of vortices? Let  $U$  be a gauge field configurations. After gauging and projection, we get a  $Z_N$  gauge field configuration of P-vortices  $Z$ . Next, we put a *thin* vortex into the unprojected configuration  $U$ . This is achieved by a discontinuous gauge transformation (section 3.4), i.e. some links are multiplied with center elements. Assuming the vortex finding property, the gauge yields (modulo center gauge transformations) the same configuration as by starting with the unmodified configuration, but multiplied by the very center elements. Finally, center projection returns the center elements closest to the links, which are the same as for the first, gauged configuration, but again multiplied with the vortex generating center elements. As a result, using the gauge and center projection we get exactly the same vortices as before, plus the inserted thin vortex. Subsuming, a gauge with the vortex finding property reliably finds thin vortices. Of course, vortices in unprojected configurations are considered to be thick, thus the procedure might not always work and, and the method has to be checked numerically. Some gauges possessing the vortex finding property are discussed in the next sections.

## 4.2 Maximal Center Gauges

**Maximal center gauge** (MCG) was the first gauge used to identify vortices. The idea behind MCG is simple: Before performing the projection step which changes the link variables to their nearest center element as described in section 4.1, simply gauge the links such that they are already as close as possible – on average – at the center elements. This way one hopes to minimise the part  $V$  in the decomposition of (4.1) thrown away at the projection step. There are mainly two forms to achieve such a gauge: The

## 4.2 Maximal Center Gauges

indirect maximal center gauge (IMCG) and the direct maximal center gauge (DMCG). Historically the first type of MCG was the indirect version [DFGO97]. IMCG builds on an older gauge, the *maximal Abelian gauge* (MAG) [KLSW87]. This gauge moves the link variables as close as possible to some chosen Abelian subgroup  $U(1)$  of the gauge group  $SU(N)$ . Parallelling center projection, *Abelian projection* discards all non-Abelian degrees of freedom. It can be investigated whether this step preserves the long-range physics contained in the unprojected configurations. In a next step, Abelian monopoles can be identified in the projected configurations, and one gains an effective theory of monopoles which is hoped to describe confinement.

This theory is the dual superconductor model of quark confinement. In a superconductor electrons are coupled to Cooper pairs by a short range “pairing” force. The condensation of these doubly charged objects inhibits the penetration of magnetic flux lines into the superconductor, they are squeezed into flux tubes. The idea of the dual superconductor model is the exchange of electric and magnetic observables in the model of a real superconductor. In the confining phase of QCD magnetic monopoles are condensed in the vacuum. This leads to the formation of flux tubes, the strings, between colour charges. Because there are no magnetic monopoles in QCD, gauge fixing and projection are used to define Abelian monopoles.

After Abelian projection, the IMCG is fixed. This is done by using the remnant  $U(1)$  gauge freedom to move the Abelian link variables as close as possible towards the center elements of the  $SU(2)$  group we started with. Finally the center projection step can be performed. IMCG has the advantage to bridge the vortex picture of confinement, and Abelian and monopole based explanations. For example it has been found [DFGO98] that *monopole lines* (the world lines of Abelian monopoles) are located mostly on P-vortex worldsheets. In our opinion the vortex model is favourable, because confinement is retained not only after Abelian projection, but also after center projection which reduces the degrees of freedom even more. On the other hand, models based on monopoles alone seem to fail to explain  $N$ -ality, as introduced in section 3.4. The relation between monopoles and P-vortices will be further illuminated discussing Laplacian gauges in section 4.3. For the application of the vortex model on the topological properties of QCD, which will be treated in chapter 7, monopoles will have an important role related to the orientation of P-vortex surfaces.

In this work we primarily deal with the **direct maximal center gauge** [DFG<sup>+</sup>98]. DMCG tries to find the absolute maximum of

$$R = \sum_{\mu, x} \text{Tr}[\tilde{U}_\mu^g(x)] = \sum_{\mu, x} \text{Tr} \left[ S_g^{-1}(x) \tilde{U}_\mu(x) S_g(x + \hat{\mu}) \right] \quad (4.3)$$

by an iterative procedure. The links  $\tilde{U}$  and the gauge matrix  $S_g$  are in the adjoint representation, where  $g(x)$  notes the gauge group elements at  $x$ . DMCG is nothing but the adjoint version of Landau gauge, a gauge which maximises the traces of the fundamental links:

$$R_F = \sum_{\mu, x} \Re \text{Tr}[U_\mu^g(x)] = \sum_{\mu, x} \Re \text{Tr} [g^{-1}(x) U_\mu(x) g(x + \hat{\mu})] . \quad (4.4)$$

## 4.2 Maximal Center Gauges

Because of the adjoint representation, DMCG is center blind, and after gauge fixing there remains a residual gauge freedom stemming from the ambiguous mapping from the gauge matrices  $S_g$  to the fundamental gauge elements  $g$ . Hence DMCG possesses the vortex finding property. For the case of  $SU(2)$ , finding the maximum of (4.3) is equivalent to find the maximum of

$$R' = \sum_{\mu, x} |\text{Tr } U_\mu^g(x)|^2 \quad (4.5)$$

where  $U$  is in the fundamental representation. A reason to believe that this gauge followed by center projection indeed can localise vortices is the interpretation of DMCG as a best fit procedure [ER00a, FGO01b]: The classical vacuum state of a gauge field configuration is given by a pure gauge

$$g(x)g^{-1}(x + \hat{\mu}). \quad (4.6)$$

In order to approximate a given configuration  $U_\mu(x)$  by a pure gauge we can minimise with respect to  $g$  the distance of  $U_\mu(x)$  to  $g(x)g^{-1}(x + \hat{\mu})$  on the group manifold

$$\begin{aligned} d_F^2 &= \sum_{\mu, x} \text{Tr} [(U_\mu(x) - g(x)g^{-1}(x + \hat{\mu})) \times h.c.] \\ &= \sum_{\mu, x} \Re \text{Tr} [\mathbf{1} - g^{-1}(x)U_\mu(x)g(x + \hat{\mu})] . \end{aligned} \quad (4.7)$$

Now the gauge  $g(x)$  minimising (4.7) is exactly the gauge transformation of  $U_\mu(x)$  maximising (4.4), i.e. Landau gauge. To localise vortices, we search for an approximation of  $U_\mu(x)$  not by a pure gauge, but by a configuration of thin center vortices  $g(x)Z_\mu(x)g^{-1}(x + \hat{\mu})$ . In the adjoint representation, a thin vortex configuration equals the vacuum state. Hence we can first look for an approximation of the adjoint links by a pure gauge, and repeating the procedure for the adjoint representation, we arrive not at fundamental but at adjoint Landau gauge, which is DMCG. Having fixed  $g(x)$  up to the remnant center gauge symmetry stemming from the mapping from  $S_g$  to  $g$ , we look for the optimal  $Z_\mu(x)$  to maximise the distance to the configuration

$$\begin{aligned} d_Z^2 &= \sum_{\mu, x} \text{Tr} [(U_\mu(x) - g(x)Z_\mu(x)g^{-1}(x + \hat{\mu})) \times h.c.] \\ &= \sum_{\mu, x} 2 \Re \text{Tr} [\mathbf{1} - Z_\mu^\dagger(x)g^{-1}(x)U_\mu(x)g(x + \hat{\mu})] = \sum_{\mu, x} 2 \Re \text{Tr} [\mathbf{1} - Z_\mu^\dagger(x)U_\mu^g(x)] . \end{aligned} \quad (4.8)$$

This quantity is maximised if  $Z_\mu(x)$  is chosen to be the center element closest to  $U_\mu^g(x)$ . In the end, we arrived at the same  $Z_\mu(x)$  as we get from center projecting the configuration in the maximal center gauge. DMCG followed by center projection finds the configuration of thin vortices which is the best fit to the unprojected configuration.

We have to mention two problems with DMCG, though. First, in practice, it is numerically not possible to really infer the global maximum of the gauge functional



## 4.2 Maximal Center Gauges

$R$ . Iterative gauging procedures such as over-relaxation or simulated annealing (see section 2.5) only give local maxima of  $R$ . If one applies an arbitrary gauge transformation to the configuration before starting an DMCG algorithm, a different maximum of  $R$  corresponding to a different gauge of the configuration is found. This phenomenon is dubbed as Gribov copies, as described in section 2.5. Second, for large inverse gauge couplings  $\beta$  corresponding to small lattice spacings  $a$ , the fit of a configuration with thin vortices is necessarily bad at the very position of the thin vortices on the lattice. Using the decomposition  $U_\mu^g = Z_\mu V_\mu$  ((4.1)) of the links we can also decompose the plaquettes as

$$U_P^g = Z_P V_P \quad (4.9)$$

with  $Z_P \in \mathbb{Z}_N$ . Whereas the gauge independent traces of the plaquette variables  $U_P$  are for small lattice spacings  $a$  near 1, P-vortex plaquettes take values of the nontrivial center elements. In order to comply with (4.9) at P-vortex sites, the trace of  $V_P$  has to be far away from unity. In the maximal center gauge, all link components  $V_\mu$  are closer to the center element  $\mathbf{1}$  than to all other center elements. The only way that the product of four links  $V_\mu$  building  $V_P$  is away from  $\mathbf{1}$  is that at least one of them is far away from  $\mathbf{1}$ , but of course not nearer at other center elements. In other words, some links at the P-vortex positions spoil the DMCG condition (4.3) requiring that their trace is near unity in the adjoint representation. This problem is also apparent looking at the action density: In the continuum limit the action density is singular at the position of P-vortices, which is a bad approximation for a smooth configuration [ER00a, FGO01b]. To summarise, DMCG followed by projection is a good fit for the configuration away from the P-vortices, but a bad fit near them. How good the approximation is numeric calculations can tell only.

### 4.2.1 Numeric Tests – Overview

In the last years several numeric investigations support that P-vortices indeed localise thick vortices, and preserve the confining properties of the gauge theory. Among those are:

- projected Creutz ratios  $\chi_{cp}(I, I)$  are close to the asymptotic string tension on the unprojected lattice (**center dominance**);
- the density of P-vortices scales correctly if the coupling  $\beta$  is changed;
- The projected P-vortices are located roughly in the middle of thick center vortices on the unprojected lattice;
- removing center vortices (located via the projected lattice) from unprojected lattices also removes confinement.

Center dominance is the finding that measuring the asymptotic string tension using projected operators gives results in good agreement with unprojected measurements. Projected operators (e.g. Wilson loops) are operators used after center projection of the

## 4.2 Maximal Center Gauges

configurations. We will give detailed results on center dominance below. The density of P-vortices depending on  $\beta$  and therefore on the lattice spacing  $a$  will also be treated further below.

Maybe the strongest numerical argument in favour of the vortex finding methods is the correlation of the position of P-vortices with the position of vortices in the unprojected lattice. This correlation can be investigated using **vortex-limited Wilson loops** in SU(2) gauge theory. A vortex-limited Wilson loops  $W_n(C)$  is defined as a (planar) fundamental Wilson loop which is calculated using a sub-ensemble of the configurations in the Monte Carlo configuration only. The sub ensemble is the set of configurations where the area of the loop is pierced by  $n$  P-vortices. Hence the center projection is only done in order to select the configurations taken into account for the calculation of the expectations value of the loop operator; the calculation itself is done using the full, unprojected configurations. The argument is simple. Because thick vortices carry a flux with values in the nontrivial center (i.e.  $-1$ ), their only influence on the loop is a factor of  $-1$ , assuming they pierce the loop area not close to the perimeter. Hence the contribution of the short-range, non-vortex perturbation part of the configuration is unaffected by the presence of thick vortices somewhere inside of the loop. This perturbation part cancels in quotients of vortex-limited Wilson loops such as built below in (4.10), and we see the isolated vortex background. Only if vortices crossed by the loop are partly inside the area they give a non-center contribution to the Wilson loop. This contribution is proportional to the border of the loop area and gives a perimeter law contribution to the loop. Whereas the perimeter law governed contribution is important for small loops, it is negligible for large loops, and it follows that for large loops the ratio of vortex-limited Wilson loops behaves like

$$\frac{W_n(C)}{W_m(C)} \rightarrow (-1)^{n+m}. \quad (4.10)$$

Fig. 4.1 on the next page taken from Del Debbio et al. [DFG<sup>+</sup>98] confirms these considerations. For large loops  $W_1(C)/W_0(C)$  approaches  $-1$ . The deviation for smaller loops can be used to explain the phenomenon of Casimir scaling, as described in section 3.4.

The removal of vortices from the unprojected configuration is done by multiplying the links of the unprojected lattice by the center element got after center projection [dFD99]. This means that for the removal the unprojected configurations are changed themselves using the P-vortices found. What this procedure does is to add thin vortices into the unprojected configurations at the positions where thick vortices are assumed to be. In this way short range disorder is introduced into the configurations because of the high action density of thin vortices, but the long-range influence of the original thick vortices is cancelled. The numeric results show that indeed confinement measured using Wilson loops and Creutz ratios is lost after applying vortex removal. Even more, also the topological susceptibility and chiral symmetry breaking, two other important properties of infrared QCD beside confinement, are not present after the procedure. We will deal with the connection of the topological properties of gauge fields and the chiral symmetry to vortices in chapter 7.

## 4.2 Maximal Center Gauges

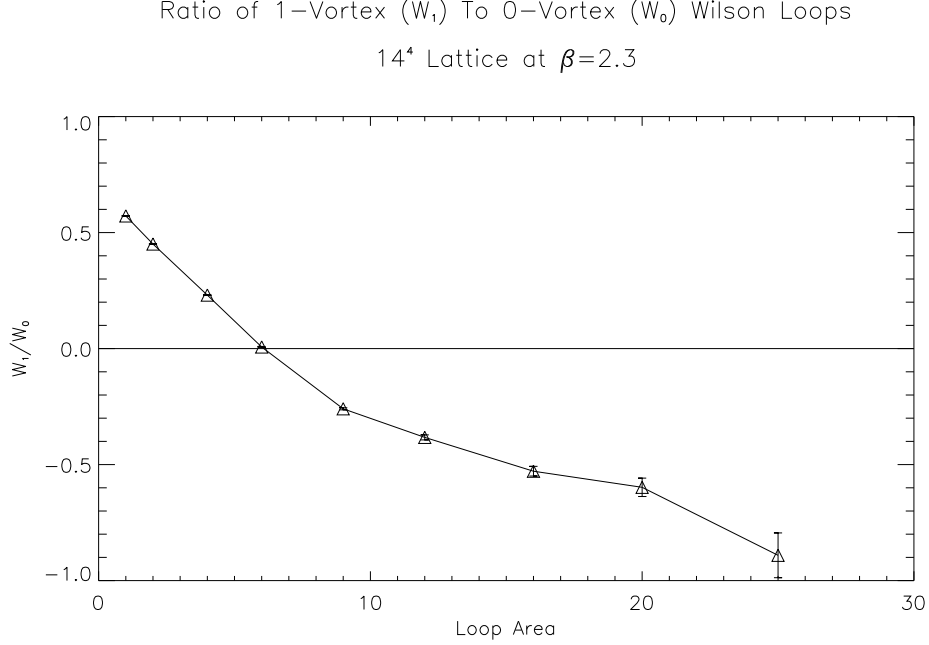


Figure 4.1: Ratio of the 1-Vortex to the 0-Vortex Wilson loops  $W_1(C)/W_0(0)$ , vs. loop area at  $\beta = 2.3$ . Taken from Del Debbio et al. [DFG<sup>+</sup>98].

### 4.2.2 Center Dominance and Vortex Density – Overview

In this section we will test the validity of MCG and center projection in detail looking at center dominance and the vortex density. Some of these results have been already reported in [BFGO00]. As mentioned in section 4.2.1, center dominance is the fact that observables can be correctly calculated after center projection. The observable mainly used in this section is the asymptotic string tension  $\sigma$  (section 3.2). The  $Z_N$  gauge field configurations yields the same value for  $\sigma$  as the full  $SU(N)$  configurations. All results presented in this section are for the gauge group  $G = SU(2)$ . For the gauge procedure, we have used the over-relaxation method on various lattices for different values of the coupling  $\beta$ , and also using different parameters controlling how over-relaxation was performed. The dependence on the way the gauge was done will be discussed further below.

A first overview over our results for center dominance is plotted in fig. 4.2 on the following page. Here we see the string tension calculated using Creutz ratios  $\chi(2,2)$  and  $\chi(3,3)$  from both the unprojected and the center projected lattice. For comparison, the asymptotic string tension inferred by two other methods is plotted: Strong coupling expansion and data from the literature. The strong coupling result is given by an analytical calculation using the strong coupling expansion up to the 14<sup>th</sup> order. This approximation is valid for small values of  $\beta$ . The literature data stems from reference lattice calculations using Wilson loops on the unprojected lattice; for  $\beta = 2.2$  it is taken

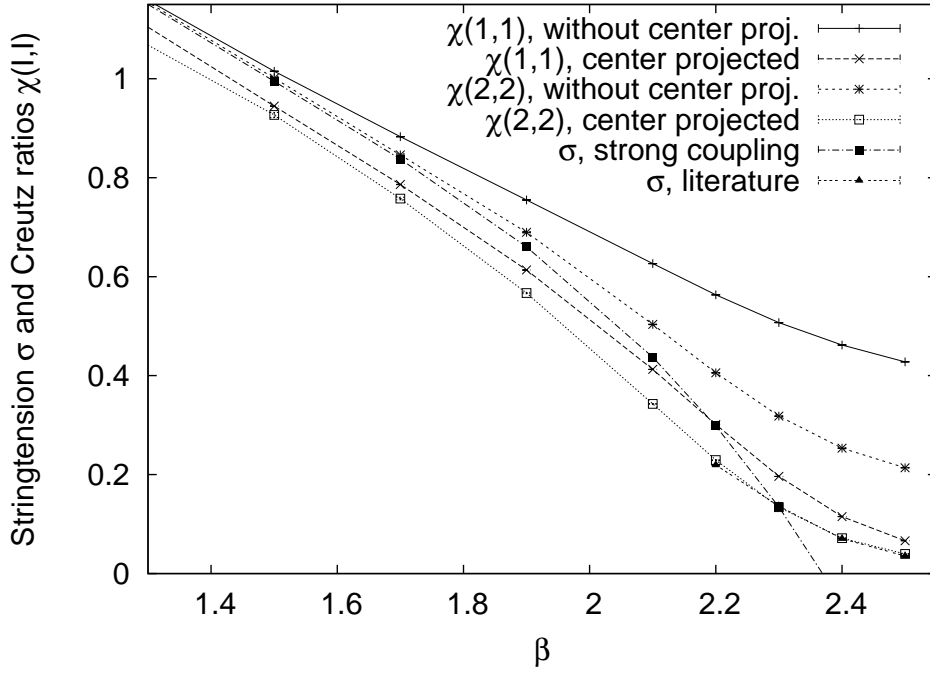


Figure 4.2: Creutz ratios  $\chi(I, I)$  compared to the asymptotic string tension  $\sigma$  inferred using various methods.

from Michael and Teper [MT87], for the other data points from Bali et al. [BSS95].

We see that starting from  $\beta = 2.2$  the center projected Creutz ratios  $\chi_{cp}(2, 2)$  nicely reproduce the asymptotic string tension taken from the literature. The projected Creutz ratios  $\chi_{cp}(1, 1)$  lie higher;  $\chi_{cp}(1, 1)$  is related to the vortex density, which we will treat in detail below and in section 5.2. For low values of  $\beta$  the projected observables are clearly below the expected result from the strong coupling expansion, whereas the unprojected quantities approach the analytical result below  $\beta = 1.5$ . At low  $\beta$  the lattice spacing  $a$  becomes bigger than the average distance of vortices. We think that vortex detection is sensible to too large values of the lattice spacing, and also to the size of the lattice, as will be shown soon.

Remarkable is that in the scaling region  $\beta \geq 2.2$  the projected Creutz ratios  $\chi_{cp}(2, 2)$  give the correct string tension, whereas the unprojected  $\chi(2, 2)$  lie higher. This fact is dubbed as **precocious linearity**. Unprojected Creutz ratios  $\chi(I, I)$  give the asymptotic string tension only for larger values of  $I$ . Center projection isolates the center degrees of freedom responsible for confinement and removes short-range perturbations thus showing the linear rising potential earlier.

For  $\beta = 2.5$ , fig. 4.3 on the next page shows the precocious linearity in detail. In figs. 4.3 to 4.10 on pages 37–43, solid (dashed) lines indicate the value (errorbar) of the asymptotic string tension on the unprojected lattice, reported in ref. [BSS95]. The unprojected Creutz ratios  $\chi(I, I)$  approach the asymptotic string tension only for higher

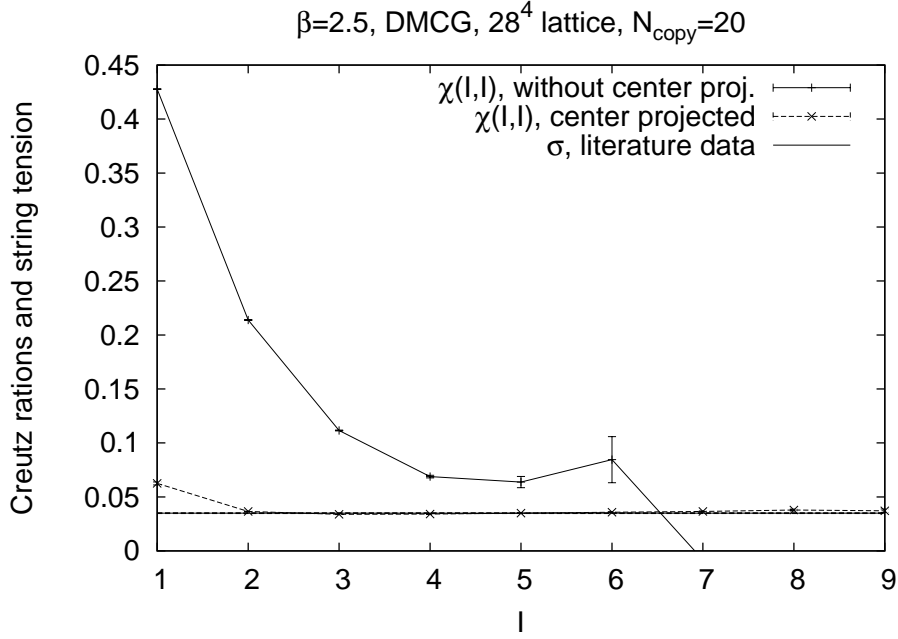


Figure 4.3: Creutz ratios  $\chi(I, I)$  calculated on unprojected and center projected lattices depending on  $I$  for  $\beta = 2.5$ . The horizontal line labelled “ $\sigma$ , literature data” represents the asymptotic string tension as reported by Bali et al. [BSS95].

values of  $I$ . Due to rather poor statistics (30 configurations), the errorbars become too large beyond  $I = 6$ , and the asymptotic value is not reached. The projected Creutz ratios, on the other hand, approach starting from  $I = 2$  perfectly the asymptotic string tension  $\sigma$ . For the other values of  $\beta$  in the scaling region precocious linearity hold, too, as can be seen from fig. 4.4 on the following page.

However, as pointed out in a paper by Bornyakov et al. [BKPV00], abbreviated BKPV henceforth, MCG might fail. The success of the method depends crucial on the parameters used for the gauge procedure [BFGO00]. In our work we use the procedure of over-relaxation. As noted above, when over-relaxation gauge-fixing procedure is applied to different gauge copies of a given lattice configuration (i.e. some random gauge transformation is applied before starting the MCG procedure), different local maxima of the gauge functional  $R$  are obtained. One way to minimise the gauge copy dependence is to carry out the over-relaxation procedure on a number  $N_{copy}$  of random gauge copies.

We judge the procedure to have converged using the criterion

$$\frac{R_n - R_{n-50}}{R_n} < \delta, \quad (4.11)$$

where the value of  $R$  after  $n$  over-relaxation steps is termed as  $R_n$ . Next the gauge copy with the largest value of  $R_n$  is taken and center projection is performed. From the projected configurations various observables depending on the used parameters can

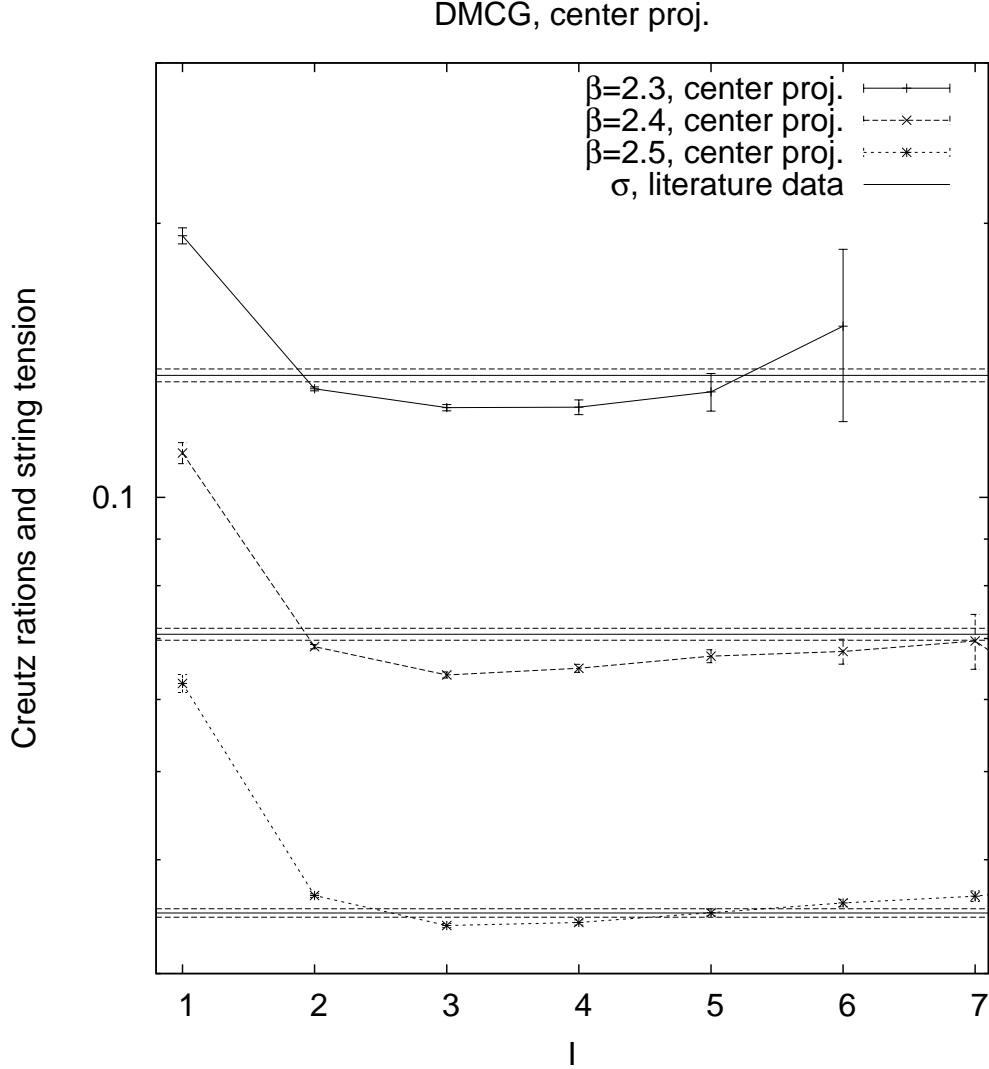


Figure 4.4: Creutz ratios  $\chi(I, I)$  calculated on unprojected and center projected lattices depending on  $I$  for  $\beta = 2.2, 2.3$  and  $2.5$ . The horizontal lines labelled “ $\sigma$ , literature data” represent the asymptotic string tension as reported by Michael and Teper [MT87] and Bali et al. [BSS95].

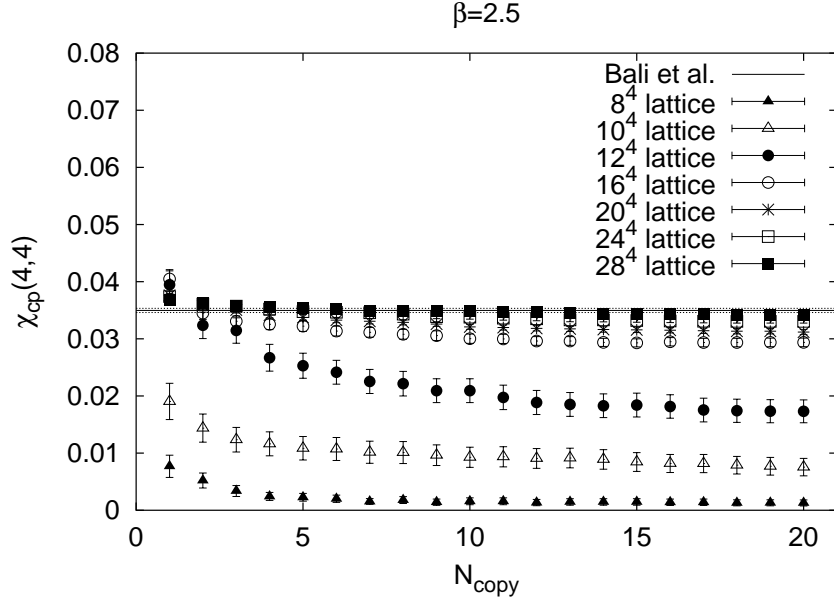


Figure 4.5: Center projected Creutz ratios  $\chi_{cp}^{N_{copy}}(4,4)$  vs.  $N_{copy}$  at various lattice volumes, for  $\beta = 2.5$ . The solid line in this figure indicates the asymptotic string tension extracted by standard methods on unprojected lattices, reported by Bali et al. [BSS95]. Dashed lines indicate the errorbar in this asymptotic string tension.

be investigated. Data obtained in this way, over a range of  $N_{copy}$  values, can then be extrapolated to the  $N_{copy} \rightarrow \infty$  limit.

### 4.2.3 $N_{copy}$ and Lattice Size Dependence

We begin with the  $N_{copy}$  dependence, whose importance was recently emphasised by BKPV in [BKPV00]. They did not use only three gauge copies as in earlier simulations [DFG<sup>+</sup>98], but calculated Creutz ratios in the range  $N_{copy} \in [1, 20]$ , and extrapolated to  $N_{copy} \rightarrow \infty$  by fitting their data to the functional form

$$\chi_{cp}^{N_{copy}}(I, I) = \chi_{cp}(I, I) + \frac{c(I, I)}{\sqrt{N_{copy}}}. \quad (4.12)$$

The result reported by BKPV is that projected string tensions, at  $\beta = 2.4, 2.5$ , underestimate the full string tension by about 20% at  $N_{copy} = 20$ , and by as much as 30% in the extrapolation to  $N_{copy} \rightarrow \infty$ . On the other hand, BKPV used rather small lattices of size  $12^4$  at  $\beta = 2.3$  and  $\beta = 2.4$ , and  $16^4$  at  $\beta = 2.5$ . The following result have been obtained by calculation at  $\beta = 2.3$  and  $\beta = 2.5$  on a variety of lattice sizes, for  $N_{copy} \in [1, 20]$ . For the convergence parameter in (4.11), we have used  $\delta = 2 \times 10^{-7}$ .

In fig. 4.5 we display results for the Creutz ratio  $\chi_{cp}^{N_{copy}}(4,4)$  vs.  $N_{copy}$  at  $\beta = 2.5$ , for lattice sizes ranging from  $8^4$  to  $28^4$ . Two features of this data are immediately

## 4.2 Maximal Center Gauges

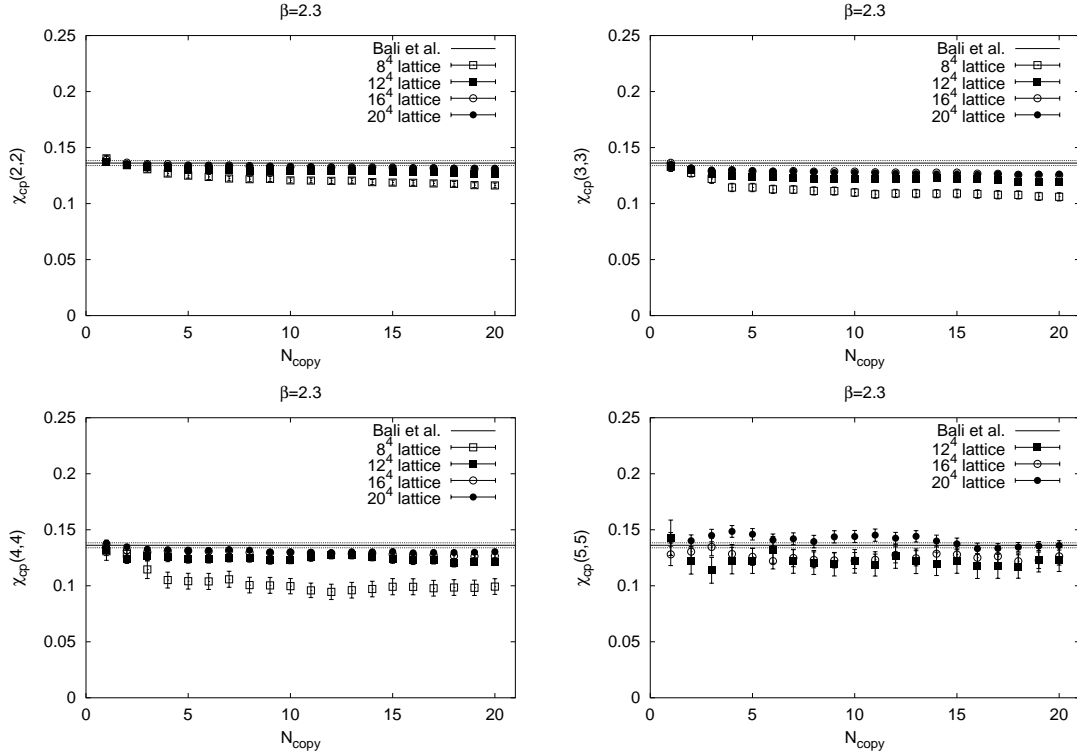


Figure 4.6: Center projected Creutz ratios  $\chi_{cp}^{N_{copy}}(I, I)$  vs.  $N_{copy}$  and lattice volume, at  $\beta = 2.3$  and  $I = 2 - 5$ . The solid line in this figure indicates the asymptotic string tension extracted by standard methods on unprojected lattices, reported by Bali et al. [BSS95]. Dashed lines indicate the errorbar in this asymptotic string tension.

apparent. First, there is indeed a slow downward trend in the Creutz ratio as  $N_{copy}$  increases, as noted by BKPV, but this effect is much more pronounced on smaller lattices than on larger lattices. Second, although Creutz ratios on the smaller lattices grossly underestimate the full string tension, the data appears to steadily increase towards the full asymptotic string tension, reported by Bali et al. [BSS95], as the lattice size increases. These trends in the data are by no means unique to the particular Creutz ratio  $\chi_{cp}(4, 4)$  at  $\beta = 2.5$ , but are typical of all of our results. For completeness we display, in figs. 4.6 to 4.7 on pages 40–41, some other projected Creutz ratios  $\chi_{cp}^{N_{copy}}(I, I)$  for  $I$  in the range  $I = 2 - 5$ , at couplings  $\beta = 2.3$  and  $\beta = 2.5$ .

In fig. 4.8 on page 42 we show the projected Creutz ratios  $\chi_{cp}^{N_{copy}}(I, I)$  for  $N_{copy} = 5, 10, 15, 20$  for the largest lattice used:  $20^4$  at  $\beta = 2.3$  and  $\beta = 2.4$ , and  $28^4$  at  $\beta = 2.5$ . We also show the values of these Creutz ratios extrapolated to the  $N_{copy} \rightarrow \infty$  limit, using the fitting function (4.12). We find that all the  $\chi_{cp}(I, I)$  for  $I \geq 2$  are close to the asymptotic string tension. As another way of showing lattice size dependence, we take the average of the projected ( $N_{copy} \rightarrow \infty$ ) Creutz ratios  $\chi_{cp}(I, I)$  in the range  $I = 2 - 5$



## 4.2 Maximal Center Gauges

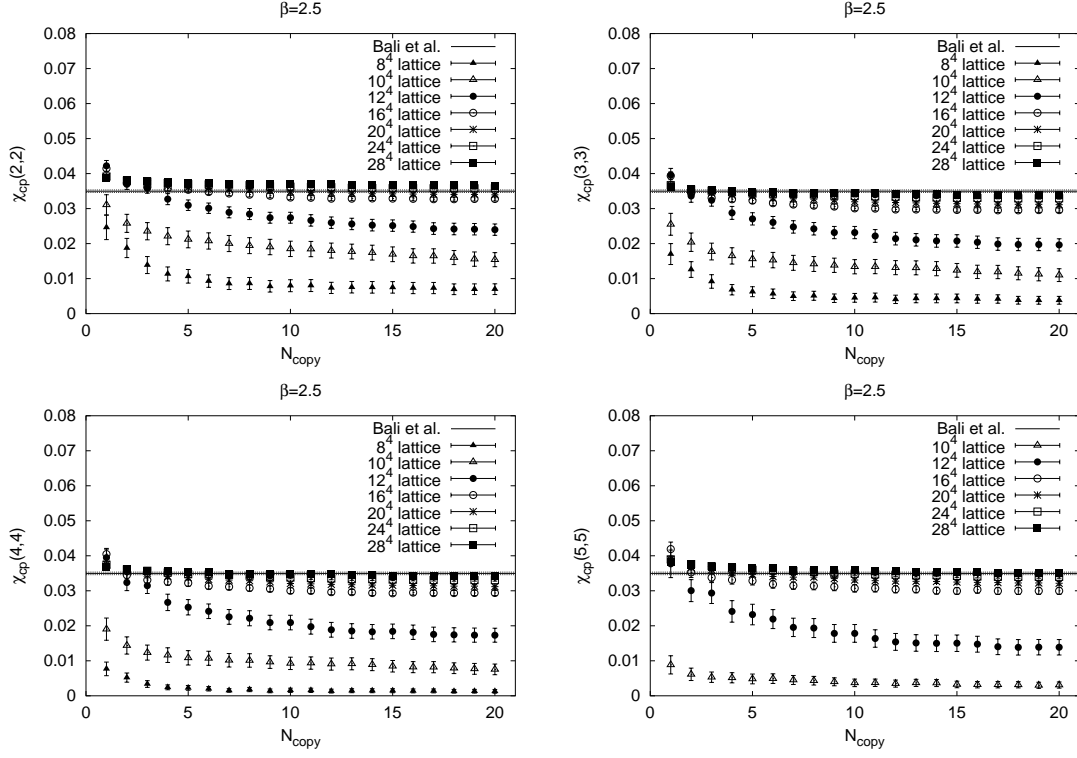


Figure 4.7: Center projected Creutz ratios  $\chi_{cp}^{N_{copy}}(I, I)$  vs.  $N_{copy}$  and lattice volume, at  $\beta = 2.5$  and  $I = 2 - 5$ . The solid line in this figure indicates the asymptotic string tension extracted by standard methods on unprojected lattices, reported by Bali et al. [BSS95]. Dashed lines indicate the errorbar in this asymptotic string tension.

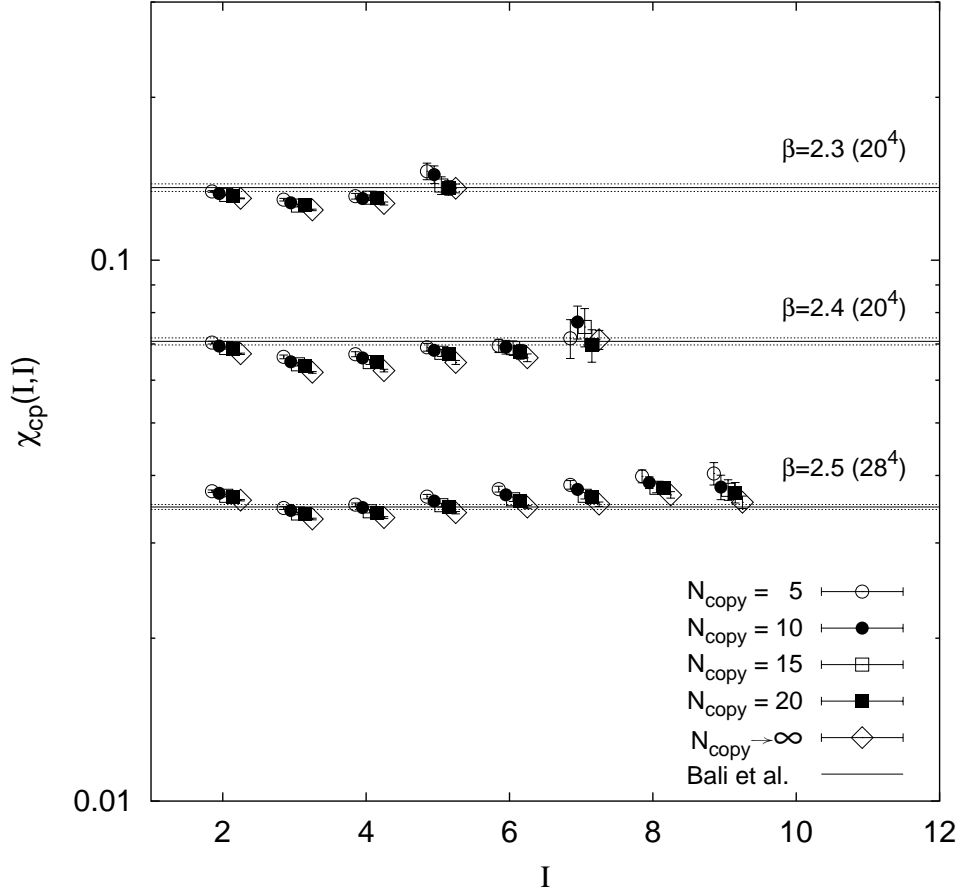


Figure 4.8: Center-projected Creutz ratios  $\chi_{cp}(I, I)$  at  $N_{copy} = 5, 10, 15, 20$ , and extrapolated to  $N_{copy} \rightarrow \infty$ .

depending on the lattice size, as depicted in fig. 4.9 on the next page. Clearly the averaged Creutz ratios approach the full asymptotic string as the lattice size increases.

#### 4.2.4 Gauge-Fixing Convergence Criterion

In addition to the lattice volume and  $N_{copy}$  dependence we have also checked whether the numerical results are stable with regard of the gauge-fixing convergence criterion  $\delta$  in (4.11). We find that if  $\delta$  is too large and the gauging process is terminated too fast, the center projected Creutz ratios  $\chi_{cp}(I, I)$  come out too high. This can be seen from fig. 4.10 on the following page, which shows results for  $\chi_{cp}$  with convergence criteria  $\delta = 10^{-2}, 10^{-3}, 10^{-4}, 2 \times 10^{-7}$  at  $\beta = 2.5$  on  $24^4$  lattices. The weakest convergence criterion, corresponding to  $\delta = 10^{-2}$ , is clearly insufficient for accurate results, but Creutz ratios obtained with the two smallest values of  $\delta$  are fairly consistent, indicating that these numbers are not far from the  $\delta \rightarrow 0$  limit.

## 4.2 Maximal Center Gauges

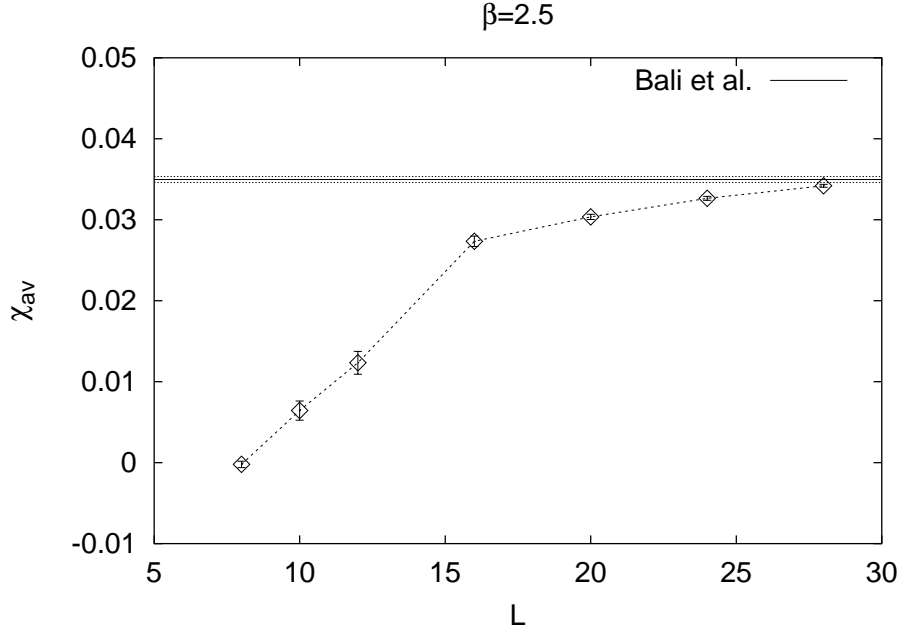


Figure 4.9: Average of projected and extrapolated  $N_{copy} \rightarrow \infty$  Creutz ratios  $\chi_{cp}(I, I)$ , in the range  $I = 2 - 5$ , depending on the lattice size.

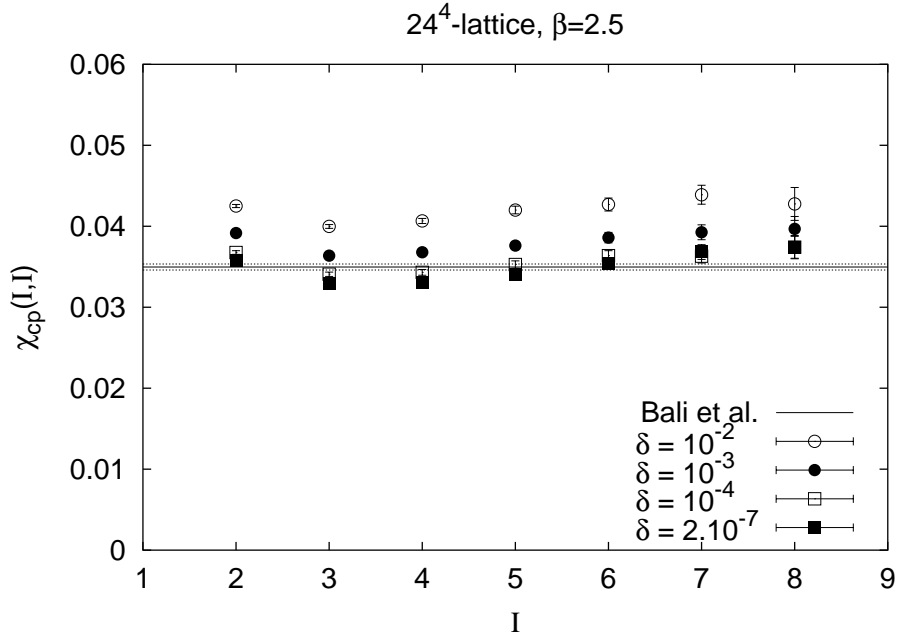


Figure 4.10: Effect of varying the convergence criterion  $\delta$  on projected Creutz ratios (extrapolated to  $N_{copy} \rightarrow \infty$ ) at  $\beta = 2.5$  on a  $24^4$  lattice.

### 4.2.5 Problems

We have seen that the maximal center gauge using over-relaxation followed by center projection is sensitive to the parameters (lattice size, number of gauge copies, etc.), but gives good results if parameter sets are chosen appropriately. But the method has also serious flaws:

- Gribov copies (see section 2.5) – Iterative, local gauging procedures like over-relaxation converge only to an (arbitrary, not uniquely defined) local maximum, not to the absolute maximum of the gauge functional  $R$ .
- Unprojected configurations can be cooled. If only a finite number of cooling steps is performed, the result of cooling is strictly local, i.e. long range physics should not be affected, which is confirmed in Monte Carlo calculations. But MCG and center projection does not work for such configurations, no vortices are found.
- Similarly, renormalisation group smoothing diminishes short range excitations, but does not change the infrared, confining properties of the theory. MCG and projections fails for such configurations, too.
- As shown by Kovacs and Tomboulis [KT99], it is possible to find a gauge where the gauge functional  $R$  (4.3) is higher as  $R$  obtained by the DMCG using standard over-relaxation. This is done by first taking the configurations to (fundamental) Landau gauge (4.5), and then apply DMCG to this configuration. Now although  $R$  is higher in this gauge, after center projection confinement is lost, and the vortex density is considerably lower than after the standard procedure!
- The reported results have been gained using the over-relaxation method for gauge fixing. If instead the algorithmically more involved, but more powerful simulated annealing procedure (see section 2.5) is used, even for large lattices, and a high number of gauge copies, one arrives also at higher values for  $R$ , but again center dominance does fail [BKP01].

The explanation for these problems has first been found by Engelhardt and Reinhardt [ER00a]: In the continuum limit, thin vortices are not the best fit for a thick vortex configuration, but a vacuum configuration – a pure gauge (4.6) – is a good one. Only the existence of Gribov copies leads the over-relaxation procedure to a local, vortex finding gauge maximum. Starting with Landau gauge, or using simulated annealing, brings the configuration closer to the true maximum which does not localise vortices. We discuss this problem in section 4.3 and also provides a solution, the Laplacian center gauges.

Although DMCG fails in the continuum limit, which comes already apparent at finite lattice spacings  $a$  as shown by the reported problems, DMCG remains a reliable tool to extract the thick vortex content from field configurations. This is supported by the numerous results reported in this section and in chapter 3. Hence we will use DMCG with the over-relaxation procedure in the calculations reported in chapters 5 to 7, but are aware of the limits of the method.

### 4.3 Laplacian Methods

*Laplacian (Landau) gauge* has been introduced by Vink and Wiese in [VW92, Vin95] as an ambiguity free substitution for Landau gauge, which does not suffer from the Gribov problem (section 2.5, section 4.2.5). A variant of the Laplacian gauge, the *Abelian Laplacian gauge* has been used for Abelian projection and for the identification of Abelian monopoles [vdS97, vdS98].

In this section we deal mainly with the variants of Laplacian center gauges serving as Gribov copy free substitutions for the maximal center gauge (MCG) which is the topic of section 4.2. In addition the Laplacian center gauges provide a way to identify vortices directly without center projection using local gauge ambiguities. We will prove the relation of vortices and Laplacian gauge singularities and investigate numerically the behaviour of the Laplacian eigenvectors around vortices inserted by hand. This elaborates further the findings of [Hir00, BFH02] and confirms results reported in [Mon01].

Laplacian methods are not restricted to the lattice and the SU(2) and SU(3) groups. They can be formulated in the continuum [vB95], and can be extended to a certain degree to arbitrary simple Lie groups [RT01]. We will stay as general as possible in the following section; the numerical investigations have been done on the lattice with gauge group  $G = \text{SU}(2)$ .

#### 4.3.1 Gauging Using Eigenvectors

The idea behind the various flavours of Laplacian gauges is to use covariantly smooth vector fields – the eigenvectors of the covariant Laplacian – to construct a smooth gauge. In section 2.1 we have regarded gauge transformations as changes of base vectors in colour space. To get a smooth gauge we perform a (passive) coordinate transformation  $S_g(x)$  which rotates the base vectors of colour space at each point as close as possible in the direction of the smooth eigenvectors:

$$\bar{e}_i = S_g^j{}_i e_j \quad (4.13)$$

$S_g$  is a representation of the gauge group element  $g$ ; the representation depends on which vector bundle  $(E, M, \pi, V, G)$  associated to the principal bundle  $(P, M, \pi, G)$  we consider. The section  $g(x)$  of the principal bundle is the gauge transformation looked for. We denote that there might be an ambiguity in getting  $g$  from  $S_g$ ; this will be discussed below.

Originally, this method was used for the fundamental representation of SU( $N$ ). This leads to Laplacian (Landau) gauge [VW92]. Here we are interested in gauges substituting maximal center gauge (MCG), which requires the adjoint representation. The covariant adjoint Laplace operator in the continuum is given by the Laplace-Beltrami operator  $\Delta$ , on the lattice it reads

$$\hat{\Delta}\varphi^i(x)e_i(x) := \sum_{\mu} \left( 2\varphi^i(x) - U_{j\mu}^i(x)\varphi^j(x + \hat{\mu}) - (U_{j\mu}^i)^{-1}(x - \hat{\mu})\varphi^j(x - \hat{\mu}) \right) e_i(x). \quad (4.14)$$

### 4.3 Laplacian Methods

Next one calculates the eigenfunctions / vectors of the covariant Laplace operator

$$\Delta\varphi^{(m)} = \lambda^{(m)}\varphi^{(m)}. \quad (4.15)$$

On the lattice, the eigenvectors are represented as  $\dim(V) \times N_{vol}$ -dimensional vectors, where  $N_{vol}$  is the number of lattice sites; for the adjoint representation, the dimension of the vector space  $\dim(V)$  is given by the dimension of the Lie algebra  $\dim \mathfrak{g}$ . The eigenvalues are real and non-negative, and the eigenvector fields are orthonormalised with

$$\left(\varphi^{(m)}(x), \varphi^{(n)}(x)\right) = \delta_{mn}, \quad (4.16)$$

where the scalar product is, due to the orthonormality / unitarity of the base, given by

$$\left(\varphi^{i(m)}(x), \varphi^{i(n)}(x)\right) = \begin{cases} \int dx \varphi^{*i(m)}(x) \varphi^{i(n)}(x) & \text{(continuum)} \\ \sum_{x,i} \varphi^{*i(m)}(x) \varphi^{i(n)}(x) & \text{(lattice)}. \end{cases} \quad (4.17)$$

(For the adjoint representation, complex conjugation  $(*)$  is not necessary.) Note that the eigenvector fields  $\varphi^{(m)}$  of the smallest eigenvalues  $\lambda^{(m)}$  (called “lowest eigenvectors” henceforth) are the most covariant smooth fields, i.e.  $\|D_\nabla \varphi^{(m)}(x)\|$  is, on average, as small as possible. Here the norm of a Lorentz scalar field is defined as

$$\|\varphi^{(m)}(x)\| = \left(\varphi^{(m)}(x), \varphi^{(m)}(x)\right), \quad (4.18)$$

whereas for fibre valued one-forms  $\varphi$  in addition the scalar product for forms in metric spaces has to be performed. In our Euclidean space the norm reads

$$\|\varphi^{(m)}(x)\| = \left(\varphi_\mu^{(m)}(x), \varphi_\nu^{(m)}(x)\right) \delta^{\mu\nu}, \quad (4.19)$$

with  $\varphi = \varphi_\mu dx^\mu$ .

The task is now to find new base vectors in colour space  $e_i(x)$  which are close to the lowest eigenvectors  $\varphi^{(i)}(x)$  at each position  $x$ . Because  $\|D_\nabla \varphi^{(m)}(x)\|$  is small,  $\|D_\nabla e_i(x)\|$  is small for such a base, too, and using the definition of  $\mathcal{A}$  ( (2.6) on page 11)

$$(D_\nabla e_i)(\partial_\mu) = \nabla_{\partial_\mu} e_i = ig \mathcal{A}_{i\mu}^j e_j \quad (4.20)$$

we conclude that we have found a gauge where on average

$$ig[\mathcal{A}_i^j]_\mu(x) \text{ as close as possible at } \mathbf{0} \quad \text{(continuum)} \quad (4.21)$$

$$[\mathcal{U}_i^j]_\mu(x) \text{ as close as possible at } \mathbf{1} \quad \text{(lattice)}. \quad (4.22)$$

For the adjoint representation on the lattice, this is a gauge which shifts the (adjoint) link variables  $U_\mu$  close to unity. This is similar to maximal center gauge, a gauge which tries to maximise the trace of the adjoint links  $\langle \text{Tr } U \rangle$  as described in section 4.2. After such a gauge fixing, there remain the center degrees of freedom from the ambiguous mapping of adjoint to fundamental variables. On the lattice, this gives the  $Z_N$  symmetry of these gauges. For the continuum, we discuss the situation in section 4.3.4.

#### 4.3.1.1 Relation to Other Gauges

Adjoint Laplacian gauges can be related to maximal center gauge as follows [FGO01a] (see [VW92] for the relation of fundamental Laplacian gauge to the Landau gauge): In MCG, one tries to find a gauge transformation  $S_g$  which maximises the average trace of the adjoint links (section 4.2)

$$R = \sum_{\mu, x} \text{Tr}[S_g^T(x) U_\mu(x) S_g(x + \hat{\mu})]. \quad (4.23)$$

But there is a serious problem with this gauge: If one finds the global maximum of this functional  $R$ , and performs center projection in this gauge, no vortices are found in the continuum limit. MCG plus center projections can be interpreted as fitting the thick vortices of a configuration with infinite thin, projected center vortices, which is a very bad approximation in the continuum limit [ER00a, FGO01b]. In our opinion, this is also the source of various problems for this gauge [KT99, BKPV00], as outlined in section 4.2.5. Only because of Gribov copies the procedure is such successful for finite lattice spacings and a finite number of gauge copies in the gauge algorithm.

In order to identify vortices, inside of a thick vortex a gauge has to allow links far from the center elements [FGO01b]. One way to cure the problem is to weight the functional  $R$  less near the position of the projected vortex. The easiest way to achieve this is to maximise a modified functional

$$R' = \sum_{\mu, x} \text{Tr}[M^T(x) U_\mu(x) M(x + \hat{\mu})], \quad (4.24)$$

where  $M$  is a real matrix which is orthogonal only in average and not at each site as  $S_g$ :

$$\int dx M_j^i(x) M_k^{jT}(x) = \delta_k^i \quad (\text{continuum}) \quad (4.25a)$$

$$\sum_x M_j^i(x) M_k^{jT}(x) = \delta_k^i \quad (\text{lattice}). \quad (4.25b)$$

The unique solution of this maximisation is given by the  $N$  lowest eigenvectors of the Laplacian [VW92, FGO01a] related to  $M$  with

$$M_i^j(x) = \varphi^{(i)j}. \quad (4.26)$$

#### 4.3.2 From Eigenvectors to Gauge Matrices

After getting covariantly smooth vector fields  $\varphi$ , the eigenvectors of the Laplacian, the question remains how to choose new base vectors  $e$  close to  $\varphi$ , i.e. construct the gauge matrix  $S_g$ . In the last years, several ways have been proposed:

##### 4.3.2.1 Laplacian Center Gauge

*Laplacian center gauge* (LCG) has been the first gauge intended to substitute MCG [AdFD00, dFP00a, dFP01]. To go to Laplacian center gauge, we perform a (passive)

### 4.3 Laplacian Methods

coordinate transformation  $S_g(x)$  in (adjoint) colour space such that in each point of space time / on the lattice the base vector  $e_1(x)$  is parallel to  $\varphi^{(1)}(x)$ , and that the vector  $e_2(x)$  points in the direction given by the component  $\varphi^{\perp(2)}(x)$  of  $\varphi^{(2)}(x)$  orthogonal to  $\varphi^{(1)}(x)$ .

After this, all adjoint base vectors are fixed. There remains a  $Z_N$  symmetry from the ambiguity to map the adjoint gauge matrix  $S_g$  to the fundamental group element  $g$  used to gauge the link field. This is the case for all center gauges using the covariant adjoint Laplace operator.

If only  $e_1$  is rotated in direction of  $\varphi^{(1)}$  without fixing the direction of  $e_2$ , we arrive at Laplacian Abelian gauge [vdS97, vdS98]. This gauge shows a remaining  $U(1)$  symmetry.

#### 4.3.2.2 Laplacian Adjoint Landau Gauge

*Laplacian adjoint Landau gauge* (LALG) [FGO01b, FGO01a] is the equivalent of the original fundamental Laplacian gauge [VW92] for the adjoint representation of the  $SU(2)$  gauge group. Singular value decomposition

$$M = VDW^T, \quad (4.27)$$

where  $V, W$  are orthogonal and  $D$  is a diagonal positive semi-definite matrices, followed by polar decomposition

$$M = [VW^T][WDW^T], \quad (4.28)$$

shows that  $M$  as a quadratic real  $3 \times 3$  matrix can be unambiguously written as the product of an  $SO(3)$  matrix  $S_g = \det[VW^T]VW^T$  and a symmetric positive semi-definite matrix  $P = WDW^T$ :

$$M = \pm S_g P. \quad (4.29)$$

This decomposition shows nicely the relation of the Laplacian gauges to MCG as described above:  $P$  acts as variable weight factor going from (4.23) to (4.24). If  $M$  would be orthogonal, the gauge transformation  $S_g = M^T$  would let point the 3 base vectors  $e_i$  exactly into the direction of the 3 lowest eigenvectors  $\varphi^{(i)}$ , and we arrive at a smooth gauge as pointed out at the beginning of section 4.3.1. In this special case, LALG is the same gauge as the MCG. Generally, the eigenvectors of the Laplacian are not orthonormal at each point, but only on average, and the task is to extract an orthogonal gauge matrix  $S_g$  out of  $M$  which is closest to  $M$ , i.e. which maximises  $|\text{Tr}[S_g(x)M^T(x)]|$  at each point. This is exactly what singular value decomposition followed by polar decomposition does.

The advantage of this gauge over LCG is that it treats the first 3 eigenvectors symmetrically, whereas LCG aligns only the first base vectors with  $\varphi^{(1)}$ , and then fixes  $e_2$  to  $\varphi^{\perp(2)}(x)$  using the remaining  $U(1)$  gauge freedom. The properties of the three lowest eigenvectors are discussed in detail in 4.3.4 and 4.3.5.

#### 4.3.2.3 Direct Laplacian Center Gauge

As we will show in section 4.3.5.3, LALG allows to many fluctuations in order to identify the confining vortices appropriately [LRS01]. A solution is to modify the map from the



### 4.3 Laplacian Methods

real matrix  $M$  to the orthogonal matrix  $S_g$ . Instead of simply taking the closest orthogonal matrix, one requires that the orthogonal matrix satisfies the Laplace equation, too [FGO01a]. Such orthogonal matrices are local maxima of the MCG gauge condition (4.23). This can be achieved by applying MCG with over-relaxation to the gauge matrices inferred from LALG and results in a damping of undesired fluctuations. This procedure is called **direct Laplacian center gauge** (DLCG). Numerical studies show that the results known from DMCG, such as precocious linearity, center dominance, and vortex limited Wilson loops hold also for DLCG [FGO01a]. Finally we note that the over-relaxation MCG step can also be performed after LCG [LRS01].

#### 4.3.2.4 Generalisation to Simple Lie Groups

It can be shown that the LCG procedure to get a gauge from two covariantly smooth fields  $\varphi^{(n)}(x)$  in the adjoint representation can be generalised to arbitrary simple Lie groups  $G$  with Lie algebra  $\mathfrak{g}$  [RT01]: For the adjoint representation,  $\varphi^{(n)}$  is a Lie algebra valued field. In a first step,  $\varphi^{(1)}$  is gauge transformed such that it lies in the fundamental domain of the Cartan subalgebra of  $\mathfrak{g}$ . For the case of  $G = \text{SU}(N)$ , this is exactly the Laplacian Abelian gauge. After this rotation there remains a residual Abelian gauge freedom, which can be fixed imposing appropriate conditions on the components of the second field  $\varphi^{(2)}$ . This step is the Laplacian Center Gauge in the case of the gauge group  $\text{SU}(N)$ . The center of the gauge group  $G$  remains unfixed, as for all adjoint gauges.

Of course the question remains how to get reasonable smooth fields  $\varphi^{(n)}$  for arbitrary simple Lie groups – using the eigenvectors of the Laplacian has only been used for the  $\text{SU}(N)$  groups so far. And the LALG and DLCG procedure to get gauge transformations from smooth fields has not yet been generalised to other groups.

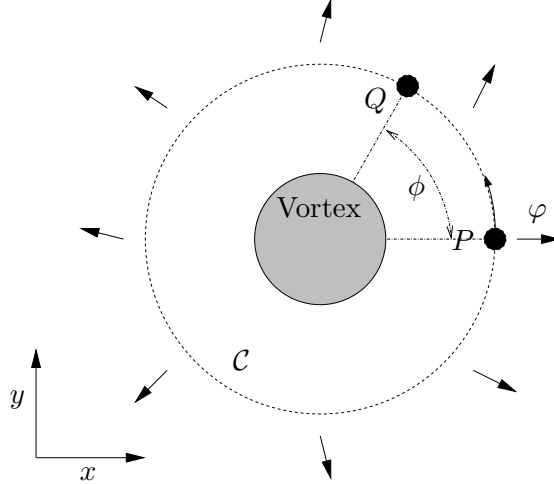
#### 4.3.3 Gauge Singularities

All Laplacian gauge methods are plagued by singularities. The eigenvectors  $\varphi^{(n)}(x)$  might vanish at some points  $x$ , or they might be linearly dependent locally. In these cases the prescription how to get the base vectors  $e_n$ , and thus the desired gauge transformation, from the vectors  $\varphi^{(n)}$  fails at the singularities. However, this problem only occurs in the continuum, on the lattice the probability of such gauge defects is zero.

Moreover, these defects can even be associated to the position of Abelian monopoles [vdS97, vdS98] and P-vortex surfaces [dFP01]. In the continuum for the gauge group  $\text{SU}(N)$ , the first eigenvector  $\varphi^{(n)}$  is zero at line-like regions identified with monopole world lines, and a linear dependence occurs at surfaces, the P-vortices. We will investigate these singularities further in section 4.3.4.1.

#### 4.3.4 A Simple Configuration

In this section we illustrate how the family of Laplacian gauges localises vortices, and how gauge ambiguities are related to vortices. The mechanism is discussed using the simple configuration drawn in fig. 4.11 on the following page. We have a plane pierced by a localised thick vortex. As described in section 3.4, such a thick vortex is defined as


 Figure 4.11:  $\varphi$  around a vortex.

a flux tube of finite diameter  $d$  carrying flux which is quantised in terms of the nontrivial center elements of the gauge group. For  $SU(2)$ , which is used in the following sections, there is only one nontrivial element in the center group  $Z_2$ . A thin vortex is a vortex with  $d \rightarrow 0$ . In a thin vortex the flux is concentrated in infinitely thin, closed lines and surfaces in 3 and 4 dimensions respectively. We recall that the idea of the various center gauges, combined with center projection, is to replace the full gauge configurations with a  $Z_N$  gauge field configuration, and the excitations of a  $Z_N$  system are thin vortices.

For the considered configuration, we require that outside the vortex of fig. 4.11 only short range fluctuations of the chromo dynamic field are admitted, i.e. the trace of the parallel transporter in fundamental representation along each closed line not linked with the vortex is small (the path  $\mathcal{C}$  is not such a line). *Linking* is a property of two cycles that they cannot continuously be shrunk to a point without crossing. Examples are two linked loops in three dimensions, or in four dimensions, as in our case, a loop and a surface such as the P-vortex surface. Linking between Wilson loops and vortices will be discussed in section 5.2.

Vortices are boundaries of a 3-volume, the Dirac volume. Hence a single vortex piercing a plane is not possible, there have to be an even number of vortex piercings. In the configuration of fig. 4.11, the second vortex is thought far away and is not considered. The numerical calculations in section 4.3.5 will investigate the eigenvectors around pairs of vortex piercings.

For a trivial field configuration (a pure gauge), we have  $\lambda^{(1)} = 0$  for the lowest eigenvalue of the adjoint Laplacian. This eigenvalue is 3-fold degenerated, and the eigenvectors are three covariantly constant fields orthogonal in colour space at each point. The next eigenvalue is 12 fold degenerate, corresponding to plane waves in 4 space time dimensions and 3 directions in colour space. A thin center vortex is “invisible” for adjoint fields. Hence it does not change the eigenvectors compared to the trivial configuration. In the configuration of fig. 4.11, the region outside the vortex is large compared to the

### 4.3 Laplacian Methods

thick vortex with small diameter  $d$ . Hence a thin vortex is a good approximation for the configuration, and we expect that the modifications for the eigenvectors compared to the trivial field are small. The lowest eigenvalue is split in three non degenerate eigenvalues, but the first three eigenvalues remain small compared to the next higher eigenvalues, and the eigenvectors of these eigenvalues are still approximately covariantly constant. More precisely, we expect that  $\varphi'^{(i)}(x) \simeq \varphi^{(i)}(x)$ , where  $\varphi'^{(i)}(x)$  is  $\varphi^{(i)}(x)$  after an (adjoint) parallel transport along an arbitrary closed line not *cutting* the interior of the vortex (the path  $\mathcal{C}$  is such a line). This means that the covariant (adjoint) difference of the vector field over finite distances is small outside the vortex.

Now, let us assume that we perform LCG fixing as described in section 4.3.2.1 starting at point  $P$  in fig. 4.11 on the preceding page. Locally, if we gauge along path  $\mathcal{C}$  in counter clockwise direction from  $P$  to  $Q(\phi)$ , it is possible to choose one of the two fundamental gauge matrices  $g(x)$  and  $g'(x)$  giving the same adjoint  $S_g(x)$  stemming from LCG in a smooth way. Because the fields  $\varphi^{(i)}(x)$  are nearly constant on  $\mathcal{C}$ , LCG moves the gauge field  $A(x)$  close to zero as explained above.  $A(x) \simeq \mathbf{0}$  is equivalent to  $A_{\text{fundamental}}(x) \simeq \mathbf{0}$ , and we arrive locally at a gauge resembling the (fundamental) Landau gauge. As stated above, the lowest eigenvector fields are nearly covariantly constant over finite distances. Thus in our gauge also the fundamental parallel transport  $U_{PQ} \simeq \mathbf{1}$ . But the fundamental parallel transport around the full path  $\mathcal{C}$  gives  $-\mathbf{1}$  because the vortex carries a flux of  $-1$ . Therefore our choice between  $g$  and  $g'$  cannot be smooth along all of the curve  $\mathcal{C}$ . This corresponds exactly to the discontinuous gauge transformation generating a thin vortex, and the discontinuity is its Dirac volume. Hence after center projections a (thin) vortex is found at this position.

In this section we have used the relation if  $D_{\nabla}\varphi^{(i)}$  is small, also  $D_{\nabla}e_i$  is small in order to explain that LCG moves the link variables close to the center elements. But this is not the case at positions where local ambiguities of Laplacian center gauge occur. If at a position  $x$  the lowest eigenvector  $\varphi^{(1)}$  vanishes, small derivations of  $\varphi^{(1)}$  around  $x$  give big derivations of the direction  $\varphi^{(1)}/|\varphi^{(1)}|$  in which we want  $e_1$  direct, and thus also big derivations of  $e_1$ . Another gauge ambiguity occurs if  $\varphi^{(1)}$  and  $\varphi^{(2)}$  are parallel. Then the orthogonal component  $\varphi^{\perp(2)}$  of  $\varphi^{(2)}$  is small around the position of the ambiguity, which leads to a big  $D_{\nabla}e_2$ . These are the gauge defects associated to monopoles and P-vortices, as introduced in section 4.3.3. In the next section, we will show that parallel eigenvectors indeed can be identified with center vortices. We will see that for each thick vortex such an ambiguity arises. This will provide us with a gauge independent way to locate vortices.

On the lattice, these gauge ambiguities never occur. Nevertheless there are regions in the thick vortex where the first two eigenvectors are nearly parallel, and  $D_{\nabla}e_i$  is not small. As a consequence, LCG does not shift the links close to the center elements somewhere inside the vortex. This cures the problem of MCG in the continuum limit as described in section 4.3.2.2.

For our conclusions, as well as for the considerations in the next section, we made two essential assumptions:

1. The gauge field shows only small short range fluctuations outside the vortex. This

### 4.3 Laplacian Methods

means that the gauge field can be separated in a part described by thick vortices and a part consisting only of short range fluctuations.

2. The vortex diameter is small compared to the region outside the vortex, such that the first three eigenvectors are only slightly modified compared to a trivial field configuration.

But there are indications that in Monte Carlo generated field configuration the distance between vortices is of the same order as the vortex thickness, and we have rather a liquid and not a dilute gas of vortices, as we will see in section 5.7. Therefore our conclusions might not hold for realistic field configurations. However, for configurations fulfilling these two conditions we could numerically confirm our results.

For thin vortices, the second condition is always fulfilled. Thus most of our results hold exactly for thin vortices. This corresponds to the vortex finding property of a class of gauges including MCG and LCG as described in section 4.1.

#### 4.3.4.1 Laplacian Eigenvectors Around a Vortex

In this section we will show that, under the conditions outlined at the end of the last section, each thick vortex can be located using the gauge singularities of LCG. Again we consider a plane pierced by a (thick) vortex as drawn in fig. 4.11 on page 50. Outside the vortex, the field has only short range fluctuations.

As stated in the last section, the lowest eigenvectors of the covariant adjoint Laplacian do not feel the center vortex far outside the vortex. If  $\varphi'^{(i)}(x)$ ,  $x \in \mathcal{C}$ , is the vector  $\varphi^{(i)}(x)$  after a parallel transport along the closed line  $\mathcal{C}$ , then we have  $\varphi'^{(i)}(x) \simeq \varphi^{(i)}(x)$ , because the parallel transporter equals  $\mathbf{1}$  in the adjoint and  $-\mathbf{1}$  in the fundamental representation. For the following considerations, we assume that  $\varphi'^{(i)}(x) = \varphi^{(i)}(x)$  holds exactly and expect the small variation induced by the final thickness of the vortex not to change the result principally.

Therefore, in the continuum, if we choose any smooth gauge, the fundamental parallel transporter  $U_{PQ} = U(\phi)$  is a function of  $\phi$  which maps the circle  $\mathcal{C}$  (see fig. 4.11) on a path in the group  $SU(2)$  connecting the two center elements – for  $\phi = 0$  we have  $U = \mathbf{1}$ , and for  $\phi = 2\pi$  we have  $U = -\mathbf{1}$ . In the adjoint representation,  $U(\phi)$  is a non contractible closed path on  $SO(3)$ , corresponding to the nontrivial element of the fundamental group  $\pi_1(SO(3)) \simeq \mathbb{Z}_2$ . Thus the lowest eigenvector fields  $\varphi^{(i)}$ , which are approximately covariantly constant over finite distances outside the vortex, show a rotation of  $2\pi$  in colour space around the vortex in any smooth gauge. This is plotted in fig. 4.11, too.

Thus we can conclude that vortices can be identified by looking for rotations of  $2\pi$  of the eigenvectors along closed lines. But on the lattice, this method is not as straightforward as in the continuum. The direction of the eigenvectors can be chosen independently at each lattice site using a gauge transformation. To see the rotation, we have to choose a smooth gauge and small lattice spacing  $a$ . In section 4.3.5 we will describe appropriate gauges. In general, it can be difficult to see the rotation of  $2\pi$ , because the non contractible path on  $SO(3)$  can be very complicated.

### 4.3 Laplacian Methods

In the continuum, the lowest adjoint eigenvectors fields  $\varphi^{(i)}(\phi)$  on the closed line  $\mathcal{C}$  can be generated by applying the  $\text{SO}(3)$  parallel transporters  $U(\phi)$  on some vectors  $\varphi^{(i)}(0)$  at point  $P$  using  $\varphi^{(i)}(\phi) = U(\phi)\varphi^{(i)}(0)$ . The matrices  $U(\phi)$  form a non contractible path on  $\text{SO}(3)$ . In a next step, if we look at the interior of the area  $\mathcal{B}$  bordered by  $\mathcal{C}$ , the lowest eigenvector fields are some smooth continuation of the fields given on  $\mathcal{C}$ . Now let us assume that two of these vector fields are linearly independent at each point of  $\mathcal{B}$ . Then we can construct at each point three orthonormal vectors  $e_i$  from these two linearly independent vectors in a smooth way. Next we assign to each point  $x$  an unique  $\text{SO}(3)$  element  $U(x)$  using  $e_i(x) = U_i^j(x)e_j(P)$ . This gives a smooth mapping from  $\mathcal{B}$ , which is homeomorphic to the filled disk  $D_2$ , on  $\text{SO}(3)$ . All mappings of  $D_2$  on  $\text{SO}(3)$  are topological trivial, i.e. contractible. But we have assumed that the mapping of the contour  $\mathcal{C}$  on  $\text{SO}(3)$  is not contractible. The only solution for this contradiction is that the vector fields are linearly dependent at least at one point inside  $\mathcal{C}$ .

In this way we conclude that independent of the internal structure of the thick vortex an ambiguity for the Laplacian center gauge arises somewhere inside the thick vortex. Because the linear dependence of the lowest eigenvectors of the adjoint covariant Laplace operator is a gauge independent property, we can use it to detect thick center vortices in a gauge independent way as proposed in [dFP01, AdFD00].

On the lattice, these ambiguities never occur exactly. But the smaller the lattice spacing  $a$  is, the more parallel the first three eigenvectors become somewhere inside the vortex. How can the position of the vortex determined on the lattice? One could look at places where the angle between two of the lowest eigenvectors is smaller than some fixed angle  $\theta$ . But this introduces an arbitrary parameter and is not well defined.

An alternative is to use the triple product of two of the eigenvectors with some linearly independent reference vectors  $\xi$  and  $\zeta$ . If  $\varphi^{(1)} \cdot (\varphi^{(2)} \times \xi)$  changes sign between two lattice sites, the product vanishes somewhere between, i.e. the three vectors are coplanar. This occurs on a closed three-dimensional hypersurface on the dual lattice. Another 3d hypersurface is given by the condition that  $\varphi^{(1)}$ ,  $\varphi^{(2)}$  and  $\zeta$  are coplanar. The intersection of these hypersurfaces is a closed two-dimensional surface in four dimensions, where  $\varphi^{(1)}$  and  $\varphi^{(2)}$  are collinear. This is the position of a thin vortex indicating the position of the thick vortex.

Unfortunately its not trivial to find appropriate reference vectors  $\xi$  and  $\zeta$ . Choosing random vectors gives a randomly fluctuating triple product and no information. In order to get gauge covariant reference vectors, one might try higher eigenvectors of the Laplacian  $\varphi^{(i)}$ . For  $\varphi^{(3)}$ , the triple product with  $\varphi^{(1)}$  and  $\varphi^{(2)}$  never changes sign in our simple configuration. They form a left or right handed system on the whole lattice because they rotate together around the vortex. Nevertheless minima of  $\varphi^{(1)} \cdot (\varphi^{(2)} \times \varphi^{(3)})$  indicate the vortex position as shown in section 4.3.5. Higher eigenvectors  $\varphi^{(i)}$  seem not to be smooth enough to see the collinearity of the first two vectors, at least on a coarse lattice. They correspond to “wave” solutions of the Laplacian and introduce sign changes not related to the vortex (see section 4.3.5).

Finally we want to give a comment to the limit of thin vortices. The simplest configuration of thin vortices is generated, starting from the trivial configurations, by flipping the sign of the links of some strip. Because the adjoint Laplacian does not see center

elements, the eigenvectors are not changed with regard to the trivial configurations. The vectors do not become shorter, and no gauge ambiguities occur. Nevertheless the Laplacian gauges work: all links are gauged to  $\pm 1$ . Also the rotation of the vectors can be seen using a smooth *fundamental* gauge, the vectors are the same as for the trivial configuration, but the gauge to look onto the colour vector rotation is different. Only our findings on the linear dependence of the lowest eigenvectors somewhere at the vortex does not hold for thin vortices. In the continuum thin vortices are singular objects, and our topological arguments rely on smooth eigenvectors fields.

### 4.3.5 Numerical Investigations

Next we study the four lowest eigenvectors of the covariant Laplacian for configurations with vortices inserted by hand, and for configurations generated using Monte Carlo simulation of QCD. First we look at a very simple vortex, a pair of plane vortices, and then at a spherical vortex. All calculations were done on a  $20^4$  lattice.

#### 4.3.5.1 Plane Vortex

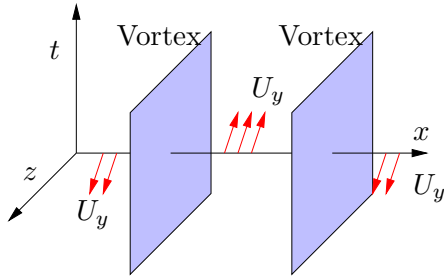


Figure 4.12: Two plane vortices.

We start investigating a pair of “plane” vortices which were inserted into two given  $z$ - $t$ -planes of the lattice. Fig. 4.12 is a schematic picture of this configuration. We write the  $SU(2)$  links variables as  $\cos(\alpha)\mathbf{1} + i\sin(\alpha)n_i\sigma_i$  with  $\sigma_i$  being the Pauli matrices and  $n_i n_i = 1$ . All links of the configuration are equal  $+1$ , only for  $y = 16$  all the links  $U_\mu$  in direction  $\mu = y$  vary with  $x$  from  $+1$  to  $-1$ . The links vary in direction  $\sigma_z$  in colour space. The center of the first vortex is at  $x = 16.05$  and the second is located at  $x = 10.05$ . The thickness of the vortex is 4 lattice spacings. Between these val-

ues of  $x$  the trace of the links  $U_y$  is negative. For this configuration, the four lowest eigenvectors of the covariant Laplacian as well as the triple products and the norms of these vectors are calculated.

In order to see the rotation of the eigenvectors around the vortices, fundamental Landau gauge was chosen for the plots of the vector fields. In this gauge the rotation of  $2\pi$  is distributed smoothly along the closed paths around the vortex. Because this configuration is constant with respect to  $z$  and  $t$ , in the following plots only one  $xy$  slice is drawn. For the plots of the vectors only  $\sigma_x$  and  $\sigma_y$  components are drawn,  $\sigma_z$  is omitted. The colour space components of  $\sigma_x$  and  $\sigma_y$  are plotted in the space directions  $x$  and  $y$ , respectively.

The four lowest eigenvectors  $\varphi^{(i)}$  of the covariant lattice Laplacian in Landau gauge are plotted in fig. 4.13 on the next page. The corresponding eigenvalues are given in

$\lambda^{(1)}$	7.56830D-16
$\lambda^{(2)}$	1.91805D-02
$\lambda^{(3)}$	1.91805D-02
$\lambda^{(4)}$	4.23054D-02

Table 4.1: Eigenvalues  $\lambda^i$  of  $\varphi^{(i)}$

### 4.3 Laplacian Methods

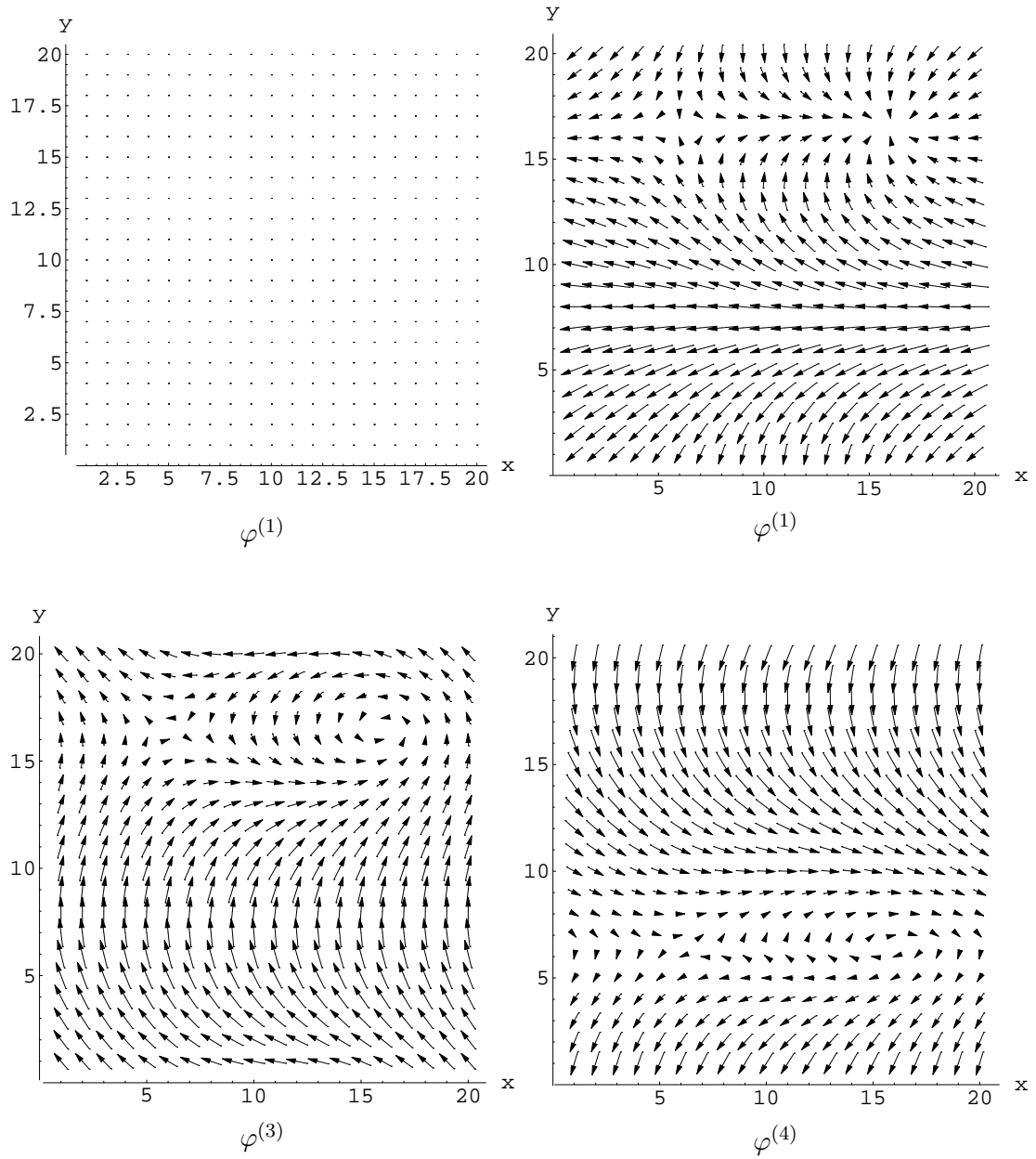


Figure 4.13: The four lowest eigenvectors  $\varphi^{(i)}$  for a plane vortex.

### 4.3 Laplacian Methods

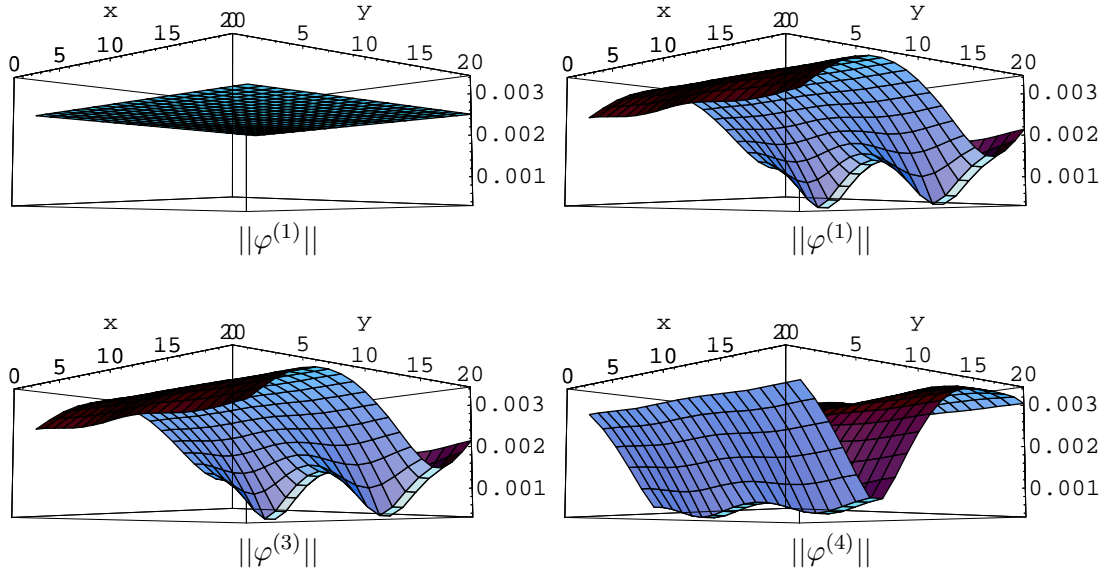


Figure 4.14: The norm of the four lowest eigenvectors  $||\varphi^{(i)}||$  for a plane vortex.

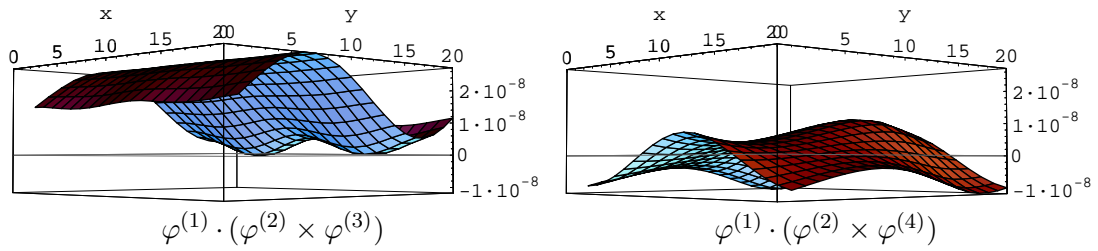


Figure 4.15: Triple products  $\varphi^{(1)} \cdot (\varphi^{(2)} \times \varphi^{(3)})$  and  $\varphi^{(1)} \cdot (\varphi^{(2)} \times \varphi^{(4)})$  for a plane vortex.



### 4.3 Laplacian Methods

table 4.1. We only see points for the lowest eigenvector  $\varphi^{(1)}$ , because it has only a component in  $\sigma_z$  direction. The links  $U_\mu$  rotate vectors only in direction  $\sigma_z$ , thus  $\varphi^{(1)}$  is not affected by the parallel transport. The covariant derivative is the same as the normal derivative for this vector,  $\varphi^{(1)}$  is up to machine precision a perfect solution of the Laplace equation, and it is an eigenvector of the Laplacian with eigenvalue  $\lambda^{(1)} = 0$ .

The next two eigenvectors have the same eigenvalues. This degeneracy is due to the symmetry of the configuration with respect to  $\sigma_x$  and  $\sigma_y$  in colour space. These eigenvectors are orthogonal to each other and to the first eigenvector at each point of the lattice. We have checked this by calculating the normalised triple product

$$\frac{|\varphi^{(1)} \cdot (\varphi^{(2)} \times \varphi^{(3)})|}{\|\varphi^{(1)}\| \|\varphi^{(2)}\| \|\varphi^{(3)}\|}.$$

This product equals 1 on the whole lattice. The vectors  $\varphi^{(2)}$  and  $\varphi^{(3)}$  show exactly the behaviour we have expected. The two vectors rotate perfectly around the positions of the two vortices. In addition we see some change in direction at  $y = 7$ . This is necessary to fulfil the periodic boundary conditions. One can also check that these two vectors get no component in direction  $\sigma_z$  approaching the positions of the vortices; they simply become shorter and seem to vanish in the middle of the thick vortices.

This can be checked looking at fig. 4.14 on the preceding page, where the norm of the eigenvectors is plotted. The constant first vector  $\varphi^{(1)}$  has constant norm. The next vectors  $\varphi^{(2)}$  and  $\varphi^{(3)}$  both are longer outside the vortex, and approaching the vortex their norm approaches zero.

The triple product of the three lowest eigenvectors is plotted in fig. 4.15 on the previous page. It behaves like  $\|\varphi^{(1)}\|$  and  $\|\varphi^{(2)}\|$  and indicates the Laplacian gauge ambiguity and thus the vortex position.

The fourth lowest eigenvector field  $\varphi^{(4)}$  is an excited state compared with  $\varphi^{(2)}$  and  $\varphi^{(3)}$  (see table 4.1), as described in section 4.3.4. It is the lowest plane wave solution of (4.15) on page 46. Thus the fourth vector should show some “wave” compared with the first three vectors. We see some wave (fig. 4.13), and in addition there is some rotation around the positions  $y = 6, x = 6, 16$ . There is no vortex at this positions, but it is the vortex positions shifted by a half of the lattices extent in direction  $y$ . Maybe this is due to the orthogonality requirement with respect to  $\varphi^{(2)}$  and  $\varphi^{(3)}$ : Exactly where these two vectors are short, this vector is long, and vice versa, as can be seen in fig. 4.14.

Because  $\varphi^{(4)}$  does not rotate together with  $\varphi^{(2)}$  and  $\varphi^{(3)}$ , the triple product  $\varphi^{(1)} \cdot (\varphi^{(2)} \times \varphi^{(4)})$  is not strictly positive as  $\varphi^{(1)} \cdot (\varphi^{(2)} \times \varphi^{(3)})$ . It shows some “irregular” behaviour and is plotted in fig. 4.15 on the previous page.

We conclude that the eigenvectors of the adjoint covariant Laplacian behave just as expected in section 4.3.4.1. As a next step, we have a look on the more complicated spherical vortex.

## 4.3.5.2 Spherical Vortex

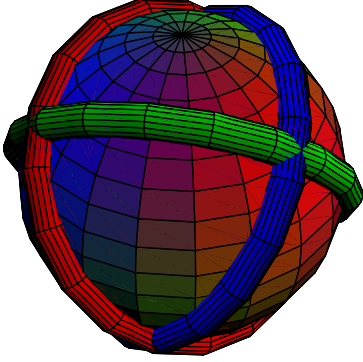


Figure 4.16: Model of the spherical vortex.

The spherical vortex is shaped like a sphere and is defined as follows: All links  $U_\mu(t, \vec{x})$  are  $+1$  for  $t \neq 10$  and  $\mu \neq \mu_t$ . The center of the sphere is at  $x = 10.05$ ,  $y = 10.05$  and  $z = 10.05$ , its radius is  $R = 6$  and the thickness of the vortex surface is  $d = 1.9$ . The links  $U_t(r)$  vary from  $-1$  to  $+1$  between  $r = R - d/2$  and  $r = R + d/2$ . The direction in colour space  $\vec{n}\vec{\sigma}$  in which the links vary from  $-1$  to  $+1$  is given by the radius vector  $\vec{x}$  on the Euclidean lattice by setting  $\vec{n} = \vec{x}/\|\vec{x}\|$ . Thus this vortex takes values in the whole  $SU(2)$ .

A symbolic picture of this vortex is plotted in fig. 4.16. The vortex has the shape of a three-dimensional sphere. It is contained in a single time slice  $t = 10$  and extends only in spatial directions. Because we have a symmetric lattice, one could swap  $t$  and  $z$  direction and get a vortex evolving in time. This would correspond to a circle

created at some time, expanding to radius  $R$  with time evolution, and again shrinking to zero. The temporal links are  $+1$  outside the sphere and in other time slices, and  $-1$  only inside of the plotted sphere. Between these regions there is a smooth change in the surface of the sphere which has a finite thickness.

The colour of the sphere in fig. 4.16 indicates the colour direction  $\vec{n}\vec{\sigma}$  of the  $U_t$  links in the vortex surface.  $+\vec{n}$  has been assigned the same colour as  $-\vec{n}$ , opposite points on the sphere have the same colour. Be aware that the “red”, “blue” and “green” regions on the sphere are in orthogonal directions, but they are not plotted in the  $\vec{\sigma}_i$  directions. The reason of this choice is explained later. The red, blue and green tori around the sphere are monopole loops. These monopoles arise if one gauges the configuration to maximal Abelian gauge (see section 4.2) with the

$U(1)$  subgroup of  $SU(2)$  that leaves the links indicated by the red, blue or green regions invariant, respectively<sup>2</sup>, followed by Abelian projection. This can easily understood from the very definition of the spherical vortex: The links of one half of the sphere change from  $-1$  to  $+1$  crossing the vortex surface in direction  $+\vec{n}\vec{\sigma}$ , the other links change in direction  $-\vec{n}\vec{\sigma}$ . Between a monopole line is found. The fact that monopole lines lie often on vortex worldsheets has been reported in [DFGO98]; it is found that at  $\beta = 2.4$  about 97% of the monopoles are located on P-vortex surfaces, where monopoles and vortices are detected using abelian and indirect center gauge and projection. If vortices are detected using the singularities of the Laplacian gauges as described in section 4.3.3, monopole are automatically located on P-vortex surfaces. In chapter 7 we will treat the significance of such monopole lines for the vortex picture.

We have also checked our calculations using spherical vortices with other radii  $R$  and

$\lambda^{(1)}$	3.28851D-03
$\lambda^{(2)}$	3.28851D-03
$\lambda^{(3)}$	3.28872D-03
$\lambda^{(4)}$	9.63221D-02

 Table 4.2: Eigenvalues  $\lambda^{(i)}$  of  $\varphi^{(i)}$ .

<sup>2</sup>This is the isotropy group for this direction.

### 4.3 Laplacian Methods

thickness  $d$ . For all these vortices the results are in good agreement.

In fig. 4.17 on the next page, again the four lowest eigenvectors of the covariant Laplacian are drawn. The corresponding eigenvalues are written in fig. 4.2 on the preceding page. Because of the symmetry of the configuration in colour space, the first three eigenvectors have exactly the same eigenvalues. The fourth eigenvalue is excited with a factor of  $\sim 30$ .

Originally, we plotted the eigenvectors of the adjoint Laplacian in fundamental Landau gauge, just as for the plane vortex. We could not see any rotation of the vector field around the vortex. Some rotations appeared far from vortices. We think that this is because Landau gauge does not only try to shift the links lying in the plane pierced by the vortex as close as possible to  $\mathbf{1}$ . In addition, the trace of the links orthogonal to the considered plane is maximised too. For the plane vortex described in section 4.3.5.1, this does not matter because this configuration is constant in  $z$  and  $t$  direction. For the spherical vortex, this is not the case and our approach failed. Thus we use a modified gauge: We consider  $xt$ -planes cutting the spherical vortex. For our modified gauge we maximise the functional  $\sum_{x,\mu} \text{Tr}[U_\mu(x)]$ , where  $\mu$  is restricted to  $\mu = x, t$ . This gauge maximises the traces of  $x$  and  $t$  links for each  $xt$ -plane independently of the other  $xt$ -planes and independently of links in  $y$  and  $z$  direction.

Fig. 4.17 on the next page shows the  $xt$ -plane with  $y = 10$  and  $z = 10$ . The vector fields are drawn in the modified gauge. This plane is pierced by the spherical vortex in two points with coordinates  $t = 10$ ,  $x = 4$  and  $x = 16$ . As for the plane vortex, also for the thick vortex the first three eigenvectors show a rotation of  $2\pi$  exactly at the position of the two vortex piercings. We have observed that at some cuts through the vortex one of the three lowest eigenvectors localises only one vortex piercing. If one looks carefully at all vortex cuts, one sees that on the points of the sphere indicated by the intersections of the tori in fig. 4.16 on the preceding page, always one of the vectors does not localise the vortex. This corresponds to the behaviour of the first eigenvector for the plane vortex. We will discuss this in detail below. The fourth eigenvector is again an excited state.

In fig. 4.18 on page 61, the norm of the lowest vector is plotted. In this figure we have chosen a space like cut through the vortex, a  $xy$ -plane with  $z = 10$  and  $t = 10$ , and a space time cut using the  $xt$ -plane with  $y = 10$  and  $z = 10$ . The norm of the vector is decreased where the vortex intersects the planes. If one looks at all cuts through the vortex, one sees that the norm of all three lowest eigenvectors decreases exactly on the vortex sphere. Fig. 4.18 on page 61 shows also that this decrease is not spherical symmetric, but the vectors “feels” the vortex with different intensity on the vortex surface. This can be inferred from fig. 4.19 on page 61. Here the norm of the two lowest eigenvectors  $\|\varphi^{(i)}\|$  is plotted for the  $xy$ -plane with  $z = 8$ ,  $z = 10$  and  $z = 12$ , and  $t = 10$ . We have truncated the plot if  $\|\varphi^{(i)}\| > 0.0015$ , and we see only the parts where  $\|\varphi^{(i)}\|$  is strongly decreased.

Following through all  $z$ -slices, one can infer that the norm of each vector is strongly reduced on a great circle on the vortex sphere. The more we move away from the circle, the weaker becomes the decrease. Analogous to the plane vortex we conclude that each of the lowest three eigenvectors does not feel the vortex at points where

### 4.3 Laplacian Methods

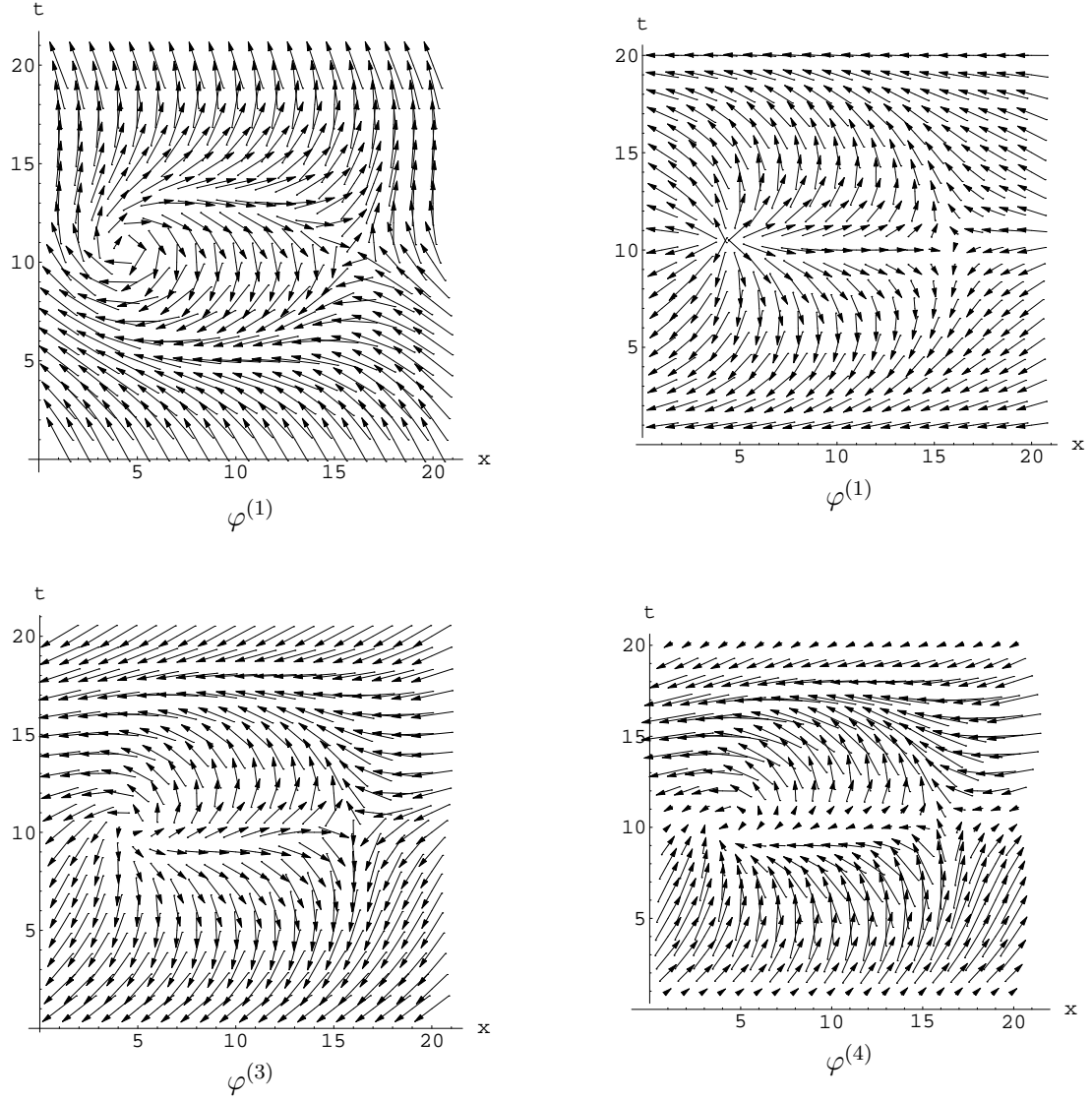


Figure 4.17: The four lowest eigenvectors  $\varphi^{(i)}$  for a spherical vortex. The  $xt$ -plane for  $y = 10$  and  $z = 10$  is plotted.

### 4.3 Laplacian Methods

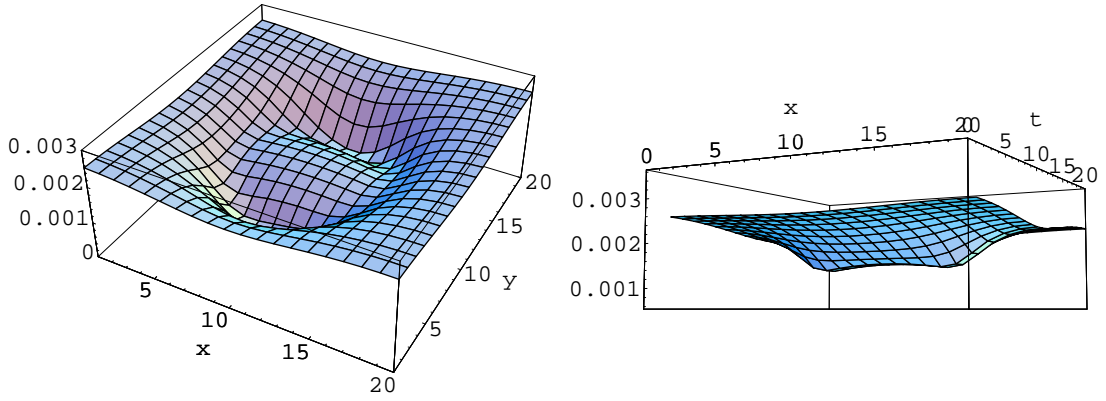


Figure 4.18: The norm of the lowest eigenvector  $\|\varphi^{(1)}\|$  for a spherical vortex. The  $xy$ -plane for  $z = 10$  and  $t = 10$ , and the  $xt$ -plane for  $y = 10$  and  $z = 10$  are plotted.

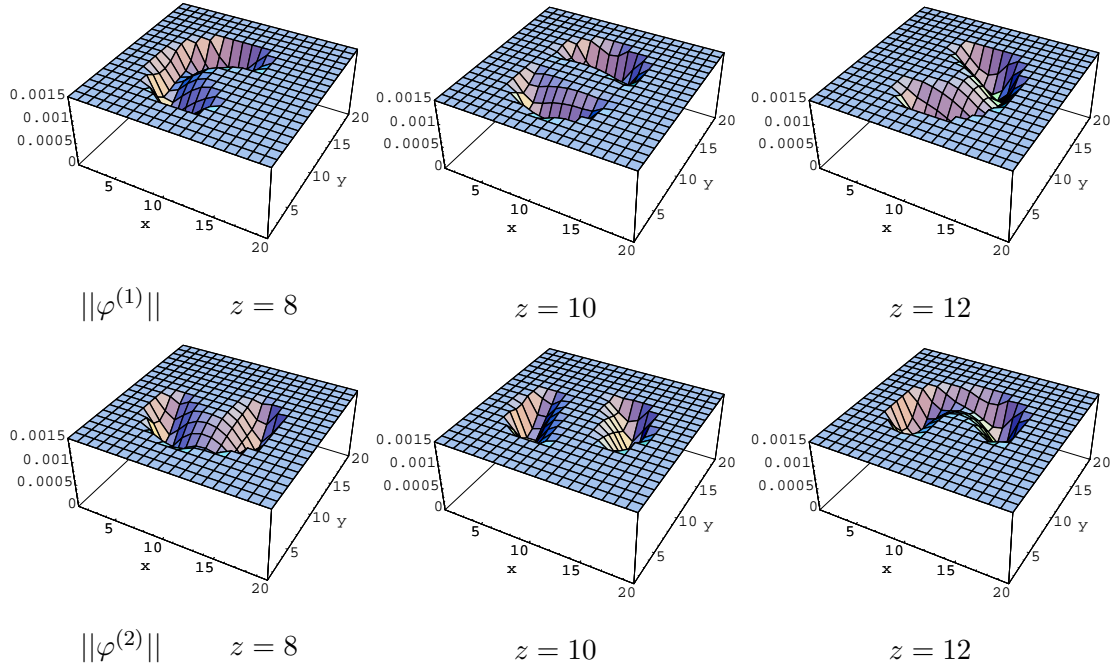


Figure 4.19: The norm of the two lowest eigenvectors  $\|\varphi^{(i)}\|$  for a spherical vortex. The  $xy$ -plane for  $z = 8$ ,  $z = 10$  and  $z = 12$ , and  $t = 10$  is plotted. The norm is truncated in this plots if  $\|\varphi^{(i)}\| > 0.0015$

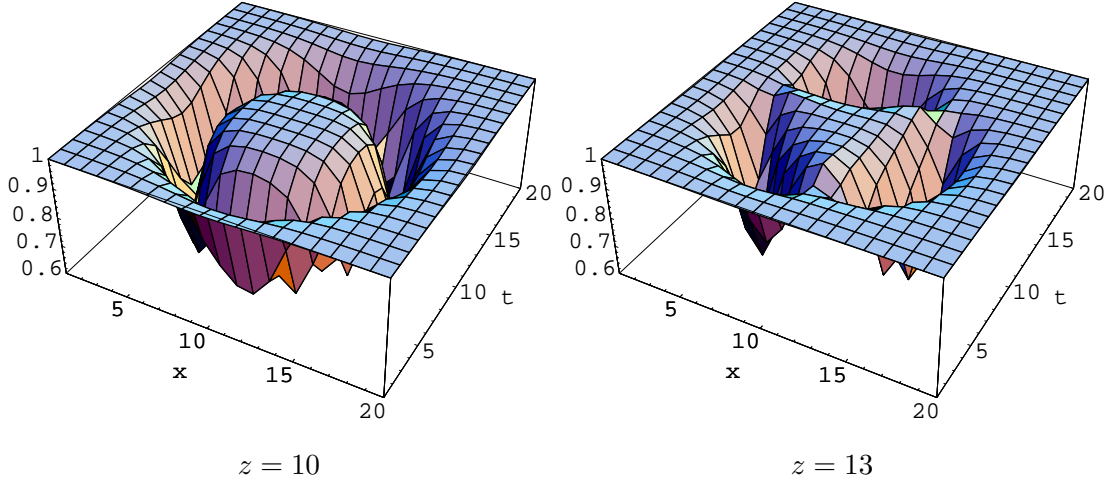


Figure 4.20: The normalised triple product  $(\varphi^{(1)}(\varphi^{(2)} \times \varphi^{(3)}))(|\varphi^{(1)}||\varphi^{(2)}||\varphi^{(3)}|)$  for a spherical vortex. The  $xy$ -plane for  $t = 10$  and  $z = 10, 13$  is plotted.

the adjoint  $U_t$  links in the vortex are in the Abelian subgroup of  $SO(3)$  leaving the eigenvector invariant. This is indicated in fig. 4.16 on page 58: For instance the red region on the sphere symbolises a part of the vortex where the local gauge field lets a certain eigenvector invariant. On the region of the sphere indicated by the red torus, the eigenvector is orthogonal to this local invariant direction, it has no invariant component. But as we have seen for the plane vortex, the orthogonal components vanish approaching the vortex, and thus the vector vanishes on this great circle. It is remarkable that this circle is also the position where an Abelian monopole arises if we project the full  $SU(2)$  on the Abelian subgroup letting the considered eigenvector invariant. We thus find the observation of [vdS97, vdS98] that Abelian monopoles are characterised by vanishing of the lowest eigenvector, and that the monopoles lie on the vortex surface.

The three orthogonal circles indicated by tori in fig. 4.16 on page 58 correspond to the monopoles of three different Abelian subgroups given by the three orthogonal eigenvectors. Because of the three fold degeneracy of the lowest eigenvalue, we can choose arbitrary other eigenvectors by linear combinations of our eigenvectors. This way we can move around the corresponding monopoles on the vortex sphere in an arbitrary way. This reflects the perfect spherical symmetry of our configuration.

For each eigenvector of the configurations there is a local invariant direction. These directions are not necessarily identical with the directions  $\sigma_i$ , and such it is plotted in fig. 4.16. On the intersection of the tori, one vector points in the invariant direction of the local gauge field, and the other two are orthogonal. Therefore approaching the vortex these two vectors become shorter and shorter, but all three vectors remain orthogonal. On other points of the vortex, at least two vectors have invariant components, and the normalised triple product measuring the angle between the vectors

$$\frac{|\varphi^{(1)} \cdot (\varphi^{(2)} \times \varphi^{(3)})|}{|\varphi^{(1)}||\varphi^{(2)}||\varphi^{(3)}|}.$$

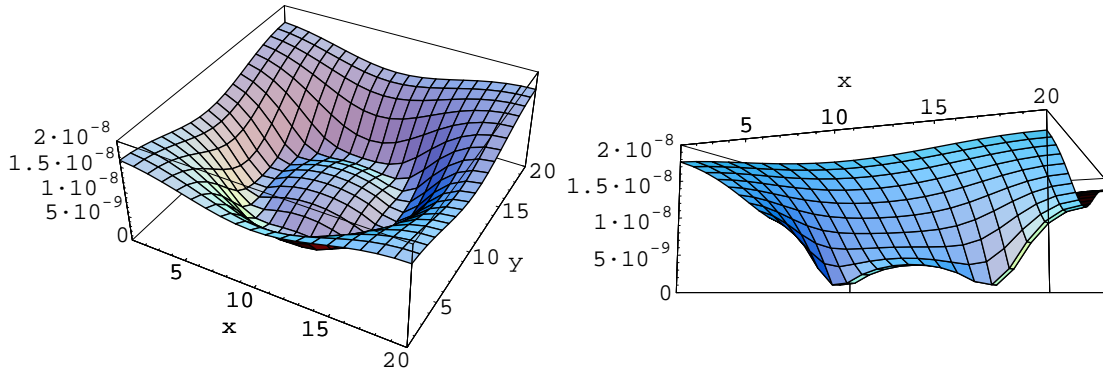


Figure 4.21: The triple product  $\varphi^{(1)} \cdot (\varphi^{(2)} \times \varphi^{(3)})$  for a spherical vortex. The  $xy$ -plane for  $z = 10$  and  $t = 10$ , and the  $xt$ -plane for  $y = 10$  and  $z = 10$  are plotted.

becomes smaller than 1. This is plotted in fig. 4.20 on the preceding page. The product is decreased on the vortex sphere, but there are six isolated points on the vortex – the intersections of the tori in fig. 4.16 on page 58 – where the vectors remain orthogonal.

The norms of the eigenvectors depend on the choice of our vectors in our configuration with a degenerate lowest eigenvalue. But the triple product is an invariant quantity indicating exactly the vortex position as can be seen from fig. 4.21. The product is decreased in a spherical symmetric way.

#### 4.3.5.3 Monte Carlo Generated Configurations

Having studied the eigenvectors of the Laplacian for very special configurations constructed by hand, we discuss in this section the results obtained with configurations generated by simulating the pure lattice SU(2) gauge theory with standard Monte Carlo techniques.

The first problem we face is the high vortex density for the usual coupling. We have done a simulation on a  $32^4$  lattice at an inverse coupling  $\beta = 2.74$ . At this  $\beta$  the piercings of vortices with a given plane should be, according to asymptotic scaling, about 15 lattice spacing apart on average.

In fig. 4.22 on the next page, the triple product of the three eigenvectors is plotted. The green and red vertical lines symbolise vortex piercings found using LCG and MCG, respectively, followed by center projection. The density of Laplacian center gauged and center projected vortices is much higher than the estimated density. It has been shown that this density does not scale [LRS01]. It seems that the Laplacian gauged and projected vortices do not contain only the infrared degrees of freedom of QCD which are responsible for confinement, but also perturbative contributions. The density of MCG vortices is as expected.

It is interesting that the triple scalar product is very small over large parts of the lattice. It is concentrated in rather small regions. We think that the reason for this large regions, and for the non-scaling of the vortex density after center projection, is

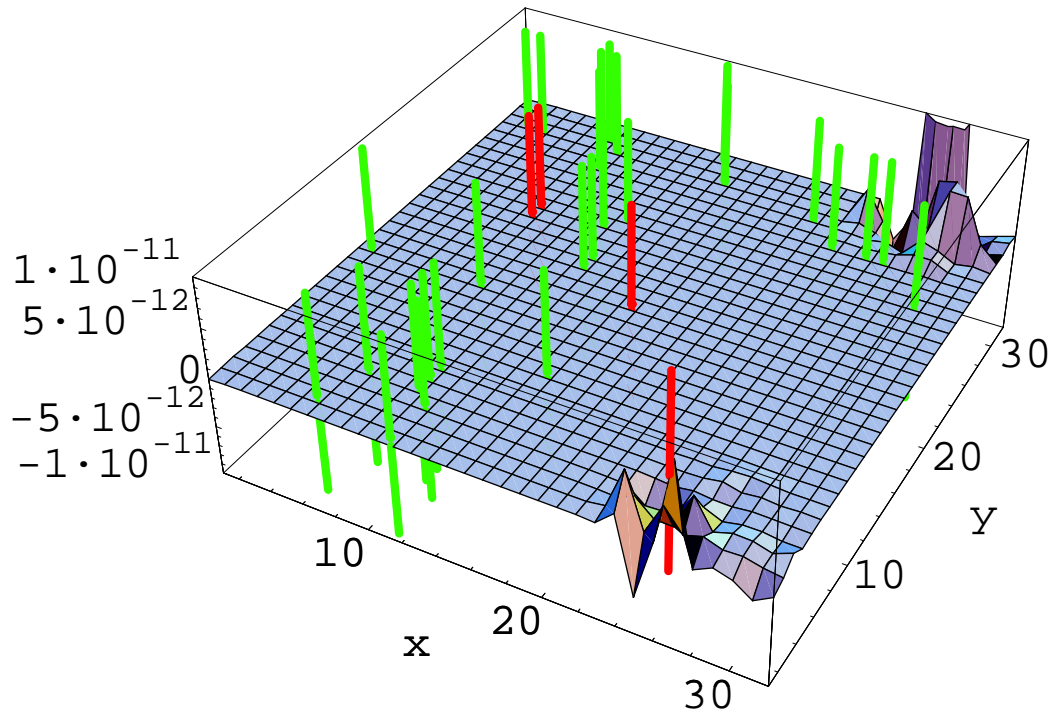


Figure 4.22: The triple product  $\varphi^{(1)}(\varphi^{(2)} \times \varphi^{(3)})$  of a Monte Carlo generated configuration. One plain is plotted. The green and red lines indicate the position of vortices found using LCG and MCG, respectively, followed by center projection.



found in (4.24) on page 47. MCG ((4.23)) fails in the continuum limit because it weights the derivations of thin vortices from thick vortices to strong, and hence to few vortices are found. For the Laplacian gauges, the opposite is true. Because (4.24) weights the gauge matrix  $S$  of (4.23) with an arbitrary positive semidefinite (though orthogonal in average) weight matrix  $M$ , the main part of the contributions to  $R'$  comes from rather small regions of the lattice where it is possible to gauge the links quite close towards the center elements. All other parts of the lattice are weighted less. For a detailed study for the localisation of the Laplacian eigenmodes, we refer to the recent extensive investigation reported in [GOP<sup>+</sup>05].

## 4.4 Conclusions

Using various gauges we have found that vortices can successfully be detected in gauge field configurations. Nevertheless there are serious problems with this detection methods. In the continuum limit P-vortex are a bad approximation for the thick vortices which have to be identified. The consequences of this failure are visible already at finite lattice spacings  $a$ . An example is the underestimate of center projected Creutz ratios in various circumstances such as DMCG with many gauge copies and the simulated annealing method, MCG for cooled or renormalisation group smoothed field configurations, or performing fundamental Landau gauge before doing the center gauge. On the other hand the Laplacian gauges followed by center projection yield many perturbative contributions, and the long range content of the gauge fields encoded in thick vortices cannot be isolated properly. Also the identification of vortices using ambiguities of the Laplacian gauge, working very well for configurations generated by hand, could not yet be applied to Monte Carlo generated gauge field configurations.

Various ways to overcome these problems have been proposed or are already in use. These includes the direct Laplacian center gauge, which combines a Laplacian gauge with maximal center gauge, and a proposal to not insist on finding the global maximum of the MCG functional (4.3) on page 31 but to average over various local maxima. Formally, this is akin to the well-known procedure of introducing a gauge-fixing term with a finite gauge fixing parameter into the action, without insisting on any particular limit for this parameter [ER00a, LERT00]. Finally the methods not related to center projection, such as the investigation on the vortex free energy, are not touched by these difficulties.

Apart from these difficulties, MCG with over-relaxation remains a reliable tool in order to detect vortices, as the convincing results reported in section 4.2.1 show. Therefore we will further use this method with a low number of gauge copies, but pay attention to the limits of the method as investigated in section 4.2.

# 5 Structure of Vortices

## Abstract

We investigate the structure and other properties of vortices detected in Monte Carlo calculations using maximal center gauge and center projection. These properties are in perfect agreement with the requirements from the vortex model of confinement.

In chapter 4 we showed that the thick vortices present in Monte Carlo generated gauge field configurations can be detected using various methods. From now on, we use the maximal center gauge with over-relaxation using 6 gauge copies followed by center projection, limited to SU(2) gauge theory. The choice of MCG with over-relaxation is justified by the fact that although this method seems not to work in the continuum limit, for the parameters used in our calculations the MCG results agree with the better funded DLCG results mentioned in section 4.3.2.3.

Center projection yields  $Z_2$  gauge configurations, as described in section 4.1. The excitations of a  $Z_2$  configuration are thin center vortices, P-vortices. In this chapter, we investigate the properties of P-vortices and their relation to confinement. Parts of the results presented here and some additional details can be found in [Ber98, BFGO99].

## 5.1 P-vortex Surface

First we clarify how projected vortices look like according to their definition. After center projection, we arrive at  $Z_2$  gauge field configurations. Each link is assigned the value  $+1$  or  $-1$ . We note the  $-1$  links as **negative links**. Links are gauge dependent, but the plaquette variables defined in section 2.2 as

$$U_{\mu\nu}(x) = U_\mu(x)U_\nu(x + \hat{\mu})U_\nu(x + \hat{\nu})U_\mu(x) = \pm 1 \quad (5.1)$$

are gauge independent. Its useful to look at the plaquette variables using the *dual lattice*. The dual lattice is shifted with respect to the original lattice half a lattice spacing  $a/2$  in each direction. To each cell  $c_n$  on the original lattice corresponds a cell  $c_{D-n}$  of the dual lattice, where  $D$  is the dimension of the lattice. In three dimensions, dual to points are cubes of the dual lattice centered around the points, dual to links are plaquettes pierced midway by the links, and dual to cubes are points located in the center of the cubes. In four dimensions, the duals of points, links, cubes and hypercubes are hypercubes, cubes, links and points, respectively. We note a plaquette of the original lattice to be pierced

### 5.1 *P*-vortex Surface

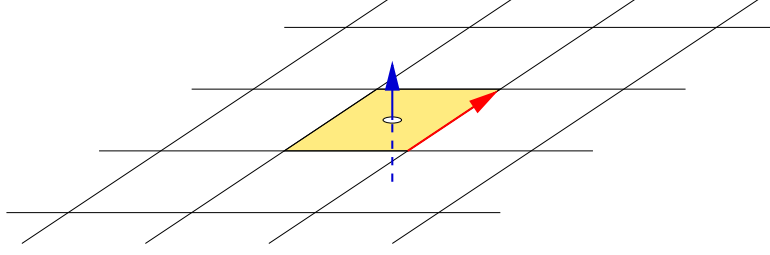


Figure 5.1: A negative link (red), a negative plaquette (yellow), and the corresponding dual P-link (blue).

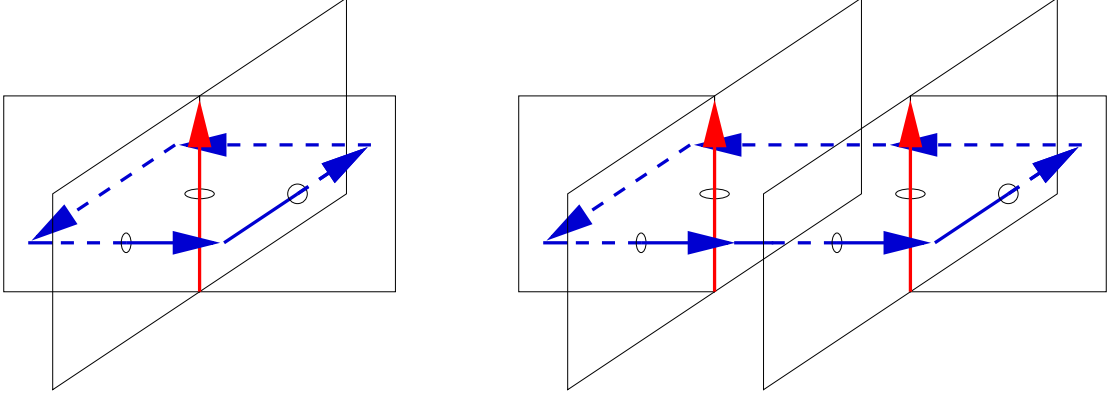


Figure 5.2: Negative plaquettes and P-links (blue) around one or two negative links (red).

by a **P-vortex** – an object defined on the dual lattice – if the plaquette variable equals  $-1$ . To each negative plaquette there corresponds a dual object, in three dimensions it is a dual link, in four its a dual plaquette. These are called **P-links** and **P-plaquettes** and form a P-vortex line or a P-vortex surface, respectively.

For three dimensions, this is sketched in fig. 5.1. In this configuration, all links are positive with exception to the one plotted red. Thus the plaquette plotted yellow is negative. Dual to this plaquette is the blue link, which is a P-link. It is part of a P-vortex piercing the yellow plaquette and carrying a center flux of  $-1$ , corresponding to the  $-1$  factor of the product of the links around the negative plaquette. Note that negative plaquettes and P-vortices are gauge independent, a gauge transformation multiplies all links connected to a given site with  $-1$ . For each plaquette attached to the site, two links are changed which gives a factor of  $+1$  for the plaquette leaving it invariant.

Negative plaquettes do not come alone. If there is only one negative link in a configurations, all plaquettes attached to this link are negative. The corresponding P-links form a closed loop, as can be seen from fig. 5.2 (left part). We note such a closed loop of P-links bordering a single dual plaquette as **elementary plaquette**. Adding more negative links to the configurations adds more elementary loops to the configuration. Two elementary loops touching common P-links cancel, and form a larger loop as depicted

### 5.1 P-vortex Surface

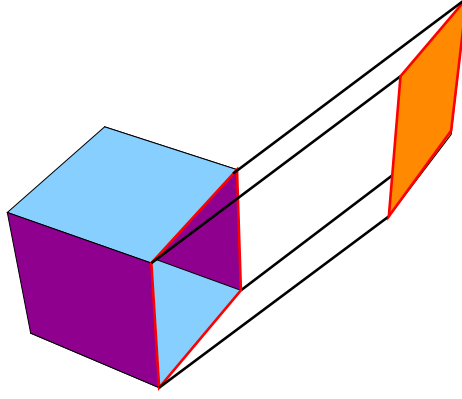


Figure 5.3: P-vortex resulting from the union of two elementary cubes. Links with temporal plaquettes attached are plotted red. Only the bordering links of temporal plaquettes are plotted. The plot shows a  $xyz$  and a  $yzt$  elementary cube, their surface is the P-vortex.

in fig. 5.2 (right part). A connected set of P-links is called P-vortex, which is a closed loop on the dual lattice. More, a P-vortex is not only closed but is also the border of a two-dimensional volume, the **Dirac volume**, as already described in section 3.4. In terms of holonomy theory, P-vortices are not only 2-cycles but also 2-boundaries. The Dirac volumes are gauge dependent, only their boundaries, the P-vortices are gauge independent.

In four dimension, as in our investigations, the dual of plaquettes are plaquettes on the dual lattice, e.g. dual to a  $xy$ -plaquette is a  $zt$ -plaquette, where the two plaquettes are orthogonal and intersect at their common center point. A single negative link is part of 6 attached negative plaquettes. The six P-plaquettes dual to these negative plaquettes form a closed surface, the surface of a closed three-dimensional cube with volume  $a^3$ , where  $a$  is the lattice spacing. We call such a cube **elementary cube**. Adding more links to the configuration, also more elementary cubes are added forming the (gauge dependent) 3-dimensional Dirac volumes whose boundaries are the two-dimensional P-vortices. Again if two elementary cubes touch at a common plaquettes than they cancel. In general multiplication of a link with  $-1$  changes the corresponding cube on the dual lattice such that the P-plaquettes of the cube are created where no P-plaquette was present, and cancels existing P-plaquettes of the cube. This effect of a link multiplication on the P-plaquettes of the dual lattice is called **elementary cube transformation** and ensures that the P-vortex surface consisting of the P-plaquettes remains closed. An application and illustration of elementary cube transformations will be described in section 5.3. The closeness of the P-vortex surface is the lattice equivalent to the Bianchi identity of the continuum gauge theory.

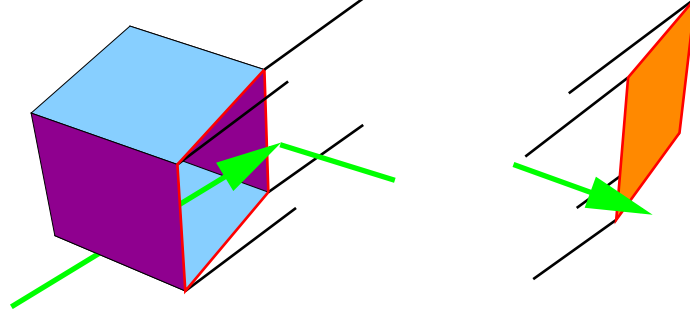


Figure 5.4: P-vortex resulting from the union of a  $xyz$  and a  $yzt$  elementary cubes. The two timeslices are plotted separate, temporal plaquettes are indicated by red links for spacelike links and small legs for timelike links. The negative links of the original lattice are plotted green. Be aware that the right green arrow points in  $x$  direction and starts at  $x = x_0 + a/2$ , where  $x_0$  is the  $x$ -coordinate of the right,  $yzt$  elementary cube, and ends at  $x = x_0 + a/2$ . The left arrow is a  $t$ -link on the original lattice.

### 5.1.1 Visualisation of P-vortex Surfaces

In order to visualise two-dimensional P-vortex surfaces on the four-dimensional lattice, we single out one direction as time direction and plot time like links in a arbitrarily chosen direction in the 3D subspace spanned by the other directions. In fig. 5.3 on the preceding page, we depict a P-vortex which is the surface of a  $xyz$  and a  $xzt$  cube which touch each other. Links where a temporal plaquette is attached are plotted red. The temporal plaquettes themselves are not plotted, only their bounding links in order to make the plot more readable.

For larger P-vortex configurations, such a plot quickly becomes confusing. Hence we depict each 3D timeslice in a separate plot and indicate the  $t$ -links bordering a P-plaquette using small legs, as shown in fig. 5.4 which depicts the same P-vortex as fig. 5.3. Here also the two negative links of the original lattice generating the P-vortex are depicted as green arrows. (of course there are other gauge equivalent negative link configurations generating the same P-plaquettes). As an example for a Monte Carlo generated, center projected configuration, fig. 5.5 on the following page shows a 3D timeslice of the dual of a configuration on a  $12^4$  lattice with  $\beta = 2.3$ . Already from this picture some features of the vortex surface can be seen. The surface is closed, as it should be. At a first glance this is not obvious, but taking into account the periodic boundary conditions and the continuation of surfaces in time direction, the closeness can be confirmed. There seems to be a single big surface filling the whole volume, we see percolation (there are also smaller fragments, but they are mostly connected through other time slices). And the surface seems highly irregular.

In the next sections we investigate the properties of the P-vortex surfaces in detail. We used Monte Carlo generated  $SU(2)$  gauge field configurations gauged to MCG using over-relaxation with 6 gauge copies, followed by center projection. The chosen lattice

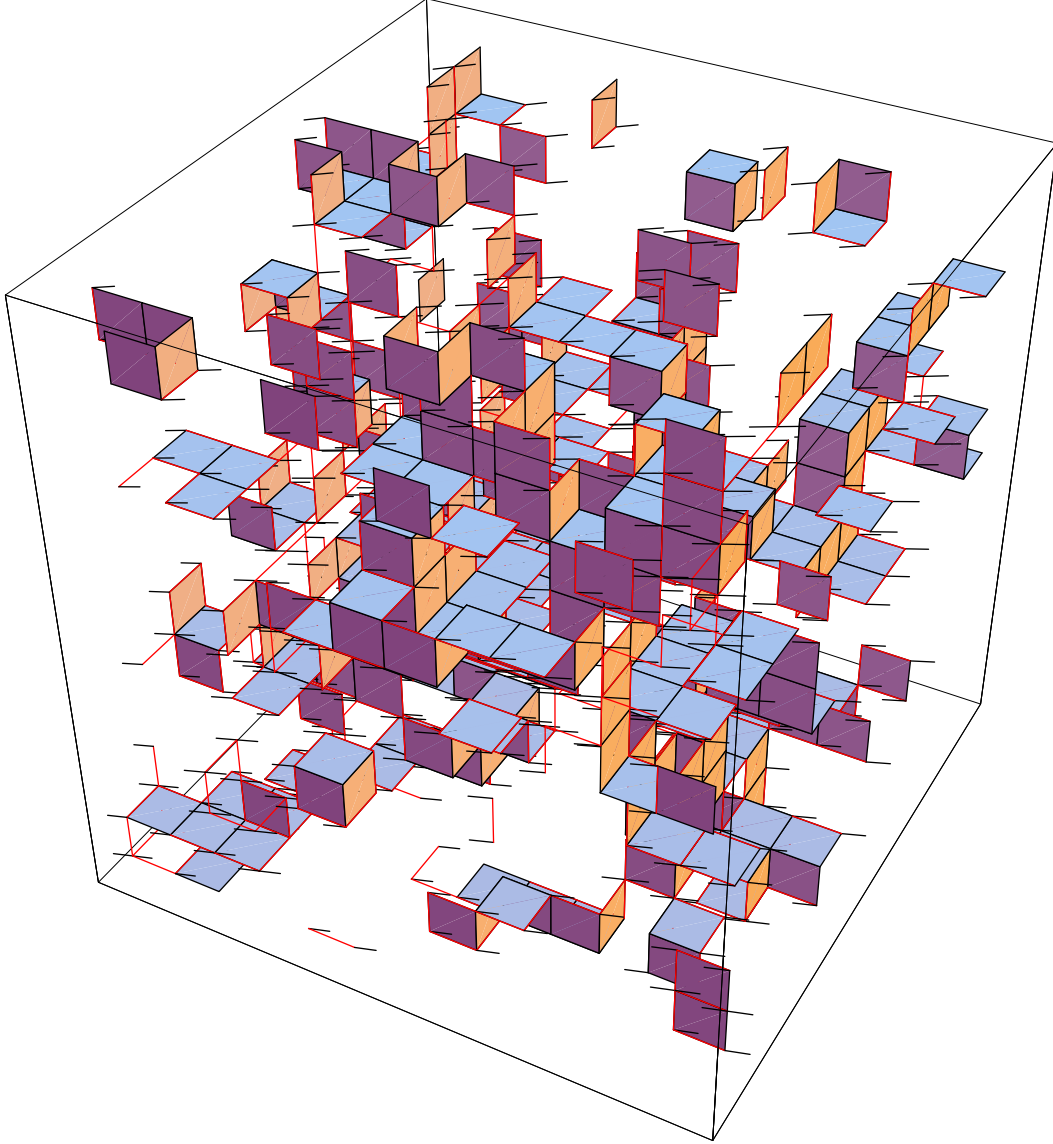


Figure 5.5: 3-dimensional cut through the dual of a  $12^4$ -lattice at  $\beta = 2.3$ . Spatial P-plaquettes are indicated. They form closed two-dimensional surfaces. Temporal P-plaquettes which extend in time direction and connect the given 3-dimensional space with neighbouring time-slices are indicated by small amputated lines in forward or backward direction. Links with temporal plaquettes attached are plotted red.

## 5.2 Vortex Density

sizes are  $N_{vol} = 12^4, 12^4, 16^4, 22^4$  for  $\beta = 2.2, 2.3, 2.4, 2.5$ , respectively.

## 5.2 Vortex Density

The P-vortex density is defined as the fraction  $p = N_P/N_{pa}$  of the number of P-vortex plaquettes  $N_P$  compared to the number  $N_{pa} = 6N_{vol}$  of all plaquettes of a given 4D lattice with  $N_{vol}$  lattice sites.  $p$  is the probability that a plaquette belongs to a P-vortex, and it is proportional to the average area taken up by P-vortices per unit lattice volume. The P-vortex density is one of the crucial test for the vortex picture of confinement. We investigate the relation of the vortex density to the string tension, and how we can infer properties of the P-vortex surface from  $p$ .

The distribution of P-vortices in space-time determines the string tension. The number  $n$  of piercings of P-vortices through the minimal surface spanned by a Wilson loop determines the value of the projected Wilson loop  $W_{cp}(I, J)$  of size  $A = I \times J$ :

$$W_{cp}(I, J) = (-1)^n. \quad (5.2)$$

$n$  is also called the **linking number**, as introduced in section 4.3.4, of the Wilson loop and the P-vortex surfaces. For projected Wilson loops, a piercing of the minimal area does not only change the sign as it is the case for full, unprojected Wilson loops – after projection, there is nothing but P-vortices left, and  $W_{cp}(I, J)$  is determined just by  $n$ . We remark that the linking number does not change if not the minimal surface, but any other surface bordered by the Wilson loop is taken. This is due to the fact that P-vortices are closed, i.e. the Bianchi identity. Now because  $p$  is the probability that a plaquette belongs to a P-vortex, by assuming the independence of piercings we get for the expectation value of  $W_{cp}(I, J)$

$$\langle W_{cp}(I, J) \rangle = [(1-p)1 + p(-1)]^A = (1-2p)^A = e^{-\sigma_{cp}A} \approx e^{-2pA}. \quad (5.3)$$

The string tension  $\sigma_{cp}$  in center projection follows from its definition (3.12) as

$$\sigma_{cp} = -\ln(1-2p) \approx 2p. \quad (5.4)$$

For the smallest Wilson loops  $W_{cp}(1, 1)$  there can be maximal one piercing of the minimal surface, and the assumption of independence of piercings is fulfilled trivially. Hence the relation

$$\langle W_{cp}(1, 1) \rangle = (1-2p) \quad (5.5)$$

holds exactly.

### 5.2.1 Scaling of the Density

Next we consider the scaling of the vortex density  $p$ . As discussed in section 2.4, the dependence of the lattice spacing  $a$  on the inverse gauge coupling  $g$  in the large  $\beta$  limit is given by asymptotic freedom in the two-loop approximation as

$$a^2(\beta) = \frac{\Lambda^2}{\sigma_p} F(\beta). \quad (5.6)$$

## 5.2 Vortex Density

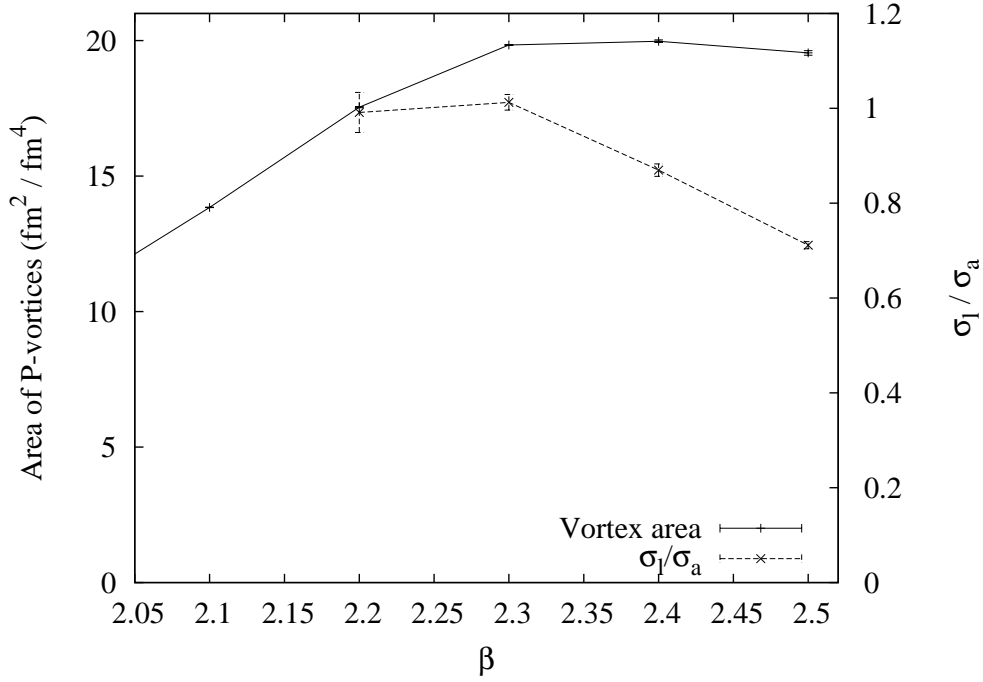


Figure 5.6: Vortex area per unit volume  $A_v$  and ratio of string tensions  $\sigma_l$  and  $\sigma_a$ , calculated on the lattice and from the asymptotic freedom expression (5.9), respectively. The values for  $\sigma_l$  are taken as reported by Michael and Teper [MT87] and Bali et al. [BSS95].

Here  $a$  is the physical lattice spacing given in fm,  $\sigma_p$  the physical string tension, and  $\Lambda$  is the lattice parameter. We use the values  $\sqrt{\sigma_p} = 440$  MeV and  $\Lambda = 62$ . The scaling function  $F$  is defined as

$$F(\beta) = \left( \frac{6\pi^2}{11} \beta \right)^{102/121} \exp \left( -\frac{6\pi^2}{11} \beta \right). \quad (5.7)$$

If the asymptotic freedom estimate of (5.7) holds, the area of the P-vortex surface per unit volume, expressed in physical units ( $\text{fm}^{-2}$ )

$$A_v = 6a^{-2} p \quad (5.8)$$

should not depend on  $\beta$  approaching the continuum. In fig. 5.6 we plot  $A_v$ . Starting from  $\beta = 2.2$  there seems to be good evidence for scaling, in agreement with previous results [DFG<sup>+</sup>98, LRT98, ELRT98, LTER99, BFGO00]. For comparison, in fig. 5.6 also the scaling for the string tensions  $\sigma_l$  inferred using lattice calculations on unprojected lattices is depicted. To this end we divide the reference values for  $\sigma_l$  – taken from Michael and Teper [MT87] for  $\beta = 2.2$  and from Bali et al. [BSS95] for the other data points – by the value  $\sigma_a$  for the string tension in lattice units calculated in two-loop approximation via

$$\sigma_a = \Lambda^2 F(\beta). \quad (5.9)$$



For perfect scaling, the ratio  $\sigma_l/\sigma_a$  should be independent from  $\beta$ , and moreover using a suitable value for  $\Lambda$  the ratio can be adjusted to 1. It is interesting to note that the scaling of  $A_v$ , in the range  $\beta = 2.3 - 2.5$ , is substantially better than the scaling of the full asymptotic string tension  $\sigma_l$  in this range.

## 5.3 Correlations and Fluctuations

The vortex area per unit volume  $A_v$  calculated from the vortex density  $p$  scales nicely with the inverse coupling  $\beta$ , as shown in section 5.2.1. However, already from the figs. 4.2 to 4.4 on pages 36–38 in section 4.2.2 it can be seen that the center projected Creutz ratios  $\chi_{cp}(1, 1)$  (the logarithm of  $1 \times 1$  Wilson loops  $W_{cp}(1, 1)$ ) lie above the asymptotic string tension  $\sigma$  [Ber98, LTER99, BFGO99], and therefore the values of  $p$  come out higher than those of  $f$  that can be inferred from  $\sigma$  using (5.4):

$$f = (1 - e^{-\sigma_{cp}})/2. \quad (5.10)$$

Why is the P-vortex density higher than necessary in order to give the correct string tension? The reason is that the piercings of the surface spanned by the Wilson loop are not independent, as assumed in (5.3), due to correlations of the P-vortex surface. Because  $\chi(I, I)$  is nearly independent of  $I$  for  $I \geq 2$  (precocious linearity), we think that these correlation between piercings violating the independence assumption are at a distance of one lattice spacing. In our opinion the reason for the correlation are short ranged fluctuation of the P-vortex surface induced by the roughness of the lattice. As already discussed in section 3.4 and in chapter 4, the vortices on the unprojected lattice have a finite thickness. Center projection replaces these thick vortices by thin P-vortices, but the exact position is not fixed and fluctuate within the thick vortex core. In addition P-vortex locations, while correlated among random Gribov copies, do vary somewhat from one random copy to another [DFG<sup>+</sup>98]. We find that these fluctuations are indeed of the order of the lattice spacing  $a$ , at least for the values of  $\beta$  we have investigated, as will be shown by the smoothing procedure described below.

For the 3-dimensional case, fluctuations of a P-vortices are depicted in fig. 5.7 on the next page. The small elementary loop at the right side of the figure does not influence the Wilson loop, because the two piercings cancel. Similarly, the S-formed fluctuation of the P-vortex in the middle gives three piercings, which is equivalent to a single piercing of the surface as at the left side of the figure. For loops  $W_{cp}(I, J)$  with  $I, J > 1$ , such fluctuations only influence the loop if they are partly inside and partly outside of the loop. Hence the fluctuations contribute to the perimeter part of the Wilson loop only (see section 3.4), and not to the string tension.

In order to remove the small fluctuations of the P-vortex surfaces we introduce several smoothing steps which are depicted in fig. 5.8 on the following page. This **vortex smoothing procedure** iteratively scans for cubes of the lattice and transforms them according to the following rules: In a first step a) we identify single isolated P-vortex cubes consisting of six P-plaquettes only (i.e. the surface of elementary cubes) and remove them. The next step b) identifies cubes covered by 5 P-vortex plaquettes. Such

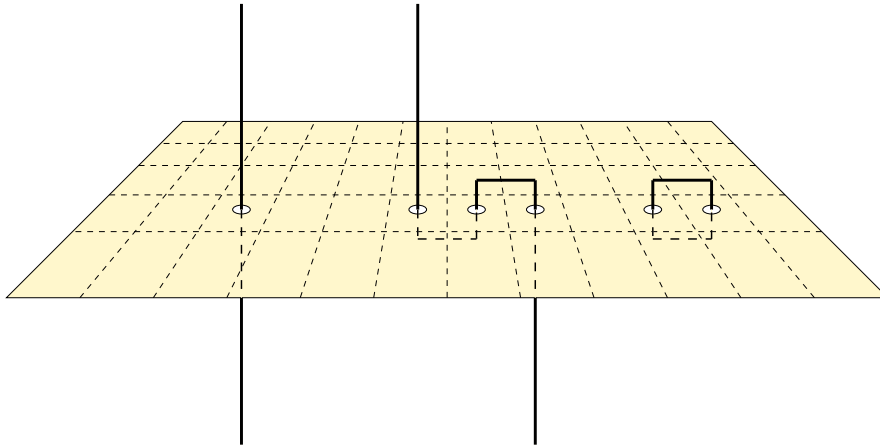


Figure 5.7: P-vortices piercing the minimal surface of a Wilson loop.

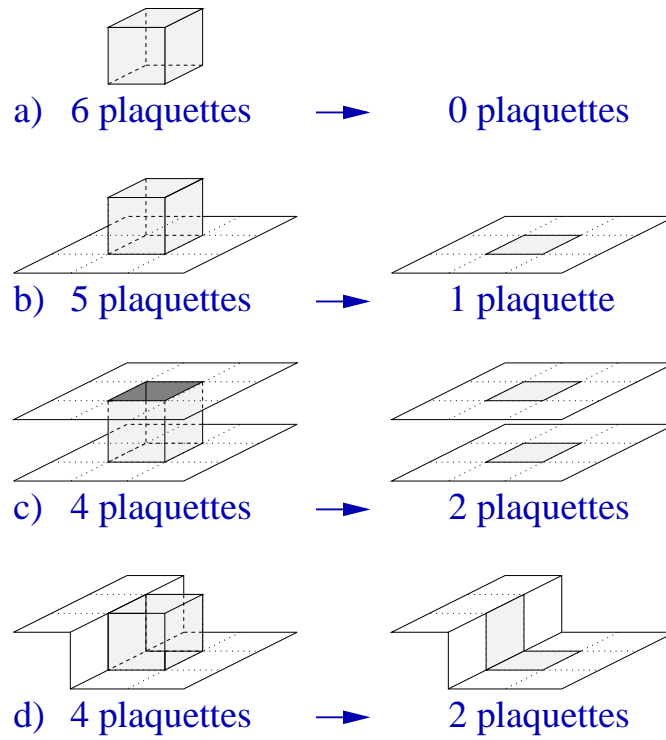


Figure 5.8: Various smoothing steps for vortices.

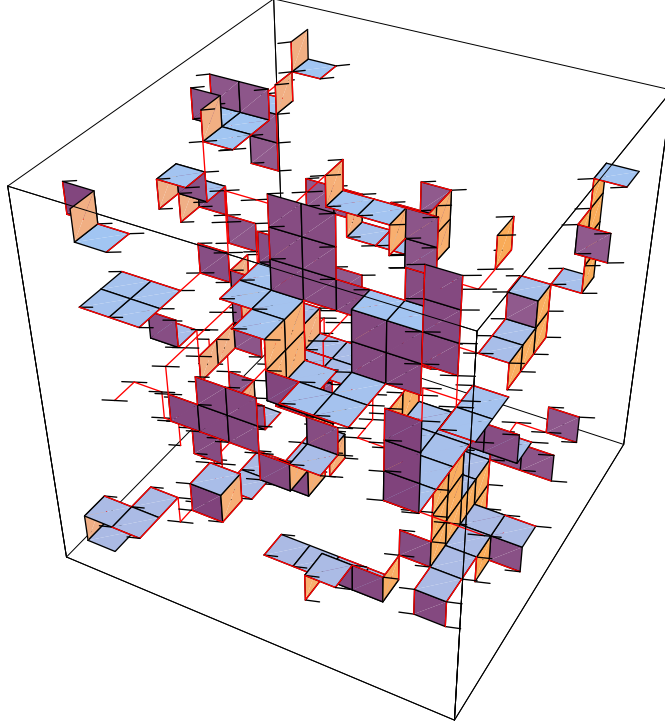


Figure 5.9: Result of applying repeatedly all smoothing steps a)–d) on the configuration of fig. 5.5 on page 70 after.

cubes can be substituted by one complementary plaquette which closes the attached P-vortex surface. Step c) substitutes cubes which 4 P-plaquettes which are positioned opposite on the cube by the two missing plaquettes. This step disconnects at least locally two surfaces which have been joint before. Finally, in step d) the two missing plaquettes join a common link. Note that each of these smoothing steps consists of elementary cube transformations as defined in section 5.1, and preserves the closeness of the P-vortex surface. Of course the negative links of the original lattice are changed accordingly with the P-vortices on the dual lattice such that the P-vortices are the ones calculated from the links. In our investigations, we take a configuration of P-vortices and apply repeatedly some combination of the smoothing steps until the configuration does not change any more. Applying all smoothing steps a)–d) on the configuration depicted in fig. 5.5 on page 70 yields fig. 5.9. The P-vortex density has decreased considerably, and on small scale the surface appears to be smoother. Nevertheless, there is still a large percolating P-vortex surface which looks rather random.

The effect of the smoothing procedure on the vortex density is plotted in fig. 5.10 on the next page. The P-vortex density  $p$  labelled “unsmoothed” is clearly above the estimate  $f$  from the stringtension labelled “from stringtension”. Removing the isolated elementary cubes in smoothing step a) reduces  $p$  somewhat, and this reduction is fairly independent from  $\beta$ . There seem to be some excitations creating elementary cube vortices due to the coarseness of the lattice, and independent from the physical size of the

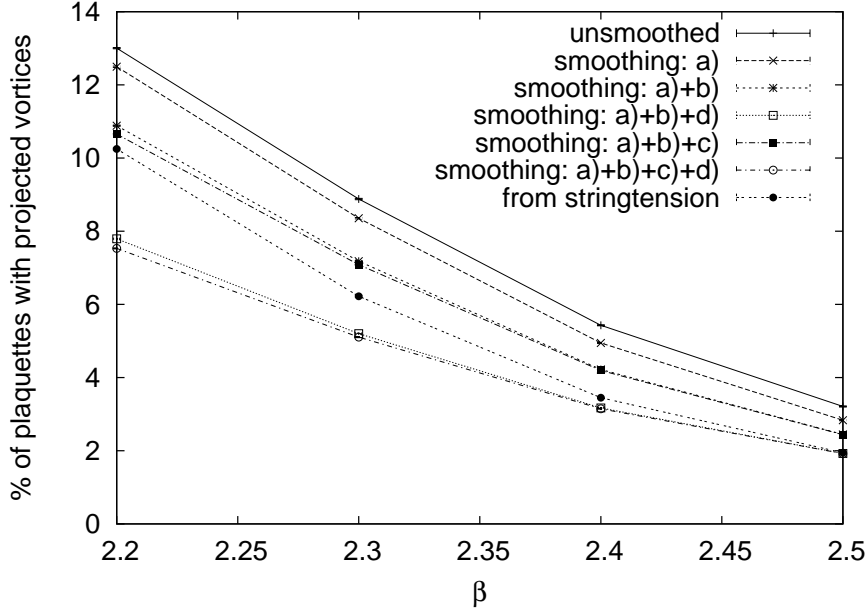


Figure 5.10: Percentage  $p$  of P-vortex plaquettes for various  $\beta$ -values and smoothing steps is compared with the fraction  $f$  (labelled “from stringtension”) of plaquettes which should be pierced by a P-vortex according to the asymptotic string tension  $\sigma$ .

lattice constant  $a$ . Applying step b) in addition drops  $p$  considerable, and this drop depends on  $\beta$ . For both smoothing steps  $p$  remains larger than  $f$ . Most aggressive is the addition of step d), whereas adding step c) to the a)+b) or to the a)+b)+d) combination does not change the density considerably. The connecting bridges of step c) as plotted in fig. 5.8 on page 74 simply do occur rather rarely. For  $\beta = 2.2$  and 2.3, the inclusion of step d) brings  $p$  below  $f$ , this smoothing is on coarse lattices too aggressive. Starting from  $\beta = 2.4$ ,  $p$  matches  $f$  quite nicely using step d). This indicates that the only significant correlation among P-plaquettes is at a distance of one lattice spacing, and we expect to have removed exactly the fluctuations which are responsible for this correlation.

In order to check whether the smoothing procedure leaves the string tension invariant, projected Creutz ratios  $\chi_{cp}(I, I)$  calculated after smoothing are plotted in fig. 5.11 on the next page. Whereas  $\chi_{cp}(1, 1)$ , which is directly related to the P-vortex density, is lowered by the smoothing procedure, at  $\beta = 2.4$  starting from  $I = 2$  the Creutz ratios are not influenced at all by the smoothing procedure. The lowering of  $\chi_{cp}(1, 1)$  by applying also the strongest smoothing step d) results in precocious linearity starting already at  $I = 1$ . We have truly removed the short ranged fluctuations. For  $\beta = 2.2$  and 2.3, the inclusion of smoothing step d) lowers  $\chi(I, I)$  also for  $I > 2$ , and it is lowered somehow ( $\sim 5\%$ ) below the asymptotic string tension  $\sigma$ . In more detail, this results are shown for  $\chi(3, 3)$  in fig. 5.12 on page 78. All in all, the results on  $\chi_{cp}(I, I)$  are in perfect agreement

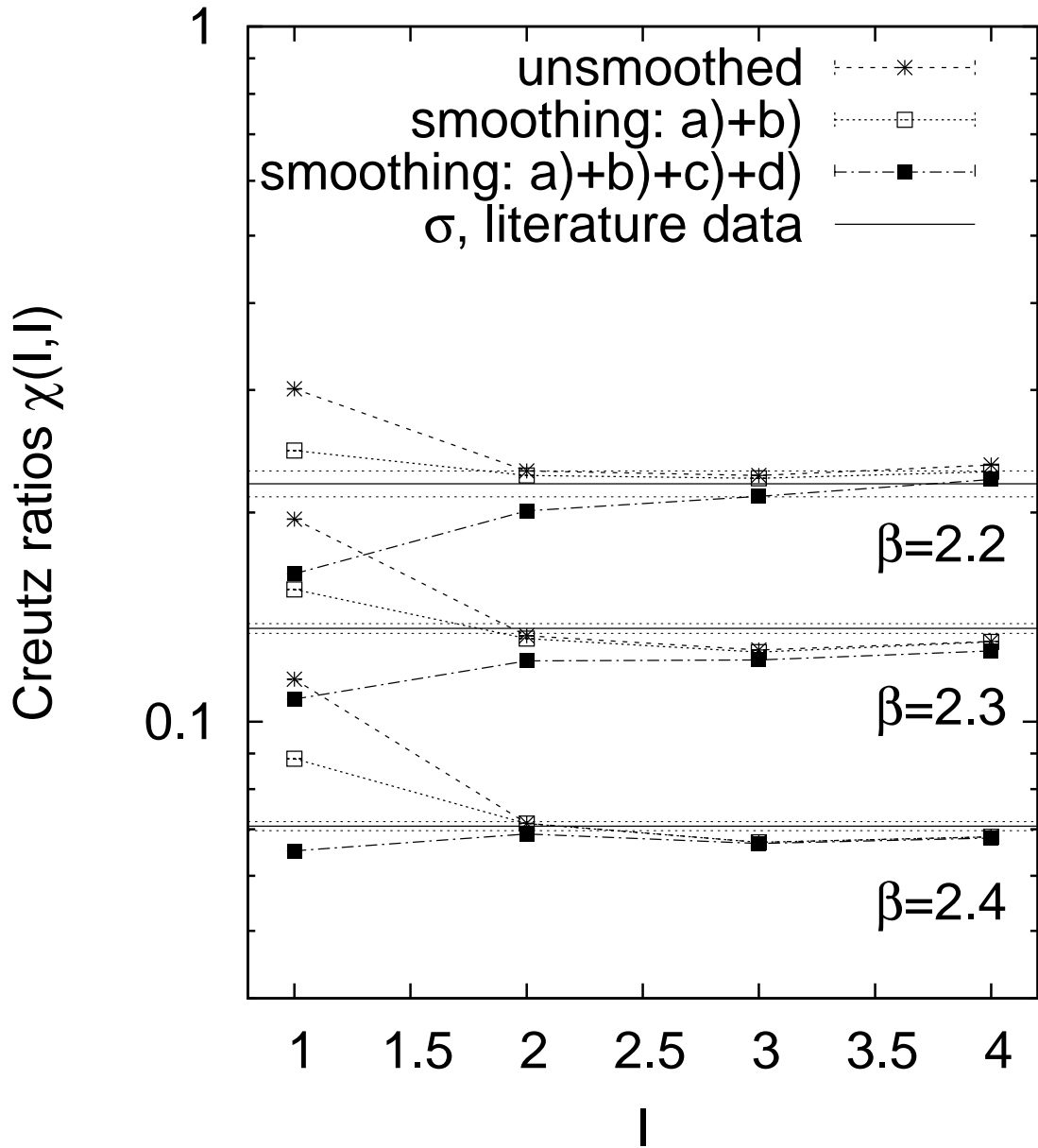


Figure 5.11: Creutz ratios  $\chi(I, I)$  for different smoothing steps. The horizontal lines labelled “ $\sigma$ , literature data” represent the asymptotic string tension as reported by Michael and Teper [MT87] and Bali et al. [BSS95]

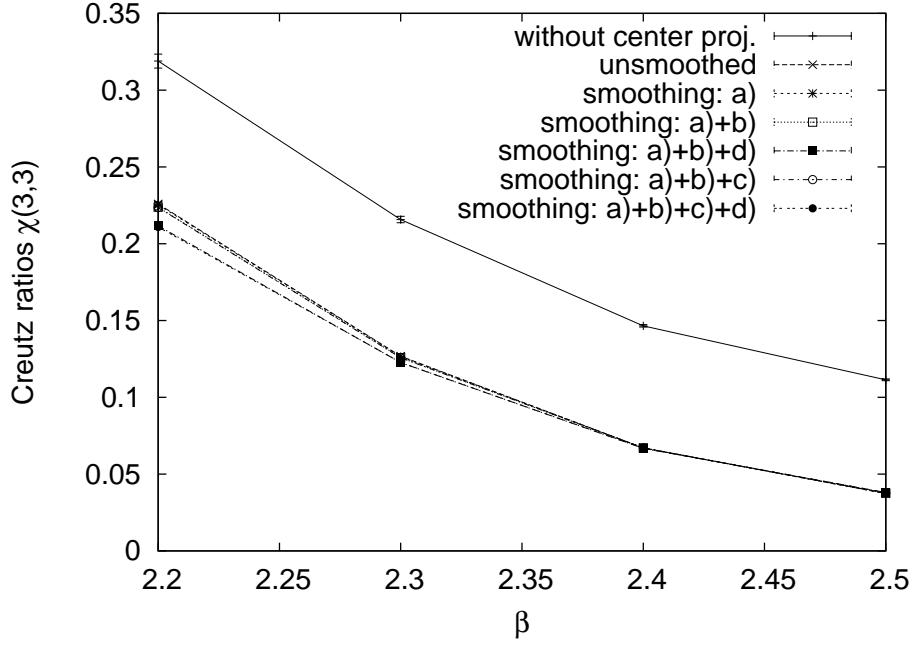


Figure 5.12: Creutz ratios  $\chi(3,3)$  after applying different smoothing steps.

to the findings for the influence of smoothing on the P-vortex density  $p$ .

The influence of the smoothing steps on observables depending on  $\beta$  is also consistent with findings for the correlation of vortex plaquettes presented in [ELRT98]; there a correlation length of  $0.2 - 0.6$  fm for P-vortex plaquettes lying in a plane is found. At  $\beta = 2.2$  the lattice spacing is about  $a = 0.21$  fm, and the most aggressive step d) can change the Creutz ratios, whereas starting from  $\beta = 2.4$  with  $a = 0.13$  fm the local smoothing procedure acting on the scale of one lattice spacing (and somewhat above due to the repetitive application of the smoothing steps on the configuration) does not change the vortex surface beyond the correlation length found in [ELRT98].

## 5.4 Size of P-vortices

We have seen that short range fluctuations of the P-vortex surface contribute to the perimeter part of the Wilson loop observable only. The estimate (5.3) on page 71 does not hold because the assumption of the independence of piercings is not fulfilled. The same is true for any vortex with some finite diameter. Lets assume that the linear extent of vortices is bounded by some distance  $L$ . For Wilson loops  $W(I, J)$ ,  $I, J > L$ , vortices inside the loop and far from the perimeter pierce the minimal area bounded by the loop even times, and cannot contribute to the area law fall-off of the Wilson loop. Only vortices in a region of thickness  $2L$  around the loop can contribute, and the area of this region is a function of the loop perimeter. For this reason, confining vortex configurations will have to be very large, with an extent comparable to the size of the

lattice. In other words, we expect a percolating vortex to be present on the lattice.

To check this assumption we have to particularise the individual, separated vortices present in a projected configuration. We do this by starting at a given plaquette and determine neighbouring P-plaquettes. This leads to the question when two P-plaquettes are connected. In most cases there is no doubt about the neighbouring plaquettes, since most dual links connect only two P-plaquettes. But in some cases there appear ambiguities, when dual links are attached to 4 or 6 P-plaquettes.<sup>1</sup>

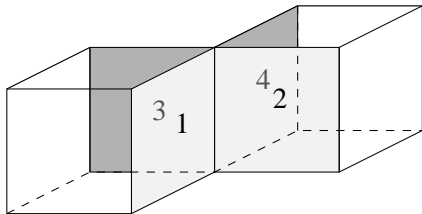


Figure 5.13: The question of connectedness can not be solved uniquely for this configuration of P-vortices.

In general P-vortices can be in contact at sites, links and plaquettes. Let's have a look at these different possibilities. A contact point is of no importance since we define the connectedness via common links. For our case of the  $Z_2$  center group a plaquette belonging to two independent vortices leads to a fusion of these vortices. The remaining possibility, a contact of P-vortices at links needs a more detailed discussion. A simple example of such field configurations are two cubes, consisting of 12 plaquettes, touching like in fig. 5.13.

For such a configuration it is not clear whether it builds one or two vortices. At the given length scale there is no unique solution for the question of connectedness. Connecting 1 with 2, 3 with 4 would result in one vortex, connecting 1 with 3, 2 with 4 in two separated vortices. In most cases the situation can be resolved by postponing the decision about the connectedness of these plaquettes until, by following the vortex surface in all other directions, the indicated plaquettes (usually) turn out to be members of the same vortex. There appear some cases where no decision is possible by these means, as in the simple example of fig. 5.13. In order to get a lower limit for the size of vortices we decide in such cases to treat the configuration as two separate vortices.

It may even occur that vortices touch along closed lines. In these cases parts of the vortex surface cannot be reached following regular connections of plaquettes. Identifying separated vortices we end with parts of P-vortices which are not closed surfaces. These cases are even not so rare, their percentage is shown in fig. 5.14 on the following page. The length of the closed line is usually very small and includes in the average 5 to 7 links. After applying smoothing step a), the percentage is very small, and starting from step a)+b), all such closed lines are removed. Be aware that the percentage is calculated using P-vortices weighted with their size, i.e. the number of contained P-plaquettes.

With the above mentioned rules for deciding connectivity of P-vortices in ambiguous cases, we determine the P-vortex sizes. For this purpose we define the **weighted average vortex size**  $s_w$ . This is the relative size  $||v_{i(a)}||/N_P$  of the vortex  $v_{i(a)}$  containing the P-plaquette  $P_a$ , averaged over all  $N_P$  P-plaquettes in the projected gauge

<sup>1</sup>This problem is only present on the lattice. In a theory of P-vortices in the continuum as in [ER00a], the probability that such ambiguities emerge has measure 0, and they do not contribute in the path integral.

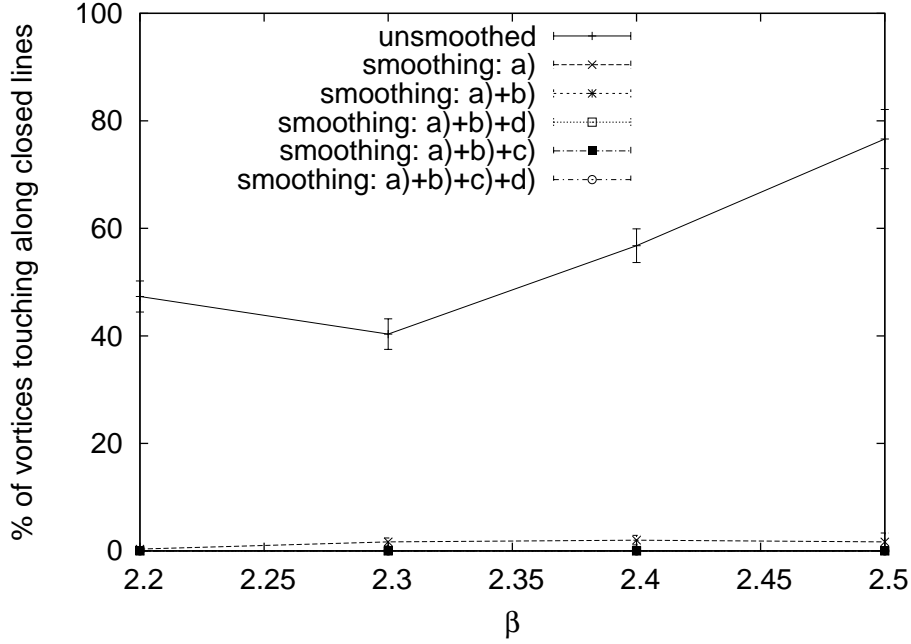


Figure 5.14: Percentage of such P-vortices which touch along closed lines for various smoothing steps. The P-vortices are weighted with their size (the number of P-plaquettes in the vortex).

field configuration<sup>2</sup>:

$$s_w := \frac{1}{N_P} \sum_{a=1}^{N_P} \frac{\|v_{i(a)}\|}{N_P} = \sum_{i=1}^{N_v} \frac{\|v_i\|^2}{N_P^2}. \quad (5.11)$$

Here  $\|v_i\|$  is the number of plaquettes in vortex  $v_i$ ,  $i(a)$  the index of the vortex containing plaquette  $P_a$ , and  $N_v$  is the number of vortices in the projected configuration. In the limit of infinite lattice volume and finite vortex density,  $s_w = 1$  if all P-plaquettes belong to a single percolating vortex, and  $s_w = 0$  for the depercolation case.

Fig. 5.15 on the next page shows  $s_w$  for various smoothing steps. It is obvious that for all investigated  $\beta$ -values there is mainly one huge vortex. After removing the elementary cube vortices using smoothing step a), the average plaquette is in a P-vortex which contains over 90% of all P-plaquettes. All other vortices are rather small and should not contribute to the string tension according to the above arguments. The stronger smoothing steps remove even more of the smaller vortices. In all investigated field configurations we found a single huge P-vortex, we never met a configuration with two large vortices. Only vortices extending over the whole space contribute to an area law at all length scales. We conclude that the string tension is determined by the area of a

<sup>2</sup>This observable resembles the average cluster size  $S$  of percolation theory. In our case the clusters are the vortices.  $S$  differs from our  $s_w$  in that i) it is not the average absolute size, but the average fraction with respect to all P-plaquettes; and ii) all clusters resp. vortices, including the percolating one, are included in the sum.



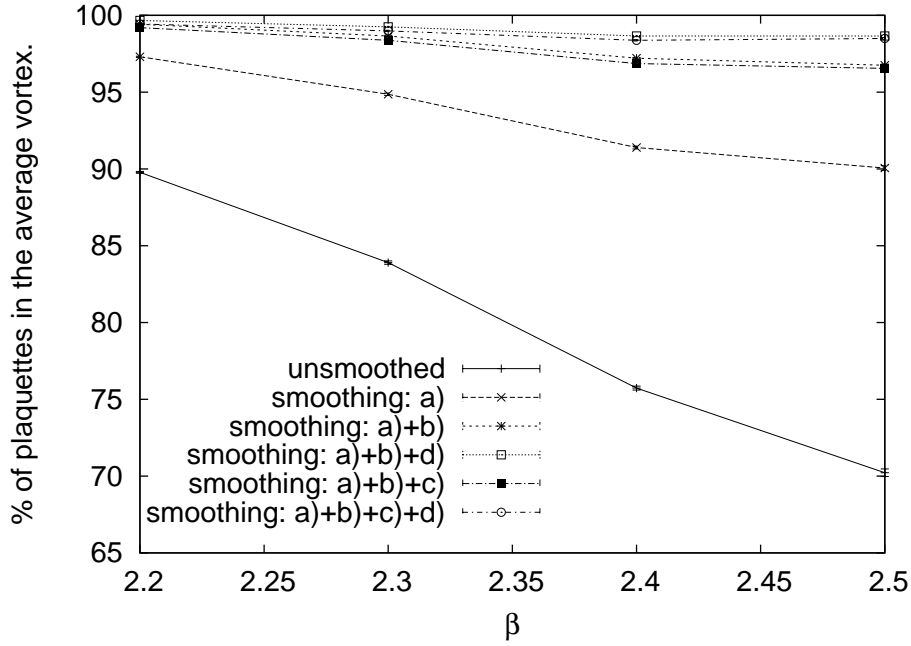


Figure 5.15: Weighted average vortex size  $s_w$  for various types of smoothing.

single huge P-vortex. Consistent with this result we also find that the linear extent of the largest P-vortex surface equals the extent of the lattice. In other words, the P-vortex does not fit into a hypercube smaller than the whole lattice confirming earlier results of Chernodub et al. [CPVZ99] on this subject.

## 5.5 Topological Properties

The basis for the investigation of the topology of P-vortices is the following rule: The type of homeomorphism of a two-dimensional, compact and closed surface is determined by a) the orientation behaviour, b) the Euler characteristic. P-vortices in dual space would fulfil the requested conditions (i.e. closeness) if every link joined only two plaquettes. As mentioned in section 5.4, P-vortex are not always regular surfaces, they can touch at points and links. We have already seen that if vortices touch along closed lines, they cannot be isolated properly, and there remain parts of vortices which are not closed surfaces. This can be solved by applying the smoothing procedure which removes the ambiguities, as shown in fig. 5.14 on the preceding page – even the first smoothing step a) is sufficient. Further, because the vast fraction of P-plaquette is part of one single percolation P-vortex, and because only this vortex is relevant for confinement, we restrict the calculations to the one dominating vortex of each configuration.

We will proceed in the following way. First, we will treat the determination of the orientability for the case that every link joins uniquely two attached P-vortex plaquettes. For each link of every P-plaquette we specify a sign. We start with an arbitrary P-

## 5.5 Topological Properties

plaquette and fix an arbitrary rotational direction. Those two links which are run through in positive axis direction get a plus sign, the other two get a minus sign. We continue at an arbitrary neighbouring P-plaquette. Its rotational sense we fix in such a way that the joining link gets the opposite sign than before. We continue this procedure for every plaquette of the given P-vortex. If at the end every link of the P-vortex has two opposite signs we call such P-vortices orientable. The simplest example is a three-dimensional cube. If some links appear with two equal signs the P-vortex is unorientable, e.g. it could be homeomorphic to a Klein bottle.

We already gave a certain classification for those cases where four or six P-plaquettes are joined by a single link, see also fig. 5.13 on page 79. In cases of this kind, where different pairs of P-plaquettes can be treated as belonging to independent vortices, we determine the orientability as though the vortices did not touch at such links. This way we get an upper bound for the orientability of vortices. Analogously we proceed for the case of a vortex touching itself at a link. We determine the orientability for a configuration where this touching is avoided. The case where a part of the surface cannot be reached because the touching links form a closed loop has already been excluded by applying the smoothing procedure.

The simulation shows that without exceptions the large vortices in all investigated field configurations, for all investigated  $\beta$ -values, turned out to be unorientable surfaces. We checked for the various employed smoothing steps whether this behaviour remains unchanged. It turns out that P-vortices remain unorientable after smoothing; apparently the smoothing procedure does not remove all of the local structures (e.g. “cross-caps”) responsible for the global non-orientability.

The second property which determines the topological properties of a closed, compact, two-dimensional surface is the Euler characteristic  $\chi$ <sup>3</sup>. For cell complexes such as P-vortices on the lattice  $\chi$  is defined by

$$\chi = \mathcal{N}_0 - \mathcal{N}_1 + \mathcal{N}_2, \quad (5.12)$$

where  $\mathcal{N}_k$  is the number of cells  $c_k$  of the cell complex, i.e.  $\mathcal{N}_0$  is the number of vertices,  $\mathcal{N}_1$  the number of links, and  $\mathcal{N}_2$  the number of plaquettes forming the P-vortex surface..  $\chi$  is directly related to the genus  $g$  of a surface, in the orientable case by

$$\chi = 2 - 2g \quad (5.13)$$

and in the unorientable case by

$$\chi = 2 - g. \quad (5.14)$$

An orientable surface of genus  $g$  is homeomorphic to a sphere with  $g$  attached handles. An unorientable surface of genus  $g$  corresponds to a sphere with  $g$  attached Möbius strips (also known as “cross-caps”).

---

<sup>3</sup>We use the same symbol for the Euler characteristic  $\chi$  and the Creutz ratios  $\chi(I, J)$ . The arguments present for Creutz ratios (e.g.  $(I, J)$ ) unambiguously distinguish the two quantities.

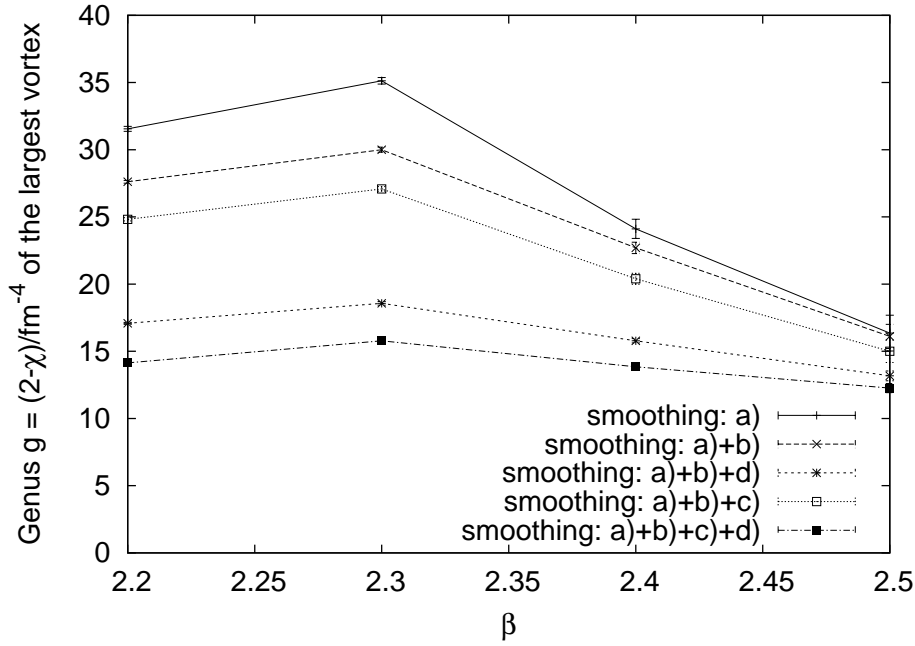


Figure 5.16: Genus  $g$  of the largest P-vortex per  $\text{fm}^4$  for various inverse couplings  $\beta$ .

The determination of the Euler characteristic of a P-vortex is not inhibited by possible self-touchings. We can simply treat the vortex as it is; the result is the average between a possible separation and a real fusing of the two parts of the vortex. For a detailed discussion of this case see [Ber98].

In fig. 5.16 we show the genus  $g = 2 - \chi$  per  $\text{fm}^4$  of the dominating P-vortex for various values of  $\beta$ . For the scaling to physical volumes we use again (5.6) on page 71. Smoothing step a) only removes elementary cube P-vortices and does not change  $\chi$  for the largest vortex, but this smoothing removes the ambiguities due to touching links which form closed loops, as discussed above. Hence in fig. 5.16 only results for smoothed configurations starting with step a) are shown. After only applying smoothing step a) the genus density takes a maximal value around  $\beta = 2.3$ . With b) smoothing, contact points and contact links can be removed, therefore a reduction of the genus of a vortex by smoothing step b) is to be expected. In fig. 5.16 this reduction is of the order of 15 %. As for the vortex density plotted in fig. 5.10 on page 76, smoothing step d) has the largest effect. This step also removes contact points and contact links. Finally, step c) can also remove regular bridges in vortices, as depicted in fig. 5.8 on page 74. Although these bridges occur rather seldom as can be seen from the small effect of smoothing step c) on the P-vortex density, there is some impact on the Euler characteristic  $\chi$ . Because c) changes  $\chi$  coercively and not only occasional if contact links and points are removed as for the other smoothing steps, its effect is disproportionate. The reduction by all smoothing steps combined amounts to 55% at  $\beta = 2.2$  and 43% at  $\beta = 2.5$ . The genus stays more nearly constant with  $\beta$  with than without smoothing. It has to

## 5.6 Structure of P-vortices at Finite Temperature

be investigated how the behaviour of  $g$  behaves at still higher  $\beta$ -values. The trend in the investigated region seems compatible with a scaling behaviour for genus  $g$ , and is not compatible with a self-similar short-range structure below the confinement length scale. Fractal structure of that kind would lead to an increase of the genus with  $\beta$ , as more handles are uncovered at ever-shorter length scales. Of course, even a smoothed P-vortex surface will be rough at length scales beyond the confinement scale, and an appropriate fractal dimension can be defined. The fractal dimension of unsmoothed P-vortex surfaces, using the definition of dimension  $D = 1 + 2\mathcal{N}_2/\mathcal{N}_1$ , where  $\mathcal{N}_2$  is the number of plaquettes and  $\mathcal{N}_1$  the number of links on the vortex surface, has been reported in [CPVZ99] and [BVZ99].

These investigations of the topology of P-vortices show that they are not topologically 3-spheres. This is not so surprising; there was no particular reason that vortices *should* have this topology. The structure which we identified, huge vortices extending over the whole lattice, unorientable with a lot of handles, is quite consistent with rotational symmetry in four dimensions. It is also consistent with the picture of a percolating random surface giving uncorrelated piercings of Wilson loops and area law behaviour for the loops and thus confinement. The unorientability of the vortex surface is also important for another feature of the vortex model besides the explanation of confinement. Chiral symmetry and the topological susceptibility in the framework of the vortex model will be treated in detail in chapter 7.

## 5.6 Structure of P-vortices at Finite Temperature

The SU(2) gauge theory possesses a high temperature phase, the *deconfined phase*. In this phase the quark-gluon plasma arises and fundamental charges are set free. The first discussion of the confinement/deconfinement phase transition in the context the vortex theory and center-projection methods, was made by Langfeld et al. in [LTER99], giving a nice explanation of the space-space string tension in the deconfined phase in terms of vortices closed in the time direction by lattice periodicity. Another very interesting investigation on the effect of finite temperature on the vortex structure is due to Chernodub et al. [CPVZ99]. In this section we will extend our study of P-vortex topology, and the effect of our smoothing steps on P-vortices, to the finite temperature case.

$\beta$	$N_s$	
1.6 - 2.1	12	As described in section 2.3.4, finite temperature can be simulated on the lattice by using an asymmetric lattice of size $N_{vol} = N_t \cdot N_s^3$ where the physical extent in time direction $aN_t$ corresponds to the inverse temperature $T$ . Because the lattice constant $a$ decreases with $\beta$ , the temperature can be adjusted using different values of $\beta$ and different temporal lattice extents. We did our finite temperature calculations on $N_t \cdot N_s^3$ -lattices with temporal lattice extents of $N_t = 2$ , $N_t = 4$ and $N_t = 6$ . For the spatial lattice extent $N_s$ we used depending on $\beta$ the values given in table 5.1, if not specified otherwise below. For each parameter set 300 configuration have been generated to measure ob-
2.2 - 2.3	16	
2.4 - 2.6	20	
2.7	28	

Table 5.1:  $\beta$  vs.  $N_s$ .

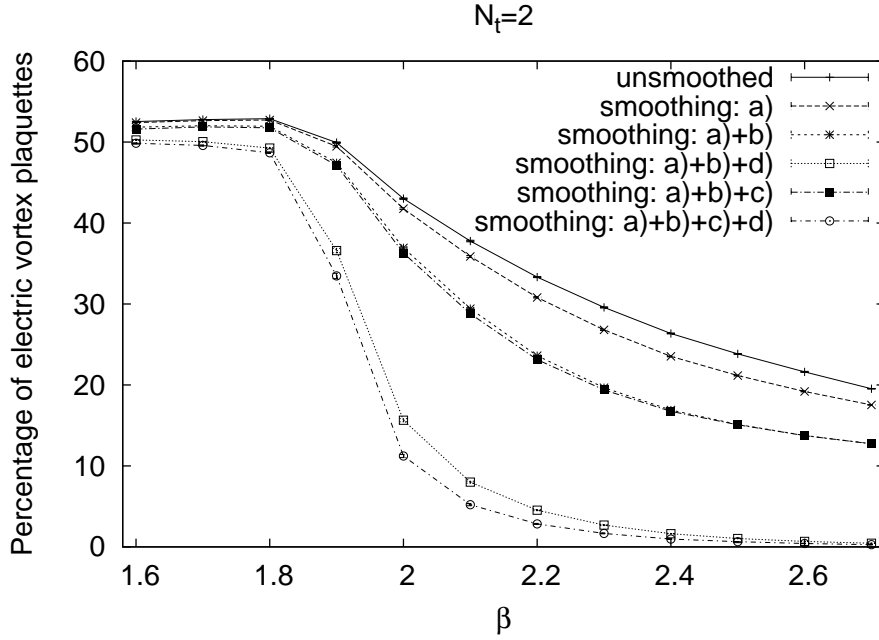


Figure 5.17: Percentage of electric  $P$ -plaquettes compared to all  $P$ -plaquettes as a function of  $\beta$  for lattices with  $N_t = 2$ .

servables. To infer the vortex content, MCG using over-relaxation with  $N_{copy} = 5$  gauge copies has been performed, followed by center projection.

The most striking difference to zero-temperature calculations is the strong asymmetry of  $P$ -plaquette distributions in the deconfined phase which can be seen in figs. 5.17 to 5.19 on pages 85–86. As a short-hand notation we use E-plaquette or electric plaquette for space-time and B-plaquette for space-space negative plaquettes of the original lattice. On the dual lattice, E-plaquettes are space-space  $P$ -plaquettes and B-plaquettes are space-time  $P$ -plaquettes. An investigation of this asymmetry was also performed in [LTER99]. In the confined phase, the densities of E-plaquettes and B-plaquettes are equal, just as for the zero-temperature calculations on symmetric lattices. Just below the phase transition the density of E-plaquettes is slightly larger than the density of B-plaquettes. Whereas this effect is almost absent for  $N_t = 6$ , at  $N_t = 4$  we have  $\sim 50.9\%$  E-plaquettes, and for a time extent of  $N_t = 2$  lattice units the fraction of E-plaquettes amounts to  $\sim 53\%$  as one can see in fig. 5.17. This excess of E-plaquettes seems to be connected with short range fluctuations of the vortices, since it is greatly reduced by smoothing, and can be considered to be a finite size effect because it is nearly absent at  $N_t = 6$ .

In the deconfined phase, the density of E-plaquettes is strongly decreasing with smoothing, and for the a)+b)+c)+d) smoothing step with  $N_t = 2$  soon reaches values close to 0% as seen in fig. 5.17. For  $N_t = 4$  and  $N_t = 6$ , with the strongest smoothing the percentage of E-plaquettes also decreases strongly with  $\beta$ , and inclines toward 0%, but

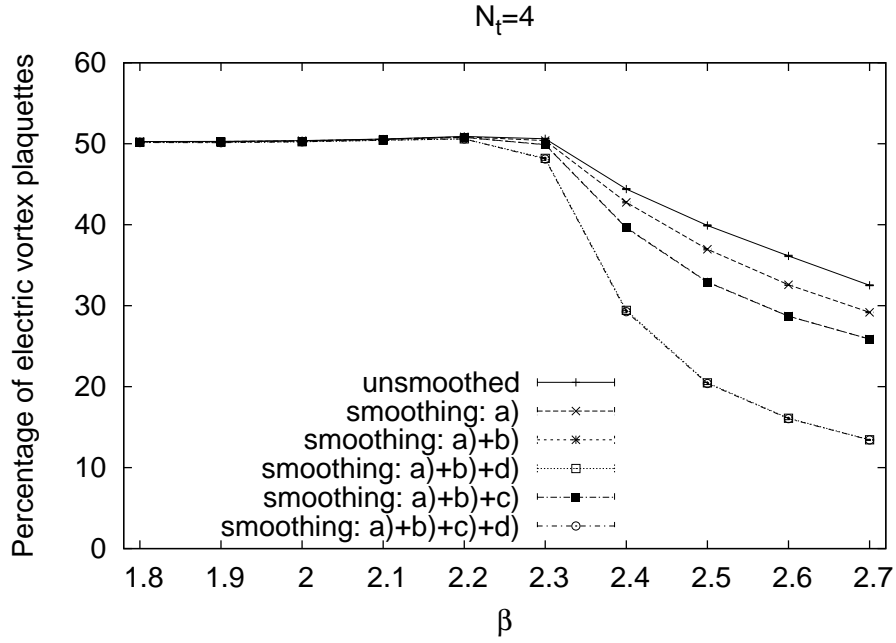


Figure 5.18: Percentage of electric  $P$ -plaquettes compared to all  $P$ -plaquettes as a function of  $\beta$  for lattices with  $N_t = 4$ .

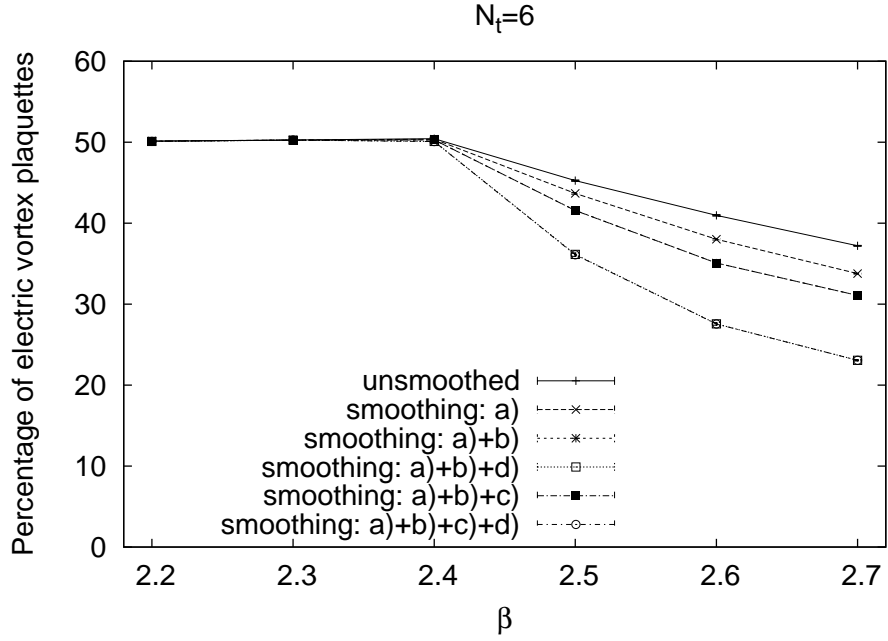


Figure 5.19: Percentage of electric  $P$ -plaquettes compared to all  $P$ -plaquettes as a function of  $\beta$  for lattices with  $N_t = 4$ .

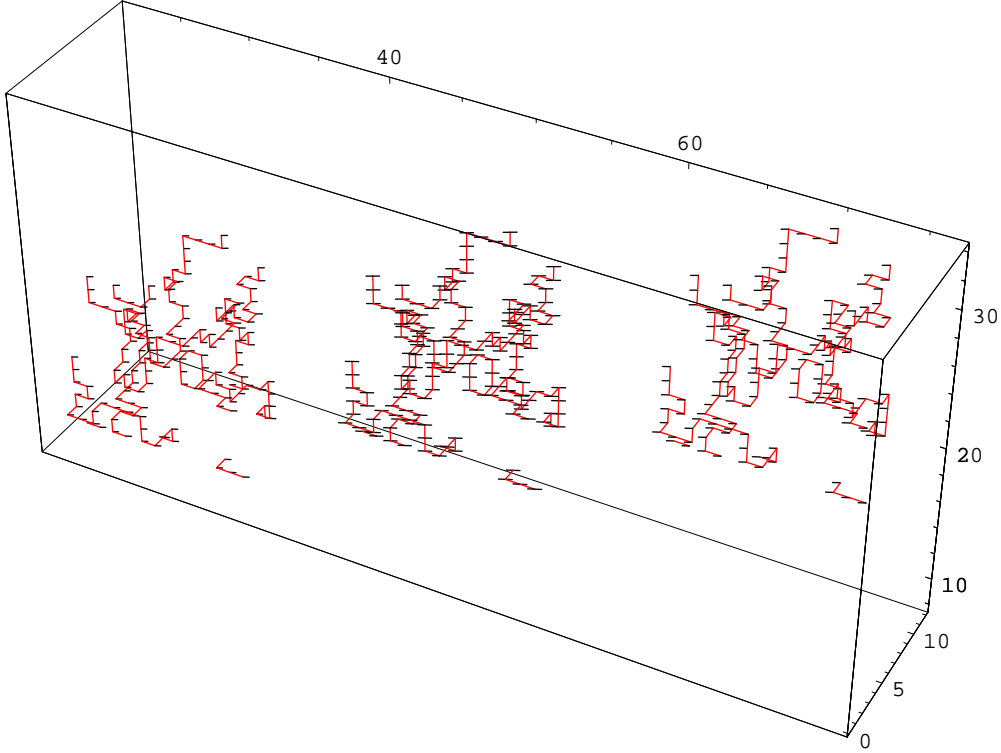


Figure 5.20:  $P$ -plaquettes of a typical field configuration at  $\beta = 2.6$ , on a  $2 \cdot 12^3$ -lattice. The two  $t$ -slices for the  $x$ - $y$ - $z$ -subspace are shown. The rightmost  $t$ -slice is a copy of the leftmost one in order to illustrate the periodic boundary conditions. Amputated lines leaving a  $t$ -slice arrive at a neighbouring  $t$ -slice.

larger values of  $\beta$  seem to be necessary in order to reach 0%.  $E$ -plaquettes in the deconfined phase appear obviously due to short range fluctuations and cannot contribute to an area law behaviour, as can be seen from the large effect of the smoothing procedure on  $E$ -plaquettes reducing their fraction considerably. The detected strong asymmetry in the deconfined phase gives a very intuitive explanation for the behaviour of space-time and space-space Wilson loops, as discussed in [LTER99]. The dominant vortex which percolates through the lattice is a (mostly) timelike surface on the dual lattice, which is closed via periodicity in the time direction. Polyakov lines are not affected by timelike vortex surfaces, and timelike Wilson loops are also unaffected. Therefore the string tension of timelike loops is lost in the deconfined phase [LTER99, ELRT00]. On the other hand, large timelike vortex surfaces (composed of  $B$ -plaquettes) do disorder spacelike Wilson loops, which accounts for the string tension of spatial loops [BFH<sup>+</sup>93, KLL95] in the deconfined regime.

Fig. 5.20 displays the  $P$ -plaquettes of a typical field configuration at  $\beta = 2.6$  on a  $2 \cdot 12^3$ -lattice. The two time-slices of the lattice are plotted separately. Actually there are three slices plotted, but the rightmost slice is a copy of the leftmost slice, illustrating

## 5.6 Structure of $P$ -vortices at Finite Temperature

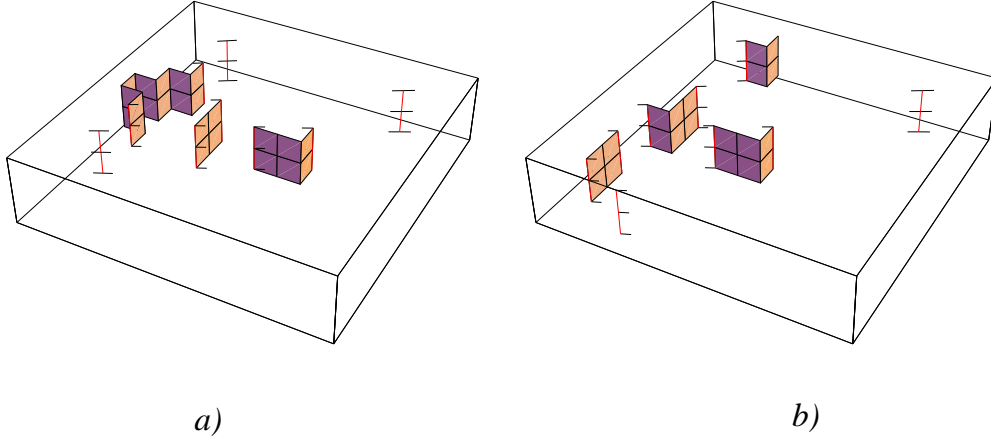


Figure 5.21:  $P$ -plaquettes in a typical field configuration at  $\beta = 2.6$ , on a  $2 \cdot 12^3$ -lattice. Two successive  $z$ -slices for the  $x$ - $y$ - $t$ -subspace are shown. The amputated lines leaving the left figure towards right arrive in the right figure from the left.

the periodic boundary conditions. Small legs indicate  $B$ -plaquettes connecting the different slices. In fig. 5.21 the same configuration as in fig. 5.20 on the preceding page is plotted. Here not the two  $x$ - $y$ - $z$ -subspaces, but two  $x$ - $y$ - $t$ -subspaces are drawn. Plaquettes extending in  $z$ -direction are indicated by small legs. This plot illustrates that the  $P$ -plaquettes form cylinders in time direction, closed via the periodicity of the lattice. Thus they are homeomorphic to a torus. Vortices of this shape are also well known in finite temperature theory under the name of ordered-ordered interfaces [HJK92].

The density of  $P$ -plaquettes is depicted in figs. 5.22 to 5.23 on pages 89–90 for unsmoothed configurations, and after applying all smoothing steps. In each figure the densities are plotted separately for  $E$ - and  $B$ -plaquettes. Below the phase transitions, which depends on the temporal lattice extent  $N_t$ , both densities coincide, and are equal to the  $P$ -vortex density found in the temperature  $T = 0$  calculations of section 5.3. Only for the unsmoothed  $N_t = 2$  calculations, the finite size effect mentioned above that  $E$ -plaquettes are somewhat increased is present;  $B$ -plaquettes seem to be somewhat decreased. At the phase transition, the situations changes drastically. The  $E$ -plaquette density falls quickly. Interesting is the density of  $B$ -plaquettes: First, it drops also faster than in the confined phase, but boldly less than the  $E$ -plaquette density. This drop can be seen nicely by comparing with the  $N_t = 4$  or later  $N_t = 6$  curves, which remain in the confined phase till higher values of  $\beta$ . But at higher temperatures, the slope of the  $B$ -plaquette density flattens, and at large values of  $\beta$  the density is clearly larger than in the zero-temperature case. This result is in perfect agreement with the findings in [BFH<sup>+</sup>93, KLL95]. The measured spatial string tension increases with the temperature  $T$ , too.

For the calculation of topological properties and of the size of vortices, again as for the case at zero-temperature the question of connectedness of the vortex surface has to be resolved, see the discussion about fig. 5.13 on page 79 in section 5.4. Fortunately, as in



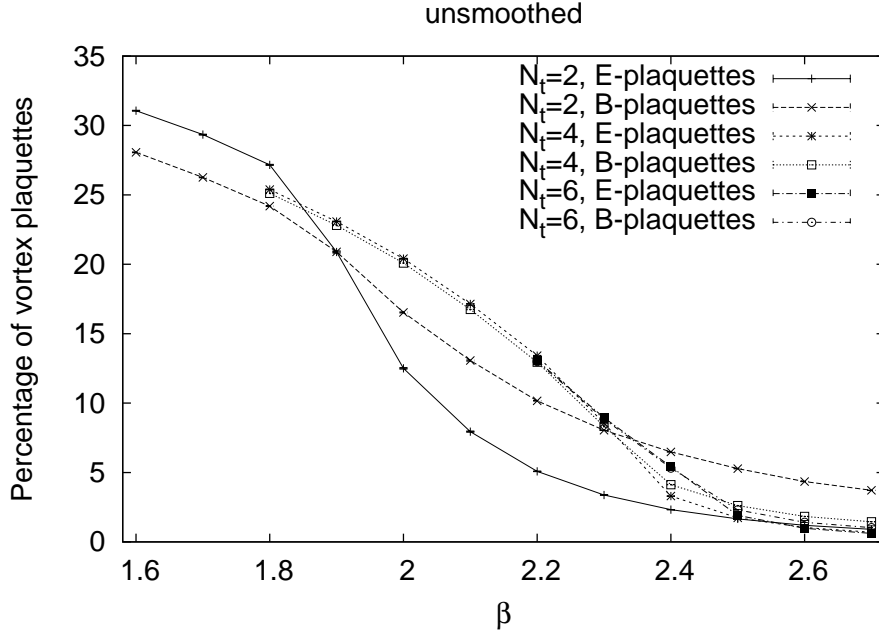


Figure 5.22: Percentage of E- and B-plaquettes, compared to the number of all space-space and space-time plaquettes as a function of  $\beta$  for  $N_t = (2, 4, 6)$ , without smoothing.

the zero-temperature case the ambiguities can be treated satisfactorily. The exception are vortices which touch along closed lines, which results in unclosed parts of  $P$ -vortices if we try to identify the individual vortex surfaces. For the temperature  $T = 0$  case, we could avoid this problem by applying the first smoothing step a) which only removes elementary cube vortices and does not influence the bigger vortices whose topological properties we are interested in. At finite temperature with  $N_t = 2$ , we have not been able to solve this problem using smoothing. On a lattice with such a small extent in time direction, there is a higher probability that some part of a  $P$ -vortex surface is connected to the rest of the surface only crossing ambiguous links. Easily these links can form two loops of length 2, each closed over the periodicity of the lattice, and separating a part of the vortex surface. But for  $N_t = 4$  and  $N_t = 6$ , smoothing step a) can successfully remove the closed line ambiguities, thus we have results for the topological properties on lattices with  $N_t = 4$  and  $N_t = 6$  only. Therefore as for the zero-temperature case, for the topological properties we only show results from smoothed lattices, because smoothing a) does not change the orientability or the Euler characteristic of the larger vortices, but helps to identify the separated  $P$ -vortex surfaces by removing elementary cube vortices.

As expected from the zero-temperature results, in the confined phase most of the  $P$ -plaquettes belong to a single large vortex. This can be seen in figs. 5.24 to 5.25 on pages 90–91, where the weighted average vortex size  $s_w$  (5.11) is plotted for  $N_t = 4$  and  $N_t = 6$ . The situation changes drastically at the phase transition where the percentage

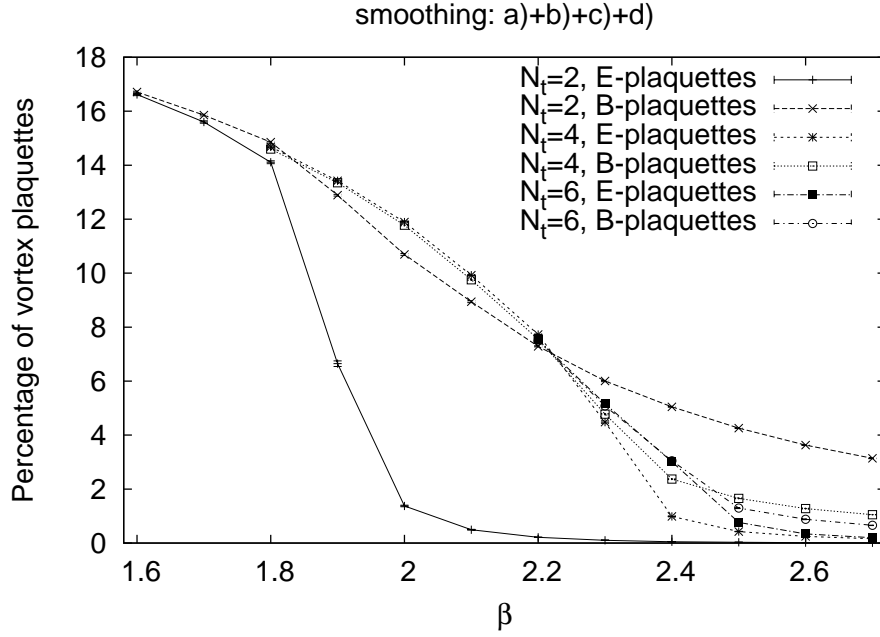


Figure 5.23: Percentage of E- and B-plaquettes, compared to the number of all space-space and space-time plaquettes as a function of  $\beta$  for  $N_t = (2, 4, 6)$  and after applying smoothing steps a)+b)+c)+d).

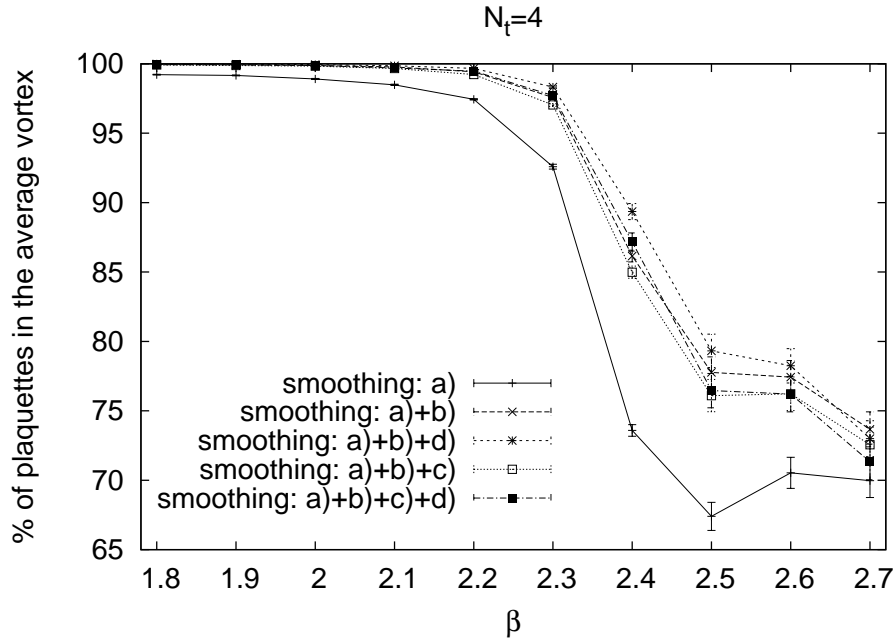
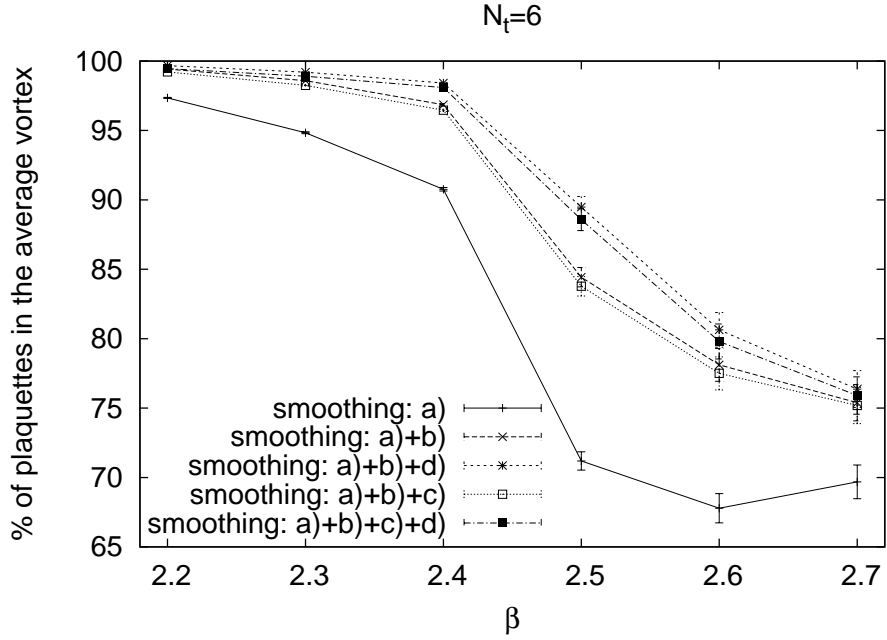


Figure 5.24: Weighted average vortex size  $s_w$  as a function of  $\beta$  with  $N_t = 4$ .


 Figure 5.25: Weighted average vortex size  $s_w$  as a function of  $\beta$  with  $N_t = 6$ .

of  $P$ -plaquettes in the average vortex drops considerably, especially for the unsmoothed configurations. The smoothing procedure shows that there is still one large vortex but its dominance is not so strong as in the zero-temperature case. The reason for the increase of the percentage from  $\beta = 2.5$  to  $\beta = 2.7$  for  $N_t = 4$ , and from  $\beta = 2.6$  to  $\beta = 2.7$  for  $N_t = 6$ , is unclear. This might be a finite size effect as presumed in [BFG00]; we have done some calculation for different spatial lattice extents  $N_s$  and could not confirm this assumption, but a definitive answer could not be given yet. This question will require detailed investigations on a large range of lattices sizes and gauge copies with better statistics, as it was done for the MCG tests at zero-temperature described in section 4.2.3. In any case, the indisputable existence of a large space-time vortex on the dual lattice is required, at finite temperature in the deconfined phase, in order to explain area law behaviour for spacelike Wilson loops. We have also found percolation for the largest  $P$ -vortex both below and above the phase transition; it extends over the whole lattice.

With the decrease in the percentage of  $E$ -plaquettes we find increasing orientability of  $P$ -vortices. The orientability is one of the few observables depending on the used spatial lattice extents  $N_s$  of our  $N_t \cdot N_s^3$  lattices, as shown in figs. 5.26 to 5.27 on pages 92–93. Be aware that the percentage is calculated using  $P$ -vortices weighted with their size, i.e. the number of contained  $P$ -plaquettes. The orientability approaches 100% for large  $\beta$ , but on the larger lattices this happens at larger values of  $\beta$ . This can readily be understood by the nature of unorientability: Any local unorientability (i.e. each “cross-cap”) makes the whole  $P$ -vortex surface unorientable, and assuming a constant density

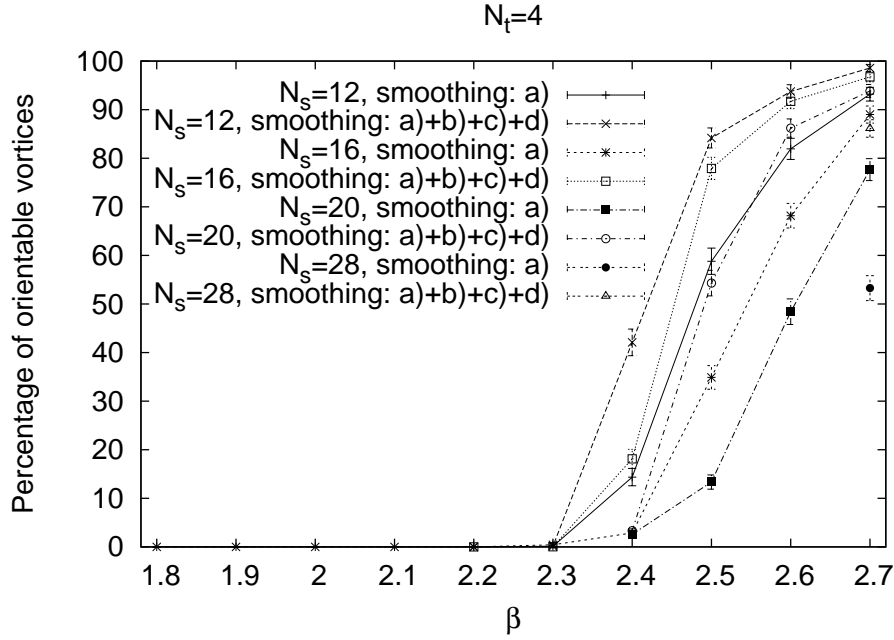


Figure 5.26: Percentage of orientable P-vortices on  $4 \cdot N_s^3$  lattices for different values of  $N_s$  depending on  $\beta$ . The P-vortices are weighted with their size (the number of P-plaquettes in the vortex).

of “cross-caps”, on larger lattices the probability that there is at least one “cross-cap” in the P-vortex is higher. Smoothing step d) strongly increases orientability.

The relations between genus  $g$  and Euler characteristic  $\chi$  are different for orientable (5.13) and unorientable surfaces (5.14). Since both types of surfaces appear in finite temperature calculations we investigate the value of  $2 - \chi$  as in the zero-temperature case. For orientable vortices this expression is the genus  $g$ , for unorientable surfaces half of the genus. In figs. 5.28 to 5.29 on pages 93–94 we show the value of  $2 - \chi$  divided by the lattice volume  $N_t \cdot N_s^3$  for the largest vortex of each configuration. These data are not scaled with the lattice constant  $a$  as in the zero-temperature case (fig. 5.16 on page 83) because changing  $\beta$  does not only change the lattice spacing  $a$  but also the temperature  $T$ . We have checked that for this observable the dependence on the lattice size is very weak. In the confined phase P-vortices are again complicated surfaces; as in the zero-temperature case, and as for the unorientability, smoothing step c) has a disproportional effect.

Above the phase transition  $2 - \chi$  approaches – independent from the lattice size – the value 2, as plotted in figs. 5.30 to 5.31 on pages 94–95. This is a consequence of the vanishing density of E-plaquettes. The largest P-vortex becomes orientable with genus  $g = 1$  and  $\chi = 0$ . It is homeomorphic to a torus, as can also be seen in fig. 5.21 on page 88.

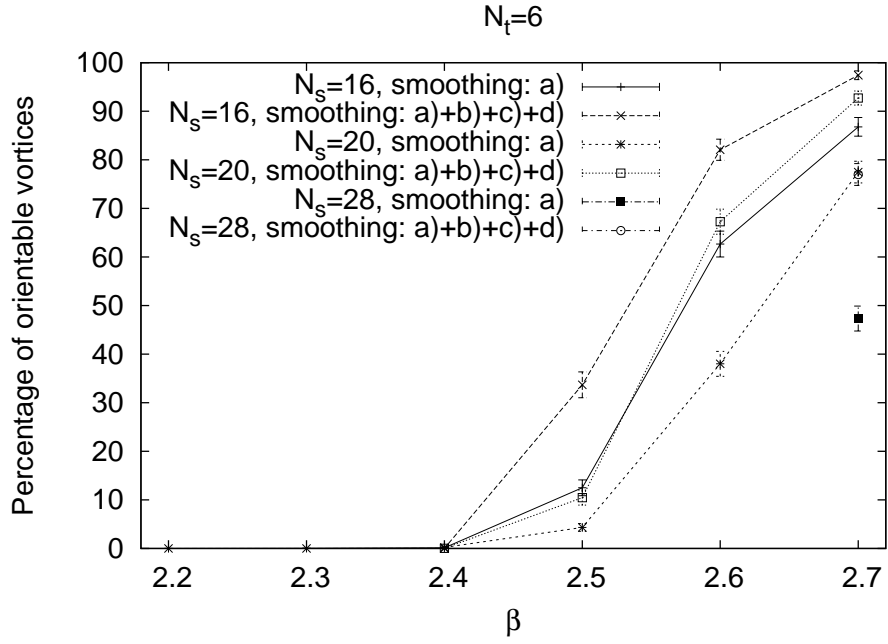


Figure 5.27: Percentage of orientable P-vortices on  $6 \cdot N_s^3$  lattices for different values of  $N_s$  depending on  $\beta$ . The P-vortices are weighted with their size (the number of P-plaquettes in the vortex).

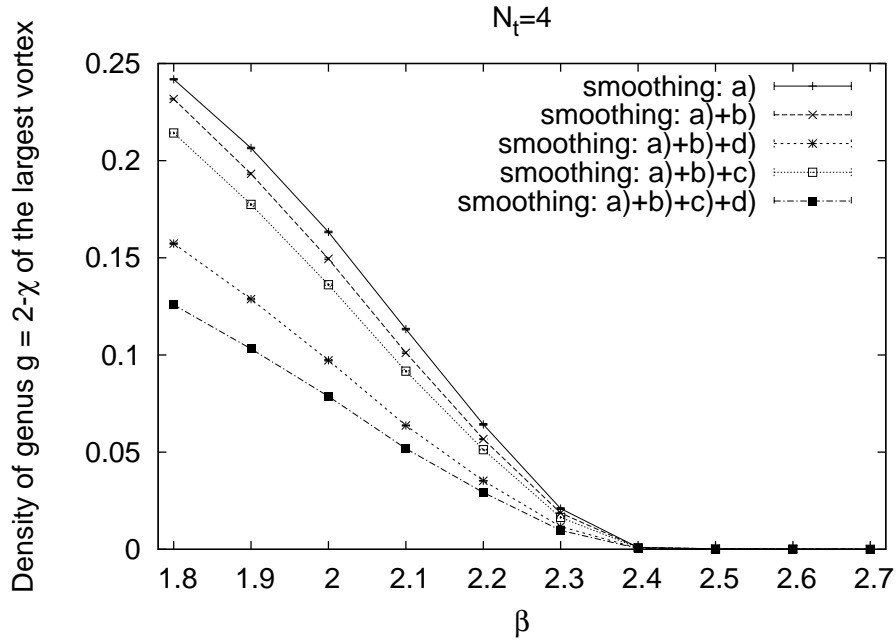


Figure 5.28:  $2 - \chi$  divided by  $4 \cdot N_s^3$  of the largest vortex for  $4 \cdot N_s^3$ -lattices.

## 5.6 Structure of $P$ -vortices at Finite Temperature

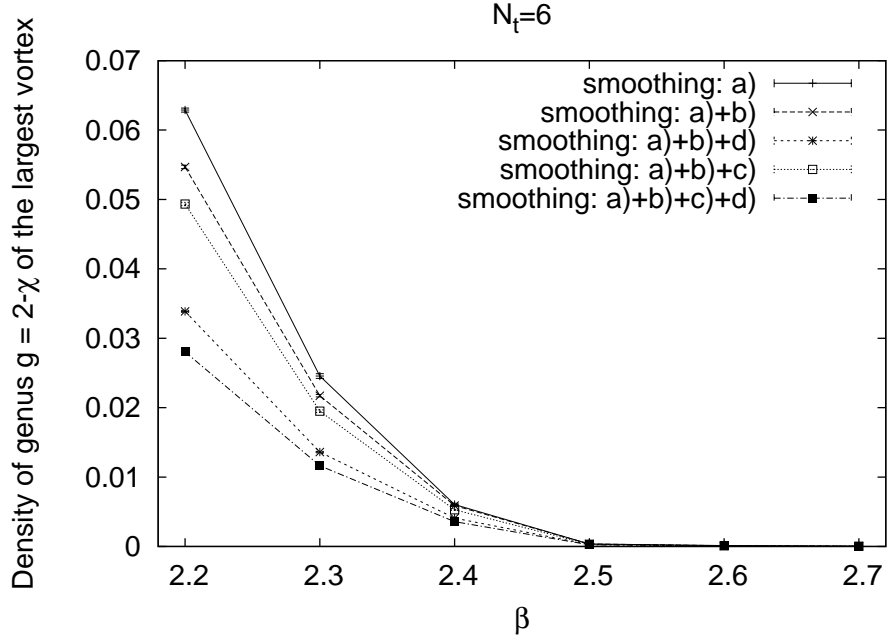


Figure 5.29:  $2 - \chi$  divided by  $6 \cdot N_s^3$  of the largest vortex for  $6 \cdot N_s^3$ -lattices.

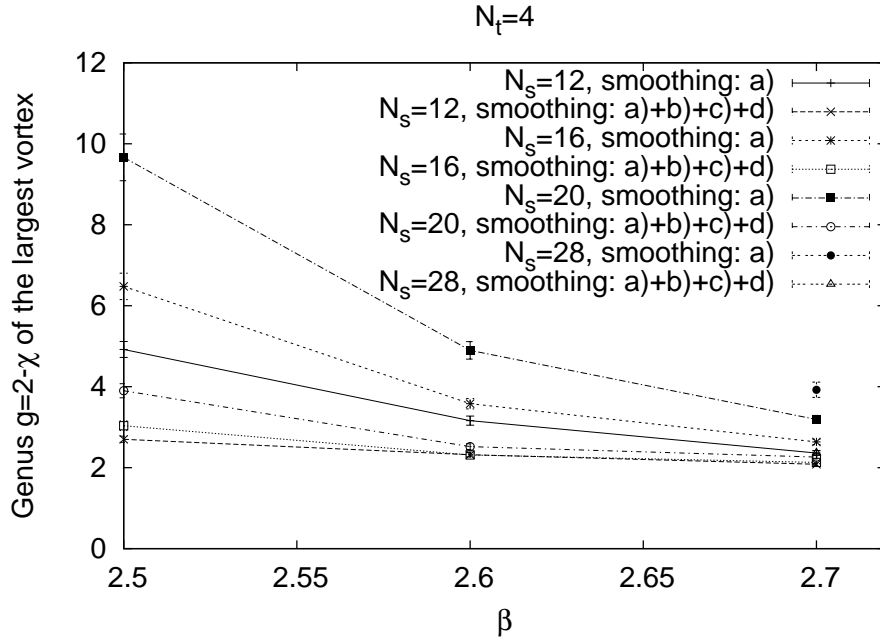
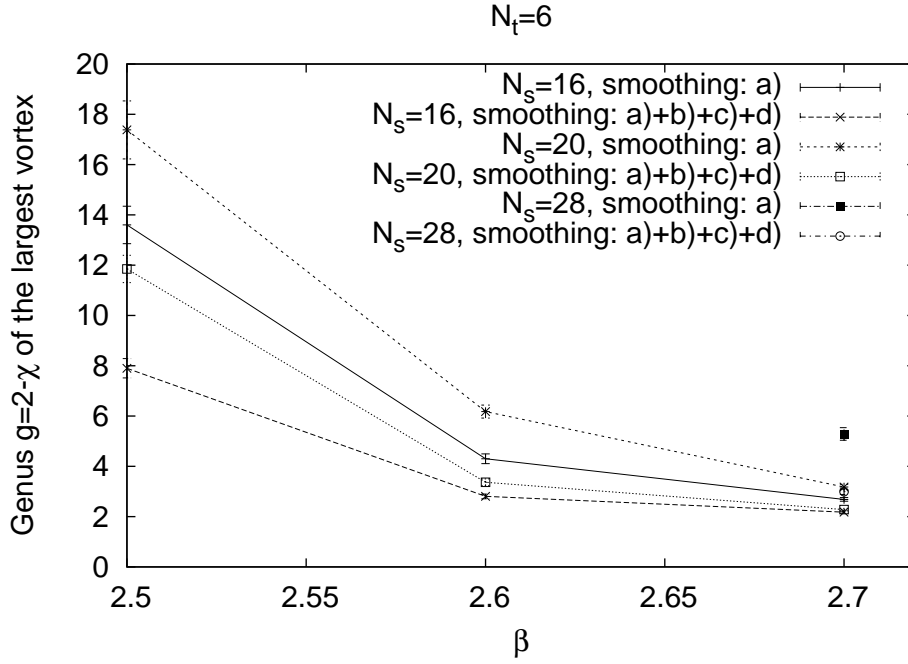


Figure 5.30:  $2 - \chi$  of the largest vortex for various  $4 \cdot N_s^3$ -lattices.


 Figure 5.31:  $2 - \chi$  of the largest vortex for various  $6 \cdot N_s^3$ -lattices.

## 5.7 Structure of Thick Vortices

In this chapter, up to this section, we have only investigated the properties of thin, projected vortices. We will now look at the structure of unprojected vortices.

A particular feature of the vortices present in the unprojected configurations which is lost in the projection step is their thickness. As described in section 3.4, the action of thin vortices on the unprojected lattice is divergent in the continuum limit. Hence vortices bordering the Dirac volume are thick, and the colour magnetic flux of the vortex, which is quantised in terms of a center element of the gauge group, extends over a finite area.

We have seen the influence of the finite vortex thickness already in our investigation of the maximal center gauge (MCG), see section 4.2.3. Calculating center projected observables after MCG and center projection, considerably larger lattices are required to avoid finite size effect, compared to unprojected observables. Only if the linear extent of the lattice is larger than the average vortex diameter, the vortices can be fully detected. In fig. 5.32 on the following page, we plot the P-vortex density  $p$  against the linear extent  $L$  of our  $L^4$  lattices using  $N_{copy} = 20$  gauge copies. It can clearly be seen that  $p$  is quite low on smaller lattices and increases with  $L$ . At  $L = 16$  the density starts to level off. This indicates that the vortex thickness is smaller than 16 lattice spacings at  $\beta = 2.5$ .

There are three independent ways to actually estimate the thickness of center vortices,

## 5.7 Structure of Thick Vortices

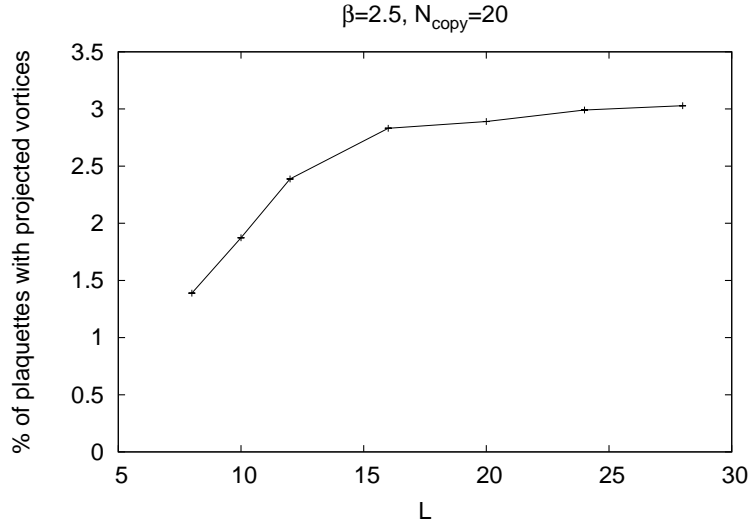


Figure 5.32: Vortex density  $p$  vs. the extent  $L$  of the hypercubic lattice (volume  $L^4$ ) at  $\beta = 2.5$ .

which can be deduced from either

1. the ratio of “vortex-limited” Wilson loops [DFG<sup>+</sup>98];
2. the vortex free energy as a function of lattice size [KT00];
3. the adjoint string-breaking length [dFP00b].

Vortex-limited Wilson  $W_n$  loops have been defined in section 4.2.1. Data for  $W_1/W_0$  vs. loop area at  $\beta = 2.3$  taken from [DFG<sup>+</sup>98] has been plotted already in fig. 4.1 on page 35. We can expect that

$$\frac{W_1(C)}{W_0(C)} \rightarrow -1 \quad (5.15)$$

in the limit where the vortex core is entirely contained within the loop. Judging from this figure, the vortex appears to almost fit inside a  $5 \times 5$  loop, which leads to a rough estimate of the vortex radius, as it pierces a plane, of about 3 lattice spacings. Calculating the lattice spacing in physical units using (5.6) we find that the estimated vortex diameter of 6 lattice spacings corresponds to a vortex thickness of about one fm. Of course this neglects the possibility that the vortex is not contained entirely within the loop because it lies not at center point of the rectangular loop, but more towards the border of the loop. There are some simulations taking into account the position of the projected vortex in vortex-limited Wilson loops [Ste00], they indicate a smaller value for the diameter of the vortex core. More calculations are needed for this method to estimate the vortex thickness.

A second estimate is obtained from the calculation of the vortex free energy vs. lattice size, carried out numerically by Kovács and Tomboulis [KT00]. The vortex free energy is



close to zero when the lattice extent is greater than the vortex thickness, and this again gives an estimate for the vortex thickness of a little over one fm. Finally, if confinement is due to center vortices, then an  $I \times J$  Wilson loop in the adjoint representation must change from a (Casimir scaling) area law falloff to a (colour-screening) perimeter law falloff for charge separation  $I$  greater than the vortex thickness [FGO98, FGO99b], see also section 3.4. The adjoint string-breaking distance has been measured, by de Forcrand and Philipsen [dFD99], to be 1.25 fm, and this distance provides us with a third estimate of the vortex thickness, which is roughly consistent with the other two.

It is instructive to compare the vortex thickness with the average distance between the vortices which can be inferred from the vortex density. We use the estimate  $f$  calculated from the string tension using (5.10) for the P-vortex density. This estimate agrees well with the actual P-vortex density  $p$  after smoothing the short range fluctuations of the vortex surface, as has been shown in section 5.3. For  $\beta = 2.3$  we find  $f = 0.063$ . This implies an average distance of  $f^{-1/2} \approx 4$  lattice spacings between the centres of vortex cores piercing a plane. Since we have already estimated the vortex thickness at  $\beta = 2.3$  to be about 6 lattice spacings, it's clear that there must be a substantial overlap between vortex cores, even on a very large lattice. There is nothing in principle wrong with that; vortex cores are not impenetrable objects, and their long-range effects are associated with Dirac 3-volumes, rather than the detailed structure of the core. Our findings for vortex thickness and separation simply indicate, in accordance with some old ideas of the Copenhagen group [NO79, AO80b, AO80a], that the QCD vacuum is more like a liquid of vortices than a dilute gas.

Other features of thick, unprojected vortices include the colour structure. The center projection squeezes thick vortices into thin P-vortices carrying a flux of exactly  $-1$ , whereas thick vortices can have a profile extending the whole gauge group. We have discussed this colour structure already in the context of the Laplacian center gauges in section 4.3.5.2. Some part of the colour structure can even be saved for projected vortices and be encoded in the orientability of the two-dimensional P-vortex surface. This is an important feature for the topological properties of QCD in the vortex model, which will be dealt with in chapter 7.

## 5.8 Conclusions

We have investigated the size and topology of P-vortices in SU(2) lattice gauge theory; P-vortices are surfaces on the dual lattice which lie at or near the middle of thick center vortices. We have found that in the confined phase the four-dimensional lattice is penetrated by a single huge P-vortex of very complicated topological structure. This huge P-vortex is a closed surface on the dual lattice which is unorientable and has many ( $\sim 10/\text{fm}^4$ ) handles. There exist also a few very small vortices. They contribute together with short range fluctuations of the large P-vortex to the perimeter law falloff of projected Wilson loops only. These short range fluctuations may simply be due to a slight ambiguity in the precise location of the middle of a thick center vortex and are not necessarily characteristic of the thick center vortices themselves.

## 5.8 Conclusions

By a smoothing procedure, we were able to remove these perimeter contributions due to short-range fluctuations, keeping the Creutz ratios constant. Thus the short-range P-vortex fluctuations are found to account for the difference between the percentage  $p$  of plaquettes which are pierced by P-vortices, and the comparatively smaller fraction  $f$  which, in the simplest version of the vortex model (with uncorrelated P-plaquettes), contributes to the string tension. Upon smoothing away the short-range fluctuations, we find the fraction  $p$  closely approaching the value of  $f$  extracted from the asymptotic string tension.

The density of vortices does not vanish in the deconfined phase, but a strong space-time asymmetry is found. P-vortices at finite temperature are mainly composed of space-space plaquettes forming timelike surfaces on the dual lattice. These surfaces are closed via the periodicity of the lattice in the time direction, they are orientable, and have the topology of a torus, i.e. genus  $g = 1$ . The dominance of the largest vortex is not as strong as in the zero-temperature case. The space-time asymmetry of P-vortices in the deconfined phase nicely explains [LTER99] the corresponding asymmetry in Wilson loops, which have area-law falloff for spacelike, and vanishing string tension for timelike loops.

Finally we find that thick vortices present in the unprojected configurations are not well separated objects, but overlap considerably. This suggests rather the picture of a liquid of vortices than that of a dilute vortex gas.

# 6 Vortices with Matter Fields

## Abstract

We investigate the influence of matter fields on vortices. Because fermions are costly to simulate on the lattice, we use scalar fields instead. Our model is the  $SU(2)$ -gauge Higgs theory.

### 6.1 The $SU(2)$ -Higgs Model

Up to now, our numerical investigations have concerned pure gluonic QCD only (or the simpler pure  $SU(2)$  gauge theory). As already mentioned in section 3.1, if dynamical fermions are included, it is well known that the long range part of the potential between static charges changes qualitatively compared to the quenched approximation: Schematically depicted in fig. 6.1, at some screening distance  $r_0$  the string between a quark-antiquark pair breaks. Out of the vacuum an additional quark-antiquark is formed, and the potential levels off. This is roughly shown in fig. 6.2 on the next page. At small distances we have a Coulomb-like  $1/r$  potential, at intermediate distance we see the linear rising potential characteristic for confinement, and beyond  $r_0$  the potential  $V(r)$  is constant.

The simulation of dynamic fermions on the lattice is rather involved and costly with regard to computer time. Fortunately string breaking has been observed numerically also for a simpler model, the gauge-Higgs system [KS98]. More precisely, the model used in this chapter is lattice  $SU(2)$  gauge-Higgs theory with Higgs fields in the fundamental

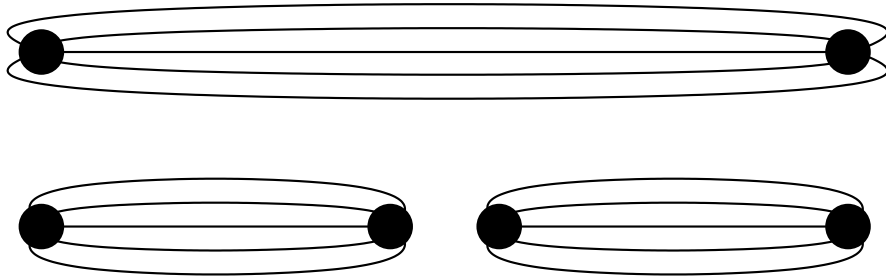


Figure 6.1: Schematic picture of the breaking of the string between a quark and an antiquark.

## 6.1 The $SU(2)$ -Higgs Model

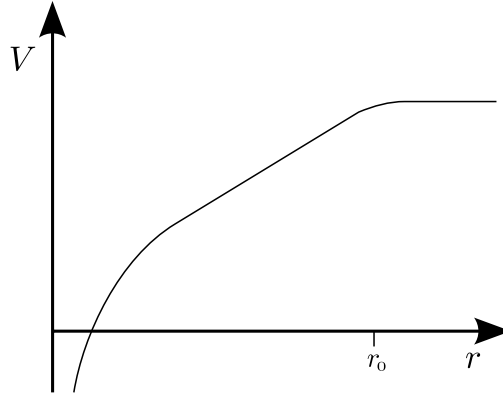


Figure 6.2: Schematic plot of the static potential between a quark and an antiquark.

representation; the action is given by

$$S[\omega, \Phi] = S^{YM}[\omega] + \int |D_{\nabla}\Phi|^2 + V(\Phi) \quad (6.1)$$

$$V(\phi) = m|\phi|^2 + \lambda|\phi|^4. \quad (6.2)$$

On the lattice this action can be written as

$$S[U, \Phi] = S_W + \sum_x \left[ \Phi^\dagger(x)\Phi(x) + \lambda \left( \Phi^\dagger(x)\Phi(x) - 1 \right)^2 \right] - \kappa \sum_{\mu, x} \left( \Phi^\dagger(x)U_\mu(x)\Phi(x + \hat{\mu}) + \text{cc} \right) \quad (6.3)$$

$$S_W = \beta \sum_{\mu < \nu, x} \left( 1 - \frac{1}{2} \text{Re Tr } U_{\mu\nu}(x) \right), \quad (6.4)$$

where  $S_W$  is the Wilson plaquette action (2.33) on page 16, and  $\Phi = \begin{pmatrix} \phi_1 \\ \phi_2 \end{pmatrix}$ , with  $\phi_1, \phi_2 \in \mathbb{C}$ , is a massive scalar field in the fundamental representation of  $SU(2)$ . A schematic phase diagram for the  $SU(2)$ -Higgs model is depicted in fig. 6.3 on the next page. In the “confined”<sup>1</sup> phase, the potential between fundamental charges rises linearly at intermediate distances. Due to colour screening of fundamental charges, there is **string breaking** at some finite distance  $r_0$ , and the potential levels off. In the *Higgs phase*, the Higgs mechanism is at work, and the potential is Yukawa-like; the string tension vanishes at all separations. However, these are not thermodynamically distinct phases. The phase diagram is connected, in the sense that one can always find a path between any two points in the phase diagram which avoids any non-analyticity in thermodynamic quantities. The transition line which might have separated the Higgs and

<sup>1</sup>We have introduced in section 3.1 the confined phase as a phase with non vanishing asymptotic string tension  $\sigma$ . Thus we quote the term “confined” in order to indicate that  $\sigma$  is asymptotically zero due to string breaking.

## 6.1 The $SU(2)$ -Higgs Model

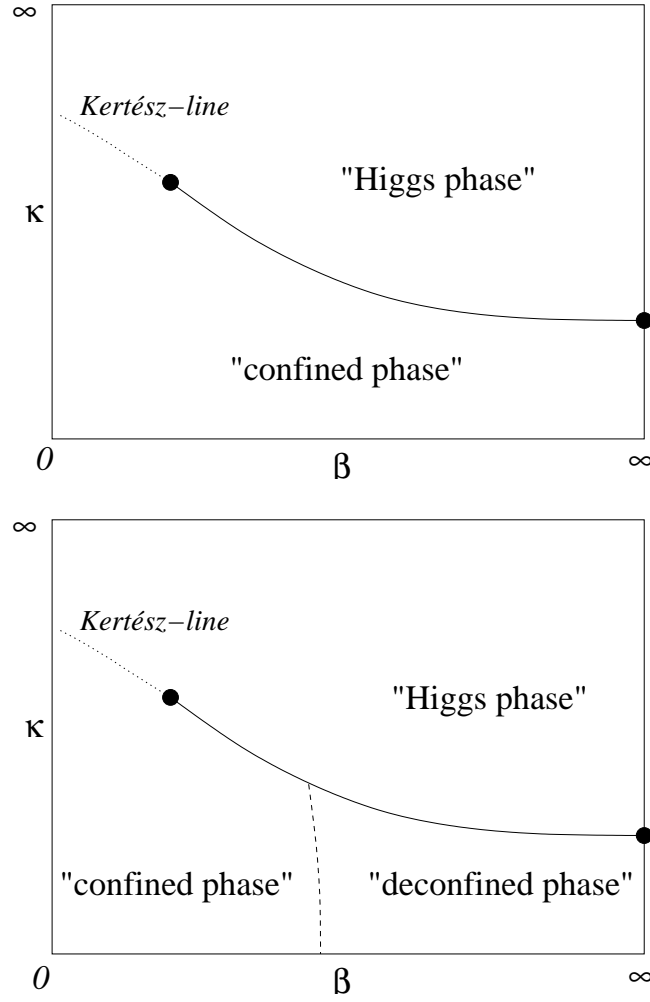


Figure 6.3: Schematic phase diagram for the  $SU(2)$ -Higgs system at zero temperature (top), and on lattices with a fixed extent in the time direction (bottom).

## 6.2 Finite Temperature

confinement phases ends at a critical point in the strong coupling region, and from there changes over to crossover behaviour. Thus if we speak of the Higgs or the “confined” phases in this model, we are aware that we speak rather of regions belonging to a single phase of the system [FS79].

At finite temperature and  $\kappa = 0$  there is an additional phase, namely, the deconfined phase. In this phase the quark-gluon plasma arises and fundamental charges are set free. For  $\kappa > 0$  there is no true phase transition between the “confined” and “deconfined” phases, but only crossover behaviour indicated by the dashed line in fig. 6.3 on the preceding page (lower figure). Hence we still have only one phase in the  $\beta - \kappa$  plane.

The vortex picture of confinement was first applied to the SU(2) gauge-Higgs system in the early 1980s [MMO82, MO84]. Numerically we have seen in section 5.6 that the vortex density  $p$  drops across the deconfinement transition, and that because of the suppression of E-plaquettes timelike loops are not disordered any more. Newer investigations [Lan02, BF02] show that in the Higgs phase the vortex density is suppressed too, which raised the expectation that also in the gauge-Higgs system confinement can be described within the vortex model [BFGO04]. In this chapter we investigate the properties of center projected observables and of the center vortex surfaces themselves in the various phases of the model depending on couplings and temperature.

It is most efficient to carry out Monte Carlo simulations of the gauge-Higgs system in *unitary gauge*, where  $\Phi = \begin{pmatrix} \phi \\ 0 \end{pmatrix}$ ,  $\phi \in [0, \infty]$ , and only one degree of freedom has to be simulated for the Higgs field. In the unitary gauge we get the partition function

$$Z = \int \mathcal{D}[U] \mathcal{D}[\phi] \exp(-S_W - S_{\text{Hu}}) \quad (6.5)$$

$$S_{\text{Hu}} = \sum_x \left[ \phi^2(x) + \lambda (\phi^2(x) - 1)^2 \right] - \kappa \sum_{\mu, x} \left( \phi(x) \phi(x + \hat{\mu}) \text{Tr}[U_\mu(x)] \right) \quad (6.6)$$

with  $\phi = \sqrt{\Phi^\dagger \Phi}$  and integration measure

$$\int \mathcal{D}[\phi] = \prod_x \int_0^\infty d\phi(x) \phi^3(x). \quad (6.7)$$

In contrast to the simulations presented in the other chapters, where we used the heat-bath algorithm, it was necessary to fall back on the Metropolis algorithm to generate the 1000 Monte Carlo configurations used for each parameter set. Again center gauge using over-relaxation and center projection are used.

## 6.2 Finite Temperature

We start with calculations at finite temperature  $T$  where it is much easier to study string breaking, as we will see below. At finite temperature, confinement and deconfinement

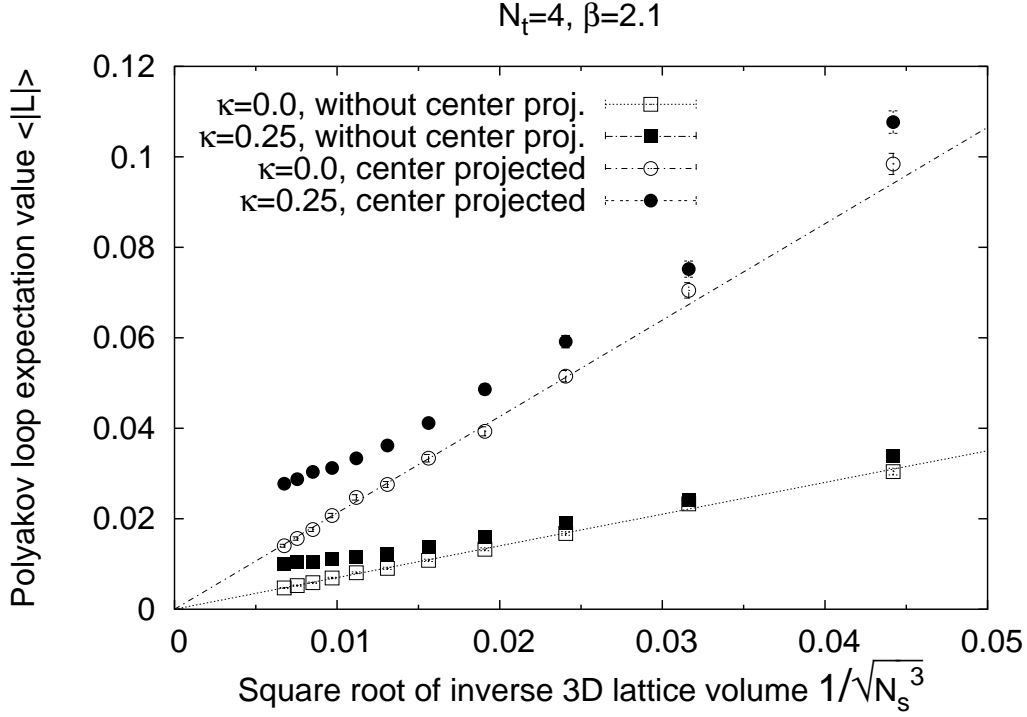


Figure 6.4: Expectation values of the Polyakov loop in the “confined” phase at  $\beta = 2.1$ . Open symbols denote measurements at  $\kappa = 0.0$ , filled symbols at  $\kappa = 0.25$ . Squares are used for measurements on unprojected, full SU(2) configurations and circles for center projected fields.

can be studied using the expectation value of the modulus of the Polyakov loop as defined in section 3.3:

$$\langle |L| \rangle = \left\langle \left| \frac{1}{N_s^3} \sum_{\vec{x}} L(\vec{x}) \right| \right\rangle \stackrel{N_s \rightarrow \infty}{\approx} e^{-F/T} \quad \text{for } N_s \rightarrow \infty \quad (6.8)$$

where

$$L(\vec{x}) := \frac{1}{2} \text{Tr} \prod_{x_4=1}^{N_t} U_4(\vec{x}, x_4) \quad (6.9)$$

and  $F$  is the free energy of a single static quark relative to vacuum at temperature  $T$ . Without dynamical matter fields, we have

$$\lim_{N_s \rightarrow \infty} \langle |L| \rangle = 0 \quad (6.10)$$

in the confined low temperature phase. If matter is included, screening becomes possible. In that case  $\langle |L| \rangle$  is non-zero, and  $F$  is finite, in the large volume limit. This means a single static quark can exist because it is screened by the dynamic matter field.

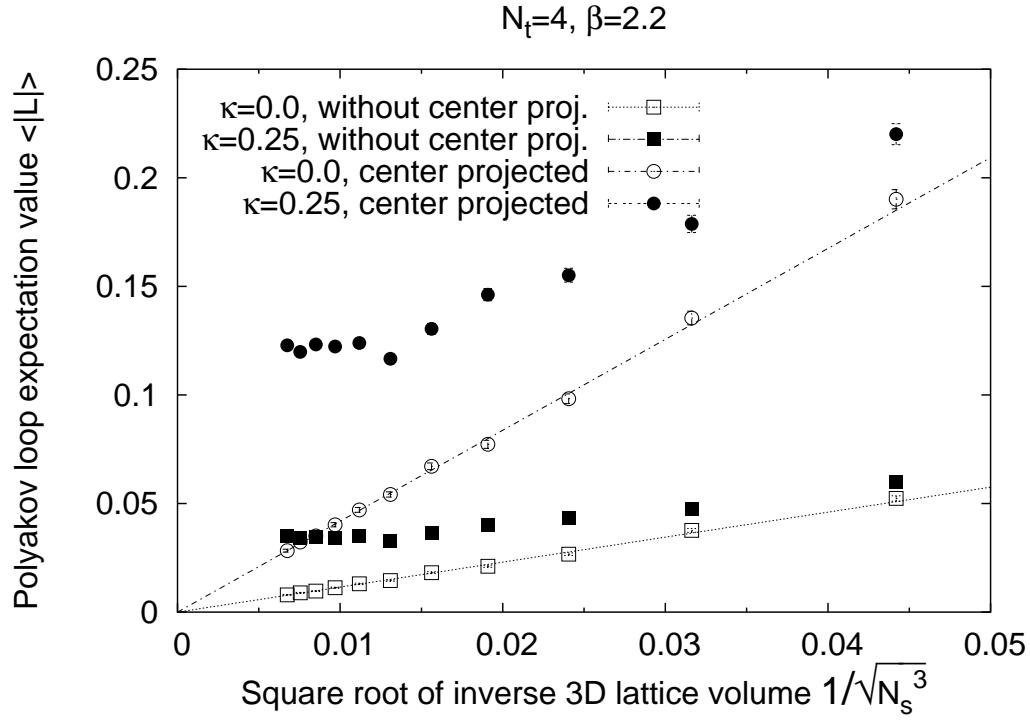


Figure 6.5: Expectation values of the Polyakov loop in the “confined” phase at  $\beta = 2.2$ . Open symbols denote measurements at  $\kappa = 0.0$ , filled symbols at  $\kappa = 0.25$ . Squares are used for measurements on unprojected, full  $SU(2)$  configurations and circles for center projected fields.



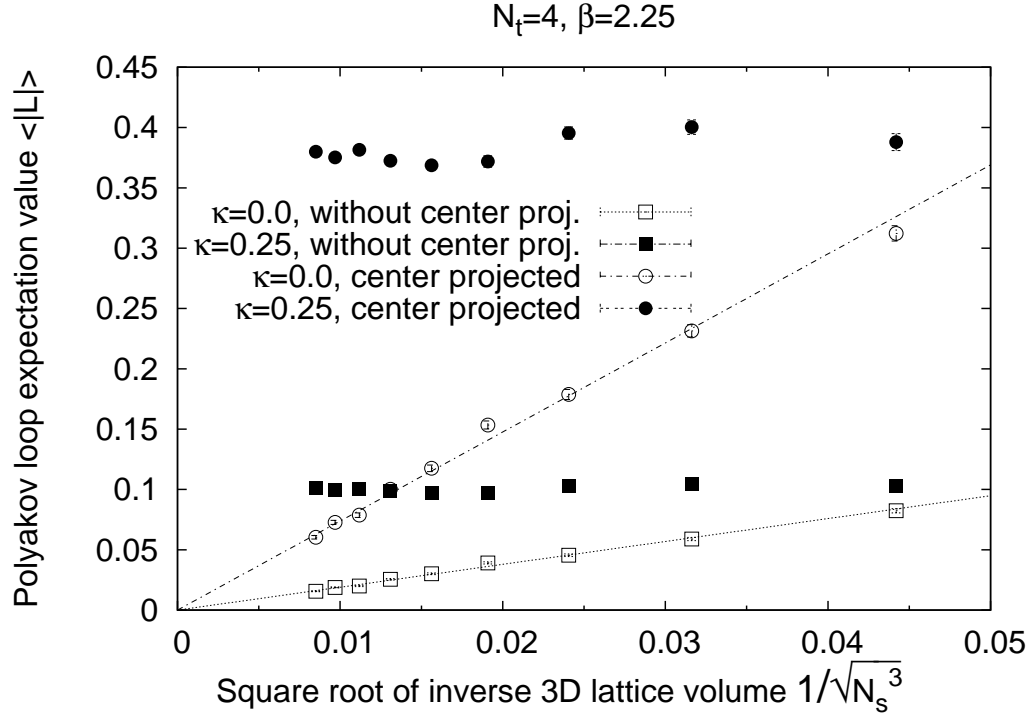


Figure 6.6: Expectation values of the Polyakov loop in the “confined” phase at  $\beta = 2.25$ . Open symbols denote measurements at  $\kappa = 0.0$ , filled symbols at  $\kappa = 0.25$ . Squares are used for measurements on unprojected, full SU(2) configurations and circles for center projected fields.

### 6.3 Zero Temperature

To test whether center dominance holds also in the gauge-Higgs model, we do Monte Carlo simulations without ( $\kappa = 0$ ) and with ( $\kappa = 0.25$ ) the scalar field for various lattice sizes and inverse gauge couplings  $\beta$ , and perform DMCG and center projection. For the quartic coupling we use  $\lambda = 0.5$ . Some results for  $\beta = 2.1, 2.2$  and  $2.25$  are shown in figs. 6.4 to 6.6 on pages 103–105. In this region, as seen in section 5.6, the system is in the low temperature “confined” phase. Clearly for  $\kappa = 0$  the expectation value of  $\langle |L| \rangle$  vs.  $1/\sqrt{N_s^3}$  on unprojected lattices extrapolates linearly to zero in the  $N_s \rightarrow \infty$  limit of infinite spatial volume. In contrast, at finite gauge-Higgs coupling  $\kappa = 0.25$ ,  $\langle |L| \rangle$  tends to a non-zero constant at infinite spatial volume, as expected. This well known result is also found on center projected lattices. Due to suppressed self energy contributions and ultraviolet fluctuations in the projected configurations, the expectation value of the Polyakov loop observable  $\langle |L_P| \rangle$  on projected lattices is larger than the corresponding expectation value  $\langle |L| \rangle$  on unprojected lattices, but the qualitative behaviour of the two observables, in the large-volume limit, is the same. Again for  $\kappa = 0$  the Polyakov loop tends to zero, whereas at  $\kappa = 0.25$   $\langle |L_P| \rangle$  remains finite. Even though the levelling off to a finite values starts at different lattice sizes depending on  $\beta$ , projected and unprojected loops behave in the same way: As can be seen from fig. 6.7 on the next page, the ratio of the projected and unprojected Polyakov expectation values is virtually constant, and nearly independent of both lattice extent  $N_s$  and coupling  $\kappa$  for  $\beta = 2.1, 2.2$  and  $2.25$ .

As mentioned above, without Higgs field at the transition to the deconfined phase  $\langle |L| \rangle$  becomes finite in the large volume limit. This holds also after center projection [DFGO97] and can be explained by vortex polarisation and depercolation, as described in section 5.6. The inclusion of the scalar matter field does not qualitatively change the behaviour of the system in the deconfined phase, as can be seen from the measurements at  $\beta = 2.3$  and  $2.4$  depicted in figs. 6.8 to 6.9 on pages 108–109.

At  $\beta = 2.3$  the Higgs field leads to an increase of  $\langle |L| \rangle$  and  $\langle |L_P| \rangle$ . This increase becomes quickly very small at higher temperatures  $T$  as shows the result at  $\beta = 2.4$  (fig. 6.9). The important result is center dominance. As in the “confined” phase, the projected values are higher than the unprojected ones, but their ratio is almost constant with respect to  $N_s$  as plotted in fig. 6.10 on page 110. Also in the deconfined phase the dependence of the ratio on  $\kappa$  is still weak.

To conclude, at any temperature with or without dynamical matter fields  $\langle |L| \rangle$  and  $\langle |L_P| \rangle$  are in the infinite volume limit either both zero, or both non-zero. This means the confining properties of QCD are again shown to be contained in the center vortex content isolated using DMCG and center projection. In particular, the presence of a dynamical matter field must influence the spatial distribution of P-vortices, in such a way that P-vortex fluctuations no longer bring  $\langle |L_P| \rangle$  to zero in the large volume limit, even in the low temperature regime. This will be discussed below.

### 6.3 Zero Temperature

For the investigations at zero temperature,  $T = 0$ , we have performed simulations for a wide range of the parameters  $\beta$  and  $\kappa$ . In detail, we have generated 800 configurations

### 6.3 Zero Temperature

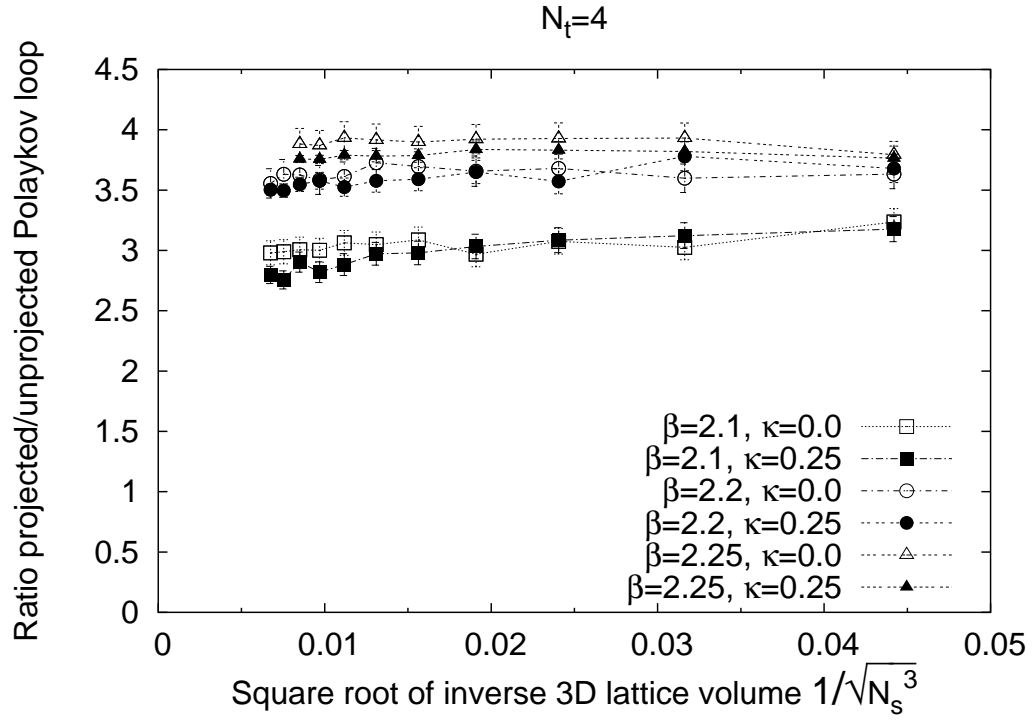


Figure 6.7: Ratio of projected to unprojected Polyakov loop expectation values in the “confined” phase. Open symbols denote measurements at  $\kappa = 0.0$ , filled symbols at  $\kappa = 0.25$ .

### 6.3 Zero Temperature

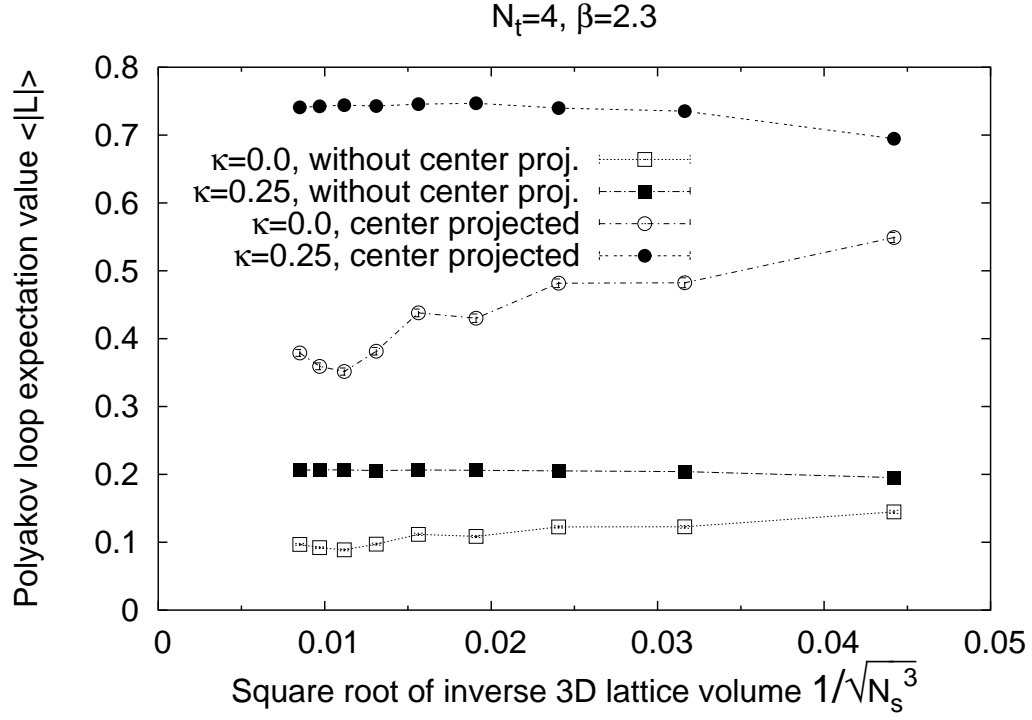


Figure 6.8: Expectation values of the Polyakov loop in the deconfined phase at  $\beta = 2.3$ . Open symbols denote measurements at  $\kappa = 0.0$ , filled symbols at  $\kappa = 0.25$ . Squares are used for measurements on unprojected, full SU(2) configurations and circles for center projected fields.

### 6.3 Zero Temperature

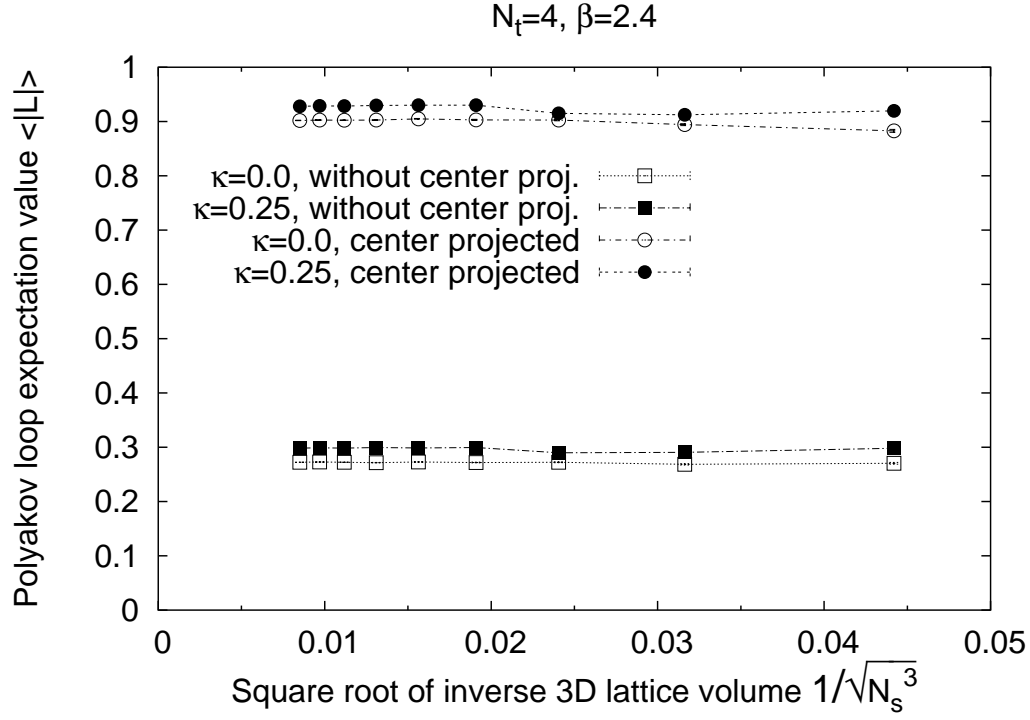


Figure 6.9: Expectation values of the Polyakov loop in the deconfined phase at  $\beta = 2.4$ . Open symbols denote measurements at  $\kappa = 0.0$ , filled symbols at  $\kappa = 0.25$ . Squares are used for measurements on unprojected, full  $SU(2)$  configurations and circles for center projected fields.

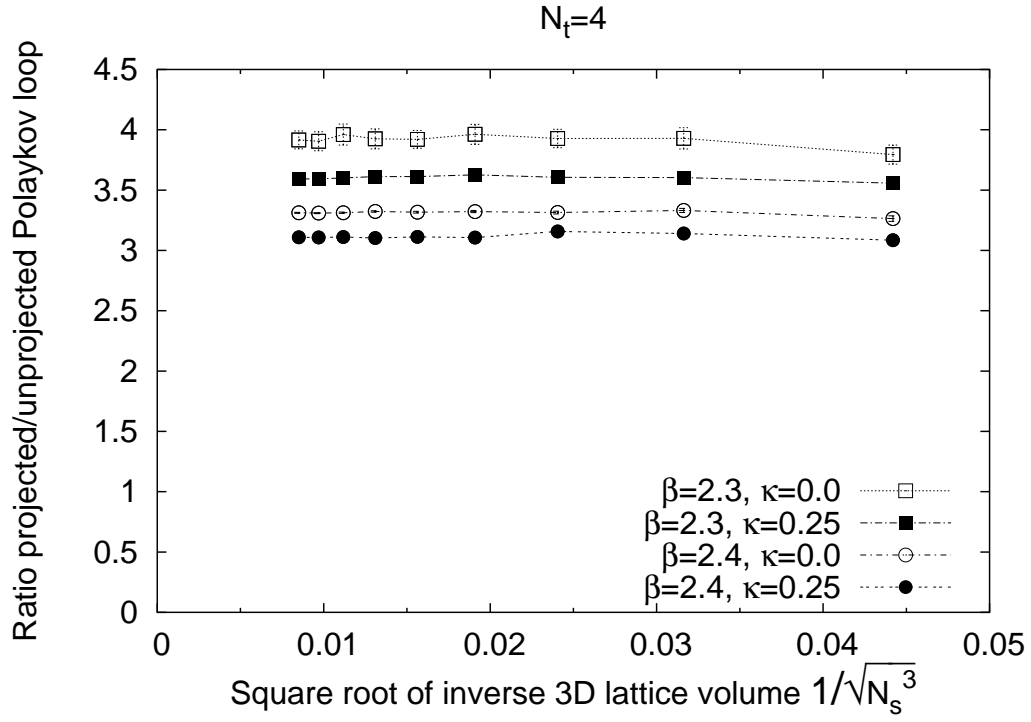


Figure 6.10: Ratio of projected to unprojected Polyakov loop expectation values in the deconfined phase. Open symbols denote measurements at  $\kappa = 0.0$ , filled symbols at  $\kappa = 0.25$ .

### 6.3 Zero Temperature

with  $\lambda = 1.0$  on hypercubic  $10^4$  lattices for  $\beta \leq 1.9$ , on  $12^4$  lattices for  $\beta = 2.1$ , and on  $16^4$  lattices at  $\beta = 2.3$ . For  $\beta = 0.25$ , we have performed a detailed scan over  $\kappa$  on a  $16^4$  lattice in order to look closer at the region below the critical point shown in fig. 6.3 on page 101. Otherwise, we have used the same parameters and methods as for the simulations at finite temperature.

As described in section 3.2, the Wilson loop  $W(I, J)$  gives the static potential  $V(I)$  in the limit of infinite temporal size  $aJ \rightarrow \infty$ . But at finite sizes  $J$  the correct result may be overshadowed by excited states in the expression (3.4) on page 23 due to a small overlap between the true ground state of the configuration of two static charges at distance  $J$ , and the flux-tube state created by the Wilson loop operator (3.7). This is exactly the case for values of  $aI$  beyond the screening distance  $aI > r_0$ . At these values the ground state is described by two isolated static charges, each screened by dynamic light charges. In order to measure string breaking in the “confined” phase using Wilson loops only, very large loops and extremely high statistics are needed.<sup>2</sup>

On the other hand, using more involved observables instead of Wilson loops, it is possible to investigate string breaking with high accuracy. Such investigations have been done by Knechtli and Sommer [KS98, Kne99]. They supplement the Wilson loop by operators such as  $\hat{\Phi}(\vec{x})\hat{\Phi}^\dagger(\vec{y})$ . These operators are modelled on the expected state and generate static charges screened by dynamical Higgs fields. In addition also smoothed versions of these operators are used.

This problem is reflected in the vortex model. All over the “confined” phase, after center projection the influence of the Higgs field on the Wilson loop observable  $W(I, J)$  can be effectively described — for our available small loops  $I, J \leq 4$  — by some shift  $\beta \rightarrow \beta_{eff}$  [BF02]. Consequently we also do not see any notably change in the P-vortex surface properties investigated in chapter 5, because these are tightly connected to the Wilson loop observable. This means that the Wilson loop observable behaves in the same way before and after center projection. No remarkable effect of the matter field was found in both cases – center dominance holds again.

At the transition to the Higgs phase, on the other hand, the string tension measured by Wilson loops disappears even for small distances. At the phase transition line in the gauge-Higgs model a rapid drop in the vortex density  $p$  is observed, as shown in fig. 6.11 on the next page. Here the density of P-vortex plaquettes in percents is plotted as contours in the  $\beta - \kappa$  plane. Data for the phase transition line are taken from [JLNV85]. In the “confined” phase, the vortex density is almost independent of  $\kappa$ , whereas the vortex density decreases rapidly, with increasing  $\kappa$ , in the neighborhood of the phase transition line, a result first reported independently by Langfeld [Lan02] and in [BF02]. Again this result supports center dominance. The loss of the linear rising potential inferred from Wilson loops is in agreement with the suppression of P-vortices. An interesting fact is that this rapid decrease in density appears to extend beyond the actual thermodynamic transition line, which ends in a critical point, as depicted in fig. 6.3 on page 101, further down to the  $\beta = 0$  axis. This phenomenon deserves some more accurate investigation.

---

<sup>2</sup>We note that recently adjoint string breaking has been successfully measured using Wilson loops in [KdF03], using a powerful algorithm for noise reduction devised by Lüscher and Weisz [LW01].

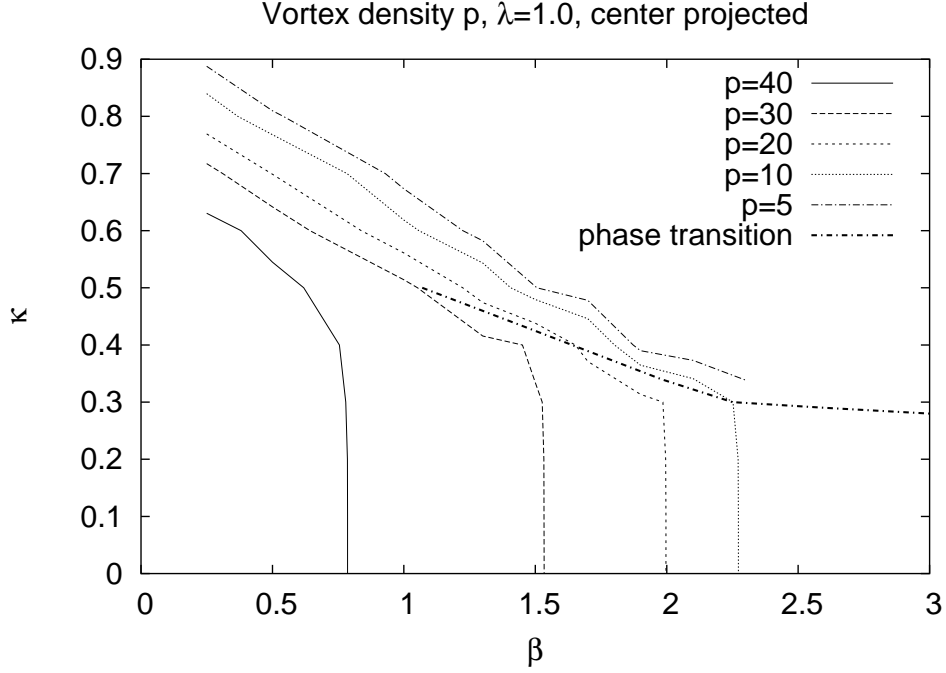


Figure 6.11: P-vortex density  $p$  in the  $\beta - \kappa$  plane. Lattice sizes are indicated in the text. The phase transition line is taken from [JLNV85].

### 6.3.1 The Kertész Line

Whereas thermodynamic observables change to a crossover behaviour below the critical point, the drop of the vortex density  $p$  remains rather sharp even in this region. It was suggested by Langfeld [Lan02] that the crossover line at small  $\beta$ , where there is a sudden drop in the vortex density, could be a “**Kertész line**” of the sort found in the Ising model [Ker89, Sat02]. A Kertész line is a line of percolation transitions which is free of any non-analyticity in the corresponding free energy, and hence is *not* a line of thermodynamic phase transitions, as usually defined. (As mentioned above, there is only one single true thermodynamic phase in the gauge-Higgs model.)

In our case, the “Kertész line” consists of a P-vortex depercolation transition, as can be seen in fig. 6.12 on the next page. This plot shows the data for a  $16^4$  lattice at  $\beta = 0.25$ , a  $\beta$ -value far below the end of the thermodynamic phase transition line around  $\beta = 1$ . We depict depending on  $\kappa$  the following observables:

- The one-link contribution to the gauge-Higgs energy density

$$O_{\text{GH}} := \langle \Re \left[ \Phi^\dagger(x) U_\mu(x) \Phi(x + \hat{\mu}) \right] \rangle. \quad (6.11)$$

This is a local, thermodynamic observable.

- The P-vortex density  $p$ .



### 6.3 Zero Temperature

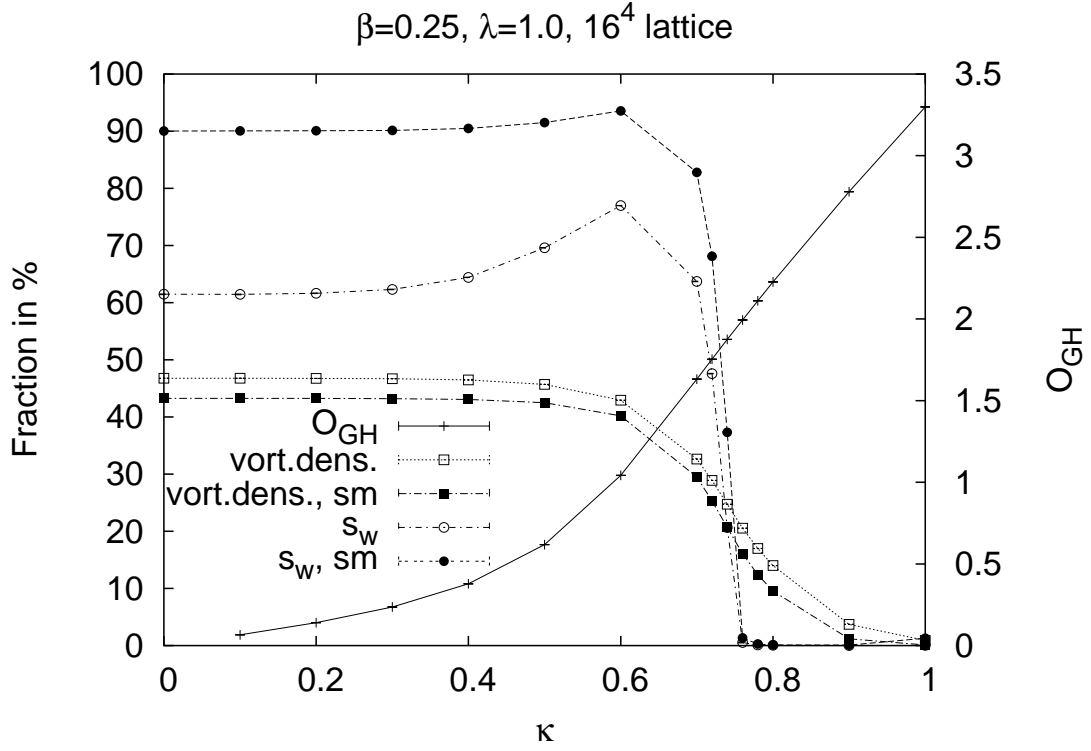


Figure 6.12: P-vortex density  $p$ , weighted average vortex size  $s_w$ , and the one-link gauge-Higgs energy density  $O_{GH}$  for  $\beta = 0.25$ . Open symbols denote measurements after center projection, for filled symbols (labelled with “sm”) elementary vortex cubes are removed using smoothing step a).

### 6.3 Zero Temperature

- The weighted average vortex size  $s_w$ , as defined in (5.11) on page 80. This is a highly non-local observable, and it is the quantity which we use to detect a percolation transition.

Fig. 6.12 clearly shows that the one-link energy density  $O_{GH}$  is a smooth function of  $\kappa$ , and displays no evidence of a transition. The vortex density, although dropping rapidly in the interval  $\kappa \in [0.6, 0.9]$ , see also fig. 6.11 on page 112, shows no sign of any discontinuity, too.

For the evaluation of  $s_w$  we face again the problem that parts of a P-vortex surface may not be reached because vortices touch sometimes along closed lines. As in section 5.4, this occurs usually only along very small lines, and can be cured applying the smoothing procedure introduced in section 5.3. Because smoothing has a bigger impact at lower  $\beta$ , we use only the first smoothing steps a) which removes elementary cubes. We have checked that down to  $\beta = 1.0$  this removal does not modify projected Creutz ratios  $\chi(I, I)$ ,  $I \geq 2$ . In fig. 6.12, unsmoothed vortex observables are depicted using open symbols, whereas filled symbols (labelled with “sm”) denote observables extracted from projected configurations after applying smoothing step a). The smoothing procedure decreases the vortex density  $p$  slightly, but does not qualitatively change the shape of the curve. Smoothed or not, the vortex density decreases continuously from just under 50% to zero as  $\kappa$  increases, with no evidence of any sudden change in phase.

There is, however, a clear sign of a sudden transition, around  $\kappa = 0.74$ , in the weighted average vortex size  $s_w$ . The plot of  $s_w$  in fig. 6.11 on page 112 shows a sharp depercolation transition for this observable. For  $\kappa \leq 0.7$ , the majority of P-plaquettes belong to one big, percolating vortex surface, but for  $\kappa \geq 0.74$ , this surface is split into many small vortices. This is even more pronounced if we remove the smallest (one cube) vortices using the smoothing procedure. After smoothing, but below the transition, the average vortex contains over 90% of all P-plaquettes. Just after the transition, this number drops to under 1.5%. This is a fairly convincing sign of the existence of a percolation transition. Considering the problem of touching vortices, smoothing step a) is able to remove all closed touching lines starting from  $\kappa = 0.8$  which shows that there are really many small separated vortices above the “Kertész line”. (Below  $\kappa = 0.8$  it needs at least smoothing step a)+b) to remove all ambiguities, but even smoothing step a)+b)+c)+d) which changes drastically the Creutz ratios and the P-vortex density cannot break up the dominant vortex surface in this region.)

We have also checked percolation directly, by measuring the spatial extent of the largest vortex surface on the lattice. In the Higgs phase, the largest vortex always fits inside a hypercube which is smaller than the full lattice, while in the “confined” phase this is not possible; the largest connected vortex surface extends through the entire lattice, irrespective of lattice size. Thus we find center vortex percolation in the “confined” phase of the gauge-Higgs theory, and no percolation in the Higgs phase. There is a first-order phase transition line, which has an endpoint in the interior of the  $\beta - \kappa$  plane but then continues as a Kertész line, completely separating these two regions of the phase diagram. This result is not so surprising regarding percolation theory: Either a surface percolates, or it does not. Thus a depercolation transition between two regions cannot

end at some critical point.

## 6.4 Discussion at Conclusions

We have found strong evidence for center dominance in the  $SU(2)$  gauge-Higgs theory, as before in the quenched theory. For finite temperature  $T > 0$ , the Polyakov line observable behaves the same way before and after center projection, both at low and high temperatures, throughout the  $\beta - \kappa$  coupling plane. Polyakov line expectation values  $\langle |L| \rangle$  and  $\langle |L_P| \rangle$ , on the full and projected lattices respectively, are either both zero, or both non-zero, in the infinite volume limit.

Similarly, in the zero temperature case looking at the P-vortex density  $p$  we could reproduce the two regions of the system, namely a “confined” and a Higgs region. The confinement-like region is characterised by an area-law decay of Wilson loops up to a certain string-breaking scale, while in the Higgs-like region there is no area-law falloff at any scale. Using the highly non-local observable  $s_w$ , the average vortex size which is sensitive to percolation, we could show that the thermodynamic phase transition line ending at some critical point can be continued down to the  $\beta = 0$  axis by a “Kertész” line. As in the Ising spin system, the Kertész line is a line of percolation transitions, with the free energy analytic across the transition. It separates the region of P-vortex percolation present in the “confined” phase from the Higgs phase without P-vortex percolation.

We remark that the sharp transition between the Higgs and confinement-like regions has been seen also in other ways. Langfeld [Lan02] has noted that after fixing to Landau gauge, there is a remnant unfixed global symmetry, and that this symmetry is unbroken in the confinement-like phase, and broken across the Kertész line in the Higgs phase. A similar observation, this time in Coulomb gauge, has been made Greensite, Olejník, and Zwanziger in [GO04, GOZ04]. It should be noted that the order parameter for remnant symmetry breaking, if expressed as a gauge-invariant observable, is highly non-local, as is the order parameter for percolation.

On the other hand, there is a significant influence of the Higgs field we could *not* find in the center projected configuration. For  $\kappa > 0$ , but below the phase transition, the static potential is strictly not confining any more, but here occurs string breaking. This is true for any gauge theory with matter in the fundamental representation of the gauge group. However for zero temperature no significant change in the P-vortex properties could be detected with regard to the  $\kappa = 0$  case. Fortunately, this does not contradict the vortex picture: Also for the unprojected configurations it is very hard to see string breaking using Wilson loops only. The vortex mechanism requires that vortex piercings of the minimal area of a Wilson loop are uncorrelated, but percolation alone is not enough to ensure this property. As an example, consider a percolating P-vortex surface having the form of a branched polymer (a form which often arises in numerical simulations of random surfaces). In this case each piercing of a plane surface will be accompanied by a second nearby piercing, with the pair contributing no net center flux, and therefore no net disordering, to the Wilson loop. In this example there is no

confinement, even though the P-vortex percolates throughout the lattice. Percolation is therefore a necessary, but not a sufficient condition for confinement [GR02]. A hint that there is some change in the P-vortex distribution in the “confined” phase for  $\kappa > 0$  is the result for Polyakov loops at finite temperature. The projected loops  $\langle |L_P| \rangle$  is an observable calculated only from P-vortices, and behaves different in the large volume limit depending on  $\kappa = 0$  or  $\kappa > 0$ . But more involved investigations are needed to detect the influence of the scalar matter field on the properties of percolation P-vortices in the “confined” phase of the gauge-Higgs theory.

# 7 Vortices and the Topological Properties of QCD

## Abstract

Interestingly enough, the vortex model is not only suited to describe the confining properties of QCD. In this chapter we use vortices in order to explain the topological properties of chromodynamics. Particularly, we show how the topological susceptibility arises from self intersections of vortex surfaces.

## 7.1 Topological Properties of Yang-Mills Fields

Until this chapter we have used the vortex model essentially to explain confinement. But there are two other important properties of low-energy, non-perturbative QCD, namely

- a) the topological susceptibility and
- b) the spontaneous breaking of the chiral symmetry.

In this chapter we investigate how to treat these other non-perturbative phenomena in the framework of the vortex model. In particular we will show how the topological susceptibility can be calculated from singular points of the P-vortex surface.

The **topological susceptibility** is connected to the topological properties of the SU(2) gauge field. The *topological charge* or *topological winding number* was defined in section 2.1 as

$$Q = -\frac{1}{8\pi^2} \int \text{Tr } \Omega \wedge \Omega; \quad (7.1)$$

written in components it reads

$$Q = -\frac{1}{16\pi^2} \int_{T_4} \text{Tr } \hat{F}^{\mu\nu}(x) F_{\mu\nu}(x) d^4x, \quad (7.2)$$

where the integral runs over all the hyper-torus  $T_4$  which is our base manifold  $M$  due to the periodic boundary conditions.  $\hat{F}^{\mu\nu} = \epsilon^{\mu\nu\alpha\beta} F_{\alpha\beta}$  is the dual of the field strength. In mathematics  $Q$  is known as **Pontryagin index**, in physics also known as a topological quantum number. It is strictly half-integer valued on the hyper-torus; hence SU(2) gauge field configurations can be classed into topological sectors characterised by the value of  $Q$ . Configurations of a sector can be continuously deformed into one another, whereas configuration of two different sectors are not continuously connected in the space of

## 7.1 Topological Properties of Yang-Mills Fields

field configurations. Bear in mind that the half-integer valuedness strictly holds only in the continuum. On a lattice with finite lattice spacing  $a$  all possible gauge field configurations are smoothly connected due to the discreteness of the lattice. Thus we first discuss the continuum. Nevertheless a topological charge can be approximately defined also on the lattice, as discussed below. Finally the topological susceptibility  $\chi_q$ <sup>1</sup> measures the fluctuations of the topological charge in the vacuum and is given by

$$\chi_q = \langle Q^2 \rangle / V, \quad (7.3)$$

where  $V$  is the space-time volume under consideration.

The importance of  $\chi_q$  stems from its relation to the anomaly breaking the  $U_A(1)$  part of the quark flavour symmetry. A consequence of this anomaly is the anomalously large mass of the  $\eta'$  meson, which is directly related to  $\chi_q$  by the Witten-Veneziano estimate [Wit79, Ven79]

$$m_{\eta'}^2 + m_\eta^2 - 2m_K^2 = 2N_f \chi_q / f_\pi^2, \quad (7.4)$$

where  $f_\pi$  is the pion decay constant,  $m_{\eta'}$ ,  $m_\eta$  and  $m_K$  are the masses of the  $\eta'$ ,  $\eta$  and  $K$  mesons, respectively, and  $N_f$  is the number of flavours. Further, the winding number  $Q$  is related through the Atiya-Singer index theorem [AS68a, AS68b] to the exact zero modes of the Dirac operator:  $Q = N_- - N_+$ , where  $N_-$  and  $N_+$  are the number of exact zero modes with negative and positive chirality, respectively. The not exact, but near zero modes are also important for the other important infrared property of QCD mentioned above, the breaking of the chiral symmetry ( $\chi$ SB). The Banks-Casher relation [BC80]

$$\langle \bar{\psi}\psi \rangle = -\pi\rho(0) \quad (7.5)$$

relates directly the quark condensate  $\langle \bar{\psi}\psi \rangle$  to the density  $\rho$  of small eigenvalues  $\lambda$  of the Dirac operator in the limit  $\lambda \rightarrow 0$ .

### 7.1.1 An Interlude about Instantons

As mentioned above, on a discrete lattice all field configurations can be continuously deformed to trivial configurations. There are several methods to get some approximation for  $Q$  on the lattice. One can cool down, i.e. iteratively minimise the action in order to get smooth configurations which cannot be deformed to trivial configurations without considerably increasing the action. Such a cooling leads to interesting topological objects called instantons, which are the ingredients of a model which is able to describe both the topological susceptibility and  $\chi$ SB, the **instanton** model [BPST75, CDG78, Shu82, Shu88, SV93]: Instantons are self-dual solutions for the classical Euclidean Yang-Mills action (2.31); they are the minima for the action in each topological charge sector. In instanton models, gauge field configurations are thought as a gas of localised instantons and anti-instantons, each contributing +1 or -1 to the topological charge. Further, instantons and anti-instantons can overlap and interact, which perturbs the exact zero

---

<sup>1</sup>We use the same symbol for the topological susceptibility  $\chi_q$ , the Creutz ratios  $\chi(I, J)$  and the Euler characteristic  $\chi$ . The subscript  $q$  of the susceptibility  $\chi_q$  and the arguments  $(I, J)$  of the Creutz ratios  $\chi(I, J)$  unambiguously distinguish the three quantities.

modes into a band of near zero modes, yielding via the Banks-Casher relation the quark condensate. Although these instanton models are able to describe chiral properties of QCD, they fail to treat confinement correctly and cannot reproduce the string tension.

## 7.2 Topological Charge from Vortices

Cooled instantons are spread out hyper-spherical objects. This is quite the opposite to the vortex detection procedure. Here the action is concentrated in infinite thin P-vortices. Nevertheless there are results supporting that center vortices are connected both to the topological susceptibility and the breaking of the chiral symmetry. There are indications that P-vortices are found at the position of instantons in configurations created by hand [ADdF00]. This supports the hope that instantons are not genuine objects on Monte Carlo generated configurations, but are created by cooling from thick center vortices. It has been observed [dFD99] that after removing vortices from field configurations (see section 4.2.1), not only confinement is lost, but also the two other important infrared properties of QCD are affected: The configurations are moved into the topologically trivial sector  $Q = 0$ , and chiral symmetry is restored. Center projected configurations yield both at zero and at finite temperature the breaking of the chiral symmetry, as do unprojected configuration [ADdF00, AdFD00]. For the calculation of the chiral condensate from P-vortices we refer to the work of Engelhardt [Eng02]; in this work we will only describe how to extract the topological susceptibility  $\chi_q$  from projected center vortex configurations.

In order to define the topological charge of P-vortices we can start with a configuration in the continuum containing thick vortex of some given finite diameter  $d$  only. For the limit of zero diameter  $d$  we arrive at a configuration of thin  $Z_2$ -vortices in the continuum. Calculating the winding number as (7.2) we get for  $\lim_{d \rightarrow 0} Q$  the expression [Cor98, Cor00, ER00a]

$$Q = -\frac{1}{16} \epsilon_{\mu\nu\alpha\beta} \int_S d^2\sigma_{\alpha\beta} \int_S d^2\sigma'_{\mu\nu} \delta^4(x(\sigma) - x(\sigma')), \quad (7.6)$$

where  $x(\sigma)$  is a parametrisation of the two-dimensional P-vortex surface  $S$  in four-dimensional space-time. Hence P-vortices contribute to  $Q$  at points where vortex surfaces intersect. This definition of  $Q$  can readily be used also for P-vortices on the lattice. Each intersection of two surfaces (or self-intersection of a single surface) gives a contribution of  $\pm 1/2$  in (7.6); in addition there are important contributions of other points [Eng00], which will be discussed below in section 7.3. We will denote all points contributing to  $Q$  as *singular points* of the P-vortex surface henceforth.

It is important to note that the sign of the surface element  $d^2\sigma_{\mu\nu}$  defines an orientation of the P-vortex surface  $S$ . To calculate  $Q$  for a given P-vortex configuration an orientation has to be specified for the vortex surfaces. As discussed thoroughly in section 5.5, P-vortices in the confined phase are unorientable surfaces. This means we cannot assign a single orientation to all of the surface. The surface has to be divided into patches. At the boundaries separating two patches the orientation can flip. These

boundaries can be related to Abelian monopole trajectories [ER00a]. We have seen this already at the discussion of the spherical vortex depicted in fig. 4.16 on page 58 and described section 4.3.5.2: After performing maximal Abelian gauge for some  $U(1)$  subgroup of  $SU(2)$  given by some direction in colour space  $\vec{n}\vec{\sigma}$ , followed by Abelian projection on this subgroup, an Abelian monopole line indicated by a torus in fig. 4.16 is found. Hence the location of the patch boundaries, if associated with Abelian monopole lines, can save some information about the colour structure of the thick vortex even after center projection is performed, and this information might be important for the topological properties of QCD encoded in P-vortices. We will investigate this below.

The expression (7.6) defined in the continuum can be also formulated on the lattice [Eng00] and has been successfully used to reproduce the correct topological susceptibility, first for the model of random vortex surfaces described in section 3.4, then also for vortices detected with center projection [BEF01]. We will describe here the procedure for the latter case.

### 7.3 Topological Charge of P-vortices on the Lattice

Given a P-vortex configuration on the dual lattice, the topological charge  $Q$  cannot be determined immediately using (7.6). The oriented patches and the monopole lines as described above have to be inferred. In principal the indirect version of the maximal center gauge IMCG could be used. As described in section 4.2 this gauge first transforms the  $SU(2)$  configuration to maximal Abelian gauge. Abelian projection reveals the monopole lines. Next gauging towards the center elements using the remaining  $U(1)$  symmetry, followed by center projection yields the P-plaquettes. The monopole lines can then be used as the borders of the oriented patches. However the monopole lines are not guaranteed to lie exactly on the vortex surfaces [DFGO98]. If vortices and monopole lines are detected using the singularities of a Laplacian gauge (section 4.3.3), monopole lines are located exactly on the P-vortex surface, but this method does not succeed to detect the thick vortices of the lattice properly. Fortunately we will find that the topological charge barely depends on the location of monopole lines. Hence we follow a simpler procedure: We just assign to the P-vortex plaquettes some random orientation. Next we iteratively change the orientation of the P-plaquettes of the lattice, one time such as to maximise the density  $\rho_m$  of the monopole lines, one time such to minimise it. The topological charge evaluated for the two cases does not differ within the statistical error, as we will see in section 7.4, where we will explain this result.

The second problem for the calculation of the topological charge  $Q$  are ambiguities due to the coarseness of the lattice. We can distinguish two types of ambiguities: The first one has already been discussed in section 5.4. In contrast to the continuum, where the probability of such an ambiguity vanishes, on the (4-dimensional) lattice surfaces intersect (and touch) not only at points but also at links. In such a situation it is in general not clear which plaquettes sharing such a link are connected, and are locally part of which surface. Because the assignment of plaquettes to surfaces influences the disposition of the oriented patches forming the P-vortex surfaces, and thus the sign of



the contribution to  $Q$ , it is crucial to resolve these ambiguities. In addition for links with 6 P-vortex plaquettes attached there are contributions to  $Q$  not only from isolated points but from all along the links, and the integral in (7.6) diverges. The second type of ambiguities occurs if monopole lines intersect with lattices sites contributing to  $Q$ . At such sites the orientation of the surface is not properly defined, and  $Q$  cannot be evaluated [Eng00]. Because this type is again due to the coarseness of the lattice, such ambiguities appear in the continuum with vanishing probability.

#### 7.3.1 Resolving Lattice Ambiguities

In order to resolve the ambiguities, we deploy a local procedure.

##### Resolving intersections at links

In order to remove singular links, i.e. links with more than two plaquettes attached, a procedure related to the smoothing procedure described in section 5.3 is used. First the P-vortex configuration is transferred to a lattice with  $1/3$  of the original lattice spacing. Next the lattice is scanned for elementary cubes which contain at least one singular link, and successively for each of these cubes an elementary cube transformation is done reducing, if possible, the number of P-plaquettes attached to singular links. If the number of singular links is not changed by the transformation it has proven to be efficient to do elementary cube transformation with a probability of  $1/2$ . The orientation of newly created P-plaquettes is chosen such as to change the number of monopole lines as little as possible. Because the transformation is done at most one time for each cube, the P-vortex surfaces are moved maximal  $1/3$  of an original lattice spacing. Remembering that the position of the thin P-vortex surface within the thick vortex of the unprojected lattice is not significant below the accuracy of a lattice spacing we expect such a small shift not to change important properties of the configuration. In practice it is enough to perform this procedure twice in order to get rid of all singular links, which means we end with a lattice with  $1/9$  of the original lattice spacing.

##### Resolving intersections of monopole lines with singular points

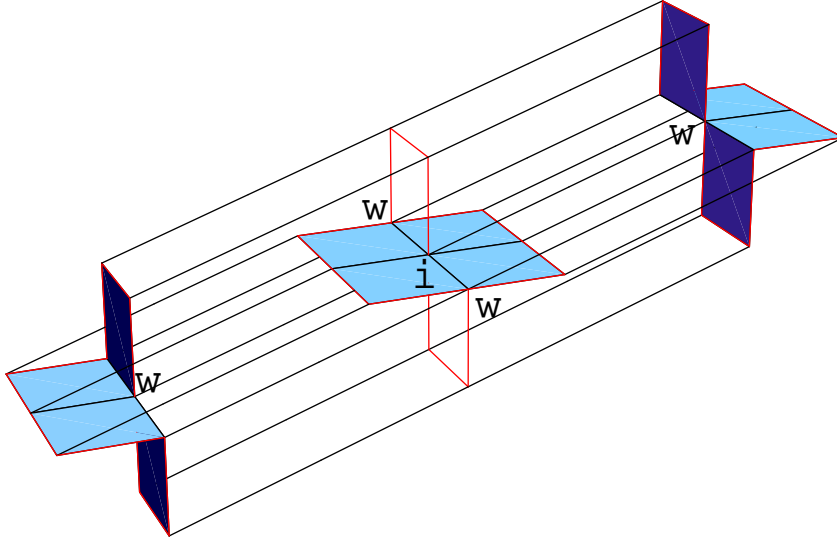
The second type of ambiguities occurs if monopole lines intersect with singular points, and hence the orientation of the surfaces is not well defined at the intersection. This ambiguity is resolved for each singular point independently. First a copy of all the 24 plaquettes attached to the point is made. Starting from randomly selected plaquettes neighbouring plaquettes are reoriented such as to move monopole lines away from the singular point. After this the contribution of the point to  $Q$  can be evaluated.

#### 7.3.2 Types of Singular Points

After removing the ambiguities three different type of singular points can be distinguished. A singular point is here defined as a lattice site where the P-plaquettes span all four directions of the Euclidean space-time and hence can contribute to (7.6):<sup>2</sup>

---

<sup>2</sup>In the continuum singular points can be defined as points of the surfaces where the tangent vectors span all four directions


 Figure 7.1: A  $P$ -vortex with writhing and intersection points.

a **Intersection points**

b **Touching points**

c **Writhing points**

Examples of singular points are depicted in fig. 7.1 which shows a  $P$ -vortex surface introduced first by Engelhardt in [Eng00]. To plot the two-dimensional vortex surface on the four-dimensional lattice we use the procedure described in section 5.1.1. Links in time direction are plotted in some chosen direction of the three-dimensional space spanned by the spacelike directions. The timelike links are plotted longer in order to separate the different time slices. Only E-plaquettes are coloured, B-plaquettes are indicated by the timelike links and by the red colour of space-link links bordering the plaquette. The plotted  $P$ -vortex extends over three timeslices and is a closed surface, as no border can be seen with closer inspection of fig. 7.1. Assuming the absence of monopole lines the  $P$ -vortex is an oriented surface, which means that its contribution to  $Q$  vanishes, as discussed below.

Two of the types of singular points are present in fig. 7.1. Intersection points are lattice sites where two surfaces intersect plainly. The two surfaces are perfectly orthogonal. In fig. 7.1 there is one intersection point, labelled with “i”. One of the surfaces is the horizontal, light blue plane, the other is indicated by the vertical red lines and extends in time direction. The other type of singular points depicted in fig. 7.1 are writhing points. They are points where one surface has tangent vectors in all four direction. The

### 7.3 Topological Charge of P-vortices on the Lattice

four writhing points in fig. 7.1 are labelled with “w”. It can be easily checked that there is indeed only one surface attached to the “w” site. A small loop around the writhing point travels over all P-plaquettes around the site, in contrast to intersection points where the two surfaces are not directly connected by links. All other types of singular points, i.e. points with two involved surface segments, but not having the simple form of intersection points, are in fact touching points. An infinitesimal displacement of one of the surfaces dissolves the singular point and the surfaces are completely separated. As argued in [Eng00], touching points do not contribute to the topological charge. This is not true for writhing points. For example the configuration in fig. 7.1 shows an oriented vortex surface. Such a surface can be represented [Eng00] by a gauge field which is nonzero only on a compact region of space-time [ER00a]. The contribution of such a gauge field to  $Q$  is independent from boundary conditions. Assuming hyper-spheric space-time, the Pontryagin index must be integer valued. Intersection point contributes with  $\pm 1/2$  only. Therefore, writhing points must contribute to  $Q$ , too, and (7.6) has to be replaced by

$$Q = \sum q_n$$

$$q_n = \frac{1}{16} \sum_{i,j=1}^4 \sum_{\mu < \nu} \sum_{\alpha < \beta} \epsilon_{\mu\nu\alpha\beta} Z_{\mu\nu}^{(i)} Z_{\alpha\beta}^{(j)}. \quad (7.7)$$

Here  $Q$  is given as the sum of contributions  $q_n$  from the distinct lattice sites.  $Z$  is  $\pm 1$  depending on the orientation for P-plaquettes, and 0 if a plaquette of the lattice is not a P-plaquette. The indices  $i, j$  label the four plaquettes attached to the site for a given pair of space and time directions  $\mu, \nu$  or  $\alpha, \beta$ . Each pair of mutually orthogonal P-plaquettes attached to a site contributes with  $\pm 1/16$  to  $q_n$  for the site. In agreement with (7.6) this results in a contribution of  $\pm 1/2$  for intersection points. Whereas touching points do not contribute writhing points do. All  $q_n$  sum up to zero for the P-vortex in fig. 7.1 on the previous page. In general, on the hyper-torus given by a lattice with periodic boundary conditions,  $Q$  is quantised in half-integer units in accordance with the result for unprojected configurations [tH79, vB82, GPGAM<sup>+</sup>00]. This is remarkable considering the fact that the individual contributions  $q_n$  from writing points can be as small as  $1/8$ , and in the continuum take even continuous values [Eng00, BEF01].

We note one particular difference between intersection and writhing points: Whereas the contributions of intersection points can change their sign if the orientation of plaquettes change – one of the intersecting surface segments could change its orientation – writhing points are invariant. Since there is only one single writhed surface element involved a change of orientation for one P-plaquette reorients, after applying the ambiguity removal procedure, also all other P-plaquettes attached to the singular point because no monopole line may cross the writhing points (this would be the second type of ambiguity defined above). This feature of writhing points will be revealed to be important in section 7.4.

### 7.3.3 Elimination of Short Range Fluctuations

Having removed all ambiguities the topological charge  $Q$  can be calculated. But as discussed in section 5.3, the thin P-vortex surfaces can fluctuate somewhat within the diameter of the original thick vortices of the lattice. The P-plaquette density is higher than expected from the string tension extracted from Wilson loops. For the treatment of confinement in the center vortex model this is of minor importance since these short range ultraviolet fluctuations cannot contribute to the asymptotic potential. But the fluctuations greatly increase the number of singular points leading to a strong influence on the Pontryagin index  $Q$ . In order to control the short range fluctuations, we have used two independent procedures:

The first one is the vortex surface smoothing procedure presented in detail in section 5.3. In order to estimate which combination of smoothing steps is appropriate, we take into account the following observations: As a local procedure smoothing does not change the asymptotic string tension. But the strongest smoothing step a)+b)+c)+d) lowers Creutz ratios  $\chi(I, I)$  up to  $I = 3$  for inverse couplings  $\beta \leq 2.3$  and seems to have an influence up to intermediate distances, distances where important non-perturbative properties like Casimir scaling (see section 3.4) are visible. Above  $I = 2$  the other smoothing steps have no effect on  $\chi(I, I)$ . At  $\beta = 2.4$  the lattice spacing  $a$  starts to become so small that even the strongest smoothing step does not remove important features.

The other procedure is blocking. This is done by transforming the P-vortex configuration on a coarser lattice with a lattice spacing of  $a' = na$ , where  $n$  is a natural number (we used  $n = 2, 3$  and  $4$ ). To each plaquette of the new coarser lattice corresponds a  $n \times n$  loop on the finer lattice, and we assign to each new plaquette the holonomy of the loop on the original lattice. This means that a plaquette of the coarser dual lattice is a P-plaquette iff the associated plaquette of the coarse normal lattice is pierced by an odd number of P-vortices of the finer lattice. This procedure smooths out all fluctuation below the scale of  $a'$  while preserving the asymptotic string tension  $\sigma$  since Wilson loops of the coarse lattice are the same as the corresponding loops on the finer lattice. As for the smoothing procedure the question arose how strong the blocking should be in order to remove the spurious ultraviolet fluctuations without touching long and middle range information from the P-vortex surfaces. As an upper bound, we can take the average distance of nearest vortices in a plane, which we have estimated in section 5.7 to be about 0.6 fm, as a target value for  $a'$ . The ultraviolet correlations of the vortex surfaces measured in [ELRT98] and described in section 5.3 are present up to  $0.4 \pm 0.2$  fm. We conclude that the target lattice spacing  $a'$  should be somewhere in the range of 0.4 – 0.6 fm.

## 7.4 Numerical Measurements and Discussion

After presenting all elements, the procedure to calculate the topological charge  $Q$  from P-vortices can be summarised as follows:

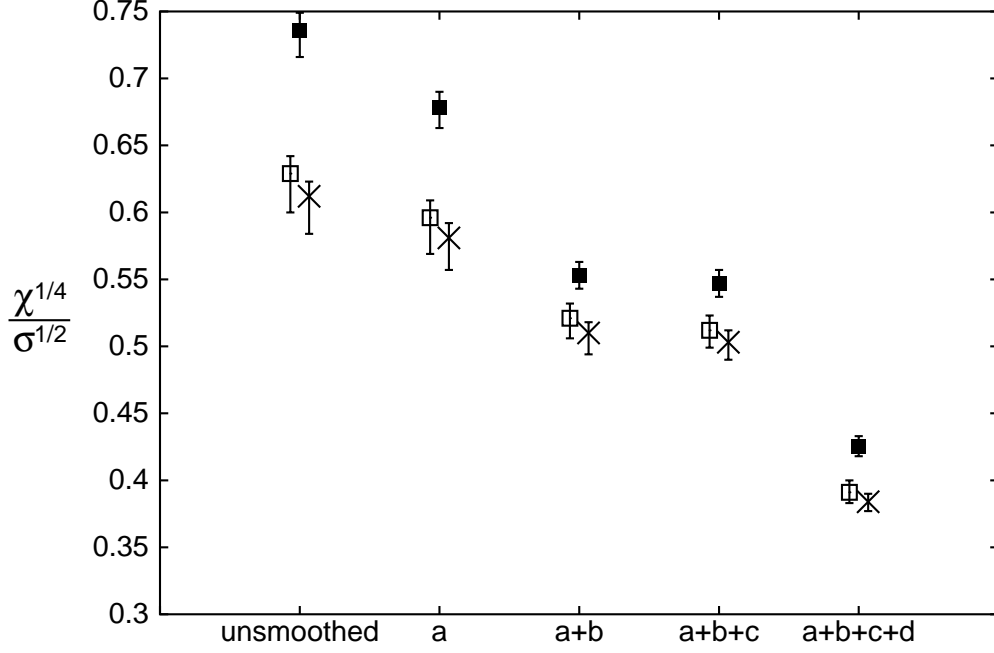


Figure 7.2: Fourth root of the topological susceptibility  $\chi_q$  from P-vortices, in units of the square root of the string tension  $\sigma$  depending on the performed smoothing steps. Open squares correspond to  $\beta = 2.3$  on a  $12^4$  lattice, crosses to  $\beta = 2.3$  on a  $16^4$  lattice, and filled squares to  $\beta = 2.5$  on a  $16^4$  lattice. Error bars are discussed in the main text.

- Generate an ensemble of SU(2) gauge field configurations on the lattice using Monte Carlo techniques.
- Transform the configurations to the maximal center gauge and perform center projection. The gauging is done using over-relaxation with 6 gauge copies, which gives good results for the string tension  $\sigma$  as discussed in section 4.4.
- Remove ultraviolet fluctuations of the center projection vortex surfaces by either blocking or smoothing, see section 7.3.3.
- Randomly assign orientations to the P-plaquettes such to either maximise or minimise the monopole line density  $\rho_m$ , see section 7.3.
- Remove ambiguities in the vortex surfaces, i.e. lines along which vortices intersect and monopole lines coinciding with singular surface points, see section 7.3.1.
- Evaluate the topological charge  $Q$  carried by the singular points as described in section 7.3.2.

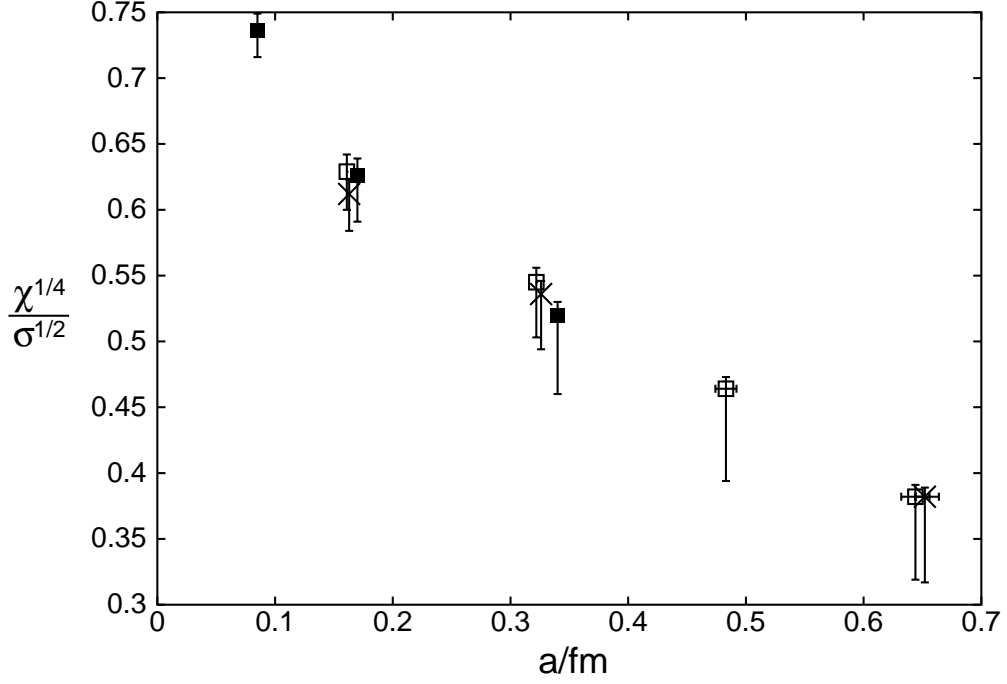


Figure 7.3: Fourth root of the topological susceptibility  $\chi_q$  from P-vortices, in units of the square root of the string tension  $\sigma$  depending on the blocked lattice spacing  $a'$ . Open squares correspond to  $\beta = 2.3$  on a  $12^4$  lattice, crosses to  $\beta = 2.3$  on a  $16^4$  lattice, and filled squares to  $\beta = 2.5$  on a  $16^4$  lattice. Error bars are discussed in the main text.

Our results for the topological susceptibility  $\chi_q$  are depicted in figs. 7.2 to 7.3 on pages 125–126 for various values of  $\beta$ , and after applying smoothing or blocking. In order to compare the result for different values of  $\beta$  we scale the susceptibility with the string tension  $\sigma$  inferred from Creutz ratios and plot the dimensionless quantity  $\sqrt[4]{\chi_q}/\sqrt{\sigma}$ .

The vertical error bars are compound from three sources: The statistical error from the susceptibility measurement, the statistical error from the string tension measurement, and a systematic uncertainty stemming from the removal of vortex surface ambiguities. This systematic error is estimated as follows: It can be checked that the ambiguity removal procedure systematically increases the density of P-vortices  $p$ . We take this change of density as a measure for the change of the topological susceptibility  $\chi_q$ . Due to the dimensions of the two quantities we estimate this error for  $\chi_q$  to depend quadratic on the variation of  $p$ . Because the ambiguity removal procedure increases  $p$  we compound the calculated error only into the downward uncertainty of the measurements plotted in figs. 7.2 to 7.3. Thus as can be seen for the blocked configurations in fig. 7.3, the downward error bar is always larger than the upward error bar. Clearly the systematic error surpasses the statistical one. Blocking to a coarser lattices increases the vortex density measured in lattice units which leads to more singular links, which have to be removed again by a strong use of the ambiguity removal procedure. In contrast the systematic error is very small after applying the smoothing procedure, as can be seen from the small difference between the upward and the downward error bars plotted in fig. 7.2 on page 125. This result is not surprising at all: As we have seen in section 5.4, the smoothing procedure firmly suppresses touching (and intersecting) of P-vortices along closed lines. This touching is nothing else but the occurrence of a particular type of singular links. After smoothing only a few of the singular links are left, and are treated by the ambiguity removal procedure. In addition to these errors for  $\chi_q/\sigma^2$ , fig. 7.3 shows also horizontal error bars. These come from the statistical error in the lattice measurement of the string tension  $\sigma$  which was used to calculate the lattice spacing  $a$  using (5.6) on page 71.

Before discussing the results for  $\chi_q$  we have to consider an additional ambiguity. As written in section 7.3 the orientation of the patches building the P-vortex surface, and thus the associated monopole lines, are not inferred by some procedure from the unprojected configuration but assigned in a random way. To control the influence of the monopole lines all measurements have been done twice, one times maximising and one times minimising iteratively the density of the lines. The results reported in figs. 7.2 to 7.3 on pages 125–126 were obtained after maximising the monopole density  $\rho_m$ . If one instead minimises  $\rho_m$  the values for  $\sqrt[4]{\chi_q}/\sqrt{\sigma}$  vary by at most 1%, which is negligible compared with the statistical and systematic errors. The topological susceptibility seems to independent from  $\rho_m$ . This result has to be contrasted with the large variation of  $\rho_m$  itself depicted in figs. 7.4 to 7.5 on pages 128–129. For comparison, the zero-temperature monopole line density measured for the full  $SU(2)$  lattice gauge theory in maximal Abelian gauge amounts to  $\rho_m^{(mag)} = 64 \text{ fm}^{-3}$  [BIL<sup>+</sup>91].

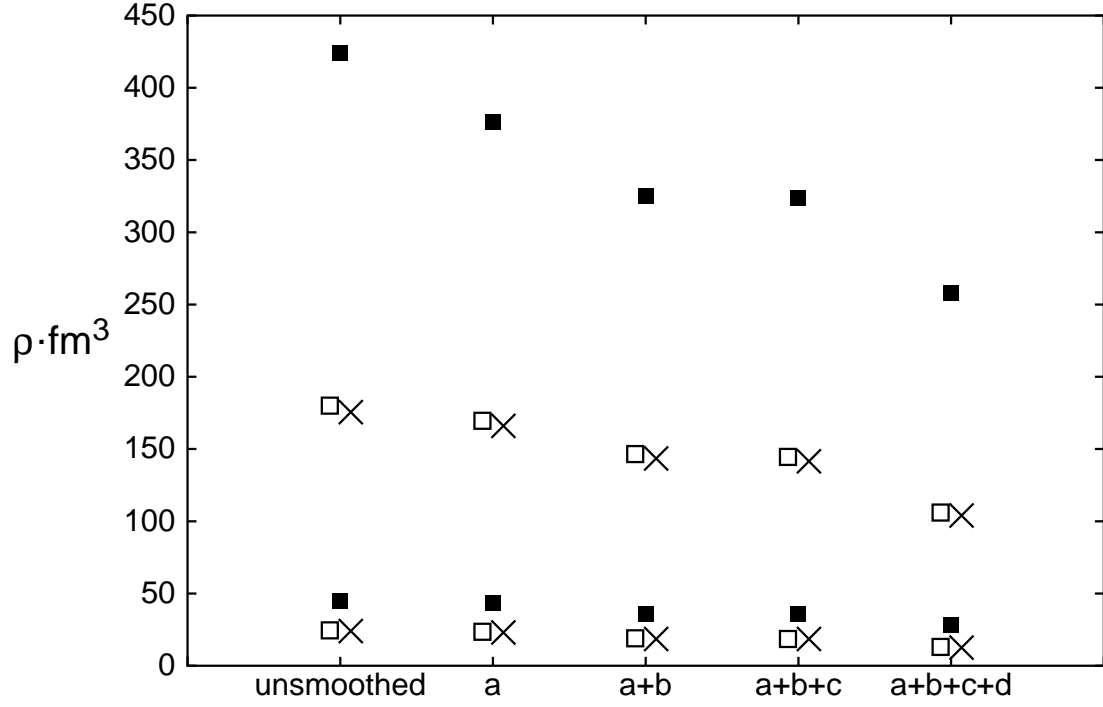


Figure 7.4: Monopole line density  $\rho_m$  depending on the smoothing step. For each point on the horizontal axes, both the maximal and the minimal densities reached by the reorientation procedure of section 7.3 are shown. Open squares correspond to  $\beta = 2.3$  on a  $12^4$  lattice, crosses to  $\beta = 2.3$  on a  $16^4$  lattice, and filled squares to  $\beta = 2.5$  on a  $16^4$  lattice. Error bars are negligible.



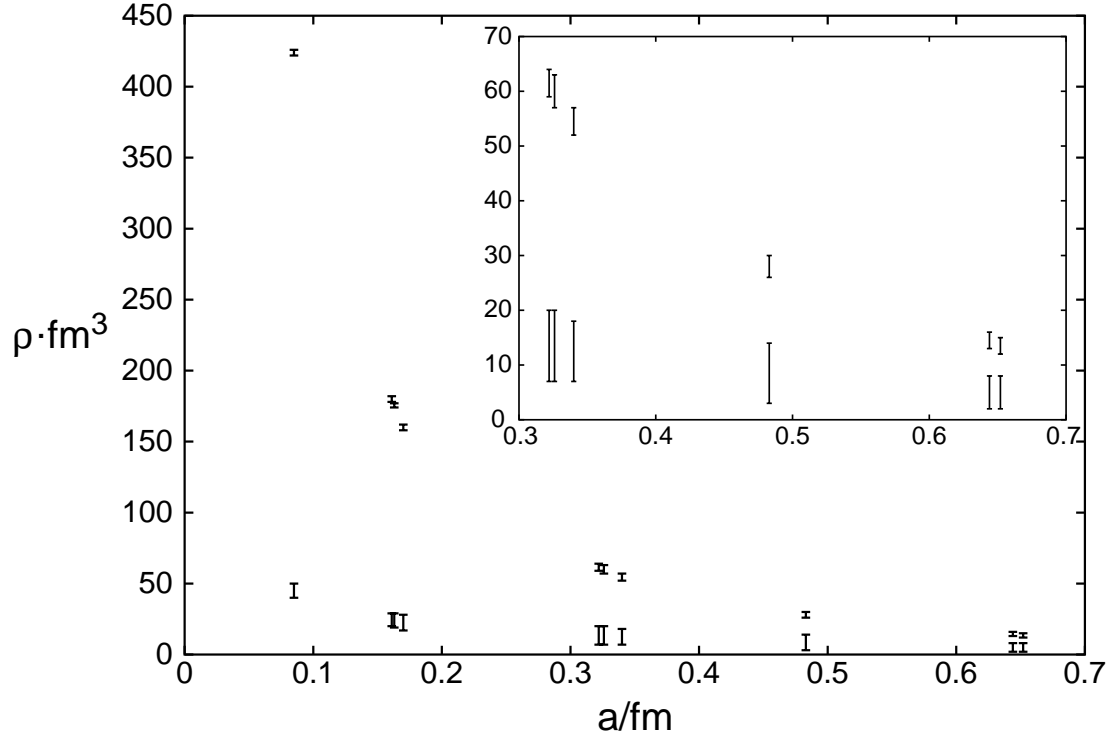


Figure 7.5: Monopole line density  $\rho_m$  depending on blocking and  $\beta$ . For each point on the horizontal axes, both the maximal and the minimal densities reached by the reorientation procedure of section 7.3 are shown. The error bars indicate the rise induced by the ambiguity removal procedure. To associate the data points with the values for  $\beta$  and for the lattice size, compare them with the data in fig. 7.3 on page 126 which have the same ordering. The inset is simply an enlargement of the range  $a \in [0.3 \text{ fm}, 0.7 \text{ fm}]$ .

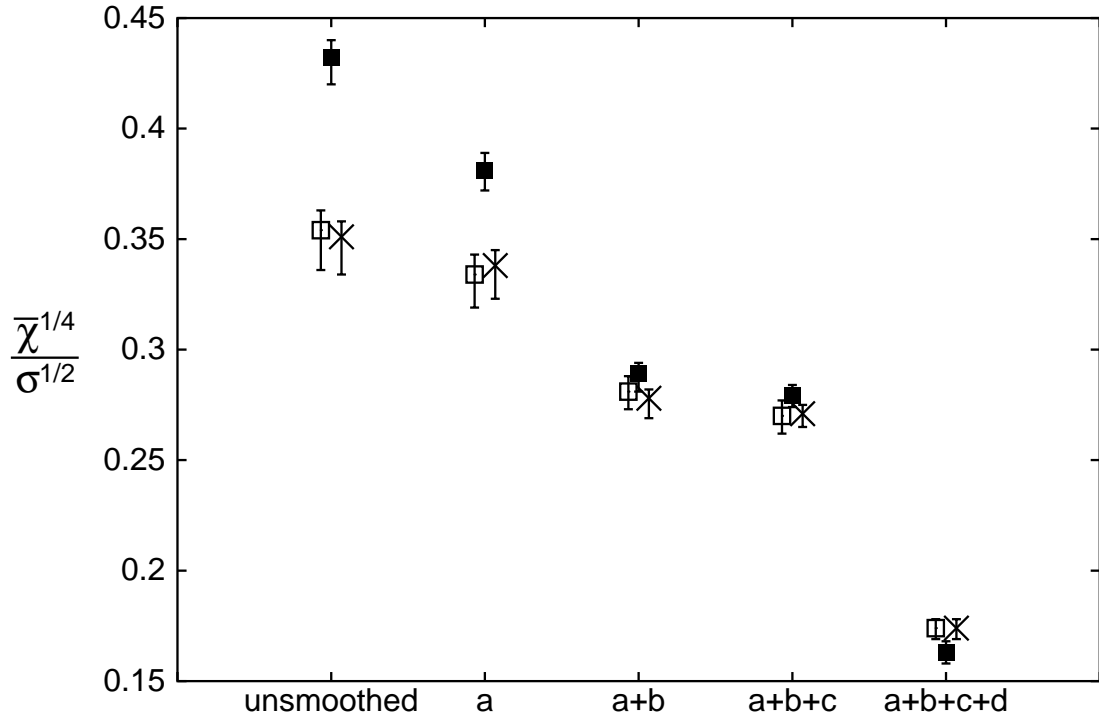


Figure 7.6: Fourth root of the truncated topological susceptibility  $\bar{\chi}_q$  from P-vortices depending on the performed smoothing steps. The results were obtained by taking into account only the contributions from intersection points. The plot is done the same way as in fig. 7.2 on page 125.

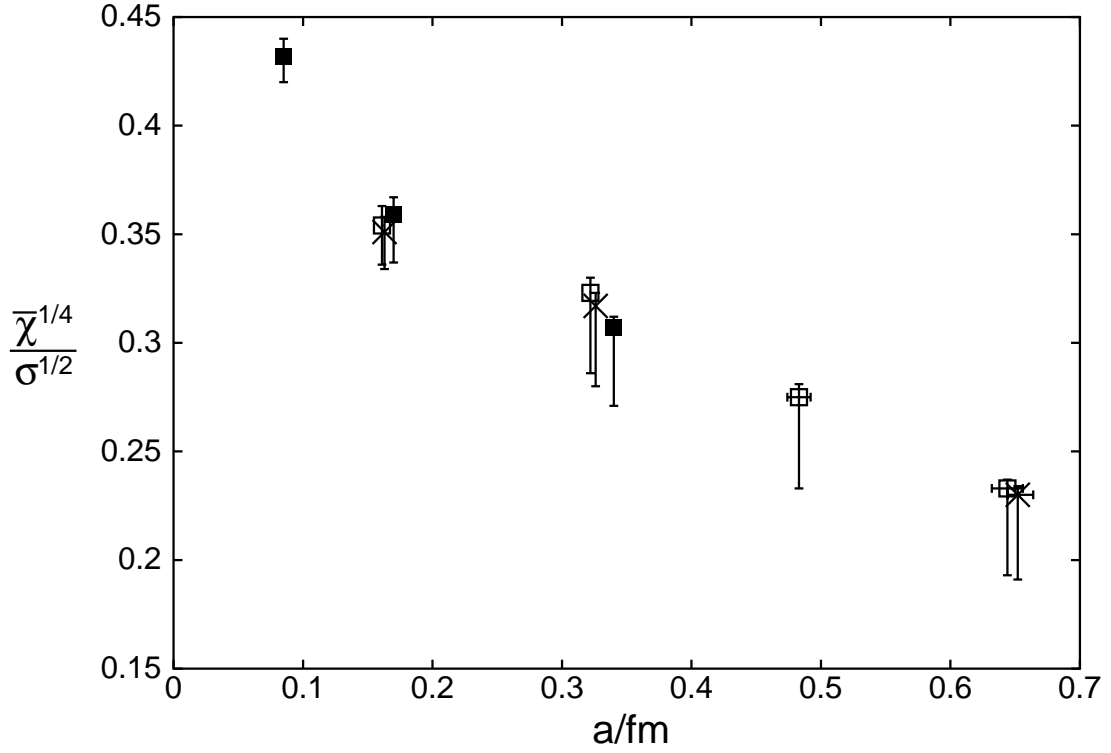


Figure 7.7: Fourth root of the truncated topological susceptibility  $\bar{\chi}_q$  from P-vortices depending on the blocked lattice spacing  $a'$ . The results were obtained by taking into account only the contributions from intersection points. The plot is done the same way as in fig. 7.3 on page 126.

This result has also been observed in the random vortex surface model introduced by Engelhardt [Eng00]. It can be explained analysing the contributions  $q_n$  to the topological charge  $Q$ . The main part stems not from intersection points but from writhing points. In order to separate the contribution of intersection and of writhing points, in figs. 7.6 to 7.7 on pages 130–131 the truncated topological susceptibility  $\bar{\chi}_q$ , which is calculated from the contributions of intersection points only neglecting writhing points, is depicted.<sup>3</sup> Comparing these results with the analogous data shown in figs. 7.2 to 7.3 on pages 125–126 we see that  $\sqrt[4]{\bar{\chi}_q}$  is roughly half as large as  $\sqrt[4]{\chi_q}$ , which means that the truncated susceptibility is suppressed with a factor of  $2^4 = 8$  compared to the result including contributions from writhing points. Now as already shown in section 7.3.2, the dominant contribution from writhing points is not affected by reorientations of patches and shifts of monopole lines. But this is not the full story. The results depicted in figs. 7.6 to 7.7 on pages 130–131 were again obtained after maximising the monopole line density  $\rho_m$ . Minimising the density instead changes the result not more than 5%, which lies inside the statistical uncertainty. This reveals that even the contribution of the intersection points is rather insensible to the density of monopole lines. To explain this result we note that even minimising  $\rho$  cannot remove the density completely. Due to the inherent unorientability of the P-vortex surface in the confined phase reported in section 5.5 there is always a lower bound for the density of monopole lines. Evidently already this minimal density suffices to randomise the signs of the intersection point contributions to the topological charge  $Q$  to such an extent that additional random changes of the signs, induced by adding monopole loops on the P-vortex surfaces, cannot strongly influence the associated topological susceptibility any more. These results show that the topological susceptibility  $\chi_q$  can be evaluated from P-vortex configurations without caring for the density and position of monopole lines.

Having treated all ambiguities the task remains to determine the correct value for  $\chi_q$  from the calculations presented in figs. 7.2 to 7.3. Looking first on fig. 7.3, we remember from the discussion in section 7.3.3 that we estimate the desired blocked lattice spacing  $a'$  to be in the range of 0.4 – 0.6 fm. This gives for the limits taking in account also the error bars

$$(150 \text{ MeV})^4 \leq \chi_q^{(phys)} \leq (224 \text{ MeV})^4 \quad (7.8)$$

using  $\sqrt{\sigma} = 440 \text{ MeV}$ . The results using smoothing in order to remove the ultraviolet fluctuations are depicted in fig. 7.2 on page 125; at  $\beta = 2.3$  the correct value should lie between the results gained by applying the combined smoothing steps a)+b)+c) and a)+b)+c)+d), respectively. Thus we get for the limits in the extreme cases admitted by the error bars

$$(166 \text{ MeV})^4 \leq \chi_q^{(phys)} \leq (230 \text{ MeV})^4. \quad (7.9)$$

This is nicely consistent with the value  $\sqrt[4]{\bar{\chi}_q} = (187 \pm 3) \text{ MeV}$  (only statistical error quoted) obtained at  $\beta = 2.5$  with smoothing steps a)+b)+c)+d). As discussed for these parameters the Creutz ratios  $\chi(I, I)$  with  $I \geq 2$  are not decreased any more.

---

<sup>3</sup>Of course the topological charge  $\bar{\chi}_q$  inferred only from writhing points does not fulfil the requirement of half-integer valuedness as discussed in section 7.3.2. We use it only to distinguish the effects of the different types of singular points and do not assign further some topological meaning to  $\bar{\chi}_q$ .

## 7.5 Local Correlations

The limits for the topological susceptibility  $\chi_q$  reported above are in good agreement with the values gained using a completely different procedure, namely cooling of unprojected SU(2) gauge field configurations as described in section 7.1.1. As reported in [Sta00] these results give a range of

$$(191 \text{ MeV})^4 \leq \chi_q^{(phys)} \leq (208 \text{ MeV})^4, \quad (7.10)$$

which lies roughly in the middle of the limits obtained from P-vortices. All in all, while considerable systematic uncertainties are inherent in all the steps starting from the SU(2) configurations followed by gauging, projection and ambiguity removal, the result indicates that not only the confining properties of the gauge theory, but also the topological properties can be described reasonably in the framework of the vortex model.

## 7.5 Local Correlations

We have successfully shown that the topological susceptibility  $\chi_q$  can be inferred from P-vortex configurations with reasonable accuracy. Comparing  $\chi_q$  from P-vortices with results obtained using other methods, such as cooling, shows compatible values. These values are expectation values, i.e. averaged over many Monte Carlo generated gauge field configurations. Now the interesting question arises whether the different methods agree not only on average, but for each distinct configuration.

As a first test, we correlate the topological charge  $Q$  calculated from cooled unprojected configurations with  $Q$  evaluated from the same configurations after DMCG and center projection using (7.6). We find a negligible correlation, which is quite natural: The topological charge  $Q$  is the result of the remainder of the cancelling of positive and negative local contributions to  $Q$ . This is true both for P-vortices, and for the calculation from instantons. The local contributions fluctuate from configuration to configuration with both methods such that the fluctuation of  $Q$ , the topological susceptibility  $\chi_q$  (7.3), is in good agreement. But we cannot expect that on a large lattice these fluctuations cancel and sum up to the same value for both methods.

Therefore in a next step we did rather look at local correlations. To this end we correlate for each Monte Carlo generated configuration the topological charge density

$$q(x) = \text{Tr} \left( \hat{F}^{\mu\nu}(x) F_{\mu\nu}(x) \right) \quad (7.11)$$

from the unprojected configurations with the contributions  $q_n$  (7.7) to the topological charge from P-vortex surfaces. Unfortunately both  $q(x)$  and  $q_n$  are plagued with ambiguities and imponderableness. As already described in section 7.1.1, on the lattice the topological charge  $Q$  is not well defined. For highly excited fields on the lattice  $Q$  is not quantised, and the density  $q(x)$  is overshadowed by short-range fluctuation, and is thus not localised and not correlated to the point-like contributions  $q_n$ .

A well established method to extract  $Q$  is cooling of the configurations towards instantons, which are also localised objects on the lattice, as described in 7.1.1. This smoothing is done using a iterative procedure monotonous which decreases the action.

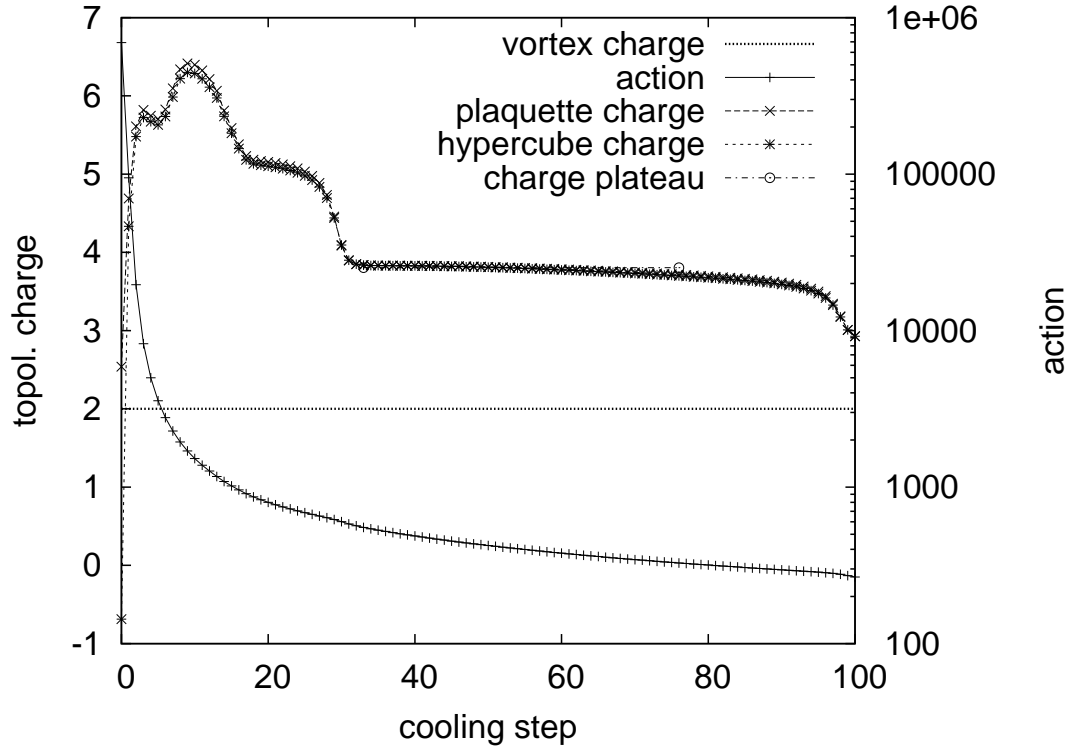


Figure 7.8: Detecting plateaus of the topological charge  $Q$  depending on the cooling step. For comparison the charge  $Q = 2$  evaluated from P-vortices is plotted, too. For the charge from the unprojected configuration, two different lattice definitions for  $Q$  are used; they agree quite well. The first  $\sim 15$  cooling steps decrease the action quickly; afterwards the topological charge which was a continuous quantity without cooling shows plateaus of constant charge, separated by quick transitions between the topological sectors.

The problem of this method is that finally after enough cooling steps on the lattice the configurations are always cooled down to a trivial field, a pure gauge. A solution is to look for plateaus in the topological charge, as depicted in fig. 7.8 on the previous page. Here we show the action and the topological charge depending on cooling for a configuration on a  $24^4$  lattice at  $\beta = 2.5$ . For the calculation of the topological charge  $Q$  (7.2), two distinct lattice definitions, the plaquettes and the hypercube definition, are used, and they agree pretty well. The first  $\sim 15$  cooling steps rapidly lower the action. At the same time  $Q$  changes in a non quantised, continuous way. For highly disordered configurations the topological sector of the configuration is not well defined. But soon the field becomes smooth, and there arise plateaus of constant charge, separated by quick transitions between the topological sectors. There is some ambiguity at which cooling step a stable instanton configuration is reached; the used algorithm searches for ranges of cooling steps where  $Q$  only changes within some threshold for a given number of cooling steps. Such a found plateau is labelled as “charge plateau” in fig. 7.8 on the preceding page.

Although localised, instantons are extended objects with a smeared charge density  $q(x)$ , whereas the contributions  $q_n$  inferred from P-vortices are point-like. In order to get sensible correlations between the two quantities, we smear out also  $q_n$  using various methods. Because the lattice on which  $q_n$  is given has been transferred to a finer one with up to  $1/9$  of the original lattice spacing, and / or have been blocked to remove ambiguities as described in section 7.3.1, first both configurations have to be blocked such that they are on the same lattice. Next one or both configurations are folded with some test function, e.g. a Gaussian function, in order to smear out  $q_n$ . Because the sign of the  $q_n$  is arbitrary due to the randomness in assigning monopole lines to the P-vortex surface (see section 7.3), we correlate  $|q(x)|$  and  $|q_n|$  or  $q^2(x)$  and  $q_n^2$ .

The result is rather poor. We have done excessive studies using a wide range of values for the different parameters such as smoothing steps and blocking, coupling constants, lattice sizes, test function for smearing, parameters controlling cooling, and more. The best we find are correlations of about 4%, and we see no systematic dependence of this poor correlation on the used parameters. We think that there is, apart from all the ambiguities present in evaluating  $q(x)$  and  $q_n$ , a deeper reason for the failure in correlating the topological charge densities from P-vortices and from cooled instantons. Both radically change the Monte Carlo generated field configurations, which are, according to the vortex model, dominated with regard to long-range physics by thick, intersecting center vortices. Center gauge and center projection concentrate the action into infinitesimal thin P-vortex surfaces, whereas cooling yields extended, hyper-spherical instantons. Both are non-local operations which are able to considerably move around the topological charge densities on the lattice, and thus destroy the correlation.

We have some evidence for this explanation considering a configuration of thick vortices set up by hand. It consists of a spherical vortex as introduced in section 4.3.5.2, which is intersected at the north and south pole by a plain vortex as described in section 4.3.5.1. This configuration gives two contributions of  $+1/2$  for each intersection, which sum up to  $Q = 1$ . Cooling shows two lumps of topological charge density which move away from the intersection region during the cooling procedure. Hence the density

### 7.5 Local Correlations

is badly correlated with the contributions after center projection which are of course exactly at the middle of the intersections of the thick vortices present on the unprojected lattice. We remark that this result does not contradict findings [KHK<sup>+</sup>02] that instantons are well correlated with low-lying eigenmodes of the Wilson-Dirac operator, evaluated on the uncooled lattice. Both the evaluation of the cooled  $q(x)$  and of  $\bar{\psi}\psi$  are non-local operations, and at least for our vortex configuration set up by hand both densities are correlated, but away from the intersections of thick vortices carrying  $q(x)$  on the original, unprojected and uncooled configurations.

All in all, we conclude that it is possible to describe not only the confining properties, but also the topological properties of SU(2) gauge theory in a satisfying way within the vortex model.



## 8 Conclusions and Outlook

The main focus of this work was the investigation of center vortices detected in Monte Carlo generated lattice gauge field configurations. The most widely used method to identify vortices in field configurations is a combination of two steps. First, an appropriate gauge is chosen which should help to isolate most of the non-perturbative, long range content of the configuration. Then center projection is performed. This discards all non center degrees of freedom and yields a  $Z_N$  gauge theory, where  $Z_N$  is the center of the gauge group  $SU(N)$ . We mainly worked with the group  $SU(2)$ . The excitations of the  $Z_N$  gauge theory are thin P-vortices which have the shape of closed two-dimensional surfaces on the dual four-dimensional space-time lattice.

In chapter 4, we have performed detailed numerical studies in order to test whether the inferred P-vortices correspond to the thick vortices present in unprojected configurations. We show that for the maximal center gauge (MCG) one has to take care of the used parameters. Especially large enough lattices have to be used to avoid finite size effects. We could demonstrate that the relevant degrees of freedom are contained in the obtained P-vortex configurations. Because MCG is supposed to fail in the continuum limit, the alternative Laplacian center gauges (LCG) have been investigated. In hand-made configurations we demonstrated how LCG identifies vortices. In particular we could prove that thick vortices are associated with singularities of the Laplacian gauges. This method does not work for Monte Carlo generated configurations, though. Because of the strong localisation of the eigenfunctions of the Laplace operator, the detected vortices contain perturbative fluctuations overshadowing the degrees of freedom relevant for confinement. There are different proposals to overcome these shortcomings, but despite the convincing success of different vortex detection methods there is still no undisputed way to isolate vortices under all circumstances.

Having shown that it is possible to extract the vortex content from field configurations, we investigate the properties of the detected P-vortex surfaces in chapter 5. We have found that in the confined phase the four-dimensional lattice is penetrated by a single huge P-vortex of very complicated topological structure. This huge P-vortex is a closed surface on the dual lattice which is unorientable and has many ( $\sim 10/\text{fm}^4$ ) handles. Using a smoothing procedure we could remove from these surfaces spurious fluctuations caused by the coarseness of the lattice. The resulting vortex structure is in good agreement with the required properties in order to explain quark confinement. The density of vortices does not vanish in the deconfined phase, but a strong space-time asymmetry is found. P-vortices at finite temperature are mainly composed of space-space plaquettes forming timelike surfaces on the dual lattice. These surfaces are closed via the periodicity of the lattice in the time direction, they are orientable, and have the topology of a torus, i.e. genus  $g = 1$ . This space-time asymmetry of P-vortices in the

deconfined phase nicely reflects the properties of the potential between colour charges in this phase. The diameter of the thick vortices in unprojected configuration have been investigated, too. We find that vortices overlap considerably and rather resemble a liquid than a dilute gas.

The investigations reported above have been done in the quenched approximation, where the influence of dynamic matter fields is neglected. In chapter 6 we find for the SU(2) gauge-Higgs theory strong evidence for center dominance, as we have found before for the quenched theory. Vortices still can encode the degrees of freedom responsible for quark confinement. Using the highly non-local observable  $s_w$ , the average vortex size which is sensitive to percolation, as an order parameter, we could show that the thermodynamic phase transition line in the SU(2) gauge-Higgs phase diagram ending at some critical point can be continued down to the  $\beta = 0$  axis by a “Kertész” line. As in the Ising spin system, the Kertész line is a line of percolation transitions, with the free energy analytic across the transition. It separates the region of P-vortex percolation present in the “confined” phase from the Higgs phase without P-vortex percolation. In the confined phase, the influence of the Higgs field on vortices is very weak, in agreement with the center model of confinement. Methods to investigate this influence have yet to be developed.

Finally, we applied in chapter 7 the vortex model to another property of infrared, long range QCD, namely the topological properties of gauge fields. We could show that the topological charge characterising the topological sector of gauge field configurations can be calculated from intersections and writhing points of P-vortex surfaces. After removing various ambiguities we get a value for the topological susceptibility which is compatible with the result obtained from unprojected configurations.

To conclude the vortex model provides a unified picture for the low energy, non-perturbative sector of the strong interaction, explaining both confinement and the topological properties of QCD.

# Bibliography

- [ACY78] Y. Aharonov, A. Casher, and S. Yankielowicz. Instantons and confinement. *Nucl. Phys.*, B146:256, 1978.
- [ADdF00] C. Alexandrou, M. D’Elia, and P. de Forcrand. The relevance of center vortices. *Nucl. Phys. Proc. Suppl.*, 83:437, 2000.
- [AdFD00] C. Alexandrou, P. de Forcrand, and M. D’Elia. The role of center vortices in QCD. *Nucl. Phys.*, A663:1031, 2000.
- [Adl81] S.L. Adler. Over-relaxation method for the Monte Carlo evaluation of the partition function for multiquadratic actions. *Phys. Rev.*, D23:2901, 1981.
- [AO80a] J. Ambjørn and P. Olesen. A color magnetic vortex condensate in QCD. *Nucl. Phys.*, B170:265–282, October 1980.
- [AO80b] J. Ambjørn and P. Olesen. On the formation of a random color magnetic quantum liquid in QCD. *Nucl. Phys.*, B170:60–78, August 1980.
- [AOP84] Jan Ambjorn, P. Olesen, and C. Peterson. Stochastic confinement and dimensional reduction. 2. three- dimensional  $su(2)$  lattice gauge theory. *Nucl. Phys.*, B240:533, 1984.
- [AS68a] M. F. Atiyah and I. M. Singer. The index of elliptic operators. 1. *Annals Math.*, 87:484–530, 1968.
- [AS68b] M. F. Atiyah and I. M. Singer. The index of elliptic operators. 3. *Annals Math.*, 87:546–604, 1968.
- [BC80] Tom Banks and A. Casher. Chiral symmetry breaking in confining theories. *Nucl. Phys.*, B169:103, 1980.
- [BEF01] Roman Bertle, Michael Engelhardt, and Manfred Faber. Topological susceptibility of Yang-Mills center projection vortices. *Phys. Rev.*, D64:074504, 2001.
- [Ber98] Roman Bertle. Die Struktur projizierter  $Z_2$ -Vortices in der gluonischen Gitter QCD. Master’s thesis, Technischen Universität Wien, 1998.

## Bibliography

- [BF02] Roman Bertle and Manfred Faber. Vortices, confinement and Higgs fields. In Nora Brambilla and Giovanni M. Prosperi, editors, *Quark Confinement and the Hadron Spectrum V: Proceedings*, Singapore, 2002. World Scientific.
- [BFGO99] Roman Bertle, Manfred Faber, Jeff Greensite, and Štefan Olejník. The structure of projected center vortices in lattice gauge theory. *J. High Energy Phys.*, 03:019, 1999.
- [BFGO00] Roman Bertle, Manfred Faber, Jeff Greensite, and Štefan Olejník. P-vortices, gauge copies, and lattice size. *JHEP*, 10:007, 2000.
- [BFGO04] Roman Bertle, Manfred Faber, Jeff Greensite, and Stefan Olejnik. Center dominance in SU(2) gauge-Higgs theory. *Phys. Rev.*, D69, 2004.
- [BFH<sup>+</sup>93] G. S. Bali, J. Fingberg, Urs M. Heller, F. Karsch, and K. Schilling. The spatial string tension in the deconfined phase of the (3+1)-dimensional su(2) gauge theory. *Phys. Rev. Lett.*, 71:3059–3062, 1993.
- [BFH02] Roman Bertle, Manfred Faber, and Albert Hirtl. Vortices in the SU(2)-Higgs model: Vortices and the covariant adjoint Laplacian. *Nucl. Phys. Proc. Suppl.*, 106:664–666, 2002.
- [BIL<sup>+</sup>91] V. G. Bornyakov, E. M. Ilgenfritz, M. L. Laursen, V. K. Mitryushkin, M. Müller-Preussker, A. J. van der Sijs, and A. M. Zadorozhnyi. The density of monopoles in SU(2) lattice gauge theory. *Phys. Lett.*, B261:116–122, 1991.
- [BKP01] V. G. Bornyakov, D. A. Komarov, and M. I. Polikarpov. P-vortices and drama of Gribov copies. *Phys. Lett.*, B497:151–158, 2001.
- [BKPV00] V. G. Bornyakov, D. A. Komarov, M. I. Polikarpov, and A. I. Veselov. P-vortices, nexuses and effects of gauge copies. *JETP Lett.*, 71:231, 2000.
- [BPST75] A. A. Belavin, Alexander M. Polyakov, A. S. Shvarts, and Yu. S. Tyupkin. Pseudoparticle solutions of the yang-mills equations. *Phys. Lett.*, B59:85–87, 1975.
- [BSS95] G. S. Bali, K. Schilling, and C. Schlichter. Observing long color flux tubes in SU(2) lattice gauge theory. *Phys. Rev.*, D51:5165–5198, 1995.
- [BVZ99] B. L. G. Bakker, A. I. Veselov, and M. A. Zubkov. Central dominance and the confinement mechanism in gluodynamics. *Phys. Lett.*, B471:214, 1999.
- [BW87] Frank R. Brown and Thomas J. Woch. Overrelaxed heat bath and metropolis algorithms for accelerating pure gauge monte carlo calculations. *Phys. Rev. Lett.*, 58:2394, 1987.

## Bibliography

- [CDG78] Jr. Callan, Curtis G., Roger F. Dashen, and David J. Gross. Toward a theory of the strong interactions. *Phys. Rev.*, D17:2717, 1978.
- [Cer85] V. Cerny. Thermodynamical approach to the traveling salesman problem: An efficient simulation algorithm. *Journal of Optimization Theory and Applications*, 45(1):41–51, 1985.
- [Cor79] J. M. Cornwall. Quark confinement and vortices in massive gauge-invariant QCD. *Nucl. Phys.*, B157:392–412, October 1979.
- [Cor98] John M. Cornwall. Nexus solitons in the center vortex picture of QCD. *Phys. Rev.*, D58:105028, 1998.
- [Cor00] John M. Cornwall. Center vortices, nexuses, and fractional topological charge. *Phys. Rev.*, D61:085012, 2000.
- [CPVZ99] M. N. Chernodub, M. I. Polikarpov, A. I. Veselov, and M. A. Zubkov. Aharonov-bohm effect, center monopoles and center vortices in SU(2) lattice gluodynamics. *Nucl. Phys. Proc. Suppl.*, 73:575–577, 1999.
- [Cre80] Michael Creutz. Monte carlo study of quantized SU(2) gauge theory. *Phys. Rev.*, D21:2308–2315, 1980.
- [Cre87] Michael Creutz. Overrelaxation and monte carlo simulation. *Phys. Rev.*, D36:515, 1987.
- [DDFGO96] Luigi Del Debbio, Manfred Faber, Jeff Greensite, and Štefan Olejník. Casimir scaling vs. abelian dominance in qcd string formation. *Phys. Rev.*, D53:5891–5897, 1996.
- [dFD99] Philippe de Forcrand and Massimo D’Elia. On the relevance of center vortices to QCD. *Phys. Rev. Lett.*, 82:4582–4585, 1999.
- [DFG<sup>+</sup>98] Luigi Del Debbio, Manfred Faber, J. Giedt, Jeff Greensite, and Štefan Olejník. Detection of center vortices in the lattice Yang-Mills vacuum. *Phys. Rev.*, D58:094501, 1998.
- [DFGO97] Luigi Del Debbio, Manfred Faber, Jeff Greensite, and Štefan Olejník. Center dominance and Z(2) vortices in SU(2) lattice gauge theory. *Phys. Rev.*, D55:2298–2306, 1997.
- [DFGO98] Luigi Del Debbio, Manfred Faber, Jeff Greensite, and Štefan Olejník. Center dominance, center vortices, and confinement. In P. H. Damgaard and J. Jurkiewicz, editors, *New Developments in Quantum Field Theory*, New York – London, 1998. Plenum Press.
- [dFP00a] P. de Forcrand and M. Pepe. Laplacian center vortices. In H. Suganuma, M. Fukushima, and H. Toki, editors, *Quantum chromodynamics and color confinement*, pages 141–149, Singapore, 2000. World Scientific.

## Bibliography

- [dFP00b] Philippe de Forcrand and Owe Philipsen. Adjoint string breaking in 4d SU(2) yang-mills theory. *Phys. Lett.*, B475:280, 2000.
- [dFP01] P. de Forcrand and M. Pepe. Center vortices and monopoles without lattice Gribov copies. *Nucl. Phys.*, B598:557–577, 2001.
- [ELRT98] Michael Engelhardt, Kurt Langfeld, Hugo Reinhardt, and Oliver Tennert. Interaction of confining vortices in SU(2) lattice gauge theory. *Phys. Lett.*, B431:141–146, 1998.
- [ELRT00] Michael Engelhardt, Kurt Langfeld, Hugo Reinhardt, and Oliver Tennert. Deconfinement in SU(2) Yang-Mills theory as a center vortex percolation transition. *Phys. Rev.*, D61:054504, 2000.
- [Eng00] Michael Engelhardt. Center vortex model for the infrared sector of yang-mills theory: Topological susceptibility. *Nucl. Phys.*, B585:614, 2000.
- [Eng02] Michael Engelhardt. Center vortex model for the infrared sector of yang-mills theory: Quenched dirac spectrum and chiral condensate. *Nucl. Phys.*, B638:81–110, 2002.
- [ER00a] Michael Engelhardt and Hugo Reinhardt. Center projection vortices in continuum yang-mills theory. *Nucl. Phys.*, B567:249, 2000.
- [ER00b] Michael Engelhardt and Hugo Reinhardt. Center vortex model for the infrared sector of yang-mills theory: Confinement and deconfinement. *Nucl. Phys.*, B585:591–613, 2000.
- [Fey81] R. P. Feynman. The qualitative behavior of Yang-Mills theory in (2+1)-dimensions. *Nucl. Phys.*, B188:479, 1981.
- [FGO98] Manfred Faber, Jeff Greensite, and Štefan Olejník. Casimir scaling from center vortices: Towards an understanding of the adjoint string tension. *Phys. Rev.*, D57:2603–2609, 1998.
- [FGO99a] Manfred Faber, Jeff Greensite, and Štefan Olejník. Center projection with and without gauge fixing. *JHEP*, 01:008, 1999.
- [FGO99b] Manfred Faber, Jeff Greensite, and Štefan Olejník. Evidence for a center vortex origin of the adjoint string tension. *Acta Phys. Slov.*, 49:177, 1999.
- [FGO00] Manfred Faber, Jeff Greensite, and Štefan Olejník. What are the confining field configurations of strong-coupling lattice gauge theory? *JHEP*, 06:041, 2000.
- [FGO01a] Manfred Faber, Jeff Greensite, and Štefan Olejník. Direct Laplacian center gauge. *JHEP*, 11:053, 2001.

- [FGO01b] Manfred Faber, Jeff Greensite, and Štefan Olejník. Remarks on the Gribov problem in direct maximal center gauge. *Phys. Rev.*, D64:034511, 2001.
- [FGOY99] Manfred Faber, Jeff Greensite, Štefan Olejník, and D. Yamada. The vortex-finding property of maximal center (and other) gauges. *JHEP*, 12:012, 1999.
- [FS79] Eduardo Fradkin and Stephen H. Shenker. Phase diagrams of lattice gauge theories with Higgs fields. *Phys. Rev.*, D19:3682, 1979.
- [GLSR00] J. Gattnar, K. Langfeld, A. Schafke, and Hugo Reinhardt. Center-vortex dominance after dimensional reduction of SU(2) lattice gauge theory. *Phys. Lett.*, B489:251–258, 2000.
- [GO02] Jeff Greensite and Štefan Olejník. K-string tensions and center vortices at large  $n$ . *JHEP*, 09:039, 2002.
- [GO04] Jeff Greensite and Štefan Olejník. Adventures in Coulomb gauge. In H. Suganuma, N. Ishii, M. Oka, H. Enyo, T. Hatsuda, T. Kunihiro, and K. Yazaki, editors, *COLOR CONFINEMENT AND HADRONS IN QUANTUM CHROMODYNAMICS*, pages 152–163. World Scientific, May 2004.
- [GOP<sup>+</sup>05] Jeff Greensite, Štefan Olejník, M. Polikarpov, S. Syritsyn, and V. Zakharov. Localized eigenmodes of covariant laplacians in the yang-mills vacuum. *Phys. Rev.*, D71:114507, 2005.
- [GOZ04] Jeff Greensite, Štefan Olejník, and Daniel Zwanziger. Coulomb energy, remnant symmetry, and the phases of non-Abelian gauge theories. *Phys. Rev.*, D69:074506, 2004.
- [GPGAM<sup>+</sup>00] M. Garcia Perez, A. Gonzalez-Arroyo, A. Montero, C. Pena, and Pierre van Baal. Recent results on self-dual configurations on the torus. *Nucl. Phys. Proc. Suppl.*, 83:464–466, 2000.
- [GR02] F. Gliozzi and A. Rago. Monopole clusters, center vortices, and confinement in a Z(2) gauge-Higgs system. *Phys. Rev.*, D66:074511, 2002.
- [Gre03] Jeff Greensite. The confinement problem in lattice gauge theory. *Prog. Part. Nucl. Phys.*, 51:1, 2003.
- [Hir00] Albert Hirtl. Untersuchungen zur Vortexstruktur des Quarkconfinements. Master’s thesis, Technischen Universität Wien, 2000.
- [HJK92] H. J. Herrmann, W. Janke, and F. Karsch, editors. *3. Proceedings of the Workshop on Dynamics of First Order Phase Transitions*, 1992.

## Bibliography

- [HLST00] A. Hart, B. Lucini, Z. Schram, and M. Teper. Vortices and confinement in hot and cold  $d = 2+1$  gauge theories. *JHEP*, 06:040, 2000.
- [Ish89] Chris J. Isham. *Modern Differential Geometry for Physics*. Lecture notes in Physics. World Scientific, 1989.
- [IV97] B.R. Iyer and C.V. Vishveshwara. *Geometry, fields and Cosmology*. Kluwer Academic Publishers, 1997.
- [JLNV85] J. Jersák, C. B. Lang, T. Neuhaus, and G. Vones. Properties of phase transitions of the lattice  $SU(2)$  Higgs model. *Phys. Rev.*, D32:2761, 1985.
- [KdF03] Slavo Kratochvila and Philippe de Forcrand. Observing string breaking with wilson loops. *CERN-TH-2003-119*, 2003.
- [Ker89] János Kertész. Existence of weak singularities when going around the liquid-gas critical point. *Physica*, A161:58, 1989.
- [KGV83] S. Kirkpatrick, C. D. Gelatt, and M. P. Vecchi. Optimization by simulated annealing. *Science, Number 4598, 13 May 1983*, 220, 4598:671–680, 1983.
- [KHK<sup>+</sup>02] Daniel-Jens Kusterer, John Hedditch, Waseem Kamleh, Derek B. Leinweber, and Anthony G. Williams. Low-lying eigenmodes of the wilson-dirac operator and correlations with topological objects. *Nucl. Phys.*, B628:253–269, 2002.
- [KLL95] F. Karsch, E. Laermann, and M. Lütgemeier. Three-dimensional  $SU(3)$  gauge theory and the spatial string tension of the  $(3+1)$ -dimensional finite temperature  $SU(3)$  gauge theory. *Phys. Lett.*, B346:94–98, 1995.
- [KLSW87] A. S. Kronfeld, M. L. Laursen, G. Schierholz, and U. J. Wiese. Monopole condensation and color confinement. *Phys. Lett.*, B198:516, 1987.
- [KN63] Kobayashi and Nomizu. *Foundations of Differential Geometry*. Wiley, New York, 1963.
- [Kne99] Francesco Knechtli. *The static potential in the  $SU(2)$  Higgs model*. PhD thesis, Humboldt-Universität zu Berlin, 1999.
- [KPS81] J. Kuti, J. Polonyi, and K. Szlachanyi. Monte Carlo study of  $SU(2)$  gauge theory at finite temperature. *Phys. Lett.*, B98:199, 1981.
- [KS98] Francesco Knechtli and Rainer Sommer. String breaking in  $SU(2)$  gauge theory with scalar matter fields. *Phys. Lett.*, B440:345–352, 1998.
- [KT99] Tamas G. Kovacs and E. T. Tomboulis. On P-vortices and the Gribov problem. *Phys. Lett.*, B463:104–108, 1999.



## Bibliography

- [KT00] Tamas G. Kovacs and E. T. Tomboulis. Computation of the vortex free energy in  $SU(2)$  gauge theory. *Phys. Rev. Lett.*, 85:704–707, 2000.
- [Lan02] Kurt Langfeld. Lattice effective theory and the phase transition at finite densities. *to appear in proc. Strong and Electroweak Matter*, 2002.
- [LERT00] Kurt Langfeld, Michael Engelhardt, Hugo Reinhardt, and Oliver Tennert. Quantum gauge fixing and vortex dominance. *Nucl. Phys. Proc. Suppl.*, 83:506–508, 2000.
- [LRS01] Kurt Langfeld, Hugo Reinhardt, and A. Schafke. Center vortex properties in the Laplace center gauge of  $SU(2)$  Yang-Mills theory. *Phys. Lett.*, B504:338–344, 2001.
- [LRT98] Kurt Langfeld, Hugo Reinhardt, and Oliver Tennert. Confinement and scaling of the vortex vacuum of  $SU(2)$  lattice gauge theory. *Phys. Lett.*, B419:317–321, 1998.
- [LTER99] Kurt Langfeld, Oliver Tennert, Michael Engelhardt, and Hugo Reinhardt. Center vortices of Yang-Mills theory at finite temperatures. *Phys. Lett.*, B452:301, 1999.
- [LW01] Martin Lüscher and Peter Weisz. Locality and exponential error reduction in numerical lattice gauge theory. *J. High Energy Phys.*, 09:010, 2001.
- [Mac80a] G. Mack. Properties of lattice gauge theory models at low temperatures. In Gerard 't Hooft et al, editor, *Recent Developments in Gauge Theories*. Plenum, New York, 1980.
- [Mac80b] Gerhard Mack. Predictions of a theory of quark confinement. *Phys. Rev. Lett.*, 45:1378, 1980.
- [MM94] I. Montvay and G. Münster. *Quantum Fields on a Lattice*. Cambridge University Press, 1994.
- [MMO82] Gerhard Mack and Hildegard Meyer-Ortmanns. A disorder parameter that tests for confinement in gauge theories with quark fields. *Nucl. Phys.*, B200:249, 1982.
- [MO84] Hildegard Meyer-Ortmanns. The vortex free energy in the screening phase of the  $Z(2)$  Higgs model. *Nucl. Phys.*, B235:115, 1984.
- [Mon01] Alvaro Montero. Detection of vortices with Laplacian center gauge. *Phys. Lett.*, B517:142–148, 2001.
- [MP79] G. Mack and V. B. Petkova. Comparison of lattice gauge theories with gauge groups  $Z(2)$  and  $SU(2)$ . *Annals Phys.*, 123:442, 1979.

## Bibliography

- [MP80] G. Mack and V. B. Petkova. Sufficient condition for confinement of static quarks by a vortex condensation mechanism. *Annals Phys.*, 125:117, 1980.
- [MP82] G. Mack and E. Pietarinen. Monopoles, vortices, and confinement. *Nucl. Phys.*, B205:141, 1982.
- [MT87] C. Michael and M. Teper. Towards the continuum limit of  $su(2)$  lattice gauge theory. *Phys. Lett.*, B199:95, 1987.
- [Nak90] Mikio Nakahara. *Geometry, topology and physics*. Bristol, 1990.
- [NO79] H. B. Nielsen and P. Olesen. Gauge and rotational invariance of domain and quantized homogeneous color fields. *Nucl. Phys.*, B160:380–396, December 1979.
- [Ole82] P. Olesen. Confinement and random fields. *Nucl. Phys.*, B200:381, 1982.
- [Rot92] H. J. Rothe. *Lattice Gauge Theory, An Introduction*. World Scientific, 1992.
- [RT01] Hugo Reinhardt and Torsten Tok. Abelian and center gauge fixing in continuum Yang-Mills theory for general gauge groups. *Phys. Lett.*, B500:173–182, 2001.
- [Sat02] Helmut Satz. Cluster percolation and thermal critical behaviour. *Comput. Phys. Commun.*, 147:46–51, 2002.
- [Sei78] E. Seiler. Upper bound on the color-confining potential. *Phys. Rev.*, D18:482–483, 1978.
- [Shu82] Edward V. Shuryak. The role of instantons in quantum chromodynamics. 1. physical vacuum. *Nucl. Phys.*, B203:93, 1982.
- [Shu88] Edward V. Shuryak. Toward the quantitative theory of the topological effects in gauge field theories. 1. phenomenology and the method of collective coordinates. *Nucl. Phys.*, B302:559, 1988.
- [Sta00] Ion-Olimpiu Stamatescu. On the topological structure of the QCD vacuum: Problems and results of lattice studies. In Valya Mitrjushkin and Gerrit Schierholz, editors, *Dubna 1999, Lattice fermions and structure of the vacuum*, volume 553 of *NATO science series: C: Mathematical and Physical Sciences*, pages 287–298, Dordrecht Hardbound, 2000. Kluwer Academic Publishers.
- [Ste00] P. W. Stephenson. Centre vortices and their friends. In M. Campostrini, S. Caracciolo, L. Cosmai, A. Di Giacomo, F. Rapuano, and P. Rossi, editors, *Lattice '99; Proceedings of the XVIIth International Symposium on Lattice Field Theory*, volume 83, pages 544–546. North Holland, 2000.

## Bibliography

- [SU95] Roman U. Sexl and Helmuth K. Urbantke. *Gravitation und Kosmologie*. Spektrum Akad. Verl., Heidelberg, 1995. Allgemeine Relativitätstheorie, Gravitationstheorie und Kosmologie.
- [SV93] Edward V. Shuryak and J. J. M. Verbaarschot. Quark propagation in the random instanton vacuum. *Nucl. Phys.*, B410:37–54, 1993.
- [SY82] B. Simon and L. G. Yaffe. Rigorous perimeter law upper bound on Wilson loops. *Phys. Lett.*, B115:145–147, 1982.
- [tH78] Gerard 't Hooft. On the phase transition towards permanent quark confinement. *Nucl. Phys.*, B138:1–25, 1978.
- [tH79] Gerard 't Hooft. A property of electric and magnetic flux in nonabelian gauge theories. *Nucl. Phys.*, B153:141, 1979.
- [vB82] Pierre van Baal. Some results for SU(N) gauge fields on the hypertorus. *Commun. Math. Phys.*, 85:529, 1982.
- [vB95] Pierre van Baal. Some comments on Laplacian gauge fixing. *Nucl. Phys. Proc. Suppl.*, 42:843, 1995.
- [vdS97] A. J. van der Sijs. Laplacian abelian projection. *Nucl. Phys. Proc. Suppl.*, 53:535–537, 1997.
- [vdS98] A. J. van der Sijs. Abelian projection without ambiguities. *Prog. Theor. Phys. Suppl.*, 131:149, 1998.
- [Ven79] G. Veneziano. U(1) without instantons. *Nucl. Phys.*, B159:213–224, 1979.
- [Vin78] P. Vinciarelli. Fluxon solutions in nonabelian gauge models. *Phys. Lett.*, B78:485, 1978.
- [Vin95] Jeroen C. Vink. Investigation of Laplacian gauge fixing for U(1) and SU(2) gauge fields. *Phys. Rev.*, D51:1292–1297, 1995.
- [VW92] Jeroen C. Vink and Uwe-Jens Wiese. Gauge fixing on the lattice without ambiguity. *Phys. Lett.*, B289:122–126, 1992.
- [Wil44] K. G. Wilson. Confinement of quarks. *Phys. Rev.*, D10:2445, 1944.
- [Wit79] Edward Witten. Current algebra theorems for the U(1) 'Goldstone boson'. *Nucl. Phys.*, B156:269, 1979.
- [Yon78] Tamiaki Yoneya. Z(N) topological excitations in Yang-Mills theories: Duality and confinement. *Nucl. Phys.*, B144:195, 1978.

# Index

- Abelian Laplacian gauge, **45**
- Abelian monopole, 31, 49, 62, 120, 127
- Abelian projection, **31**
- aperiodic gauge transformation, *see* singular gauge transformation
- area law, **25**, 78, 84, 97
- asymptotic scaling, **19**
- Atiya-Singer index theorem, 118
- average cluster size, 80
  
- B-plaquette, 85
- Banks-Casher relation, 118
- $\beta$ , *see* coupling constant, inverse
- Bianchi identity, 12, 68, 71
- blocking, 124
  
- Casimir scaling, **28**, 34, 97, 124
- cell complex, **13**, 82
- center, 26
  - dominance, **33**
  - projection, **29**
- charge sector, 17
- chiral symmetry breaking, 34, 117, 118
- confined phase, **22**, 100
- connection form, 11
- coupling constant
  - gauge, 11
  - inverse, 16, 33
- covariant derivative, 11
- Creutz ratio, **25**, 35
- critical point, 18
- cross-cap, *see* Möbius strip
- crossover, 102
- $\chi$ SB, *see* chiral symmetry breaking
- curvature form, 12
  
- cycle, 50
  
- deconfined phase, **84**, 102
- detailed balance, 20
- Dirac volume, **27**, 51, **68**
- discontinuous gauge transformation, *see* singular gauge transformation
- DLCG, *see* Laplacian center gauge, direct
- DMCG, *see* maximal center gauge, direct
- dual lattice, **66**
  
- E-plaquette, 85
- elementary cube, **68**, 73
  - transformation, **68**, 121
- elementary plaquette, **67**
- Euler characteristic, 81, 92
- exterior covariant derivative, 11, 46
- external charge, *see* static charge
  
- free energy
  - quark, 26, 103
  - vortex, **28**, 96
- fundamental group, 52
  
- gauge coupling constant, *see* coupling constant, gauge
- gauge field, 10
- gauge transformation, 10
- genus, 82, 92
- Gribov copies, **21**, 33, 44, 45, 47, 73
- Gribov problem, *see* Gribov copies
  
- Haar measure, 16
- Hamilton

- formalism, 16
- operator, 23
- heatbath algorithm, 20, 102
- Higgs phase, **22, 100**
- Hilbert space, 16
- holonomy, 12
- IMCG, *see* maximal center gauge, indirect
- instanton, **118**
- intersection point, **122**
- inverse coupling, *see* coupling constant, inverse
- Kertész line, **112**
- LALG, *see* Laplacian adjoint Landau gauge
- Laplace operator, 45
- Laplacian adjoint Landau gauge, **48**
- Laplacian center gauge, **47**
  - direct, **49**
- Laplacian gauge, **45, 120**
- LCG, *see* Laplacian center gauge
- Lie algebra, 11
- Lie group, 10
  - simple, 49
- linking number, 50, **71**
- Möbius strip, 82, 91
- MAG, *see* maximal Abelian gauge
- maximal Abelian gauge, **31, 58, 120**
- maximal center gauge, **30**
  - direct, **31**
  - indirect, 31, 120
- MCG, *see* maximal center gauge
- Metropolis algorithm, 20, 102
- monopole line, *see* Abelian monopole
- $N$ -ality, **26**
- negative links, **66**
- orientability, 91, 119
- orientation, 81, 119
- over-relaxation, 21, 35, 44
- overlap, 23
- P-link, **67**
- P-plaquette, **27, 30, 67**
- P-vortex, 9, **30, 67**
- P-vortex plaquette, *see* P-plaquette
- parallel transport, 12, 23
- path ordering operator, 12
- perimeter law, **25, 78, 97**
- $\pi_1$ , *see* fundamental group
- plaquette variable, 14, 66
- polar decomposition, 48
- Polyakov loop, **25**
- Pontryagin index, **13, 117**
- precocious linearity, **36, 76**
- principle bundle, 10
- pure gauge, 32
- quenched approximation, **22**
- $r_0$ , *see* string breaking, distance
- Regge trajectories, 8
- representation class, *see*  $N$ -ality
- scaling window, **19, 36**
- $\sigma$ , *see* string tension
- simulated annealing, 21, 44
- singular gauge transformation, **26, 51**
- singular point, **119**
- singular value decomposition, 48
- static charge, 17
- static potential, **23**
- string breaking, **22, 100**
  - distance, 22
- string tension, 19, **25**
- strong coupling, 15, 35
- strong ergodicity, 19
- structure constants, 11
- topological
  - charge, *see* Pontryagin index
  - quantum number, *see* Pontryagin index
  - susceptibility, 34, **117**
  - winding number, *see* Pontryagin index
- touching point, **122**

- triple product, 53
  - normalised, 57
- two-loop approximation, 19
- unitary gauge, **102**
- universality, 18
- vacuum expectation value, 15
- vector bundle, 10
- vortex
  - area, 72
  - density, 71
  - finding property, **30**, 32, 52
  - free energy, *see* free energy, vortex
  - plaquette, **27**
  - removal procedure, 33, 119
  - smoothing procedure, **73**, 121, 124
  - thick, **28**, 29, 49
  - thin, **27**, 49
- vortex-limited Wilson loops, **34**, 96
- weak coupling expansion, 15
- weighted average vortex size, **79**, 89
- Wilson
  - action, 16
  - criterion, **25**
  - loop, **23**
- Wilson line, *see* Polyakov loop
- Witten-Veneziano estimate, 118
- writhing point, **122**
- Yang-Mills action, 16
- Yukawa potential, 100
- $Z_N$ , *see* center

# Lebenslauf

Dipl.-Ing. Roman Bertle  
Dettergasse 1/2/2/7  
A-1160 Wien  
email: bertle@kph.tuwien.ac.at

**Geburt:** 2. Juni 1974 in Bludenz, Österreich

## **Ausbildung:**

- 09/80 – 06/84 Besuch der Volksschule in Schruns
- 09/84 – 06/92 Besuch des neusprachlichen Gymnasiums Bludenz
- 10/92 – 06/98 Diplomstudium der Technischen Physik an der TU Wien
- 06/97 – 04/98 Diplomarbeit am Institut für Kernphysik  
“Die Struktur projizierter Z2-Vortices in der gluonischen Gitter QCD”
- 17.6.1998 Sponsion zum Diplom-Ingenieur an der TU Wien
- 03/99 – 10/05 Doktoratsstudium an der TU Wien, Atominstitut / Abteilung für Kernphysik  
Dissertationsthema “The Vortex Model in Lattice Quantum Chromodynamics”